Aus dem Institut für Robotik und Kognitive Systeme

Direktor:
Prof. Dr.-Ing. Achim Schweikard

Design of a Surgical Robot and Brain Exploration Framework for Small Animal Stereotaxy

Inauguraldissertation
zur
Erlangung der Doktorwürde
der Universität zu Lübeck
- Aus der Technisch-Naturwissenschaftlichen Fakultät -

Vorgelegt von Lukas Ramrath
geboren in Kronberg im Taunus

Lübeck, im Oktober 2008

Prüfungsausschuss

Vorsitzender	Prof. Dr.-Ing. Erik Maehle
Berichterstatter	Prof. Dr.-Ing. Achim Schweikard
	Prof. Dr. rer. nat. Ulrich G. Hofmann
Mündliche Prüfung:	19. Dezember 2008
Zum Druck genehmigt:	30. September 2009

- gezeichnet Prof. Dr. rer. nat. Jürgen Prestin -

Dekan der Technisch-Naturwissenschaftlichen Fakultät
der Universität zu Lübeck

Für Wenke

Danksagung

Der Dank auf den ersten Seiten einer Arbeit ist eine für mich sehr wichtige Sache. Denn nur hier kann ich das persönliche Kapitel schreiben, das ebenso wichtig ist wie all die folgend fachlichen. Es gibt viele Hauptpersonen in diesem Kapitel, eine jede mit eigener Rolle.
Traditionellerweise gilt der Auftaktdank den Hauptbetreuern dieser Arbeit. An erster Stelle Herrn Prof. Schweikard, der mir zu jedem Zeitpunkt die Freiheit gegeben hat, diese Arbeit zu realisieren und mich, wenn nötig, hilfreich unterstützt hat. An zweiter Stelle danke ich Uli, der, trotz hundert anderer Dinge auf seinem Schreibtisch, immer gute Ideen, Anrufe und Ratschläge in petto hatte. Und diese dann direkt und lautstark artikuliert hat. Das war, besonders auf der nichtfachlichen Seite, immer ein Gewinn.
Gleich danach kommen die ROBler, vorneweg Conni. Ihr wart (teilweise) halbwegs würdige Kickergegner, auch wenn ihr den zweimaligen Gewinn der internen Meisterschaft nie ernsthaft gefährden konntet. Die Zusammenarbeit, auch ausserhalb des Kickertischs, hat mir Spaß gemacht. Besonders mit denen, denen das Kickern nach eigener Meinung nicht in den Schoss gefallen ist und die es trotzdem bis zum Professor gebracht haben. Bedanken möchte ich mich auch bei meinen HiWis, am Tisch solltet ihr noch ein bisschen üben, am Computer eigentlich nicht.
Und dann gab es noch eine Menge anderer Personen, ohne die wohl einige der folgenden Kapitel glatt fehlen würden. Vorneweg Gereon und Prof. Moser, die das Interdisziplinäre und damit auch das Spannende dieser Arbeit mit großem (fachlichen) Entgegenkommen unterstützt haben. Auch Prof. Tronnier und Dr. Bonsanto seien an dieser Stelle erwähnt. Sehr, weil zum Teil ganz anders, bereichernd waren auch die Mitglieder ihrer Arbeitsgruppen, mit denen es ausnahmslos Spaß gemacht hat zu arbeiten, zu verreisen oder zu grillen. Und es gab auch jemand außerhalb der Uni, ohne den diese Arbeit nicht möglich gewesen wäre: Ich danke Matthias Goeke und den involvierten Mitarbeitern seiner IBG.
Hauptpersonen, die auch ohne Fachwissen und Kickerkünste diese Arbeit immer interessant fanden (mussten), sind natürlich auch wichtig: meine Familie, besonders meine Eltern und Geschwistern, waren eine wichtige Begleitung.
Eine Faustregel gilt auch für dieses Werk: keine Spannung(en) ohne Liebesgeschichte. Und die umfasst sogar die Geburt unserer wundervollen Tochter Tomma. Mein Wenk, du hast diese Arbeit von Anfang an begleitet. Vielen Dank für deine Zeit, dein Ohr, deine Unterstützung. Es ist auch deine Arbeit.
Es sollte noch ein Dank ausgesprochen werden. Der aber braucht keine Worte.

Lukas Ramrath

Zusammenfassung

Diese Arbeit präsentiert die Entwicklung einer computer- und robotergestützten Umgebung für stereotaktische Eingriffe an Kleintieren. Auf Basis einer detaillierten Analyse dieser Eingriffe wird das Konzept für eine solche Umgebung entwickelt. Zwei Hauptbestandteile werden behandelt. Der erste Teil umfasst die Entwicklung eines robotischen Assistenzsystems für die Kleintierstereotaxie. Er informiert über die kinematische Entwicklung, die Konstruktion und die mechanischen Bauteile des Systems. Weiterhin erfolgt eine analytische Beschreibung des Systems in Form einer kinematischen Vorwärts- und Rückwärtsrechnung und die Vorstellung einer Kalibriermethode. Der zweite Teil präsentiert die Entwicklung einer Softwareumgebung zur Hirnexploration, in die das Assistenzsystem integriert ist. Zwei Unterbereiche werden adressiert. Erstens, eine stereotaktische Bedienungsumgebung, die Module zur Eingriffsplanung, Registrierung und Eingriffssteuerung enthält. Der zweite Unterbereich stellt die Nutzung der Optischen Kohärenztomographie (OCT) im Kontext von Neurobildgebung und -exploration vor.
Die Leistungsfähigkeit der entwickelten computer- und robotergestützten Stereotaxieumgebung wird dann unter Prüfstandsbedingungen und unter klinischen Bedingungen analysiert. Zuerst wird dabei die mechanische Positioniergenauigkeit untersucht. In einem zweiten Schritt werden zwei zukünftige Anwendungen im Kontext von Hirnexploration mit Hilfe der Stereotaxieumgebung getestet: robotergestützte Mikroelelektrodenableitungen und robotergestützte, intrakranielle Bildgebung mit Hilfe der OCT. Basierend auf den aufgenommenen Daten werden Konzepte zur Datenanalyse mit Hinblick auf elektrophysiologische und optische Hirnkartographierung vorgestellt und evaluiert. Im Bereich der OCT-Bildgebung werden weiterhin zwei Methoden zur Segmentierung und Filterung von OCT-basierten Bilddaten vorgestellt.
Die Analyse der mechanischen Positioniergenauigkeit zeigt, dass die vorgestellte Umgebung präzise stereotaktische Eingriffe am Kleintier ermöglicht. Die Ergebnisse der elektrophysiologischen und optischen Datenanalyse unterstützen die Idee einer robotergestützten Hirnkartographierung über charakteristische Eigenschaften einzelner Hirnareale. Die Daten motivieren außerdem die Idee der Nahfeldnavigation in der unmittelbaren Nähe der Instrumentenspitze, welche einen neuen Ansatz zur intrakraniellen Navigation darstellt. Zusammenfassend bietet das entwickelte System neue Möglichkeiten für die Hirnforschung am Kleintiermodell.

Abstract

This thesis presents the development of a computer- and robot-assisted framework for small animal stereotaxy. From a detailed analysis of stereotactic procedures on small animals, a conceptional layout of the framework is described. Two major parts are addressed. The first part presents the design of a robotic assistant for small animal stereotaxy. It provides information on the kinematic design, the construction, and the utilized components. An analytic description of the system is provided by the forward and inverse kinematics. Important issues concerning the operation such as system calibration are outlined. The second part describes the brain exploration software framework integrating the robotic assistant. Two subareas of brain exploration are elaborated on. First, a basic stereotactic control framework which provides planning, registration, and insertion control modalities is presented. Second, the technique of Optical Coherence Tomography (OCT) imaging is set into the context of brain imaging and optical brain exploration.

The resulting computer- and robot-assisted stereotactic framework is then tested with respect to its performance in a testbed setup and in the real surgical scenario. First, the mechanical positioning accuracy is analyzed. Second, the framework is applied to two future applications in the context of brain exploration: robot-assisted microelectrode recordings and robot-assisted intracranial imaging using OCT. Concepts for data analysis pointing towards electrophysiological and optical brain mapping are introduced and evaluated based on the acquired data. Arising in the context of OCT imaging, two methods of image segmentation and filtering adapted to OCT images are presented.

Analyzing the mechanical positioning accuracy shows that the presented framework allows for precise small animal stereotaxy. Results of the electrophysiological and optical data analysis support the idea of robot-assisted brain mapping via characteristic features of certain areas. This, in turn, gives rise to the idea of near field navigation in the vicinity of the probe tip, a novel navigation modality. In summary, the resulting system offers new alternatives for brain research on the small animal model.

Contents

List of Figures

List of Tables

Abbreviations

A/P	anteroposterior coordinate
APSEP	anisotropic propagation-separation
CD	complex diffusion
CoR	center of rotation
CT	computed tomography
DH	Denavit-Hartenberg
DOF	degree-of-freedom
DV	dorsoventral coordinate
FN	false negatives
FOM	figure of merit
FP	false positives
HD	Hausdorff distance
HFS	high frequency stimulation
JC	Jaccard index
MIS	minimal invasive surgery
MRI	magnetic resonance imaging
MSE	mean square error
OCT	Optical Coherence Tomography
PCR	peak contrast ratio
PD	Parkinson's disease
pdf	probability density function
PM	Perona-Malik
POSE	position and orientation matrix
PSEP	propagation-separation
PSNR	peak signal-to-noise ratio
RMP	ramp preserving
SN	substantia nigra
SNR	signal-to-noise ratio
std	standard deviation
STN	subthalamic nucleus
TN	true negatives
TP	true positives

Variables and notations

α_x	angle of rotation about x-axis	λ	Lambda (anatomic landmark on rat skull), wave length, penalty parameter
β	Bregma (anatomic landmark on rat skull)	μ	attenuation coefficient
d	bandwidth update parameter, distance	z	imaging depth, axis of coordinate system
Θ	vector of robot joint variables	t_i	translational joint value of joint i
q_i	rotary joint value of joint i	thr	threshold
O	origin (of a coordinate system)	o_x	offset in x-direction
p^{c1}	pixel coordinates of camera c_1, $p^{c1} = (x^{c1}, y^{c1})$	v	disturbance
P	4×4 position and orientation matrix	p	position vector (4th column of matrix P)
$R_z(\alpha_z)$	3×3 rotation matrix performing rotation about axis z by α_z	$(p)_x$	x-entry of vector p
n	refractive index	E	light field
t	time	c	speed of light, shift parameter
l	length	I	light intensity, image, image intensity (gray value)
Re[e]	real part of expression e	τ	time delay, weight penalty parameter
k	wave number	f	frequency, focal length
d	spot size	σ	standard deviation, threshold
$\bar{f}$	mean value of f	q_z	depth related pixel coordinate at depth z
N	total number of elements, total number of iterations, total number of time steps	$\Gamma_n(s)$	$n \times n$ neighborhood of pixel s
K	edge threshold parameter, kernel function	w	weights
h	bandwith	$\mathbb{O}$	set
$g(p)$	gray value at pixel p	dt	time increment
g	noise corrupted image	f	true (uncorrupted) image
G	Gaussian function	∇	gradient
$\mathcal{K}$	Kullback-Leibler distance	κ	gradient threshold parameter

1 Introduction

The overall goal of this work is to design a computer- and robot-assisted framework for improved brain exploration in the small animal model. The idea arose in the context of new approaches to diagnose and treat movement disorders. Here, one important premise for meaningful reseach is to target small functional areas e.g. in the rat brain. The insertion of medical devices into the animal brain is mostly performed using the technique of stereotaxy which provides an established framework for targeting intracranial areas. For small animals, this is mostly done manually and based on atlas data which easily leads to positioning inaccuracies of the device. The crucial requirement of precision naturally motivates the introduction of robotics into the field of small animal brain research.
As robotic assistants have been successfully applied to human stereotaxy, the design of a robot-assisted framework seems a promising approach to improve the medical device positioning in the small animal brain. In addition to research on movement disorders, such a framework can be used to test promising techniques for advanced brain exploration. Two possible applications are presented in this work. First, there is robot-assisted electrophysiology in the small animal which allows precise analysis and mapping of neural activity in the rodent model. Second, there is robot-assisted optical coherence tomography (OCT) as a new intracranial imaging modality which enables novel options for near field navigation in the brain and functional imaging. Both point towards future research in the context of brain exploration.

1.1 Small animal stereotaxy and problem definition

Small animal stereotaxy presents an important surgical approach in brain research on the rodent model. This kind of research is conducted with regard to manifold medical questions. An exemplary field of research with many unanswered questions is given in the context of movement disorders. Herein, research motivation is additonally pushed by the fact that in aging societies, such as the German one, the incidence of neurological diseases will increase. This tendency consequently turns the focus of research on novel methods for diagnosis and treatment of these disorders. An important element of such research approaches is the animal experiment. This also includes experiments using the small animal model, particulary the rat. An exemplary field is the analysis of deep brain stimulation (DBS) by the means of electrical high frequency stimulation (HFS) which in-

explicably suppresses disease-related symptoms. To investigate the neural network under HFS, probes such as microelectrodes are implanted into the small animal brain and allow for detailed research on the effect of DBS.

The necessary neurosurgical operations on small animals are commonly performed within a stereotactic framework. Herein, path planning is performed based on atlas information which allow for target specification and choice of a desired path of penetration. By these means, measurement devices can be placed at desired intracranial target areas. For research on HFS, exemplary areas include functional areas in the basal ganglia. Targeting these structures in the rat brain, however, cannot be done easily as they are of small size. Within the common approach, probe placement in the rat brain is performed with a manually operated stereotactic frame for small animals (e.g. *Lab Standard Stereotaxic*, Stoelting Co., Wood Dale, IL, USA). Regarding the positioning accuracy, the current stereotactic approaches feature significant deficiencies. These can be classified into two categories: (a) hardware-related shortcomings and (b) biology-related shortcomings. Hardware-related shortcomings include the inadequate design of existing frames. Some frames e.g. do not offer sufficient degrees-of-freedom (DOF) to compensate for a poor fixation of the rat skull (e.g. if the rat skull is tilted). Second, shortcomings result from the manual target calculation and the manual frame handling which is prone to positioning errors. Biology-related sources of errors result from the atlas-based nature of the planning and registration procedure. It presumes a morphological similarity between all tested animals. Additionally, planning is performed based on characteristic landmarks on the rat skull which are defined according to a best fit practice leaving room for user interpretation. In combination, stereotactic procedures result in systematic inaccuracies, low repeatability, and an imprecise correlation of measurement signals to spatial position. Hence, the localization of measured signals to a spatial position is unreliable and targeting has to be proven by post-hoc histology.

These drawbacks naturally motivate the design of an automated and precise positioning system within a stereotactic and minimal-invasive framework. Development of highly precise robotic systems for microsurgery, however, has been mostly focused on the design of supporting devices for the neurosurgeon. Other systems focus on providing the surgeon with maximum dexterity of the corresponding tool in the body (e.g. the *da Vinci System*, Intuitive Surgical Inc., Sunnyvale, CA, USA). Microneurosurgery in small animals has not been researched extensively. A robot-assisted microsurgery system for neurosurgery on the rat brain is presented in [2]. The system enhances the microdexterity of the surgeon which was tested by manipulating vessels in the rat brain. For stereotactic surgery on small animals, only one commercially available system is known. The *Stere-*

oDrive is distributed by the Neurostar GmbH (Sindelfingen, Germany) [3]. The system allows computer controlled positioning of 3 orthogonal axes. It integrates an atlas-based planning module and promises high accuracy and high throughput. Although being motorized, the system features the disadvantages of the translational-type structure, namely that no motorized tilting of the probe is allowed. This contrains the entry paths to the vertical plane of the stereotactic frame. The provided DOF of the system therefore reduce the surgical options which is undesirable for advanced stereotactic surgery in the context of small animal brain research. As a result of the current small animal stereotactic framework, probe placement within the small animal brain, especially in deep structures, cannot be performed reliably. This leads to questionable results and, in some cases, a needless number of sacrificed animals.
To summarize, the presented aspects of movement disorder related research, of stereotactic approaches to small animal brain surgery, and of the introduction of surgical robotics into the field of small animal stereotaxy lead to the basic research motivation of this work and the corresponding problem definition.

1.2 Purpose of this work

The major goal of this research is the development of a small animal neurosurgical framework to allow for high precise probe placement in the animal brain. As the current, manual frameworks for small animal brain stereotaxy (planning and surgery) feature significant shortcomings in terms of accuracy and repeatability, the introduction of robotics presents a promising approach. Therefore, this work proposes the development and application of a computer- and robot-assisted stereotactic environment for rodents. Its major contribution is to reduce the hardware-related errors of existing approaches. In addition, an integrated approach to compensate for biology-based errors such as individual image-based planning and new methods to near field brain exploration will also be outlined. The work consists of three major parts:

1. Design and construction of robotic assistant for stereotactic surgery called Spherical Assistant for Stereotactic Surgery (SASSU),
2. design and implementation of the corresponding brain exploration software, and
3. testing the framework for two potential applications in the context of advanced brain exploration, namely robot-assisted microelectrode recordings and OCT imaging.

The first research goal covers the total process of robot design, from the basic idea to the fully operational state. Based on a thorough analysis of the field of application, it includes the structural layout, the mechanical design, the choice of components (e.g. motors, encoders), the kinematic analysis, the implementation of a basic control software, and the design of a user interface.
The second part is dedicated to establish a fully integrated, computer-assisted stereotactic framework for rats. Integrating all steps of the common surgical procedure, it provides an interactive planning interface based on (a) standardized atlas data and (b) individual computed tomography (CT)-based data. Additionally, it integrates a robot-control interface adapted to the surgical steps and methods to facilitate necessary stereotactic calculations. The resulting computer- and robot-assisted stereotactic system is then tested for two applications arising in the context of precise brain exploration. Two specific techniques are investigated:

1. Robot-assisted electrophysiology using microelectrodes and
2. robot-assisted brain imaging using OCT.

For the field of electrophysiology, this contribution works towards the robot-assisted mapping of electrical activity to an intracranial position and neural structures identified from the image-based planning. This, in a larger scale, motivates the creation of a functional atlas and adequate methods of neural characterization which allow to compare neural signals in different animals. This, in turn, would provide a new dimension for positioning validation as electrical activity is measured directly at the probe tip. Thus, any positioning inaccuracies may be detected and compensated during probe insertion. Furthermore, such a functional atlas could possibly foster the development of control strategies for an accurate placement based on electrical recordings. This essentially provides a novel neuronavigation modality.
The same idea holds for OCT which presents a promising candidate for minimal-invasive, intracranial imaging. As electrophysiology, it provides a method for online target verification. Beyond that functionality, in a broader framework, it can be extended to optical brain mapping and optical identification of brain matter. This, in turn, gives rise to the idea of intraoperative near field neuronavigation which would expand the current neuronavigation framework.
The computer- and robot-assisted framework, however, is not restricted to target verification or enhanced brain exploration. In fact, the precise and repeatable insertion of probes allows a more detailed research on new methods for diagnosis and/or treatment of neural diseases and thus enables a new dimension in brain research.

1.3 Structure

This thesis is organized as follows:
The second chapter provides a short overview of the research-related background, ranging from movement disorders to small animal stereotaxy. The third chapter deduces the requirements for small animal stereotaxy, categorized into hardware and software requirements. The fourth chapter describes the design of a stereotactic micromanipulator for small animal neurosurgery. Starting with a detailed analysis of the common surgical approach and the design of existing frames, a new layout based on the center-of-arc principle is proposed. A detailed kinematic analysis including the forward and inverse kinematic calculation is performed. A comparison of the proposed structure with another center-of-arc stereotactic manipulator in terms of kinematic accuracy supports the structural design. Having found the conceptional layout, details on the mechanical design and the choice of components are provided. This includes the choice of motors, encoder components and the PCI control card. Following the mechanical design, the implementation of an adequate control software is described. Emphasis is put on the robot control framework and the incorporated safety measures.
The fifth chapter deals with the design and implementation of the robot-assisted brain exploration environment for rats. The software is subdivided into multiple modules including a planning module, a registration module, and a probe positioning control module. Special attention is put on safety features incorporated into the software. In addition to the stereotactic planning and control environment, a short introduction into OCT in the context of neuroimaging is given. The integration of OCT into a minimal-invasive setting is presented leading to a single-fibre imaging system. Subsequently, methods to analyze OCT data are presented which are based on the theoretical foundations of OCT imaging. In addition to single fibre data analysis, two methods for automated segmentation of OCT images and a method for speckle noise reduction in OCT images are outlined.
In the sixth chapter, operational results of the proposed stereotactic framework are presented. Details are given for an extensive mechanical accuracy and repeatability analysis which was done in a testing environment. Additionally, results of the afore mentioned applications are presented which comprise (a) results for depth-resolved microelectrode recordings in vivo and (b) depth-resolved single-fibre OCT imaging. In both applications, the probe was inserted gradually on the same trajectory in different animals and hemispheres of the brain. Results furthermore include the analysis of both methodologies with regard to electrical and optical characteristics of brain regions.
Chapter 7 discusses the results of the previous chapter. Special focus is put on the accu-

racy provided by the robotic system and the issues challenging the standardized approach provided by the robot-assisted stereotactic framework.
The last chapter presents a short summary of the work, gives a conclusion, and proposes future enhancements.

2 Clinical background

This chapter gives an overview of the relevant state of the art of the research fields related to this thesis. As the basic idea of the work originates in the field of movement disorder related research, a brief overview of their nature and the current (surgical) forms of treatment is given. A special focus is put on DBS by the means of electrodes, a specific, invasive form of treatment. Based on this overview, the motivation for small animal brain research is outlined. Then, an introduction into the principle of stereotaxy is given which introduces important terminology for the rest of the work.

2.1 Movement disorders: research and treatment

Movement disorders generally describe a group of conditions which are characterized by symptoms like muscle rigidity, tremor, slowing of physical movement (bradykinesia), and a loss of physical movement (akinesia). The most prominent movement disorders are

- Parkinson's disease (PD) and parkinsonism,
- dystonia,
- tremor,
- chorea and Huntington's disease.

Movement disorders are related to diseases of the basal ganglia, a brain system which is located in the basal part of the brain [4]. In a simplistic view, the basal ganglia system is responsible for the modulation of movements [5]. The system consists of different brain regions: the striatum, the caudate nucleus, the global pallidus, the subthalamic nucleus (STN), and the substantia nigra (SN) [6].
Different approaches to the treatment of movement disorders exist and are dependent on the respective syndrome. Most forms of treatment are based on models analyzing the disorder symptoms with regard to malfunctions in the neural network. A lot of models for movement disorders involving basal ganglia functions have been proposed, discarded, or refined (see e.g. [7]) and it is beyond the scope of this work to review all of them. An exemplary model, however, will be given for PD. Its current explanatory model states that a lack of the neurotransmitter dopamine causes a hyperactivity of the STN. Through the neural network, this hyperactivity over-excites activity in another brain region called the

Globus pallidus pars interna (GPi). This, in turn, inhibits activity of distinguished nuclei of the thalamus which subsequently affects the motor cortex (which is responsible for certain movements) [8], [9].
To date, no effective treatment of PD exists as the fundamentals of dopamine depletion are not fully understood. Current forms of treatment therefore focus on the reduction of PD-related symptoms. One of the options is the supply of dopamine in a medicamentous form, e.g. by the administration of L-Dopa [10]. Since 1968, this has become the major form of treatment. Among the shortcomings of this treatment is that the effect wears off after 5 to 10 years and that only parts of the symptoms (rigor and akinesia) can be reduced [11].
Besides drug administration, surgical forms of treatment have been explored [12]. These approaches have been closely related to the rise of human stereotactic surgery beginning in 1947 which will be introduced later in this work (see section 2.1.3). Different surgical scenarios have been tested: the interruption of efferent motoric pathways [13] and morphological modifications of basal ganglia structures [14]. Surgery was performed in order to introduce lesions in several cortical or subcortical sites [15]. In the 1980s, most surgeons agreed that lesions in the nucleus ventralis intermedius (VIM) are most suitable to control the tremor while providing the lowest risk of neurological deficits [16]. Also, for other movement disorders such as essential tremor and dystonia, surgical approaches have been developed and proven suitable [17].

2.1.1 Deep brain stimulation (DBS)

Associated with the introduction of lesions, another form of treatment evolved. During the process of locating specific sites in the brain it was discovered that electrical stimulation of certain brain structures suppresses the disease-related symptoms [18]. In 1987, the group of Benabid demonstrated that deep brain stimulation performed in the VIM was highly effective in alleviating various forms of medically refractory tremor including parkinsonian tremor, essential tremor, and intention tremor [19], [20]. Nowadays, DBS by the means of microelectrodes presents effective treatment to reduce or reverse PD-related symptoms [18], [21]. DBS also became an accepted technique for treatment of other cerebral disorders such as dystonia [22], [23]. Target areas for HFS are the thalamus, the GPi or the STN [24], [25]. Despite the positive effects of HFS, the biochemical mechanisms and interactions within the neural network are still unclear and are subject of extensive research. A summary of this research is provided in [22]. Significant parts of this research included the small animal model which is an important motivation for this

work.

2.1.2 Neuronavigation in DBS

DBS treatment usually involves three steps [26]. First, target areas are identified by the means of pre-operative planning based on CT or magnetic resonance imaging (MRI) data. Second, manual implantation of a stimulation electrode within a stereotactic framework is performed. Third, the patient is stimulated. Insertion of microelectrodes in the context of DBS requires an online target verification to ensure the qualitative outcome of the procedure. The need of verification arises from different sources of inaccuracies which are due to (a) mechanical inaccuracies of the stereotactic framework (see section 2.1.3), (b) image-based inaccuracies resulting from e.g. distortion or low resolution, or (c) dynamic inaccuracies resulting from brain shift or brain compression during insertion. In this work, the focus is put on two possible approaches to target verification:

1. Target verification by the means of electrophysiological recordings where the electrodes are inserted into the brain on the preoperatively planned path and the recordings are evaluated by experienced neurologists [27] and
2. target verification based on the technique of optical coherence tomography as a new intracranial imaging technology [28].

This section provides a short introduction into the area of microelectrode recordings and OCT imaging. While the first has been extensively applied to the field of brain research, the latter is novel to this context.

Microelectrode recordings

The development of microelectrodes for neural recordings has been first reported in 1921 [29]. Thenceforward, scientists were able to stimulate and record. With the onset of human stereotactic surgery, electrodes during movement disorder surgery were soon used as recording and stimulation devices. The main idea was to *image* target areas physiologically as they could not be visualized adequately by other means (e.g. CT data). In the surgical scenario, microelectrodes were mainly used for two purposes:

1. Stimulation as a form of treatment and
2. refinement of a target location by analyzing the acquired signals.

A very important achievement in the context of position refinement was the use of evoked potentials to verify positions of electrodes [30]. Signal analysis of acquired recordings, however, was also used to determine pathological situations in the brain. In the context of PD, for example, it could be shown that tremorigenic cells which feature a rhythmic cellular discharge more or less synchronous to the parkinsonian tremor are located in other brain areas than previously assumed [31], [32]. The introduction of L-Dopa, however, reduced the amount of surgical treatments significantly. Only when limitations of the L-dopa therapy became known, microrecording research was continued in larger scale. For PD, it was found that the STN is a potential therapeutic target [20], [33], [34], [35], [36]. Along with the increased interest in lesioning treatment of PD, the research on target refinement by analyzing electrode recordings continued. It has been found that microelectrode recordings are very suitable for the detection of nuclei boundaries [37], [38], [39]. In [40], the authors present spontaneous patterns of neural activity specifically related to different structures of the human basal ganglia. Their results are showing clear differences for different parts of the basal ganglia. The evaluation of brain signals for the purpose of target identification is an ongoing research issue embedded into the huge field of neural analysis. In the context of microelectrode recordings, much attention has been shifted on the task of statistical evaluation of microelectrode recordings and the analysis of spike trains via spike detection and spike sorting [41], [42], [43], [44]. Some basic methods of neural analysis will be outlined later in this work (see section 6.2.2).

Optical Coherence Tomography (OCT)

Although the use of microelectrode recordings in the field of online verification has been well established, current research activities investigate other approaches. One of the most promising candidates in this context is provided by OCT, a recently developed, powerful imaging technique. OCT has been introduced in the 1990s and has found important applications in several medical fields. Its working principle is somehow analog to ultrasound imaging using infrared light rather than sound [45]. By measuring backreflected light, OCT can be used in the analysis of biological samples by obtaining high resolution cross-sectional backscattering profiles [46]. Major advantages of OCT are the high resolution in the μm range, the video-rate scanning capability, and the non-invasive nature of OCT-imaging [46]. In order to position OCT imaging, Table 2.1 lists different imaging modalities and their characteristics.

Since the first introduction of OCT, it has been mainly used in ophthalmology, dermatology and urology [47]. Recent research activities showed that OCT possesses a strong potential for displaying brain morphology [48], [28]. In [49], the authors show that OCT

Table 2.1: Comparison of different imaging modalities used for brain imaging.

Criteria	MRT	Ultrasound	Laser scanning microscopy	**OCT**
axial resolution	1 mm	0.1 mm	$<$ 0.001 mm	**0.001-0.01 mm**
penetration depth	whole body	$>$100 mm	0.5 mm	**2-3 mm**
contact free	yes	no	yes	**yes**
portable	no	yes	no	**yes**
speed	$\approx 5 fps$	$>$ 30 fps	$\approx 5 fps$	$>$ **30 fps**

is capable of identifying necrosis, tumorous and non-tumorous tissue in neurosurgical applications via an operating microscope. In this context, OCT imaging aims at providing the surgeon with information at microscale level intraoperatively. Applications include the identification of residual tumor tissue or white matter fibres which can be integrated into the navigation environment, such as the microscope, by means of virtual reality. Another application comprises path validation in the context of probe insertion in deep brain surgery. Placement of DBS electrodes for treatment of Parkinson's disease as described in [50] is a possible scenario. As OCT probes are integrable into small instruments, it provides a possible technique for path validation. For imaging of deep brain structures, OCT is integrated into a catheter which is then advanced along the desired trajectory. The usage of OCT for imaging brain structures in such a setting, however, is not straightforward. As OCT is an imaging technique based on a coherent light source, one of its major problems is the occurence of speckle noise [51]. In the context of OCT, speckle can be considered as both, signal carrying and signal degrading. The signal degrading component causes a low signal-to-noise ratio (SNR) and makes the detection of certain structures problematic and unreliable. This establishes the need of designing algorithms for preprocessing of OCT data e.g. for speckle removal or feature enhancement to provide a reliable method for path validation.

2.1.3 Stereotaxy

The concept of stereotaxy is closely related to invasive forms of treatment and especially to the area of DBS in the field of movement disorders. The term stereotaxy is referred to as the technique of spatial localization of target points or volumes in the brain related to a cartesian coordinate system [52]. The basic idea of stereotaxy is to assist the surgeon

in mapping an image space (such as atlas information) onto the physical space in the OR. Therefore, stereotaxy also stands for the integration of mechanical guidance for intracranial probes into the field of neurosurgery [52].
The beginning of stereotactic surgery is usually credited to Horsley and Clarke who presented an animal stereotaxic instrument in 1908 [53] which was used to insert electrodes into the brain of a monkey. Fixation of the Horsley-Clarke device was achieved by insertion of bars into the external auditory canals and fixation to the intraorbital ridge and hard palpade. Although Clarke suggested to transfer the principle to human surgery, the idea was not further developed. The first human stereotactic instrument was reported by Spiegel and Wycis in 1947 [54]. It consisted of a X-Y-carrier, a probe holder, a base ring, and a plaster cast individual for each patient. The carrier and the probe holder were attached to the base ring which was mounted on the plaster cast. In the following years, numerous stereotactic apparatuses were designed, mostly by well-known neurosurgeons: The most famous instruments were developed by Leksell in Sweden [55], Tailarach in France [56], and Riechert and Wolff in Germany whose slightly modified system became known as the Riechert-Mundinger system [57]. The introduction of CT in the late 1970s [58] gave rise to the development of new stereotactic techniques and established the field of computer-assisted stereotactic surgery [59]. Later, the integration of MRI triggered new developments in the context of stereotaxy [52]. Until then, all stereotactic procedures were conducted using the so-called stereotactic frames which provided a mechanical reference coordinate frame. Surgical procedures were therefore referred to as frame-based stereotaxy. The major elements of these systems are a

1. base unit fixed to the skull of the patient,
2. a carriage device on which the probe-guide was mounted,
3. a system for stereotactic data acquisition, and
4. the probe.

For human applications, an additional target and parameter confirmation method is required. The introduction of computer workstations and advanced localization devices into the operation room has led to the so-called frameless stereotactic devices. Both concepts feature important details for the background of this work and will therefore be elaborated in more details.

Frame-based stereotaxy

A stereotactic frame is a mechanical device which is used to precisely guide instruments in the three-dimensional space. Since the beginning of the last century, a wealth of stereotactic frames has been developed which can be classified by three categories:

1. Translational-type frames which provide 3 translational DOF. An exemplary frame is described in [60]. Here, the frame is attached to a square base unit and allows orthogonal motions of the probe holder in the left-right and anteroposterior direction above the skull. The superior-inferior coordinate of the probe is provided by the probe holder. The disadvantage of these systems is that only one trajectory leads to a desired target which may not be desirable. Newer instruments therefore provide angular adjustment of the probe holder.

2. Burr hole-mounted systems which consist of a ball and socket to hold the probe. They provide 3 DOF (2 angular DOF and the depth adjustment) and are usually fixed into a coronal burr hole. The main disadvantages is the inherent inaccuracy as the position accuracy significantly depends on the angular settings of the burr hole.

3. Arc-centered frames which present the most famous design scheme for stereotactic frames. The concept was initially introduced by Leksell [55]. The general layout consists of a semicircular arc with a movable probe carrier. The center of the arc corresponds with a selected cerebral target. Arc-centered frames allow the target to be approached from two angles: the arc angle which corresponds to the left-right direction and the anteroposterior angle which is referred to as ring angle (see Fig. 2.1). The probe is always directed perpendicular to the tangent of the arc. A third, translational DOF is given by the advancement of the probe. The probe will therefore always arrive at the focal point of a sphere also called isocenter. To apply this design in stereotactic surgery, two concepts can be used. First, the arc-quadrant remains at a constant position and the patient's head is moved such that the isocenter corresponds to the target point. Second, the arc-quadrant system can be moved in order to superimpose isocenter and target. Prominent systems include the Leksell system [55], the Riechert-Mundinger system [57] and the Todd-Wells systems [61]. The Brown-Roberts-Wells (BRW) system is another arc-centered frame which features a system of interlocking arcs [62].

A comprehensive overview of all the systems is given in different textbooks on stereotaxy such as [52] and [63].

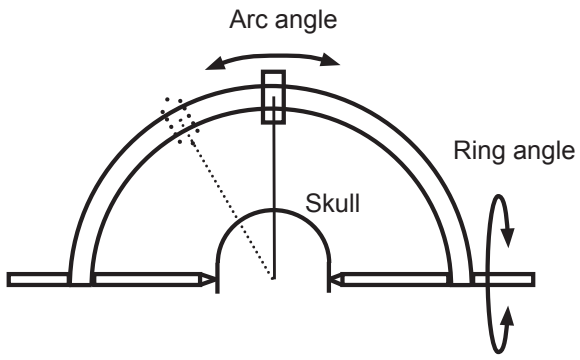

Figure 2.1: Definition of stereotactic angles, namely the arc and ring angle, in frame-based stereotaxy.

Frameless stereotaxy

From its beginnings, the term stereotaxy inherently meant the use of a mechanical frame. Frameless stereotaxy is therefore a somehow self-contradictory term. It arised in the 1980s [64], [65], [66]. The technique itself constitutes a reversal of classical stereotaxy in which the physical location of the skull was determined from images (e.g. CT data). According to [67], the frameless systems have three major components:

1. A three-dimensional localizer which can be freely moved in space and provides a position (and orientation) within its own coordinate system. To date, there are principally four types of localizers: (a) a mechanical arm [68], (b) magnetic field gradient detector [64], (c) a sonodetector [69] and (d) optical detectors [70].

2. A registration technique which establishes the relationship between an extracranial device and the image space. Instead of mapping the image space into the space of the stereotactic frame, the localizer position and orientation needs to be mapped into the image space.

3. A displaying technique which provides an adequate visualization of the localizer in the image space.

Well known frameless neuronavigation systems are the *Neuronavigator* developed by Watanabe [64], the *Operation Arm System* (Radionics, Burlington, USA) developed by Guthrie [71], the *ISG Viewing Wand* (Elekta, Stockholm, Sweden) [72], and the *Cyberknife* [73]. A comprehensive overview of frameless systems can be found in [59].

Accuracy in stereotactic surgery

The accuracy of any stereotactic system being frame-based or frameless is of uttermost importance. Especially triggered by the introduction of frameless systems, a lot of research has been done on the accuracy of stereotactic systems. Despite the advantages of frameless systems, the gold standard is still given by stereotactic frames. The mechanical accuracy of stereotactic frames has been shown to be less than 1 mm [74], [75]. In the clinical application, examinations of frame-based systems have shown an accuracy in the range of 1-2 mm [76], [77]. Inaccuracies are most often related to (a) mechanical inaccuracies [78], (b) image-based inaccuracies (e.g. voxel size and distortion) [76], [75], (c) errors due to the registration process [79], [80], and (d) intraoperative events such as brain shift [81]. For frameless systems, recent studies have reported errors of in the range of 2.5 mm. As a consequence, frameless systems are not used for neurosurgical operations where high precision is required [82].

Robot-assisted stereotaxy

The field of neurosurgery, and especially the field of stereotaxy, has been one of the first fields where surgical assistance of robotic devices was introduced. The technological advances in robotic technology combined with improved neuroimaging modalities and computer technology have been the major driving forces for the introduction of robotic technology into the field of neurosurgery. In this special context, neurosurgical robots promise different advantages such as ultimate precision, reliability in performing procedures repeatedly, and economic benefits through a better operational result.
Since the 1980s, a lot of different design approaches have been proposed. In the beginning, robotic assistance applied to the frame-based stereotactic framework. The first neurosurgical application of robotic technology occured in 1985 [83]. A standard industrial robot *PUMA 200* (Staeubli GmbH, Bayreuth, Germany) was used to position a guide tube through which a needle was inserted. The planning was done based on CT data in which the target was identified. The BRW-frame was used to localize the target in the physical and in the image space. Other robotic assistants for stereotactic procedures are the *Minerva system* [84], the *Evolution 1 system* (Universal Robotics Systems, Schwerin, Germany) [85], and a MRI compatible robot by Masamune [86]. More neurosurgical assistants comprise the *NeuroMate system* [19], [87] and the *PathFinder system* (ProSurgics, High Wycombe, United Kingdom). A very recent system entering the field of robotic neurosurgery is the *SmartAssist* proposed by Shoham et. al. [88]. Based on the concept of burr hole-systems, the system overcomes the need to immobilise the surgical

field during the robotic application.

2.2 The small animal model in brain research

The animal model forms a fundamental part of neuroscience research efforts to improve the prevention, diagnosis, understanding and treatment of neurological conditions [89]. Animals are used to investigate such topics as the underlying mechanisms of neuronal cell damage and death. Also for the field of movement disorders, animal models have been developed. A comprehensive review is given in [90]. The adequacy of a particular animal model of human neurological diseases, however, is still a subject debated by experts [91]. Although the animal model is widely appreciated in neuroscience research, critics question the fact that complex neurological deficits can be modeled adequately.
Nevertheless, mammalian neuroscience research is most often performed on rats [91]. This is mainly due to the fact that a large amount of inbred rat models exist and a large amount of data is available. Other reasons for the use of rats are based on the fact that rats are hardy animals and very resistent to infections and that animals from inbred strains offer the advantage of consistent size and comparability of the research framework [92]. In the context of PD, for example, it has been shown that dopamine depletion can be modeled by the intracerebral injection of 6-hydroxydopamine (6-OHDA) [93].

2.2.1 Small animal stereotaxy

Having established a (small) animal model for the purpose of neuroscience research, the application of a stereotactic framework is only a logical consequence. Stereotactic procedures on small animals follow an established surgical procedure.

Stereotactic reference system

As stated in section 2.1.3, stereotaxy aims at providing the basis for spatial localization of intracranial target points or volumes. To provide a constant relation between target volume and the respective coordinate system, the skull is fixed into a stereotactic frame. The same approach is taken in small animal stereotaxy. For rats, fixation of the skull into the stereotactic frame is performed using

1. two interaurally placed pins, which are inserted into the interaural holes, and
2. a mounting bracket, which locks the nose into a fixed position.

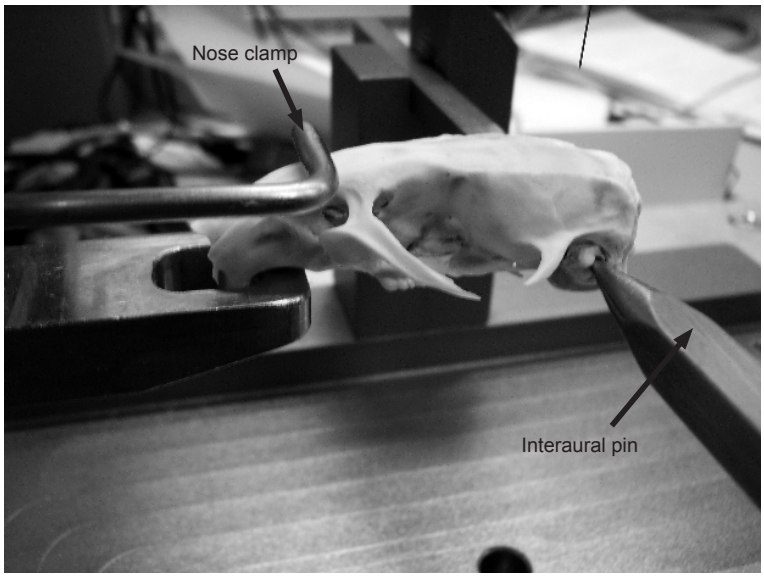

Figure 2.2: Stereotactic fixation of the rat skull. Pins are inserted into the interaural holes and the front teeth are inserted into a mounting bracket. The animal is subsequently fixed by a nose clamp.

Fig. 2.2 shows the principal approach for a rat skull. With the rat skull fixed into the frame for surgery, spatial orientation for planning and surgery is provided by anatomical characteristics of the skull. The rat skull features two major anatomical landmarks, the Lambda and the Bregma points which are indicated in Fig. 2.3. Following the Paxinos atlas [92], the Bregma point is located at the point of intersection of the sagittal suture with the curve of best fit along the coronal suture. Lambda is defined as the midpoint of the curve of best fit along the lambdoid suture [92]. For the subsequent planning and registration process, the skull is required to be in the so-called flat skull position which means that Bregma and Lambda are located at equal height.

2.2.2 Surgical scenario

The surgical scenario of small animal stereotaxy comprises different steps which will be shortly introduced in the following.

Planning

Stereotactic insertions of probes into a rat brain are typically based on atlas data such as the Paxinos atlas [92] or Swanson atlas [94]. These atlases provide neuroanatomical information of the rat brain displayed by coronal, sagittal, and horizontal sections of the

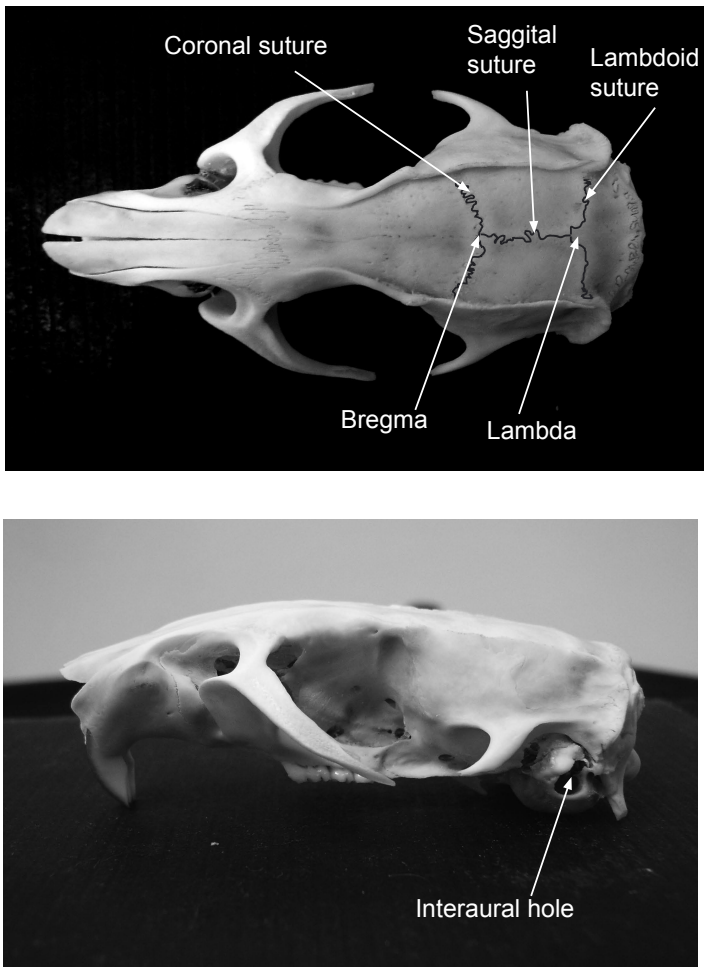

Figure 2.3: Anatomical structure of the rat skull. [top] Top view showing the Bregma and Lambda points and the saggital, coronal, and lambdoid sutures, [bottom] Side view showing the interaural hole.

brain. In addition, atlas data incorporates functional and/or histological information by labeling specific regions in the drawings. All sections are related to a stereotactic reference system, thus allowing to locate a desired target. Throughout this work, the Swanson atlas will be used for planning. In this atlas, coordinates of certain regions are provided for a standard rat which is characterized by a normalized distance between the Bregma and Lambda point. Coordinates of intracranial regions can now be specified with regard to a reference system established by the Bregma and Lambda points. A common convention is to provide the following coordinates which are also depicted in Fig. 2.4:

1. A/P position which denotes the anteroposterior distance from a vertical coronal

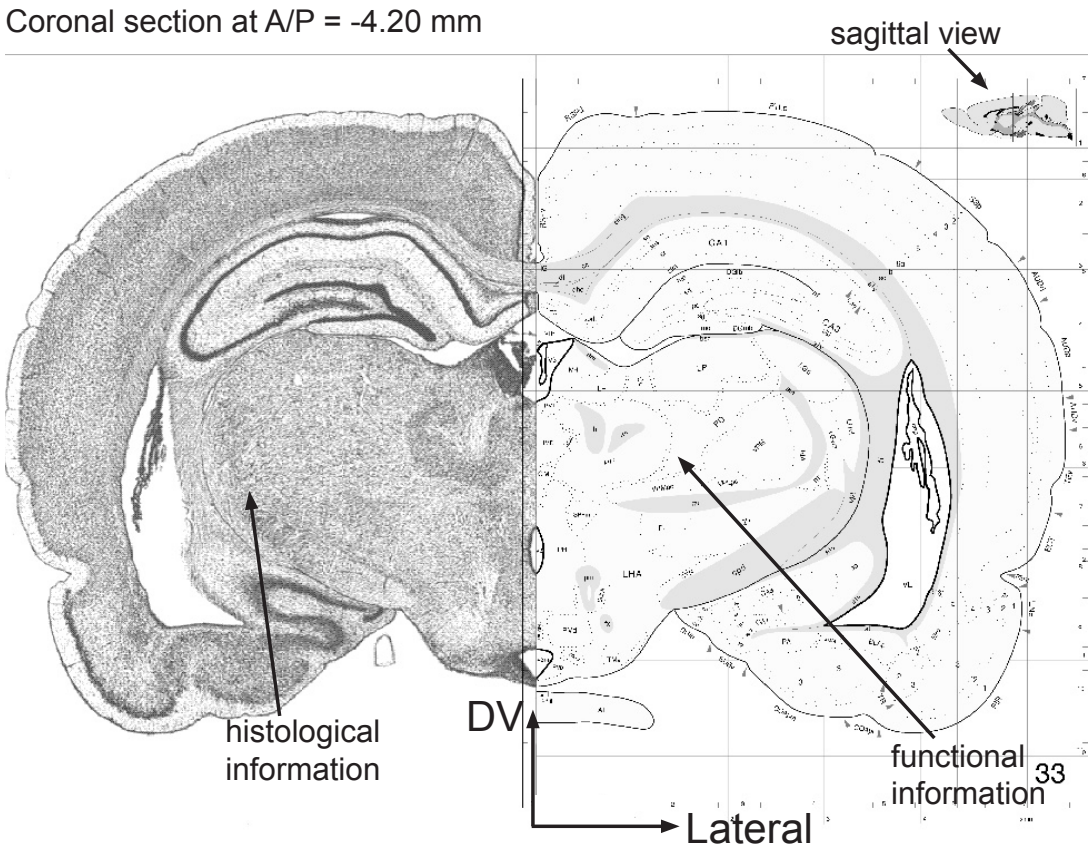

Figure 2.4: Coronal section of the Swanson atlas [94]. The left side shows histological information, the right side shows functionally labeled regions. The section allows stereotactic planning by providing the A/P-, the DV-, and the lateral coordinate.

plane passing through Bregma. The normalized position of Bregma is 0.0 mm.

2. DV position which denotes the dorsoventral distance from the horizontal plane passing through the interaural line (e.g. the DV of Bregma is 10.0 mm).
3. Lateral position which provides the distance from the midline sagittal plane (e.g. the lateral position of Bregma is 0.0 mm).

Registration

Registration is a crucial step to establish the relation between the stereotactic instrument coordinate system and the rat coordinates usually given by A/P -, DV-, and lateral position. In common procedures, registration is simply done by manually placing the probe tip under visual control onto the Lambda and Bregma landmarks on the rat skull. If

manual setscrews are used, the position information of the screws is noted for both landmarks. The spatial coordinates of both points can be used to determine the position and orientation of the rat brain with regard to the coordinate system of the manipulator. This information is crucial in order to convert any rat target coordinates to corresponding values of the manipulator joints. In the case of a manually operated frame, the notation of the Bregma and Lambda in setscrew coordinates and the calculation of the position and orientation of the rat brain forms the registration process. If the distance of Lambda and Bregma for the actual surgical scenario differ from the normalized atlas data, the planning step is corrected by linear scaling of the respective coordinates which is often referred to as linear warping [95]. The scaling ratio is given by the actual distance of Bregma and Lambda and the standardized distance of 9 mm.
The disadvantages of this approach are quite intuitive: First, the placement by setscrews is vulnerable for positioning errors. Second, the calculation of the position and orientation of the rat brain with regard to the manipulator is a delicate and time consuming procedure if it is done manually.

Surgical procedure

An exemplary stereotactic surgery on a rat is depicted by an implantation of a guide tube for simultaneous deep brain stimulation and neurotransmitter detection [96]. The procedure consists of 5 major steps after the animal is anesthetized.

1. In the first step, the animal is fixed into the stereotactic frame. This is done by inserting the interaural pins into the interaural holes in the rat skull. Additionally, the front teeth are clamped into a mounting bracket. This establishes the stereotactic framework for the insertion.

2. As soon as the animal is fixed, the scalp is opened.

3. After clamping of the skin and removing blood, the manipulator is registered to the rat. This is done by manually placing the instrument (e.g. guiding tube) under visual control onto two anatomical landmarks on the rat skull. Subsequently, the coordinates of the manipulator axes are stored and used to calculate for the transformation of the manipulator coordinates to the rat coordinates.

4. Having established the registration, coordinates from the planning, namely entry and destination point, can be transferred to the manipulator coordinate system. Subsequently, access holes are drilled into the skull under haptic feedback of the surgeon at the desired points.

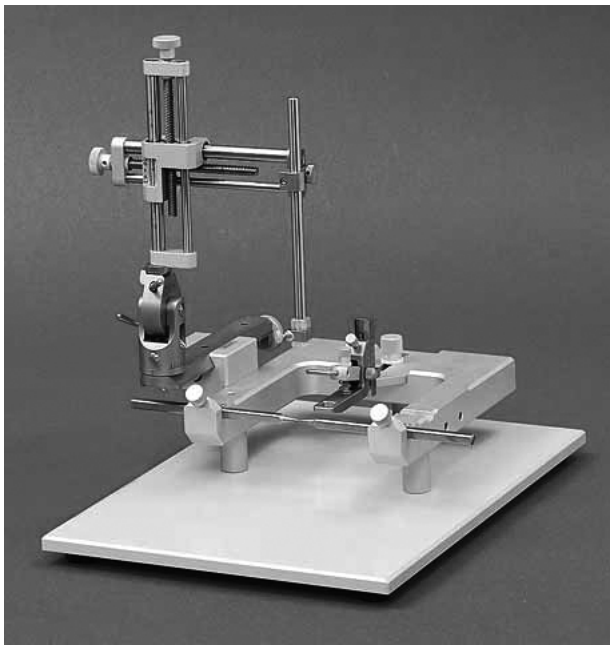

Figure 2.5: Small animal stereotactic frame Lab Standard Stereotaxic (Stoelting Co., Wood Dale, Illinois, USA).

5. The instrument is then manually advanced into the brain. Position feedback is provided by the turning knobs of the manipulator.

In this procedure, the final step is the glueing of the guiding tube for permanent usage.

2.2.3 Existing small animal stereotactic devices

Small animal stereotaxy is a well established technique and numerous instruments have been developed. The following enumeration gives an overview of the most commonly used systems.

1. The Lab Standard Stereotaxic which is distributed by Stoelting Co., Wood Dale, Illinois, USA (shown in Fig. 2.5). It consists of a U-shaped frame in which a mounting bracket for the nose and two interaural pin holders are integrated. These elements establish the stereotactic frame. The manipulator itself is attached to the frame. The base of the manipulator provides 2 rotary DOF. Referring to the fixed rat, they allow rotation in the horizontal plane and the sagittal plane but not in the coronal plane. Attached to the rotary joints is a cartesian manipulator which provides movements along 3 independent translational axes. Compared to stereotactic frames in the human case, it can be categorized as a translational-type frame as it

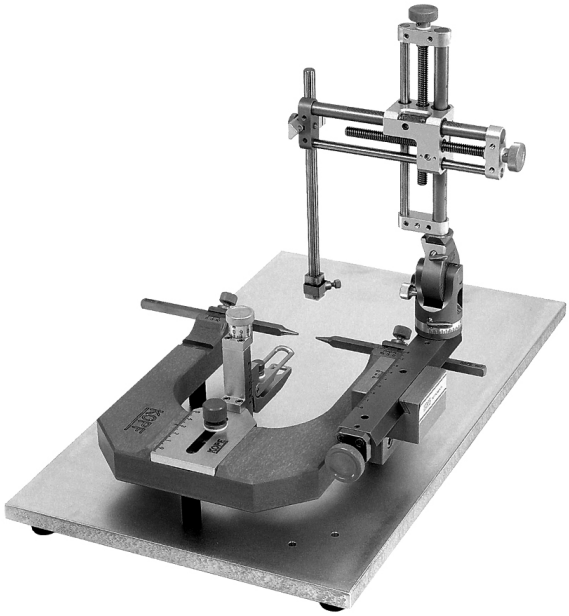

Figure 2.6: Small animal stereotactic frame Model 900 (David Kopf Instruments, Tujunga, California, USA).

does not feature a center-of-arc.

2. The Model 900 frame which is distributed by David Kopf Instruments, Tujunga, California, USA. Its design is similar to the Lab Standard Stereotaxic (see Fig. 2.6).

3. The Small Animal Stereotactic Frame (SASI) is distributed by ThomasRecordings GmbH, Giessen, Germany and can be categorized as an arc-centered frame. Fig. 2.7 shows the setup without the stereotactic fixation of the animal. A cartesian manipulator providing 3 translational DOF is attached to an arc describing a semi-circle. The manipulator can be slit along the rim of the arc while the arc itself can be rotated. Note that the SASI does not present an ideal center-of-arc structure as the last translational stage of the cartesian manipulator target does not necessarily point to the isocenter of the arc.

2.2.4 Accuracy in small animal stereotaxy

Little work has been done on analyzing the positioning accuracy of small animal stereotactic approaches. An existing stereotactic device presented by [97] features a mechanical positioning accuracy of 500 μm. To our knowledge, no other studies investigate the

Figure 2.7: Small animal stereotactic frame SASI (ThomasRecordings GmbH, Giessen, Germany).

mechanical positioning accuracy of small animal stereotactic frames. Different factors influencing the positioning accuracy, however, can be outlined. They can be classified by two categories:

Hardware-related inaccuracies

The first shortcoming of translational-type frames such as the Lab Standard Stereotaxic in Fig. 2.5 is that they do not have an adequate design to compensate for an imperfect fixation of the animal. Translational-type frames require a perfect fixation in a flat skull position (see section 2.2.1). If the skull, however, is tilted due to incorrect fixation, the three cartesian stages do not offer adequate means to compensate for the tilt. Systems such as the Lab Standard Stereotaxic feature two rotary joints but these joints do not offer the option of being fine adjustable. Another side-effect of the design is that the translational-type frames are restricted to cartesian trajectories only. This constrains the operational space of the frame. Second, positioning information are read out by the user from scale bars of the respective stages. This easily leads to unintentional misplacements. Third, calculation of target coordinates is performed in terms of stored coordinates of the manipulator axes. Particulary in non flat skull position, this requires tedious calculations which, if performed manually, are prone to errors. Attempts have been made to target these shortcomings by introducing center-of-arc systems such as the SASI or by introducing encoders and digital read-outs into the mechanical structure. These improvements, however, where only partially realized in specific systems. To our knowledge, no existing

system overcomes all of the mentioned disadvantages.

Biology-related inaccuracies

Biology-related sources of errors refer to the surgical conditions. First, most of the stereotactic procedures are atlas-based which presumes a morphological similarity between all tested animals. Although some morphological similarity may be given due to the inbred nature of laboratory rats, size and structure of the skull may vary. As a consequence, atlas information will not exactly correspond to the individual animal. A second biology-related source of error is that planning is performed based on characteristic landmarks on the rat skull which are defined according to a best fit practice. The best fit practice, however, leaves room for indiviudal interpretation and therefore does not offer an exact standard. The third biologically-based effect is related to probe insertion. Here, positioning inaccuracies arise from effects related to brain tissue properties. First, the dura has to be removed carefully from the brain surface for correct targeting. Otherwise, the brain tissue will be compressed at the probe tip location thus falsifying the position of the tip with respect to the brain. This effect is usually referred to as dimpling [98]. Second, stick and slip effects might also falsify the positioning process.

3 Requirements for robot-assisted small animal stereotaxy

To nicely integrate into the surgical scenario, the design of a robotic system for small animal stereotaxy has to adapt to certain requirements. In the following, specifications for the design of a robot-assisted stereotactic assistant will be provided. As the focus of the system is put on rats, the analysis will be exemplary performed for the case of rat stereotaxy.

3.1 Hardware requirements

The following sections focus on the derivation of hardware design criteria. This includes the definition of the required workspace, the required DOF, the required payload, and positioning accuracy.

3.1.1 Workspace and manipulator requirements

As the general procedure for stereotactic surgery on rats is well established, the workspace analysis is based on an existing stereotactic device. To derive the dimensions, the layout of the Lab Standard Stereotaxic (Stoelting Co.) in Fig. 2.5 is analyzed. Fig. 3.1 shows the top view and two sections with corresponding dimensions. If the center point O is considered to be the origin of the frame coordinate system, the workspace requirements can be derived as listed in Table 3.1. Payload requirements have been derived to cover the weight of an exemplary instrument used in stereotactic procedures. Such an instrument is the *Micro Screw Drive* fabricated by ThomasRecording GmbH (Marburg, Germany), a chronic headstage for rats. Its weight is smaller than 5 grams [99]. An exemplary 64 channel pre-amplifier offered by ThomasRecording GmbH weighs 253 grams [99]. A payload requirement of 300 grams for the manipulator is therefore considered sufficient.

3.1.2 Kinematic requirements

Common stereotactic procedures are performed using a stepwise approach:

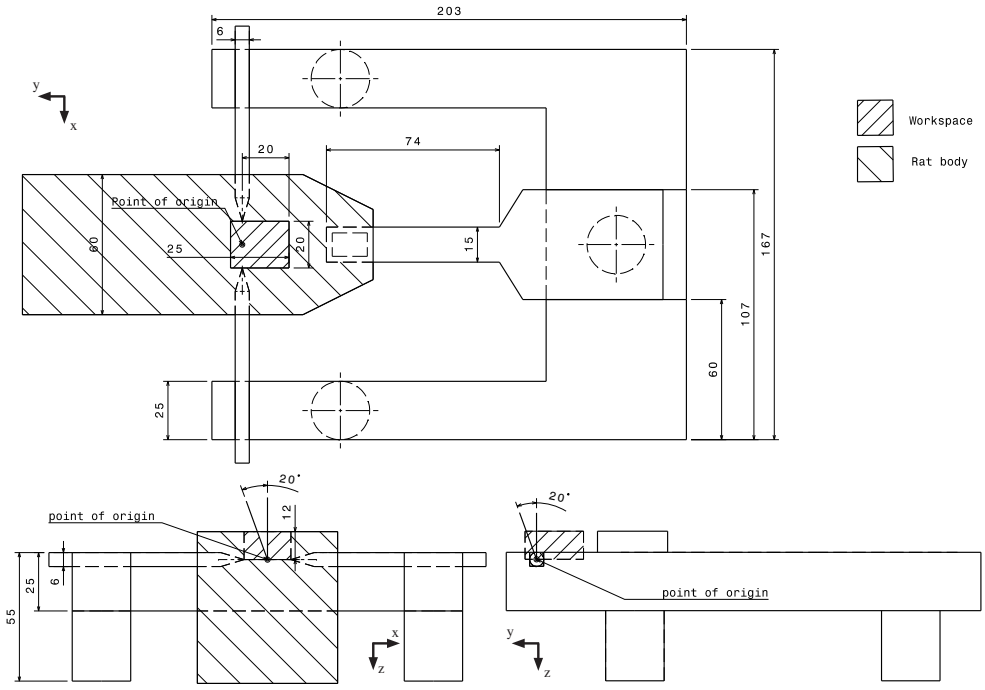

Figure 3.1: Layout and dimensions of the Lab Standard Stereotaxic (Stoelting Co.). The point of origin is indicated.

1. The first step is called prepositioning step and provides the tool orientation and position (POSE) in which the longitudinal axis of the probe points along the desired entry path outside the rat skull to the specified target.

2. The second step is referred to as penetration step and advances the tool along the direction of its longitudinal axis until the desired position within the brain is reached.

This approach and the tool geometry require the robotic system to have at least 5 DOF, 3 translational and 2 rotary ones. The translational DOF allow positioning of the probe in all three cartesian directions while the 2 rotary DOF allow to adjust the ring and the arc angle (see Fig. 2.1). As the penetration step requires one DOF (translation), the prepositioning of the probe has to provide the additional four.

3.1.3 Accuracy requirements

Positioning accuracy of the stereotactic insertion is an even bigger challenge than in the human case. Certain sites in the rat brain, especially in the basal ganglia, have a relatively small size. According to the Paxinos atlas, the STN covers a volume of approximately

Table 3.1: Workspace and positioning requirements for a small animal stereotactic manipulator (coordinate notations refer to Fig.3.1).

Description	Notation	Value
Workspace	x	$[-25 \dots 25]$ mm
	y	$[-25 \dots 25]$ mm
	z	$[0 \dots 10]$ mm
	α_x	$[-25 \dots 25]^\circ$
	α_z	$[-25 \dots 25]^\circ$
Maximal velocity	x	2 mm/s
	y	2 mm/s
	z	2 mm/s
	α_x	1°/s
	α_z	1°/s
Payload		0.300 kg

100 μm x100 μm x100 μm. This volume puts a hard constraint on the positioning accuracy. Minor errors in positioning of a research device would easily lead to a misplacement. Subsequently, measurements are not obtained in the desired brain area which would eventually lead to false results. An additional challenge is given by the fact that the designated functional areas are to be targeted with different orientations of the tool. The resulting positioning accuracy is listed in Table 3.2. It provides details on the step size resolution in each cartesian direction and for the 2 rotary DOF. Additionally, details on the positioning accuracy and the repeatability of positioning are given.

3.1.4 Safety and usability requirements

Besides the workspace and kinematic requirements, two other important design criteria exist. Both are closely related to usability of the stereotactic system in the surgical scenario. The first criteria refers to surgical safety for the animal. As for the human surgery, automated and potentially uncontrolled systems always present a safety concern. Manifold approaches to guarantee the patient's safety have therefore been pursued. Most of them rely on a combination of hardware-related safety measures (such as mechanical restrictions on motion parameters) and software-based functionalities (e.g. control strategies). As this work covers the total design process of a stereotactic assistant, safety criteria

Table 3.2: Accuracy requirements for a small animal stereotactic manipulator.

Description	Notation	Value
Step size resolution	x	10 μm
	y	10 μm
	z	10 μm
	α_x	0.1°
	α_z	0.1°
Positioning accuracy	50 μm	
Repeatability	30 μm	

will also be integrated into the design process.
The second usability requirement is the desire to adapt the designed assistant to human stereotaxy in the future. Human stereotaxy is still a very common surgical approach to intervene the brain. None of the current stereotactic robots, however, has found common acceptance by the surgeons. Thus, this field still demands new approaches. Design of the small animal stereotactic assistant should therefore realize attributes which are possibly advantageous for clincial acceptance, approval, and use in human stereotaxy.

3.2 Software requirements

Based on the analysis of the surgical workflow of small animal stereotaxy described in section 2.2.1 and the desired integration of a robotic assistant, different requirements of a stereotactic control framework can be derived:

1. Calibration module which realizes the calibration of arbitrary probes adapted to the robotic system. Calibration is a mandatory step for almost every robot-assisted operation as it determines the exact location of the probe with respect to the robots coordinate system. Surgical scenarios in small animal brain research include a variety of tools e.g. microelectrodes, probes for microdialysis, and cannulae for injections. Thus, important aspects for the calibration process are generality and robustness.

2. Preoperative path planning module which provides the functionality to specify destination point and angle of penetration. Details of the planning step are provided in section 2.2.2. Based on the established approach, the planning module should incorporate atlas information and provide an easy-to-use interface to the user.

3. Intraoperative registration module which allows the user to establish the spatial relation between the planning scenario (e.g. brain coordinates) and the real surgical scenario (e.g. the rat skull location). Registration is mandatory for robot-assisted surgery as it eventually allows to express patient-related coordinates (e.g. intracranial target) in robot-related coordinates. Only this allows the use of a robotic assitant to perform accurate surgical tasks. Moreover, registration enables functionalities such as obstacle avoidance.

4. Intraoperative insertion control module which allows to control the probe insertion process. This comprises the control of step size, velocity, and acceleration.

Moreover, the control framework should minimize the treatment time as the rat can be kept under anesthesia for a limited time only. This puts a hard constraint on treatment time. Another criterion of sofware design is given by safety aspects integrated into the user interface to assist the surgeon who is not necessarily familiar with the control of robotics. Although safety restrictions for animal surgery is less strict than for human applications, the total framework has to provide safety for the rat and the user. In addition to the inherent safety of the SASSU design (see section 4.1.2), the software should be designed such that the probability of an erroneous handling is minimized.

4 Spherical Assistant for Stereotactic Surgery SASSU [1]

This chapter describes the mechanical design of a robotic assistant for automated and precise stereotactic surgery on small animals. Major goal of the design is to overcome the shortcomings of existing stereotactic systems, namely their hardware- and operation-related inaccuracies. Based on the previously listed requirements, the conception of the stereotactic assistant is drafted. This process incoporates an evaluation of different design options in terms of usability, safety, and transferability to human applications. Subsequently, an extensive kinematic analysis of the final design is presented, namely the forward and inverse kinematics. The chosen design is validated by comparing its kinematic accuracy to an existing device with equal characteristics concerning usability and safety. The second part of the chapter is dedicated to the construction of the SASSU and operation-related tasks and characteristics. Details on the hardware such as actors, sensors, and control interface are given. Then, a detailed approach to the calibration of the system is presented. Furthermore, the basic control framework, the control interface, and the control software-based functionalities are described. A special focus is put on the compensation of positioning errors resulting from inherent mechanical properties of the system.

4.1 Hardware design

The following subsections describe the hardware design of the stereotactic assistant. Based on a short overview over existing mechanism and their (dis-) advantages regarding the specified task, a general design scheme is derived. As different solutions in terms of the kinematic structure exist for the proposed scheme, a kinematic analysis is performed. Taking the results of this analysis into account, a final design is proposed. In the latter part of this section, details on the construction and the components are provided.

4.1.1 Design options

Different fundamental kinematic structures can be taken as a starting point while designing a robotic assistant. As for most medical applications, design may be based on classical

[1] Parts of this chapter have been published in [100, 101, 102].

robotic architectures. Two major types of architecture can be distinguished [103]:

1. Serial robotic mechanisms, which feature an anthropomorphic design as the assembly resembles a human arm. These designs are also referred to as open kinematic loop. The most important advantages of serial robotic mechanisms are constituted by a large workspace and a large dexterity [104]. Major drawbacks of serial mechanisms are the poor positioning accuracy and the large mass and inertia due to the actuators which are integrated into the kinematic chain [105]. Serial mechanisms therefore feature a poor payload/weight ratio leading to large and heavy designs [105].

2. Parallel robotic mechanisms, which form a so-called closed kinematic loop. Parallel robots feature a high payload/weight ratio as the load is distributed on all links. This characteristic leads to a high stiffness of the kinematic structure. It has been shown that parallel mechanisms feature a high positioning accuracy of the end-effector [106]. The major drawback of parallel robotic mechanisms is the restricted workspace and the poor dexterity which reduces the number of applications significantly [104]. Another important disadvantage is given by the fact that general closed-form solution for the forward kinematic equations of a parallel robotic mechanism cannot be found (*forward kinematic problem*).

Generally, the requirements given in section 3.1 can be met by both, serial and parallel, architectures if the design of the robot (e.g. the link lengths) is done adequately. Both, however, require a complex control structure to provide the required safety which can not be realized easily and will results in a bulky system.
This motivates another design scheme which is often referred to as spherical mechanism. Spherical mechanisms are a special type of serial robotic mechanism. In [107] and [108], a spherical manipulator is defined as a rotational manipulator with all axes intersecting at the center of a sphere. Although other definitions exist, it will be used throughout this work. In terms of workspace, accuracy, and payload/weight ratio, spherical mechanisms generally behave as serial kinematic chains. An important property of spherical mechanisms, however, is that the origin of the sphere constitutes an isocenter of rotation. This mechanical property can be used to restrict tool motion. For medical applications which motivated this work, this forms an important feature.

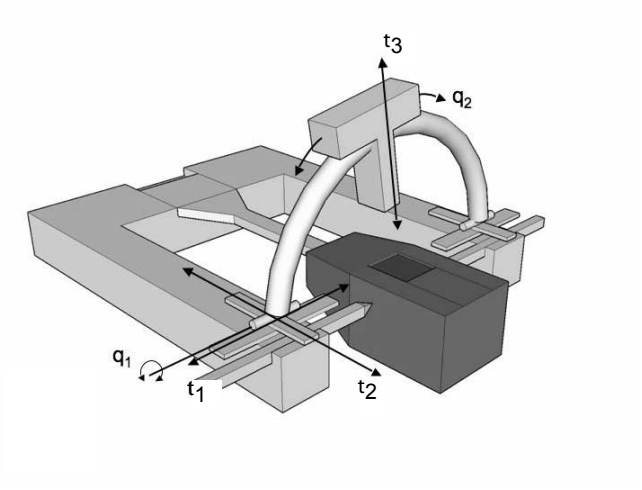

Figure 4.1: Proposed structure of the small animal stereotactic manipulator. A semi-circular arc is seated on the stereotactic frame. A slide moving along the arc carries the probe. The animal brain is shown in dark gray. The translational stages are denoted by t_i, the rotary stages are denoted by q_i.

4.1.2 Design specification

Based on these findings, a kinematic structure as shown in Fig. 4.1 is proposed. It follows the existing design of stereotactic frames in human applications (see Fig. 2.1) where the ring and the arc angle are provided by a rotating arc which allows a slide to be moved along its rim. The slide carries the final translational stage, the probe adapter and the probe itself. The rotating arc with the last linear stage is mounted on two additional linear stages. The kinematic structure establishes the previously mentioned center-of-arc-principle. Besides the fulfillment of workspace and payload requirements, the drawn design features the following advantages:

1. Safety
   The layout is designed such that the tool can only be moved in and out of a spherical workspace by the means of one axis (e.g. the last linear stage). If the other axes are actuated while the tool is outside the spherical workspace, it will never collide with a target located within the volume of the sphere. This constitutes an inherently safe kinematic structure which is of great advantage for medical applications. If the target is e.g. the animals head, only the insertion axis allows a contact of the tool thus reducing the complexity of the safety issue significantly.

2. Future adaption to human application

The chosen mechanism allows to transfer the kinematic design to the human application. In human stereotaxy, the center-of-arc principle has already been well established [52], [63]. This fact guarantees the feasibility of the design also for human application and will thus be advantageous for clinical acceptance, approval and use.

4.1.3 Kinematic specification

If a spherical manipulator featuring an arc-like link is chosen as the final design, the sequence of steps in the stereotactic approach (prepositioning and insertion) requires the last stage to be translational (insertion stage). The orientation of the probe will be provided by 2 rotary joints, one rotating the arc (ring angle) and the other moving the slide along the rim of the arc (arc angle). The described joints realize 3 DOF. The lacking 2 can be easily realized by 2 translational joints. In combination with the previously introduced rotary joints, these translational joints provide the 4 DOF prepositioning functionality.
After the joint requirements for the stereotactic approach have been found, the adequate sequence of joints has to be examined. While the last stage (insertion) is required to be translational, the sequence of joints within the prepositioning part of the manipulator can be chosen arbitrarily. For an optimal choice of the kinematic sequence, different criteria can be applied: (a) safety, (b) workspace, and (c) accuracy. If requirements of the first two criteria are met, accuracy of a manipulator is the most important feature in stereotactic surgery on small animals. The choice of the kinematic chain should therefore be conducted under the premise that positioning errors become as small as possible. Different kinematic chains for the prepositioning stage will be examined with respect to positioning accuracy in this work:

1. a $TTRRT$ chain and
2. a $RRTTT$ chain

where T refers to a translational joint and R refers to a rotary joint. Note that the design proposal in Fig. 4.1 follows the first kinematic chain structure while the kinematic structure of the SASI shown in Fig. 2.7 adopts the second chain structure.
Analyzing the positioning accuracy of robotic systems, 3 types of errors are generally distinguished (see [109]):

- Structural errors (e.g. tolerances in the manufacturing process),
- kinematic errors (e.g. link length, joint value deviations), and

- dynamic errors (e.g. inertia, friction).

Structural and dynamic errors are mostly induced by the manufacturing process. For a theoretical analysis, only errors induced by variation in the kinematic structure will therefore be investigated. Results presented in section 6.1 validate that the proposed kinematic design of a $TTRRT$ chain outperforms the $RRTTT$ chain which confirms the following design of the system.

4.1.4 Final design of the manipulator

Resulting from the specifications for small animal brain surgery, the consideration of safety issues, transferability to human applications, and an accuracy analysis of the kinematic structure, the final design of the stereotactic manipulator has been found as shown in Fig. 4.2. The geometric design follows the center-of-arc-principle. As one of the manipulator properties is to preposition a tool on a spherical surface, the system is referred to as *Spherical Assistant for Stereotactic SUrgery* (SASSU).
The stereotactic frame, in which the animal is placed, is located underneath the arc such that the workspace of the system corresponds to the target volume (brain of the fixed animal). Fig. 4.2 shows a CAD drawing of the final SASSU design. The two linear joints for the prepositioning step are integrated into the base of the system. Two angles of rotations are provided. Referring to the stereotactic angles shown in Fig. 2.1 the ring angle is provided by the rotating arc and the arc angle of rotation is then provided by a slide moving along the rim of the arc. Note that the ring angle rotates about the x_0-axis and the arc angle about the y_0-axis. The last translational slide for the penetration step is mounted onto the slide and carries the surgical instrument.
In contrast to the design proposal in Fig. 4.1, the arc is not seated on both sides. This is due to constructional issues as a potential bearing would have to provide 4 DOF (2 translational and 2 rotational). A passive bearing is hard to realize and would introduce friction affecting the positioning accuracy. Providing active joints on the other side (active bearing) would introduce additional active joints which would result in a more expensive and bulky system. Additionally, the open arc structure of the final system can be used for other types of minimal invasive surgery (MIS) where the arc would extend over the body and cannot be seated on both sides. The open arc structure, however, does behave as a lever resulting in deflection due to gravity if the slide is moving towards the outer end of the rim (see section 4.3.3).
The range of motion of all active stages is limited through the mechanical design of the system. The range of joint values defining the workspace of the final design is given in

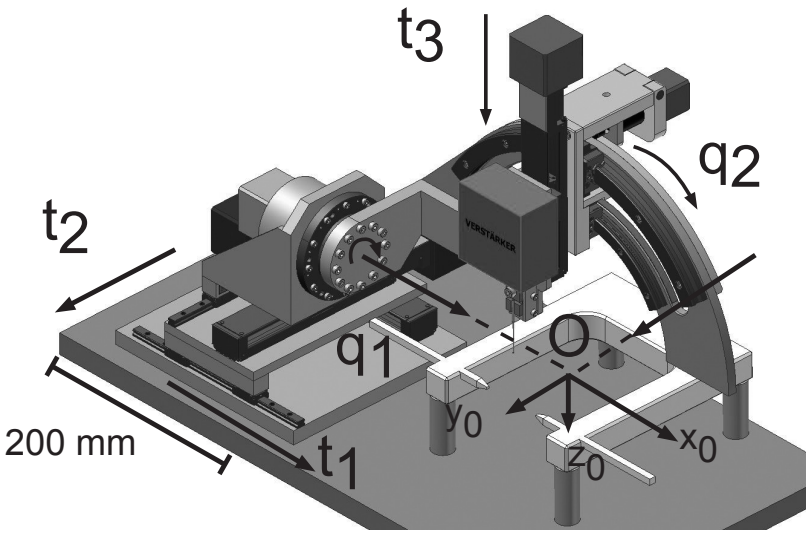

Figure 4.2: CAD drawing of the final manipulator design. The base coordinate system given by x_0, y_0, and z_0 corresponds to the common center of both rotary joints which are denoted by q_1 and q_2. The translational axes are shown as t_1, t_2, and t_3.

Table 4.1: Joint value range for the SASSU system refering to the coordinate system in Fig. 4.2.

Axis	Notation	Type	Value
1	t_1	translation	$[-30 \ldots 30]$ mm
2	t_2	translation	$[-30 \ldots 30]$ mm
3	q_1	rotation	$[-40 \ldots 40]^\circ$
4	q_2	rotation	$[-40 \ldots 40]^\circ$
5	t_3	translation	$[-30 \ldots 30]$ mm

Table 4.1. Note that the actual joint ranges provide a larger workspace than specified in Table 3.1. This allows to vary the placement of the animal within the stereotactic frame and larger target volumes of e.g. larger animals. Fig. 4.3 shows an image of the realized mechanical assembly.

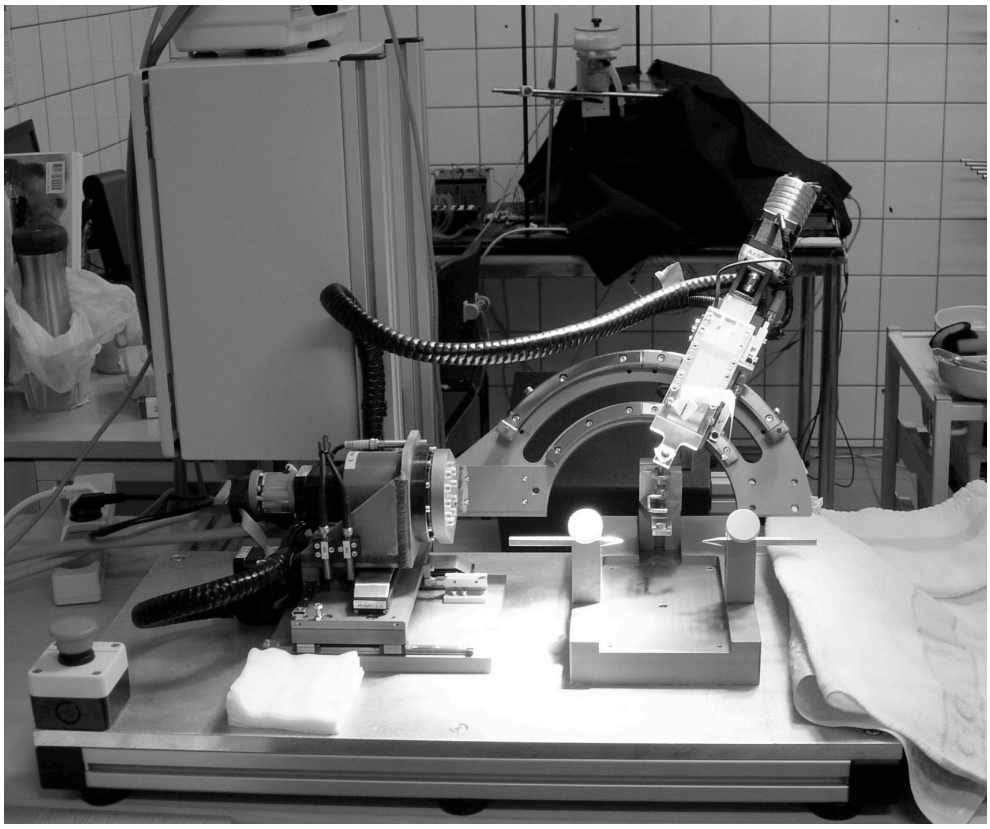

Figure 4.3: Mechanical realization of the SASSU. In the foreground, the SASSU with the five motorized stages and the integrated stereotactic frame is shown. In the background, the power amplifier box can be seen.

4.1.5 Construction and components

After having identified a kinematic structure which meets all requirements for small animal stereotaxy in terms of accuracy, constructional issues have to be adressed. In the following, information regarding the construction of the system such as details on actors, sensors, and materials are provided. Data sheets for the components can be found in the appendix (chapter 9).

Actors

To achieve the required positioning resolution, each stage (translational and rotary) is equipped with a stepper motor and an adequate gear providing the accuracy defined in Table 3.1. The stepper motors of axes 1, 2, 3, and 5 feature a step resolution of 0.9° per complete step. The motor of axis 4 features a step resolution of 1.8° per complete step. All stepper motors are driven by power amplifiers which allow for an operation with an

Table 4.2: Specifications of the stepper motors and gear boxes integrated into the SASSU.

Stage	Motor	Gear Ratio	Motion resolution
1	stepper motor	1000 μm per rev	0.3125 μm per pulse
2	stepper motor	1000 μm per rev	0.3125 μm per pulse
3	stepper motor	100:1	0.001125° per pulse
4	stepper motor	444.44:1	0.0005° per pulse
5	stepper motor	1000 μm per rev	0.3125 μm per pulse

eighth of a full step thus improving the motion resolution. Additionally, gear boxes are mounted on each axis. Gear ratios for all axes are listed in Table 4.2 which additionally lists the final motion resolution of each axis. All stepper motors and gears (except the gear of axis 3) are constructed by Nanotec Electronic GmbH, Landsham, Germany. The gear of axis 3 is provided by Harmonic Drive, Limburg, Germany.

Sensors

To avoid precision loss due to step loss within the gears, external encoders are integrated into the system setup. The encoders measure the total displacement of each axis with a higher resolution than the stepper motor resolution. Position measurements are realized by a measuring tape and a corresponding optical read head. Axis 1, 2, 4, and 5 are thus equipped with optical encoders allowing position measurements in μm range. Details are listed in Table 4.3. All optical encoders are provided by Numerik Jena GmbH, Jena, Germany. The mechanical encoder is integrated into the stepper motor of joint 3 and fabricated by Nanotec, Landsham, Germany.
The chosen measurement tapes are originally designed for linear motion measurements. In case of axis 4, the tape is attached to the arc thus providing distance measurements along the circular path. The measurements have thus to be converted from distance values to angular values. In order to correctly calibrate the system, an additional inclinometer measuring the orientation of the tool externally is attached to the adapter. It provides angle measurements about the x_0 (ring angle) and y_0 axis (arc angle) with a resolution of 0.05°.

Control interface

Motion control of all axes is realized using a motion control unit MCU-3000 PCI-card interface (Roesch und Walter, Schwanau, Germany). The MCU serves as a control in-

Table 4.3: Specification of the optical encoders integrated into the SASSU.

Stage	Encoder type	Resolution
1	optical	0.2 μm per edge
2	optical	0.2 μm per edge
3	mechanical	0.0018° per edge
4	optical	0.0000996° per edge
5	optical	0.2 μm per edge

terface for up to 8 servo or stepper motors with the help of a personal computer. Linear motion commands are executed with a trapezoidal profile with user-defined initial and target velocity in all joints. Each axis is independently controlled by a *PID*-controller in a single-input/single-output fashion. This is often referred to as independent joint control [104]. The system can be configured and controlled by high level programming languages such as C/C++. Fig. 4.4 shows a systematic overview of the SASSU where active elements are indicated by an arrow and the measurement readings are indicated by a box. The control PC connects to the MCU-3000 via a C/C++ interface using an adequate library.

Hardware

Physical construction of the hardware was realized by IBG Technology Hansestadt Luebeck GmbH (Luebeck, Germany). All mechanical parts (except the movable parts such as guiding rails) of the SASSU are made of aluminum which is hard coated in order to support cleaning and sterilization. For each stage, hardware-based mechanical end stops are integrated. The end stops consist of screws which are detected by positioning sensors attached to each stage (see Fig. 4.6(a)). If the positioning sensor detects the screw, a signal is passed to the MCU 3000 controller which stops the motion with a user-defined deceleration. While an axis is positioned at such a mechanical end stop, no normal movement command will be executed. To remove an axis from the respective end, special movement commands have to be performed.
Movements of the respective stages are guided by guiding rails. For all axes, the stepper motor actuates a gear which subsequently moves a slide. The slide, in turn, is attached to a guiding rail defining its direction of motion. An exemplary slide is shown in Fig. 4.6(b), Fig. 4.6(c) shows the guiding rails of the first two translational stages. The guiding rail of the fourth stage is bent thus leading the slide along the rim of the arc (see Fig. 4.6(d)). Note that due to construction, the bent guiding rail is not fabricated in one piece. Thus,

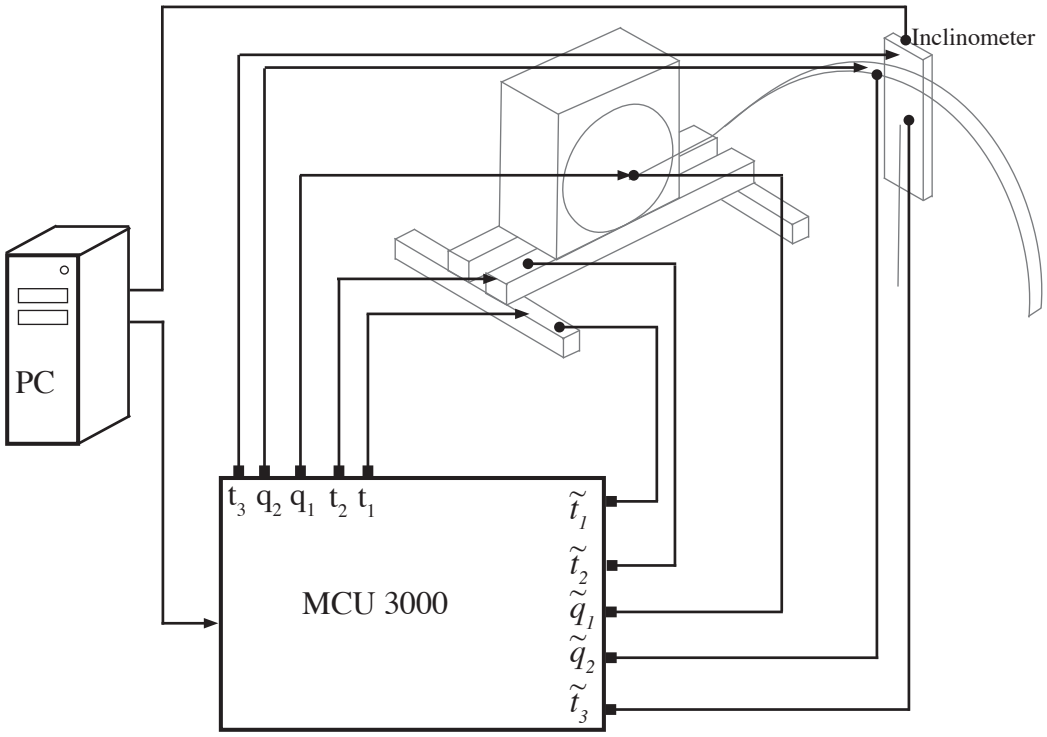

Figure 4.4: System architecture of the SASSU. Arrows indicate active elements, dots indicate the encoders. A PC integrates the PCI control card MCU-3000 which drives the stepper motors and provides an interface to all encoder values. The inclinometer is an external angular measurement device directly connected to the PC.

two different rails have been mounted onto the arc.

Stereotactic frame

The SASSU integrates a stereotactic frame for the animal which can be repeatably attached to the base plate underneath the SASSU. The frame is made of plastics (POM) and can be placed into e.g. a CT scanner. This allows to preoperatively obtain a CT scan of the animal which is already fixed into the frame. This supports the planning and registration procedure for an individual animal.

4.1.6 Hardware-based safety features

To provide safety for the animal and the surgeon, different hardware-based safety measures have been realized.

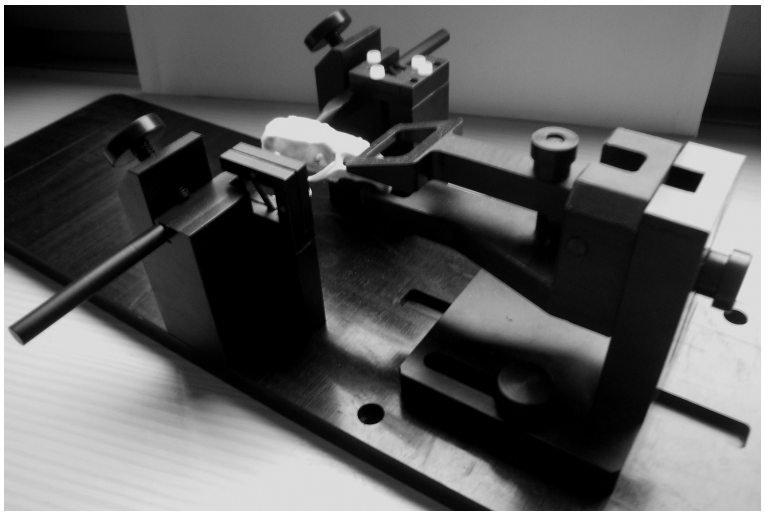

Figure 4.5: CT-compatible frame with fixed animal skull. The frame can be repeatably attached to the base plate of the SASSU and allows preoperative acquistion of a CT data set.

1. Hardware-based collision avoidance
   As outlined in section 4.1.2, the center-of-arc principle provides an inherent mechanical safety as only axis t_3 (insertion stage) moves the probe into the brain. Other joint movements will not lead to collision of the hardware with the animal.

2. Emergency stop button
   An emergency stop button has been integrated into the mechanical design (see lower left corner of Fig. 4.3). Pressing the emergency stop button immediately stops any motion.

3. Mechanical end stops
   Mechanical end stops which are integrated into each stage provide an additional safety measure to constrain the motion of each stage to a certain range (see Fig. 4.6(a)).

4.2 Kinematic analysis

Putting the proposed manipulator into the framework of small animal stereotaxy requires a thorough kinematic description of the system. Kinematic analysis allows to geometrically describe the motion of the SASSU and the attached probe in space and thus provides the functionality for surgical path planning and accurate tool placement. In the context of stereotactic procedures, the kinematic analysis provides the analytical means to insert the

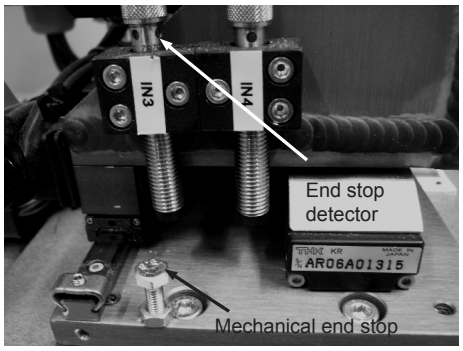

(a) Mechanical end stop and corresponding detector.

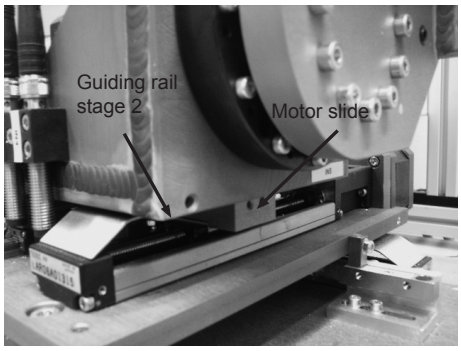

(b) Motor slide and guiding rail of the second stage.

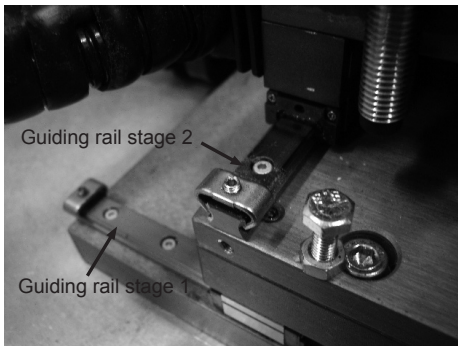

(c) Guiding rails of the first and second translational stages.

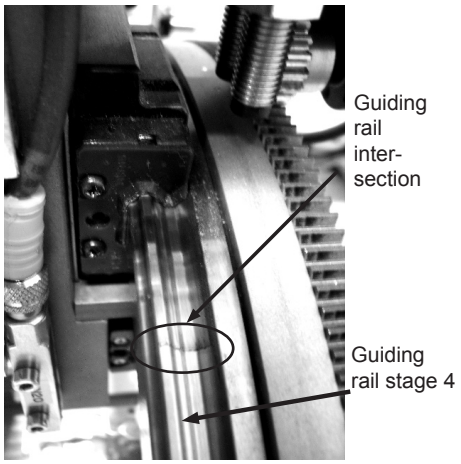

(d) Guiding rail of the fourth stage.

Figure 4.6: Details of the mechanical design and constructional components of the SASSU. (a) End stops (b) Motor slide (c) Guiding rails (d) Bent guiding rail.

probe along a specified path to reach a desired target. The following section introduces the kinematic description of the SASSU, namely the forward and inverse kinematics. Having described the system analytically, a theoretical positioning accuracy analysis is performed which shows that the kinematic structure of the SASSU provides a higher positioning accuracy than an existing structure with a comparable design.

4.2.1 Conventions and notations

For the kinematic analysis of the proposed robotic mechanism, some conventions have to be made. Fig. 4.2 shows the base coordinate system of the manipulator which is placed in the center of rotation (CoR) of both rotary joints. The rotary axes denoted

as q_1 and q_2 ideally intersect in the origin (e.g. the CoR). Referring to the stereotactic angle convention, q_1 corresponds to the ring angle (rotating about the x_0-axis) and q_2 corresponds to the arc angle (rotating about the y_0-axis). The base frame is denoted as P_0 and the corresponding axes as x_0, y_0, and z_0. Following the conventions for kinematic calculation in [103], the consecutive coordinate frames of the translational and rotary stages are denoted as P_j. Regarding the notation for active joints and the corresponding numerical joint values of a serial robotic mechanism, the following conventions will be made: the joint value of a translational or prismatic joint T will be denoted by t_i. The joint values of a rotary joint will be denoted as q_i. The parameter i refers to the i-th joint (see Table 4.1).
The vector of all joint variables will be denoted as Θ where

$$\Theta = \begin{pmatrix} t_1 \\ t_2 \\ q_1 \\ q_2 \\ t_3 \end{pmatrix}. \tag{4.1}$$

Measured joint values (e.g. by integrated position sensors) will be referred to as $\tilde{\Theta}$. For the following kinematic analysis, the concept of homogeneous matrices as a means to describe a manipulator POSE will be used. A short introduction is given in the appendix (chapter 9).

4.2.2 Forward kinematics

The forward kinematics determine the POSE of the probe in space if the joint variables of the SASSU are given. The design shown in Fig. 4.2 can be described by the so-called Denavit-Hartenberg parameters (DH parameters) [1]. The sequence of coordinate systems for each active joint is shown in Fig. 4.7. Note that all consecutive frames P_j of the ideal spherical mechanism are located at P_0. Considering the set of DH parameters, this fact is reflected by assuming no translational contributions a_i and d_i between two consecutive frames P_{j-1} and P_j except the active translational joint parameters t_i. The set of ideal DH parameters for the SASSU is summarized in Table 4.4. Here, l_T denotes the length of the probe measured from the CoR. Note that this definition allows a negative probe length if the probe tip is located above the center of the arc.
For an ideal mechanism, all frames P_j have a common origin located in the isocenter P_0. Due to different probes attached to the adapter of the last translational stage and

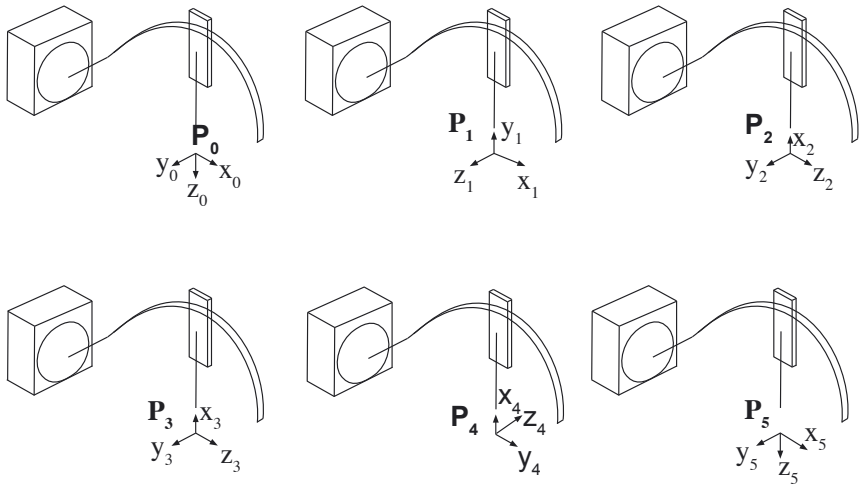

Figure 4.7: Sequence of coordinate frames for the ideal SASSU system according to the DH conventions [1]. P_j denote the consecutive coordinate frames.

constructional issues, the real location of the consecutive coordinate frames P_j differ from the isocenter. During initial operation of the realized system it has been found that, for example, the axis z_3 does not intersect the axis z_4. This means that there is no exact isocenter of rotation for ring and the arc angle. Additionally, the location of P_3 and P_4 are separated by an offset in x_0 and y_0. Integrating these findings into the kinematic description introduces a set of offsets into the DH parameters:

1. o_{z1} gives the difference between P_3 and P_4 in z_0 direction.
2. o_y is the difference between P_3 and P_4 along the y_0 direction.
3. o_x is the offset that provides the difference between P_5 and P_6 along the x_0 direction.
4. o_{z2} gives the difference between P_4 and P_5 in z_0 direction and can be considered as the probe length l_T.

The resulting set of real DH parameters is summarized in Table 4.5. Incorporating these parameters in the forward calculation, the orientational part of the POSE of the probe tip

Table 4.4: DH parameters for the ideal SASSU system according to the conventions in [1]. a_i and d_i denote translational distances (along the x_i and z_i axes) to the following coordinate frame, α_i and θ_i denote angles of rotation around the x_i and z_i axes.

Frame	a_i	d_i	α_i	θ_i
0	0	0	$\frac{-\pi}{2}$	0
1	0	t_2	$\frac{\pi}{2}$	$\frac{\pi}{2}$
2	0	t_1	0	0
3	0	0	$\frac{\pi}{2}$	q_1
4	0	0	$-\frac{\pi}{2}$	$q_2+\frac{\pi}{2}$
5	0	t_3+l_T	0	0

can now be expressed as

$$
\begin{aligned}
{}^5_0P &= \begin{bmatrix} \cos q_2 & 0 & -\sin q_2 \\ -\sin q_1 \sin q_2 & \cos q_1 & -\sin q_1 \cos q_2 \\ \cos q_1 \sin q_2 & \sin q_1 & \cos q_1 \cos q_2 \end{bmatrix} \\
&= \begin{bmatrix} n_x & s_x & a_x \\ n_y & s_y & a_y \\ n_z & s_z & a_z \end{bmatrix}.
\end{aligned}
\tag{4.2}
$$

The translational part of the POSE matrix is provided by

$$
\begin{aligned}
p_x &= \cos q_2 o_x - \sin q_2 (t_3 + o_{z2}) + t_1, \\
p_y &= -\sin q_1 \sin q_2 o_x - \sin q_1 \cos q_2 (t_3 + o_{z2}) - \sin q_1 o_{z1} - \cos q_1 o_y + t_2, \\
p_z &= \cos q_1 \sin q_2 o_x + \cos q_1 \cos q_2 (t_3 + o_{z2}) + cos q_1 o_{z1} - \sin q_1 o_y.
\end{aligned}
\tag{4.3}
$$

4.2.3 Inverse kinematics

The inverse kinematics are used to determine the joint variables of the robot given the probes POSE in space. Based on the orientational part of the POSE in Eq. 4.2, an analytic approach to the inverse kinematics can be taken. Joint parameters for a given POSE can

Table 4.5: DH parameters for the real SASSU system according to the conventions in [1]. a_i and d_i denote translational distances (along the x_i and z_i axes) to the following coordinate frame, α_i and θ_i denote angles of rotation around the x_i and z_i axes.

Frame	a_i	d_i	α_i	θ_i
0	0	0	$\frac{-\pi}{2}$	0
1	0	t_2	$\frac{\pi}{2}$	$\frac{\pi}{2}$
2	0	t_1	0	0
3	$-o_{z1}$	0	$\frac{\pi}{2}$	q_1
4	0	o_y	$-\frac{\pi}{2}$	$q_2+\frac{\pi}{2}$
5	o_x	t_3+o_{z2}	0	0

be determined as follows:

$$
\begin{aligned}
q_1 &= \operatorname{atan2}\left(\frac{-a_y}{a_z}\right),\\
q_2 &= \operatorname{atan2}\left(\frac{-a_x}{-a_z\cos q_1}\right),\\
t_3 &= \frac{p_z-\cos q_1\sin q_2 o_x - cosq_1 o_{z1}+\sin q_1 o_y}{\cos q_1\cos q_2} - o_{z2},\\
t_2 &= p_y+\sin q_1\sin q_2 o_x+\sin q_1\cos q_2(t_3+o_{z2})+\sin q_1 o_{z1}+\cos q_1 o_y,\\
t_1 &= p_x-\cos q_2 o_x+\sin q_2(t_3+o_{z2}).
\end{aligned}
\tag{4.4}
$$

where the notation a_x refers to Eq. 4.2. Two special cases for the inverse kinematics have to be considered:

1. For a joint value of $q_1 = \pm 90°$, no numerical solution for t_3 exists. Interpreting this configuration geometrically shows that in this case, the axis t_2 and t_3 are both contributing to a movement in z_0 direction. This redundancy causes a singularity of the robotic system. The joint ranges listed in Table 4.1, however, do not allow the value of q_1 to take such a value thus preventing the robotic system from a singular configuration.

2. For a joint value of $q_2 = \pm 90°$, the same scenario occurs regarding the axes t_1 and t_3.

Hence, the joint value range introduced by the mechanical design prevents singularities of the system and provides a unique solution to the inverse kinematic problem.

4.3 Modeling and control

To obtain high performance, especially positioning accuracy, accurate modeling of the robotic structure is required. Two main routes of robot modeling are usually taken: the physical modeling approach and the system identification approach [104]. While the first relies on basic physical laws to come up with a model, the latter uses experimental data to adjust parameters in a selected model structure. As physical modeling for complex mechanical structures (such as the arc-type link) is usually hard to realize, the system identification presents an adequate option to model the SASSU. Generally, system identification for robots can be categorized into three levels [110]:

- Kinematic description,
- dynamic models including rigid body dynamics and flexible body dynamics, and
- joint models.

The identification process forms the basis to develop adequate control strategies for e.g. continous path tracking but also for diagnosis, performance simulation, and supervision of the manipulator. While dynamic modeling is mandatory for advanced motion control of robotic manipulators [104], the basic motion tasks of the SASSU are predominantly point-to-point motions with a low dynamic range. Therefore, the independent joint control realized by the control interface MCU-3000 is considered an adequate control scheme and no further dynamic modeling is pursued in this work. An accurate kinematic description, however, is still a fundamental requirement to achieve positioning accuracy. While the extensive kinematic analysis in section 4.2 concentrates on an ideal kinematic system, this section describes an approach to integrate (a) different tool geometries and (b) hardware-related sources of positioning inaccuracies into the kinematic description. This will be achieved by two means: (a) an offline calibration method and (b) an online deflection compensation strategy integrated into the control scheme. Subsequently, the basic software to operate the SASSU is described. It includes the user interface and the basic motion control scheme. Special focus will be put on software-based deflection compensation which is necessitated by the mechanical design.

4.3.1 The calibration problem

Calibration is the process of identifying the real geometrical parameters in the kinematic expression of a robot [111]. It eventually leads to a higher absolute positioning accuracy than operating an uncalibrated robot. In case of the SASSU, uncalibrated states result

from the fact that a variety of tools should be mountable to the system. In stereotaxy, almost all tools are linear (e.g. microelectrodes) as other geometries might destroy healthy brain tissue during insertion. Nonetheless, attaching different linear probes to the system will naturally change the kinematic properties. Referring to section 4.2.2, the calibration method identifies the parameters o_x, o_y, o_{z1}, and o_{z2} listed in Table 4.5 which present unknown parameters for an uncalibrated adapter-probe configuration.
Identification of real geometrical parameters in this work uses a geometric approach based on the kinematic specifications defined in section 4.2. A fundamental requirement for the calibration process is the introduction of a spatially fixed reference point. Its position is required to be constant with respect to the base plate of the SASSU. The following steps of the calibration procedure will be illustrated using only the rotary joint q_1. The methodology, however, can easily be extended to rotary movements of joint q_2 as well. Under the assumption of a linear probe (e.g. a microelectrode), the SASSU joints are actuated until the probe tip is located at the reference point with the rotary joint angles being zero. This will be referred to as initial configuration (see Fig. 4.8(a)). According to the kinematic structure of the SASSU, the probe tip will be located on the surface of a sphere if only the rotary joints are actuated. The center of the sphere corresponds to the CoR. The spatial distance of tool tip and reference point depends on the radius of the sphere and the rotary joint values. The radius of the circle itself is defined by the offset parameters o_{z1}, o_x, o_y, and o_{z2}. Eq. 4.5 shows the analytic expression of the spatial distance if joint q_1 is varied and $q_2 = 0°$:

$$\begin{aligned} p_{x,\mathrm{SASSU}} &= o_x, \\ p_{y,\mathrm{SASSU}} &= -o_{z2}\sin q_1 - o_{z1}\sin q_1 - \cos q_1 o_y, \\ p_{z,\mathrm{SASSU}} &= o_{z2}\cos q_1 + o_{z1}\cos q_1 - o_y \sin q_1, \\ d &= \sqrt{p_{x,\mathrm{SASSU}}^2 + p_{y,\mathrm{SASSU}}^2 + p_{z,\mathrm{SASSU}}^2}. \end{aligned} \tag{4.5}$$

In Eq. 4.5, d denotes the spatial distance from the CoR. It can be seen that variation of q_1 only affects the $y-$ and $z-$coordinates of the spatial position. Fig. 4.8(b) shows the spatial distance if the rotary joint 1 is varied by q_1. It also indicates the translational joint values t_2 and t_3 which will return the probe tip to the initial position. Returning the probe tip and reading the external encoder information will provide a numerical value for the distances p_x, p_y, and p_z given by Eq. 4.5. Incorporating the translational joint values will

return the tool tip to the reference tip position

$$\begin{aligned} \Delta t_2 &= -(\Delta y + \Delta z \tan q_1) \text{ and} \\ \Delta t_3 &= -(\frac{\Delta z}{\cos q_1}). \end{aligned} \tag{4.6}$$

into Eq. 4.5, the differences Δy and Δz from the initial position can be expressed in terms of q_1, t_2, t_3, and the offsets o_y, o_{z1}, and o_{z2}:

$$\begin{aligned} \Delta y &= -o_{z1}\sin q_1 - o_{z2}\sin q_1 - o_y \cos q_1 + o_y \text{ and} \\ \Delta z &= o_{z2}\cos q_1 + o_{z1}\cos q_1 - o_y \sin q_1 - o_{z1} - o_{z2}. \end{aligned} \tag{4.7}$$

Incorporation of these dependencies into Eq. 4.6 yields the relationship between the joint values to compensate for the displacement and the offset parameters:

$$\begin{aligned} \Delta t_3 &= (o_{z1} + o_{z2})(\frac{1}{\cos q_1} - 1) + \frac{\sin q_1}{\cos q_1} o_y \text{ and} \\ \Delta t_2 &= (o_{z1} + o_{z2})\tan q_1 + (\cos q_1 - 1 + \sin q_1 \tan q_1) o_y. \end{aligned} \tag{4.8}$$

Note that similiars relation can be established if q_2 is varied as well.
Robust parameter identification is eventually done by moving the adapter with n predefined angle movements $Q_1 = (q_{1,1},\ q_{1,2},\ \ldots,\ q_{1,n})$ and a subsequent adjustment of t_2 and t_3 to return the probe tip to the origin of the reference system. The resulting displacements can be expressed in matrix form as

$$\begin{bmatrix} \Delta t_{2,1} \\ \Delta t_{3,1} \\ \Delta t_{2,2} \\ \Delta t_{3,2} \\ \vdots \\ \Delta t_{2,n} \\ \Delta t_{3,n} \end{bmatrix} = \begin{bmatrix} \cos q_{1,1} - 1 + \sin q_{1,1}\tan q_{1,1} & \tan q_{1,1} & \tan q_{1,1} \\ \tan q_{1,1} & \frac{1}{\cos q_{1,1}} - 1 & \frac{1}{\cos q_{1,1}} - 1 \\ \cos q_{1,2} - 1 + \sin q_{1,2}\tan q_{1,2} & \tan q_{1,2} & \tan q_{1,2} \\ \tan q_{1,2} & \frac{1}{\cos q_{1,2}} - 1 & \frac{1}{\cos q_{1,2}} - 1 \\ & \vdots & \\ \cos q_{1,n} - 1 + \sin q_{1,n}\tan q_{1,n} & \tan q_{1,n} & \tan q_{1,n} \\ \tan q_{1,n} & \frac{1}{\cos q_{1,n}} - 1 & \frac{1}{\cos q_{1,n}} - 1 \end{bmatrix} \begin{bmatrix} o_y \\ o_{z1} \\ o_{z2} \end{bmatrix} \tag{4.9}$$

which takes the form

$$\Delta \tilde{T} = Ax \tag{4.10}$$

Note that in the real scenario, the translational joint displacements will be given by the positional measurements $\Delta \tilde{t_i}$ provided by the encoders. The relation in Eq. 4.9 allows a mathematical identification of the unknown parameters by solving the normal equation

$$\left(A^\top \cdot A\right) x = A^\top \cdot \Delta T$$

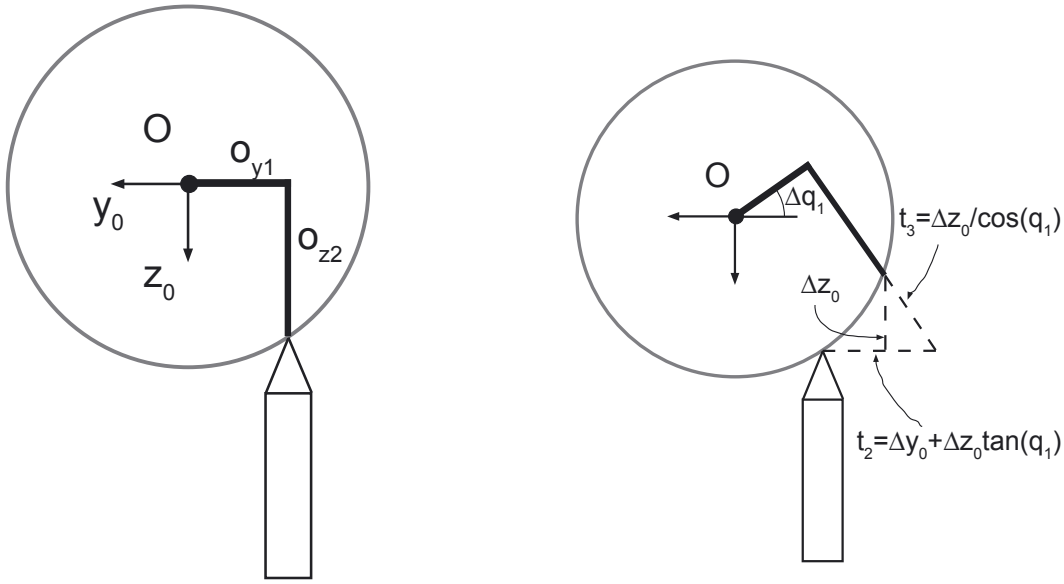

(a) Initial position for calibration with the tool tip touching the reference point. The point O denotes the origin of the SASSU coordinate system and y_0, z_0 the respective axes. The parameters o_{y1} and o_{z2} denote offset parameters.

(b) Change of the tool tip position for a rotary motion of q_1. The spatial displacement in terms of q_1 is indicated. Indicated are the translational joint values t_2 and t_3 to return the probe tip to the reference position.

Figure 4.8: Calibration scheme for a linear probe adapted to the SASSU system.

with the unique solution

$$x = \left(A^\top \cdot A\right)^{-1} \cdot A^\top \cdot \Delta T$$

if the inverse of $\left(A^\top \cdot A\right)$ exists.
A complete calibration also takes joint variations of $Q_2 = (q_{2,1},\ q_{2,2},\ \ldots,\ q_{2,n})$ into account, Eq. 4.9 is then modified and extended.

4.3.2 Implementation of the calibration method

Approaches to calibration can be classified as (a) internal calibration appproaches which make use of internal sensors and (b) external calibration approaches which use an external measurement system [112]. As external approaches typically outperform internal calibration approaches [112], one of the latter is chosen to calibrate the SASSU. A survey of external calibration approaches including methods based on calipers, ultrasound, and laser triangulation is provided in [112]. Different reasons, however led to videometry as the measuring method for calibration. First, it is among the most accurate approaches to

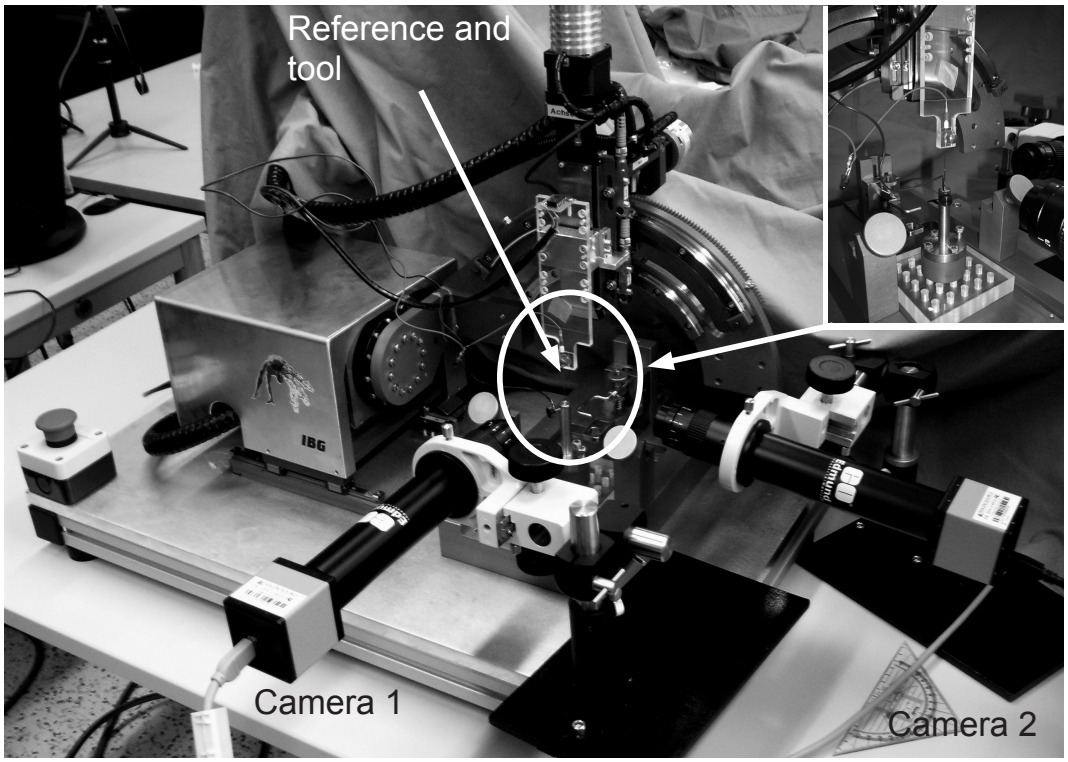

Figure 4.9: SASSU setup for the calibration procedure with two highly magnifying cameras in a stereoscopic setup. The upper right corner shows a detailed view of the probe and the reference tip.

calibration [112]. Second, it prevents mechanical interaction of the uncalibrated tool with so-called reference workpieces which might damage the tool.
In our setup, video monitoring is provided by two cameras (TheImagingSource, Charlotte, NC, USA) each featuring a magnifying lens (Edmund Optics, Karlsruhe, Germany) which allow motion resolution smaller than 5 μm. The cameras are positioned approximately at a 90° angle between the respective lines of view. The reference system described in section 4.3.1 is a virtual point provided by pixel coordinates of static cameras in a stereoscopic setup. Fig. 4.9 shows SASSU setup for calibration. An exemplary tool is provided by a microelectrode with a tip diameter of approximately 2 μm. Distance measurements between the microelectrode and the virtual reference point are enabled by basic image processing methods. To automatically identify the position of the tool tip in the camera images, the microelectrode boundaries are segmented by the Canny edge detection method [113]. The tip position is then identified as the intersection of the outer shape and the estimated centerline of the electrode. The centerline is determined via a principal

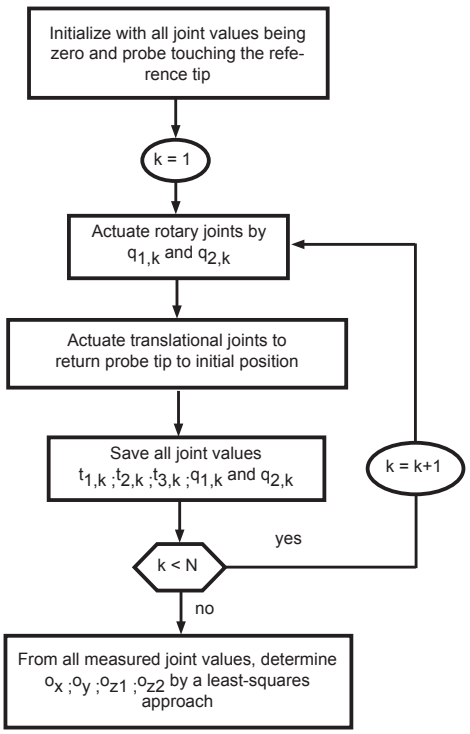

Figure 4.10: Sequence of steps during the calibration of an arbitrary probe attached to the SASSU.

component analysis (PCA)[2]. PCA fitting was chosen as it provides a general approach to determine the centerline of linear, thin probes with arbitrary (but symmetric) tip shape. Alternative approaches such as ellipsoidal fitting, in contrast, would apply only to special shapes.

To improve robustness of the edge detection, a white background is introduced and contrast and brightness properties of the camera images are adjusted. After camera calibration, spatial distances of the probe tip and the reference point are provided. In Fig. 6.4, the images for both cameras with the identified probe tip, the virtual reference point, and the corresponding spatial distance is shown. The calibration process is visualized in Fig. 4.10. A pseudo-code representation is given by algorithm 9.1 in section 9.1. In the presented approach, the step of returning the probe tip to the reference position usually requires to actuate the robot axes. As this involves a lot of time-consuming user interac-

[2]Starting point for the PCA is the binary image after thresholding which shows the segmented probe and the background. The PCA is performed on the set of pixels belonging to the probe. The first principal component (e.g. the direction of the greatest variance in the data) is subsequently considered to be the centerline of the tip. Fig 6.4 shows an exemplary scenario where the centerline is shown as a green line.

tion, the calibration process has been automated. First, the position of the probe tip in the initial configuration (namely the reference position) is saved in terms of pixel coordinates of both cameras yielding the pixel pairs $p_r^{c1} = (x_r^{c1},\ y_r^{c1})$ and $p_r^{c2} = (x_r^{c2},\ y_r^{c2})$. Now, the rotary joints are actuated and the tip of the rotated tool is again detected which yields the pixel pairs $p_c^{c1} = (x_c^{c1},\ y_c^{c1})$ and $p_c^{c2} = (x_c^{c2},\ y_c^{c2})$. Using the property that movements in x_0 direction of the robot (e.g. joint t_1) are mainly observed by the first camera (while movements in y_0 direction are mainly observed by the second) and the current pixel differences, an automated and iterative control scheme is implemented which automatically returns the probe tip to the initial position. A pseudo-code representation of the automated return procedure is provided by algorithm 9.2 in section 9.1. Note that the determination of the translational return value Δt_3 is achieved by analyzing the y-coordinate of the first camera although both cameras could be used. Herein, the constant thr denotes the pixel threshold meaning that the probe tip is returned to the initial position with a predefined pixel-based accuracy (usually $thr = 2 \ldots 4$).
The iterative procedure requires an automated detection of the tip based on the camera images I^{c1} and I^{c2}. Robust and precise detection is achieved by subsequently

1. adjusting the contrast and the brightness of the image,
2. performing a median filtering for noise reduction,
3. converting the image to a binary image based on an adjustable threshold,
4. performing an edge detection via the Canny operator, and
5. determining the centerline of the tip via a principal component analysis (PCA).

The intersection of the edge curve and the centerline is then considered the tip of the tool. The software framework for image acquisition and processing was realized in *Java* (Sun Microsystems Inc., Santa Clara, CA, USA) and is shown in Fig. 6.4. During operation, the described tip detection method has proven to be robust.

4.3.3 Deflection compensation

Deflection compensation can be considered an additional step to improve the positioning accuracy of robotic manipulators. In this work, deflection compensation refers to the compensation of sources of errors which cannot be adequately expressed by the geometrical parameters of the robotic manipulator and are thus not covered by the calibration process. These sources of errors result from manifold factors. Among those are e.g. friction, gearbox elasticity, and temperature dependency of the mechanical parts [114]. While certain

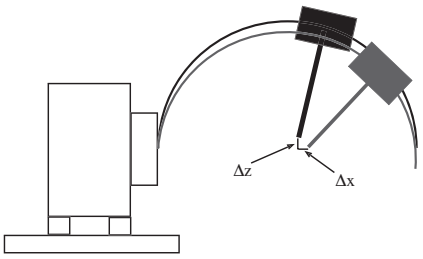

(a) Schematic of the effect of gravity induced deflection for the SASSU leading to positioning inaccuracies.

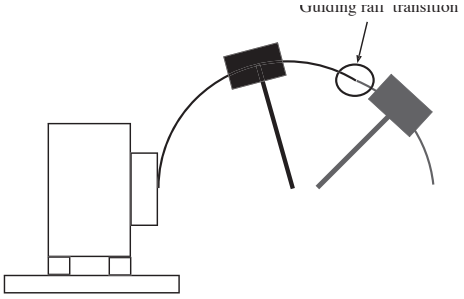

(b) Schematic of the effect of guiding rail transition induced deflection for the SASSU leading to positioning inaccuracies.

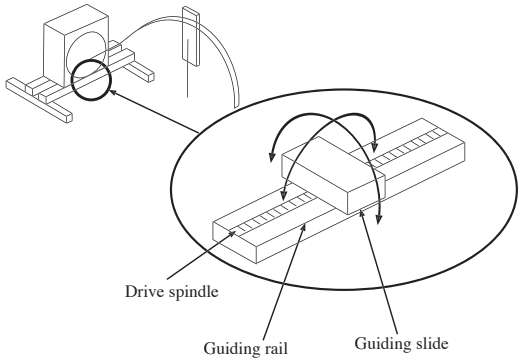

(c) Schematic of the effect of deflection induced by the tilt about the guiding slide leading to positioning inaccuracies.

Figure 4.11: Schematics of different assembly-based effects leading to inaccuracies in the probe positioning.

types of errors (e.g. step loss) might be eliminated by an adequate positioning control scheme, other types of errors cannot be compensated. In case of the SASSU system, one

major error source arises from the mechanical assembly of the system. Different sources of inaccuracy due to constructional issues can be classified:

1. The first source is given by deflection induced by gravity on the free end of the arc. Gravity will cause deflection of the levitating arc if the last linear stage is moved towards the free end (see Fig 4.11(a)).

2. Inaccuracies are also introduced by the mechanical construction of the guiding rails of the fourth stage. Due to manufacturing issues, the guiding rail which leads the slide along the rim of the arc cannot be manufactured in one piece. At the transition of the first to the second rail, the slide does not precisely stay within the same circular path (see Fig. 4.11(b)). Although both elements feature the same radius, the spatial position of their centres differs slightly due to variances in manufacturing. This, however, results in two effects: First, the slide tilts if moving across the transition and second, the kinematic properties of the system, namely the offset parameters introduced in section 4.2.2, change. Operating the system with the inappropriate set of parameters would subsequently lead to inaccurate positioning of the end-effector.

3. The third source of inaccuracy is given by the guiding rails of stages 1 and 2. The plate carrying the remaining stages is connected to the first and second stage by means of a single guiding slide. If stages 3 to 5 are actuated, the plate tilts about an axis parallel to the guiding rail and an axis perpendicular to the guiding rail due to manufacturing tolerances (see Fig. 4.11(c)). Although these effects are small, they do affect the accuracy of the system.

Due to these inaccuracies, calculating joint values for a desired POSE of the end-effector and subsequent actuation of the respective joints will therefore lead to imprecise positioning. Classical approaches for deflection compensation include the development of adequate control laws. These control laws mostly presume an entirely rigid structure [115] or consider only flexible joint models [116]. Additionally, they are based on two premises. First, an adequate model of the deflection (e.g. gravity) should be existent. Second, sensors which feed back an appropriate signal to compensate for the any misplacement of the probe tip. While both can be realized for standard industrial robots (e.g. rigid links allow to precisely determine the end-effector position from measured joint values), both premises are not given for the SASSU and the previously mentioned sources of errors. An alternative approach is the use of modeless calibration methods [117] where the robot is moved through a set of grid points and position errors are stored. During operation, errors are compensated by using e.g. interpolation methods [117].

As the observed sources of deflection are hard to model, this work develops a motion control scheme which integrates a deflection control term based on a modified version of modeless calibration. Quantitative evaluation of the positioning improvement shows that the mechanical positioning accuracy increases by nearly 0.17 mm (maximal positioning error before deflection compensation of 0.2 mm and maximal positioning error after deflection compensation of 0.032 mm). While analyzing the nature of the inaccuracies, it was found that positioning inaccuracies are mainly related to the fourth stage, namely the second rotary joint. Experimental findings support that inaccuracies are due to the movement of the slide along the rim of the arc. Hence, the approach is to introduce a deflection compensation term for each translational joint of the SASSU depending on the joint value q_2. The compensation term models the effect of inaccuracies in two states of operation:

1. The effects of inaccuracies during the calibration process, and
2. the effects of inaccuracies during the normal operation of the SASSU.

In a first approach, the compensation term takes a linear characteristic which yields

$$t_i^{corr} = t_i + (m_i q_2 + b_i). \tag{4.11}$$

The parameters m_i and b_i denote unknown correction terms for each translational stage and are determined during the calibration procedure. As stated before, deflection occurs during the calibration process and will therefore contribute to a distortion of Δt_1, Δt_2, and Δt_3 during the calibration process. Referring to Eq. 4.10, the left hand side of the measured translational distances are composed of two parts: one expressing the correct displacement and one expressing the displacement induced by deflection:

$$\tilde{t_i} = t_i + (m_i q_2 + b_i) \tag{4.12}$$

where t_i denotes the ideal joint value. To determine the unknown parameters m_i and b_i, an optimization approach is taken. Generally, the measured displacement values $\Delta\tilde{t_i}$ are compared to the ideal joint values t_i which are determined using the kinematic calculations in section 4.2. If

$$D = \begin{pmatrix} m_1 \\ m_2 \\ m_3 \\ b_1 \\ b_2 \\ b_3 \end{pmatrix} = \begin{pmatrix} M \\ B \end{pmatrix} \tag{4.13}$$

denotes the design variable vector, the following cost function will be analyzed:

$$J(D) = \sum_{i=1}^{3} \sum_{j=1}^{n} (\tilde{t}_{i,j} + (M(i)q_{2,n} + B(i)) - t_{i,j})^2. \tag{4.14}$$

where $M(i)$ denotes the i-th entry in the M-vector and n is the number of joint angles used in the calibration procedure. The optimization problem is now given as

$$\min J(D). \tag{4.15}$$

Optimization is done following an iterative procedure:

1. Set $D = 0$.
2. Perform the first three steps of the calibration as described in section 4.3.2.
3. Calculate the offset parameters using Eq. 4.10.
4. Using the kinematic equations in section 4.2, calculate the ideal joint displacement values t_i corresponding to given rotary joint values q_1 and q_2.
5. Determine the mean-square error in Eq. 4.14.
6. Alter the design variable D and return to step 2 until a convergence criteria (e.g. $\Delta J(D) < \varepsilon$) is met.

The iterative procedure indicates that the problem in Eq. 4.15 is nonlinear as the ideal joint values $t_{i,j}$ depend on the offset parameters which are again calculated using D. Therefore, a nonlinear optimization approach has to be taken. The problem formulation can be considered as an unconstrained function of 6 variables. As gradient information of the cost function

$$S = \nabla J \tag{4.16}$$

cannot be determined, a zero order optimization method is chosen. In [118], different approaches are outlined. Among the most efficient and reliable zero order methods is Powell's method which is based on the concept of conjugate directions. For details, the reader is referred to [118]. Implementation of Powell's method shows that the design variable vector D can be optimized efficiently.

After having determined D during the calibration process, the linear deflection compensation is implemented for normal operation. If the user provides a desired POSE, the inverse kinematic equations are used to determine the respective joint angle q_2. Based on the respective value, the ideally calculated translational joint values are modified using

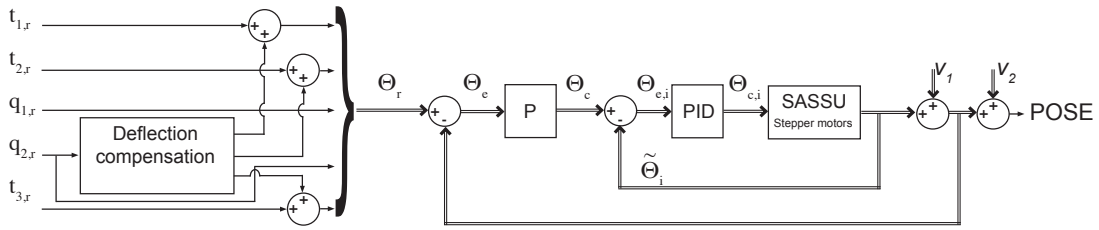

Figure 4.12: Motion control and deflection compensation architecture of the SASSU. According to the value of $q_{2,r}$, the translational joint values $t_{i,r}$ are corrected. Θ_r then denotes the desired, Θ_c the current joint value. Θ_e is the joint value error and $\tilde{\Theta}$ refers to the measured joint values. The index i refers to the internal control loop of the MCU-3000. Different sources of disturbances are indicated by v_1 and v_2.

Eq. 4.11.

Observations during implementation have shown that positioning accuracy is improved if the range of motion of the fourth stage is divided into multiple subparts, each featuring an appropriate deflection compensation vector D.

4.3.4 Motion control

Motion control of robotic manipulators is a large area of research. A good overview of existing approaches to motion control can be found in [104]. While most industrial robots require complex control strategies to e.g. allow fast and accurate path tracking, motion of the SASSU is generally constrained to point-to-point movements with low velocities. Thus, the proposed control scheme provides the required positioning accuracy but does not reflect dynamic properties of the system. It integrates the independent joint control realized by the MCU-3000, the external encoders integrated into the hardware design, the kinematic model and the deflection compensation. All parts are implemented into the software-based control framework. Fig. 4.12 shows the motion control and the integrated deflection compensation scheme. The desired joint value $q_{2,r}$ is used to adapt the translational joint values $t_{i,r}$. The resulting desired joint vector value Θ_r is compared to the measured joint value vector $\tilde{\Theta}$. The resulting joint vector error $\Theta_e = \Theta_r - \tilde{\Theta}$ is passed to a controller which calculates a movement command Θ_c. As the desired tasks of the SASSU do not involve high dynamics, a *P*-controller has been regarded appropriate (in comparison to *PI*- or *PID*-controller). This means that during operation, the movement command is proportional to the error signal Θ_e. The error signal is then passed to the

Table 4.6: Axis status information provided by the MCU-3000 control interface.

Description	Comment
Emergency out	Activated if an emergency out event occured.
Drive not ready	Provides information on the readiness of the axis.
Limit switch left hardware	Activated if the axis is in the range of the left hardware limit.
Limit switch right hardware	Activated if the axis is in the range of the right hardware limit.

internal control loop of the MCU-3000.
The movement command generates a joint movement of the stepper motors. Different disturbances v affect the positioning. One type of disturbance is measurable by the encoders (denoted as v_1) as e.g. step loss. Other types of disturbances (denoted as v_2) are not measurable and include e.g. deflection of the arm. Note that only the measurable disturbances can be compensated by the proposed control scheme. Internally, two types of joint values are used: (a) the internal, ideal joint values (Θ_r) which are modified if a new desired joint value vector is provided and (b) the external joint values ($\tilde{\Theta}$) which read out the encoder information. The software architecture provides the following functionalities:

1. Reference drive
   This functionality allows to perform a reference drive in all joints. The reference drive uses special indices on the optical encoder tapes which are constant with respect to the SASSU system. This enables the system to return to a defined POSE after the system lost joint value information (e.g. after the system was switched off). After a reference drive, the internal joint values are set to zero. Ideally, a reference drive should always be done before the SASSU is operated.

2. Software-based safety checks
   Ensure that no joint moves outside the given joint range. Note that this functionality is only provided if the system is started in its intial configuration as the safety check is based on a comparison of the internal joint values (Θ_r) to the respective joint range. Additionally, the internal joint values are always compared to internal joint limits thus providing a software-based motion range. The safety checks also comprise a check of the desired movement velocity and acceleration.

3. Forward and inverse kinematic calculation
   Instead of providing desired joint values, a target POSE can be specified. The

software internally calculates for the respective joint values by an inverse kinematic calculation according to Eq. 4.4 which are then passed to the control architecture.

4. Analysis of axis status
   Based on a special functionality of the MCU-3000, the axis status for each stage can be evaluated. Table 4.6 lists all used axis information which are provided by the MCU-3000. This especially indicates if one of the axes has reached the right or left hardware end stop.

5. End stop removal
   As stated in section 4.1.5, the MCU-3000 does not execute any movement command if the respective stage has reached the mechanical end stop. The end stop removal functionality provides a mean to remove the system from the end stop. As the internal joint values will not correspond to the real ones if the axis reached the end stop (the internal joint values always assume the complete movement to be performed), the internal joint values are set to the values of the external joint values after removal.

Passing the motion commands in the software framework is thread-based. This means that an arbitrary number of movement commands can be given while the current movement might still be executed. All commands are collected and iteratively executed. A stop command, however, will directly stop any movement and delete the remaining movement commands. In that case, the internal joint values are set to the external ones. Fig. 4.13 shows a screenshot of the implementation of the basic control module of the SASSU. Once the system is calibrated, the tool can be placed at an arbitrary POSE with a high accuracy.

4.3.5 Functionality and graphical user interface

Basic user interaction with the SASSU is provided by a graphical user interface. The interface is realized using *Java* as a programming language. The layout of the interface is shown in Fig. 4.13 and provides the following functionalities:

1. Joint movement
   Moves one joint with a given distance, velocity, and acceleration.

2. Stop movement
   Stops a movement with a predefined decceleration.

(a) Screenshot of the basic control software module. It allows to actuate each axis with a desired step size or move and stop all axes synchronously. On the bottom, the desired and the current joint values are shown.

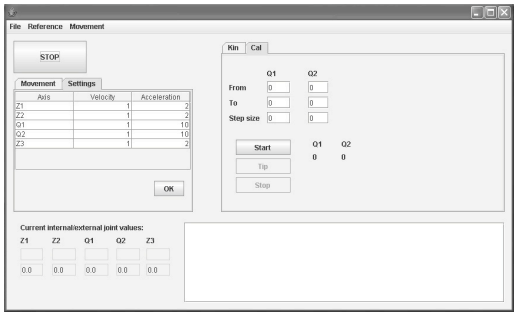

(b) Screenshot of the basic control software module. Within this framework, the user specifies the desired joint velocities and accelerations.

Figure 4.13: Screenshot of the basic control software module.

3. Move all joints
   Move all joints in parallel. Two modes are available which can be selected: (a) normal mode where all joints move in parallel with given distances, velocities, and accelerations and (b) interpolation where all joint movements start and stop at the same operational time.

4. Display internal and current joint values
   Displays the desired joint values from a software-based, internal counter and the values returned by the external encoders integrated into the SASSU.

5. Perform reference drive
   Starts a reference drive in all axes.

6. Specify an arbitrary CoR
   Saves the current tool tip position as a CoR.

7. Rotate about the CoR with arbitrary angles
   Rotates the tool tip about a CoR with given angles q_1 and q_2. After the movement, an imaginary centerline of the tool runs through the CoR.

8. Change movement parameters
   Allows an adjustment of joint velocities and accelerations.

9. Turn off the power amplifiers
   If used for electrophysiological recordings, an important requirement for the system is to introduce as little electrical noise as possible. A major source of such a noise

are the power amplifiers which drive the stepper motors. To minimize their possible effects on the recording quality, the SASSU offers the option to turn the power amplifiers on and off. While being turned off, all brakes of the SASSU are locked thus providing a stable spatial position.

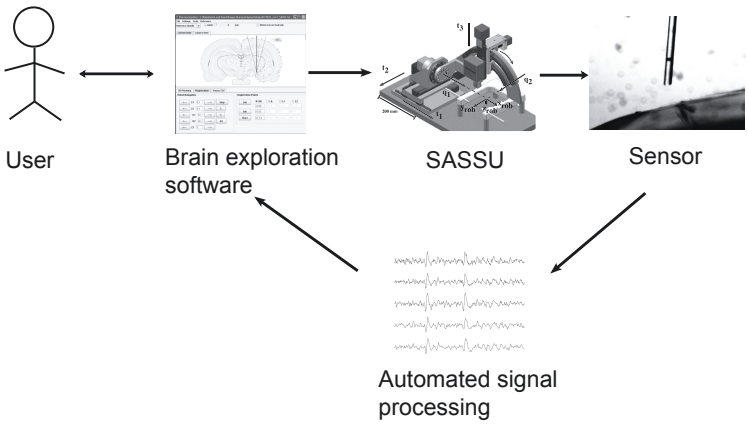

Figure 5.1: Robot-assisted stereotaxy in small animals - conceptional layout. The user controls the stereotactic robot through an easy-to-use PC planning & control interface to place the sensor probe at the exact position as defined in the planning software. Feedback from the robotic and probe sensors is processed and e.g. used by the control software to further refine the probe position.

5 Robot-assisted brain exploration[1]

While the previous chapter was dedicated to the design, construction, and the commissioning of a robotic manipulator for stereotactic procedures on small animals, this chapter introduces its integration into the surgical scenario. In contrast to existing stereotactic approaches, the manually operated stereotactic frame is now replaced by the SASSU. As a consequence, a software-based planning and control interface for the robotic assistant needs to be developed. Such a stereotactic control framework enables the surgeon to control insertion and to feed back, analyze, and process a sensor signal with respect to the exact spatial position of the probe tip. Hence, the software part allows to augment the pure stereotactic control framework to a brain exploration and analysis environment. Fig. 5.1 shows a schematic layout of such an exploration framework. A sensor component (e.g. a microelectrode), and a digital signal processing unit have been exemplary integrated into the framework. The focus of this chapter is subsequently put on the design and implementation of a brain exploration framework to perform robot-assisted stereotactic procedures on rats. In the first part, the design of a stereotactic control framework which enables plan-

[1] Parts of this chapter have been published in [100, 102, 119, 120, 121, 122].

ning, registration, and insertion of a probe into the small animal brain will be elaborated. The second part proposes the integration of OCT as a minimal invasive, real-time capable imaging modality into the brain exploration setup. In the context of integrating OCT into the stereotactic framework, different novel methodologies of using OCT in brain imaging have been developed, ranging from the processing of OCT A-scans to methods of OCT image processing. In order to motivate parts of the proposed methods, a short introduction into the general framework of OCT imaging is given. Subsequently, the focus is shifted on the processing of OCT A-scans in the context of single fibre imaging. In the latter part of this chapter, two methods for (a) segmentation of structures of interest and (b) filtering of speckled images are introduced, both novel in the field of OCT imaging.

5.1 Atlas-based stereotactic control framework

The stereotactic control software provides two main functionalities for probe insertion into the small animal brain: (a) user interface for the surgeon and (b) support of the surgical workflow. Integration of the SASSU system into the surgical workflow will replace certain steps and introduce additional requirements. The surgical workflow integrating the SASSU system is compared to the existing approach in Fig. 5.2. The preoperative steps (calibration and initialization) on the left side add to the surgical procedure without the SASSU system. As they are performed before the operation, they do not affect the duration of surgery. The steps of registration and prepositioning, previously performed by the surgeon, are taken over by the SASSU system. Existing steps as anaesthetization and fixation remain within the responsibility of the surgeon. Hence, the software-based stereotactic control should adapt to the surgical workflow of small animal stereotaxy. This is achieved using a modular structure for preoperative path planning, intraoperative registration, and intraoperative probe insertion control which is presented in the following. In addition to the surgical functionalities, this section provides details on software-based safety measures. The brain exploration framework and its functionalities are implemented using *Java* programming language (Sun Microsystems, USA).

5.1.1 Planning module

An important part of the stereotactic control framework is the user-interface before and during the surgery. The first step before surgery is the path planning. In the proposed implementation, the planning can be done using two approaches:

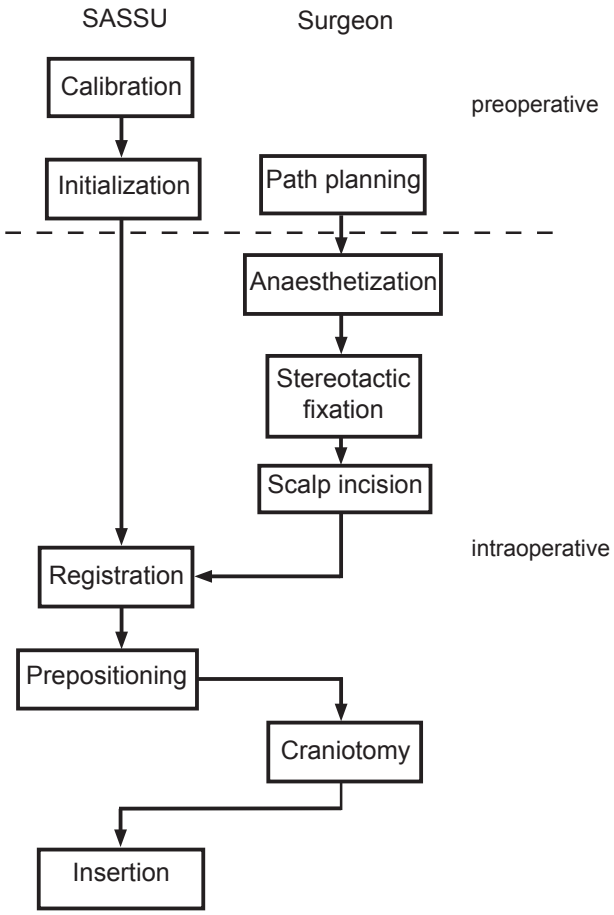

Figure 5.2: Surgical workflow integrating the SASSU system. The left column shows the steps performed by the SASSU, the right column the steps performed by the surgeon.

1. An atlas-based approach based on normalized atlas data such as the Paxinos atlas ([92]) and
2. an image-data based approach which incoporates CT- or MRI-data of the individual animal.

While the first allows two-dimensional planning based on coronal slices, it is constrained to normalized atlas data only. The latter extends to three-dimensional planning and allows individual planning for the respective animal. Also, both approaches can be combined by e.g. registration of the CT data to atlas information. Both allow the user to interactively specify the desired target point. Furthermore, the desired path of penetration can be selected. If desired or required by the surgical settings, the angular range of the insertion path can be constrained. Once the target and the entry path are specified, the forward and

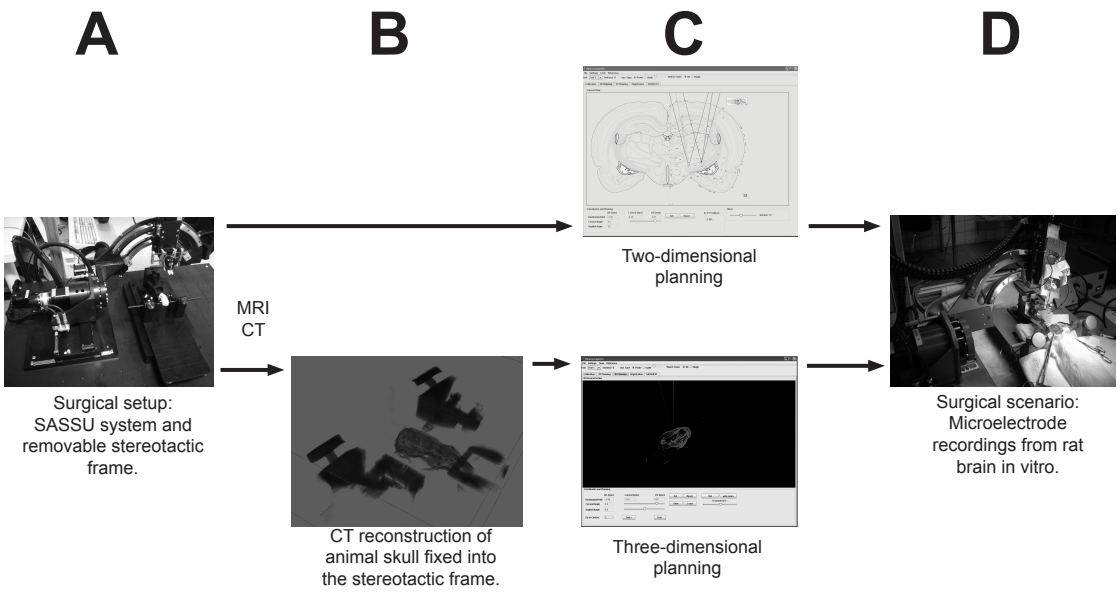

Figure 5.3: Course of surgery using the stereotactic control framework. [A] The animal is fixed into the CT-compatible frame [B] Volumetric reconstruction of the skull fixed into the frame [C] Two- and three-dimensional planning modalities [D] Surgical scenario.

inverse kinematic equations (see section 4.2) allow to calculate the corresponding motion of the stereotactic assistant automatically. Thus, no further action by the user is needed. Fig. 5.3 summarizes both modalities.

Two-dimensional planning

The planning scenario is based on the common, atlas-based approach. Herein, the target point is chosen based on anatomical atlas information which provide functionally labeled coronal slices of the rat brain. Fig. 5.4 shows the layout of the 2D planning scenario, which allows the interactive specification of up to 3 target points and the desired angle(s) of insertion. The lower third in Fig. 5.4 constitutes the coordinate panel where the planning details such as the stereotactic coordinates are provided. The target is chosen by selecting a point on a coronal slice, the coronal angle of insertion is specified via a slidebar. Note that within this planning scenario the angle of insertion is restricted to the so-called coronal angle. If the entry path should not be restricted to a coronal section, a three-dimensional planning modality should be used.
The planning module offers the application of two different probe modalities: a guiding tube modality, which is positioned with a specified distance to the target area, and a probe

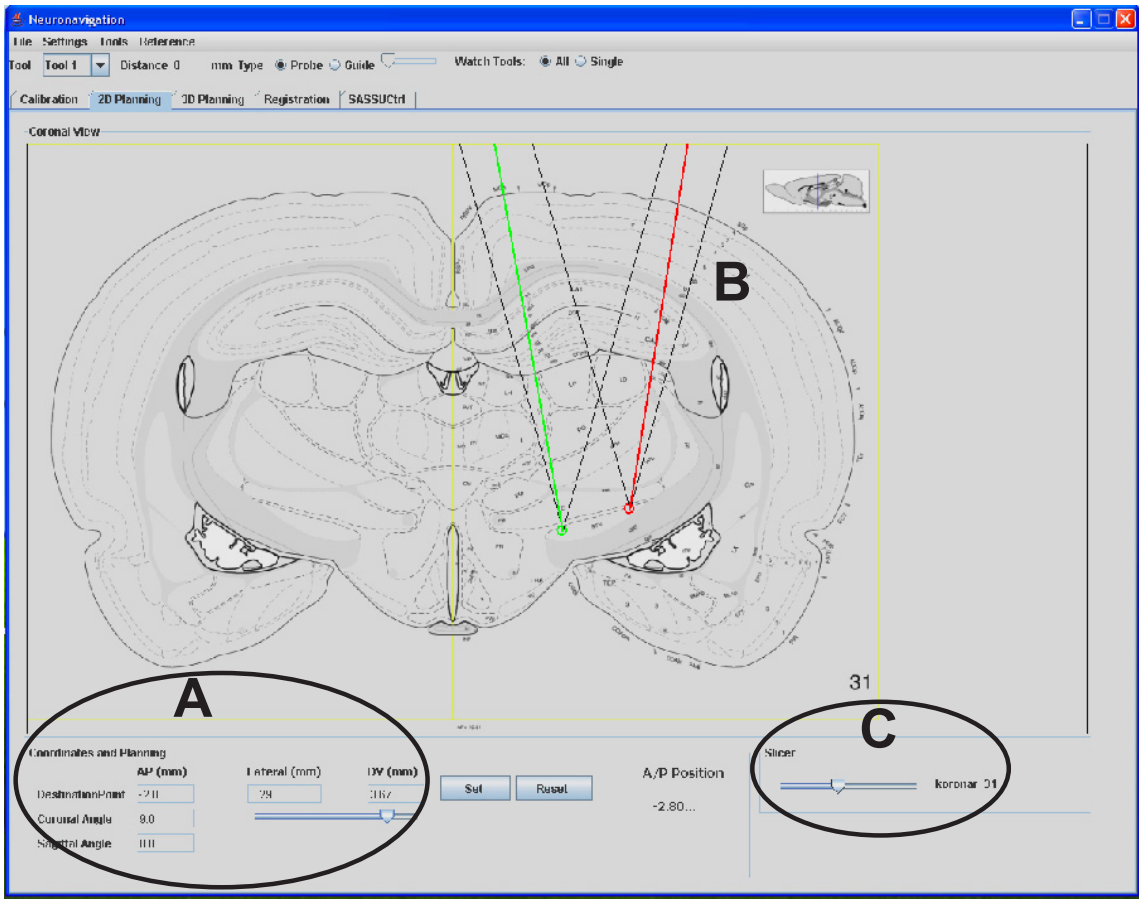

Figure 5.4: Screenshot of the two-dimensional path planning environment. The scenario shows two targets and corresponding angles of insertion marked green and red. Black lines indicate the limits for the angles of insertion. [A] Details on the planning such as stereotactic coordinates [B] Coronal slice of the rat brain which allows for interactive target selection [C] Coronal slice navigator.

modality, which directly places the probe in the desired target area. Furthermore, the software allows to save and load a planning scenario such that surgical scenarios can be repeated with little time exposure.

Three-dimensional planning

As in the common human surgical planning scenario, a three-dimensional planning modality is provided. In comparison to the two-dimensional setting, it allows to specify an entry path which is not restricted to a coronal section. Visualization of the three-dimensional setting is based on a CT-data which can be preoperatively acquired by using the stereotactic frame visualized in Fig. 4.5. A reconstruction of the skull fixed into the frame is shown

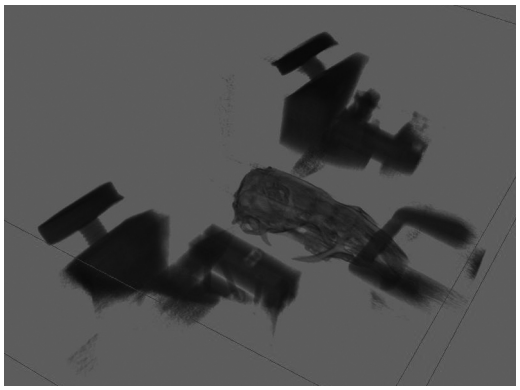

(a) Volume reconstruction of a rat skull fixed into the CT-compatible frame.

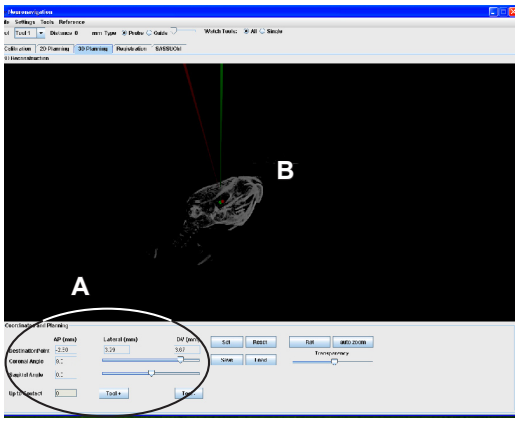

(b) Screenshot of the three-dimensional path planning based on CT data of the rat skull. The scenario shows two targets and corresponding angles of insertion marked green and red. (A) Details on the planning such as stereotactic coordinates (B) Volumetric reconstruction showing rat skull and planning details.

Figure 5.5: Three-dimensional planning scenario based on volumetric reconstruction of preoperatively acquired CT data.

in Fig. 5.5(a). Data for volumetric reconstruction was acquired using a *Galileos Comfort* system (Sirona Dental Systems GmbH, Bensheim, Germany). Within the 3D planning environment, also the sagittal angle of insertion can be adjusted. Volumetric visualization offers better orientation for the surgeon, especially if multiple probes are treated. Fig. 5.5(b) shows the 3D planning scenario.

5.1.2 Registration module

As explained in section 2.2.1, registration is a fundamental step during surgery. In our module, a slightly different rat coordinate system will be introduced. This is due to the fact that A/P, DV, and lateral coordinates do not form a right hand coordinate system and are therefore unsuitable for registration. The rat coordinate system is therefore defined as :

1. x_{Rat}-direction which is defined as the lateral direction pointing parallel to the interaural line directed towards the right side of the skull. The x_{Rat}-direction is therefore equal to the lateral direction.

2. y_{Rat}-direction which is pointing in ventral direction (towards the jawbone of the

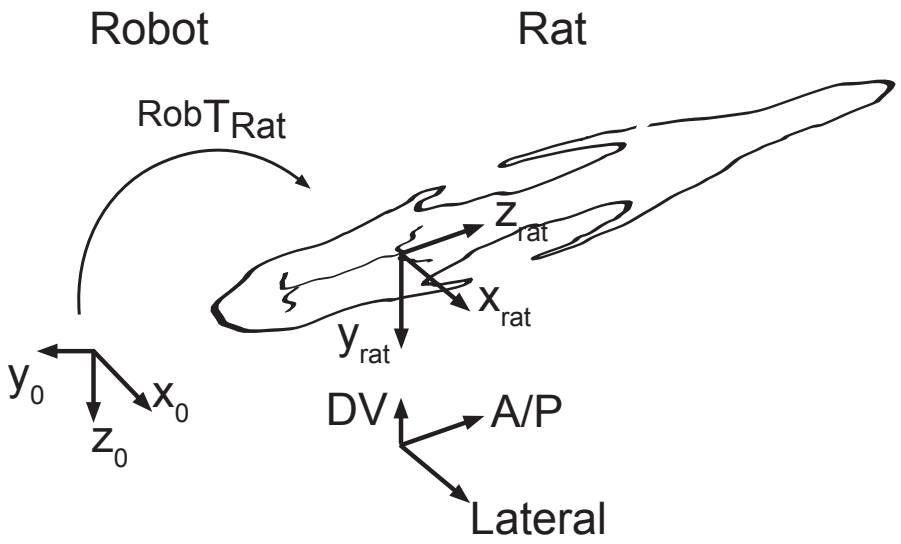

Figure 5.6: Registration of the SASSU to the rat skull. Shown are the robot, the rat, and the atlas-based coordinate system.

rat). If the DV position is given in atlas coordinates, the y_{Rat}-position is defined as $y_{\text{Rat}} = 10$ mm-DV.

3. z_{Rat}-direction which is pointing along the Lambda-Bregma line thus being equal to the A/P direction given in atlas coordinates.

The rat coordinate systems origin is located at the Bregma position. The spatial relation between the SASSU base coordinate system and the rat coordinate system is visualized in Fig. 5.6.

Tool-based registration

Like in the common procedure outlined in section 2.2.2, registration within the stereotactic control framework is done by placing the probe tip on characteristic points on the skull (e.g. Bregma and Lambda) under visual observation (e.g. using an operating microscope). Then, the respective probe tip coordinates (see Fig. 5.8) are stored. Once all necessary points on the skull are stored in such a way, the software automatically calculates the transformation matrix ${}^{\text{Rob}}T_{\text{Rat}}$ between the rat and the robot coordinate system (see Fig. 5.6). Thus, any desired destination POSE given by stereotactic coordinates can be expressed in terms of the robot coordinates. This enables the system to calculate for the necessary joint movements to reach a desired target. Two approaches to registration can be practically taken:

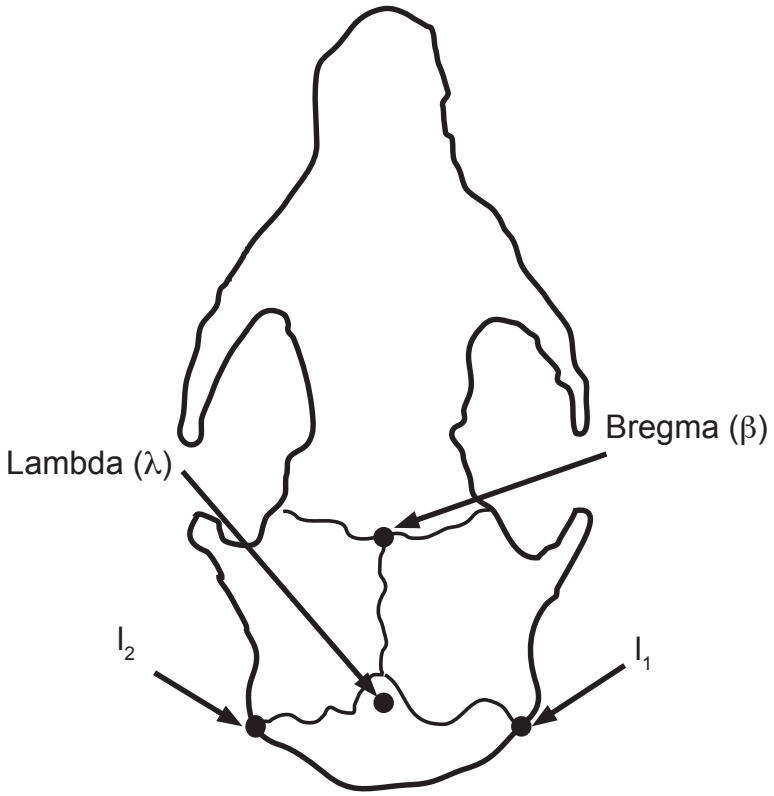

Figure 5.7: Characteristic landmarks for registration of the robot to the rat coordinate system. Bregma (β) and Lambda (λ) are used for the two-point registration and are defined in section 2.2.1. The additional points l_1 and l_2 are used in the four-point registration and are defined as the endpoints of the Lambdoid suture.

1. Two-point registration
   This approach assumes that the rat coordinate system is only rotated around the x_0- and the z_0-axis of the SASSU. This corresponds to yaw and pitch but no roll contribution to the transformation of robot into rat coordinate system. If the interaural fixations are assumed to have the same height (e.g. z_0 position), the two point registration presents a feasible approach. The user is now required to place the calibrated tool on the characteristic points Bregma and Lambda (see Fig. 5.7) and record the corresponding coordinates in the robot coordinate system. If λ_{Rob} denotes the Lambda and β_{Rob} the Bregma coordinates in the robot coordinate system, the normalized vector z_{Rat} is now given by

$$z_{\text{Rat}} = \frac{\lambda_{\text{Rob}} - \beta_{\text{Rob}}}{||\lambda_{\text{Rob}} - \beta_{\text{Rob}}||}. \tag{5.1}$$

The rotation about the z_0-axis is given by

$$\alpha_z = \arctan \frac{-(z_{\text{Rat}})_x}{(z_{\text{Rat}})_y} \tag{5.2}$$

where $(z)_x$ denotes the $x-$entry of the vector z. Rotation about the x_0-axis can be calculated by

$$\alpha_x = \arctan \frac{-(z_{\text{Rat}})_y / c_{\alpha_z}}{(z_{\text{Rat}})_z}. \tag{5.3}$$

if the rotation about the robots z-axis is always assumed to be significantly smaller than $\frac{\pi}{2}$. This is always guaranteed by the stereotactic fixation (e.g. the Lambda-Bregma line of the rat will never point into the robots x_0-direction). The transformation matrix from the robot to the rat coordinate system is now provided by

$${}^{\text{Rob}}T_{\text{Rat}} = \begin{bmatrix} & R_z(\alpha_z)R_x(\alpha_x) & & \beta_{\text{Rob}} \\ 0 & 0 & 0 & 1 \end{bmatrix} \tag{5.4}$$

with $R_z(\alpha_z)$ being a rotation about the z-axis with an angle α_{z_0} (see chapter 9).

2. Four-point registration

   This approach allows to capture a rotation of the rat coordinate system about all 3 axes of the robot coordinate system (yaw, pitch, and roll). The user is required to place the calibrated tool on four characteristic points and record the corresponding coordinates in the robot coordinate system. The points are: Bregma, Lambda, and two points on the interaural line in positive and negative x_{Rat}-direction which will be referred to as l_1 and l_2 (see Fig. 5.7). In this work, l_1 and l_2 are defined as the endpoints of the Lambdoid suture where l_1 lies in positive lateral direction and l_2 in the negative lateral direction. The vector z_{Rat} is given as in Eq. 5.1. The vector x_{Rat} can be determined by

$$x_{\text{Rat}} = \frac{\mathrm{l}_{1,\text{Rob}} - \mathrm{l}_{2,\text{Rob}}}{||\mathrm{l}_{1,\text{Rob}} - \mathrm{l}_{2,\text{Rob}}||}. \tag{5.5}$$

   The direction of the y-axis is subsequently given by $z_{\text{Rat}} \times x_{\text{Rat}}$. The transformation matrix from the robot to the rat coordinate system is now provided by

$${}^{\text{Rob}}T_{\text{Rat}} = \begin{bmatrix} & R_z(\alpha_z)R_y(\alpha_y)R_x(\alpha_x) & & \beta_{\text{Rob}} \\ 0 & 0 & 0 & 1 \end{bmatrix} \tag{5.6}$$

   where the angles α denote the rotation about the axes of the robot coordinate sys-

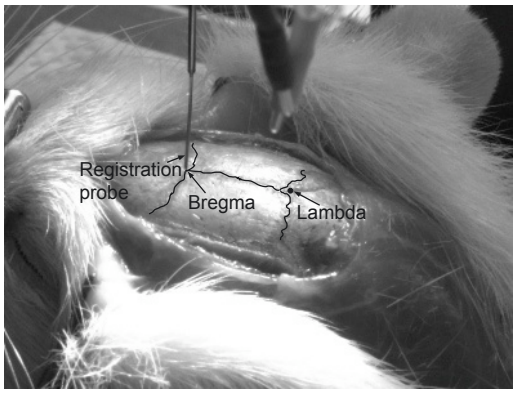

(a) Top view of the rat skull during registration while the registration probe tip is placed onto the Bregma point.

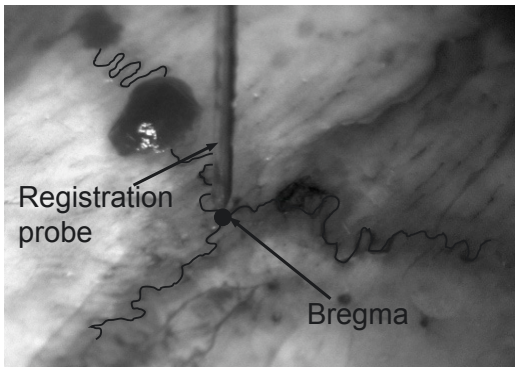

(b) Detailed view of the Bregma point during registration while the tip of a registration probe is placed.

Figure 5.8: Registration of the robot to the rat coordinate system by placing the tool tip on characteristic points on the rat skull under camera supervision.

tem. The quantitative values are provided by

$$\alpha_x = \arctan \frac{(z_{\text{rob}})_z}{(y_{\text{rob}})_z},$$

$$\alpha_z = \arctan \frac{(x_{\text{rob}})_y}{(x_{\text{rob}})_x},$$

$$\alpha_z = \arctan \frac{-(x_{\text{rob}})_z}{(x_{\text{rob}})_z / c_{\alpha_z}}. \tag{5.7}$$

(5.8)

In addition to the calculation of the transformation matrix, the Bregma-Lambda distance information is used to scale the rat coordinates linearily. Paxinos atlas-based coordinates assume a distance of 8.7 mm from Bregma to Lambda for 290 gram rats [92]. If, however, a different distance is measured during registration, all other coordinates will be scaled by the ratio

$$r = \frac{||\beta - \lambda||}{8.7}. \tag{5.9}$$

A screenshot of the registration module (four-point registration) is shown in Fig. 5.9. The lower third of the panel constitutes the registration control where (a) a basic motion control interface is implemented ([A]) and (b) the landmarks are saved in terms of the spatial position ([B]). On the right hand side, a top view of the rat skull indicates the important landmarks.

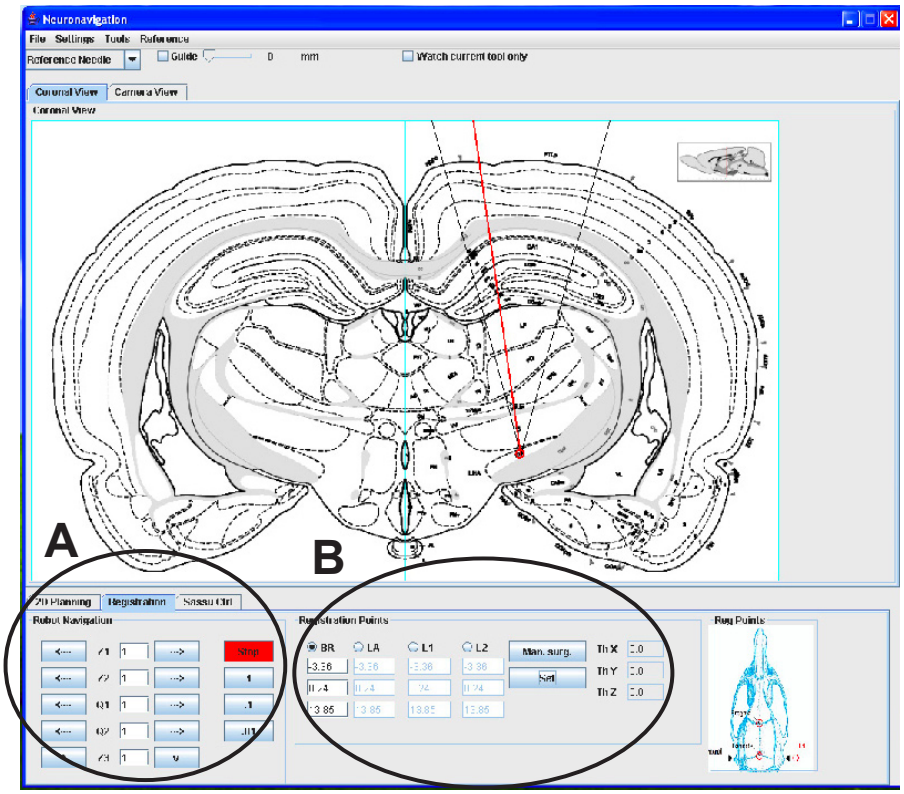

Figure 5.9: Screenshot of the registration module integrated into the SASSU stereotaxic control software. The set button stores the probe tip coordinates and automatically calculates for the transformation matrix of the robot to the rat coordinate system. [A] Basic motion control interface [B] Spatial coordinates of the landmarks.

Image-based registration

The atlas-based approach for registration heavily relies on the identification of the characteristic landmarks. These landmarks, however, are defined as best fit points. Naturally, the best fit features an inter-user dependency and has an adverse effect on the overall positioning accuracy. Additionally, atlas-based information are based on normalized data which does not always reflect the real surgical scenario. To overcome this problem, an image-based planning and registration modality is proposed. Herein, the planning and registration procedure is carried out using e.g. CT data of the individual animal. This allows image-based identification of the landmarks. Image-based registration is based on two premises. First, the spatial position and orientation of the CT-compatible frame is known in terms for SASSU coordinates. This can be done by placing a calibrated touch sensor onto characteristic landmarks provided by the frame (e.g. edges of non-movable parts). Second, a reference rat skull is fixed into the frame and CT data is acquired. Then,

rat skull landmarks such as Bregma, Lambda, the interaural holes and frame-based landmarks such as edges are manually specified. This allows to register the reference rat skull to the frame.
During surgical application, the respective animal is fixed into the frame and CT data is acquired. Now, the skull surface is segmented and registered to the reference rat skull surface by e.g. an iterative closest point algorithm [123]. This potentially requires the user to manually specify three landmarks on the rat skull (e.g. nose and ear holes) for initial registration but presents a very fast and robust approach to register a skull to the SASSU system. Now, the following spatial relations are known: (a) current rat skull to the reference rat skull, (b) frame landmarks and the reference rat skull, and (c) frame landmarks and SASSU. As a result, the position and orientation of the rat skull with regard to the SASSU can be computed.

5.1.3 Control module

The probe positioning control provides the means to control the SASSU during surgery. It is subdivided into two parts:

Control during registration

As described in section 5.1.2, the registration is performed by placing the tip of the probe onto characteristic landmarks of the rat skull. Within this part of the surgery, the robot control is limited to pure translational movements as determination of the transfer matrix from the rat to the robotic assistant requires only the spatial position of the tip and its orientation does not provide valuable information. Therefore, the control allows the user to actuate each translational joint with a desired step size, velocity, and acceleration.

Control during the insertion

After the planning and registration step is completed, the probe can be inserted into the rat brain. Control of the insertion process is split into a sequence of two operations:

1. Prepositioning of the probe, which will place the probe outside the rat skull with its centerline pointing along the desired entry path. This allows a final visual verification and additionally shows the surgeon the location of the entry point. If skull drilling is performed by the surgeon manually, the stereotactic assistance system

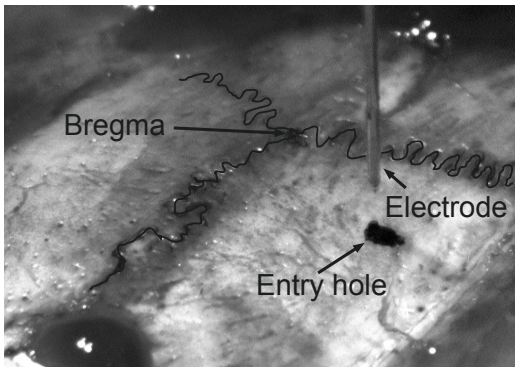

(a) Prepositioned electrode above the rat skull. The image shows the Bregma landmark and the marked entry point of the probe for final insertion.

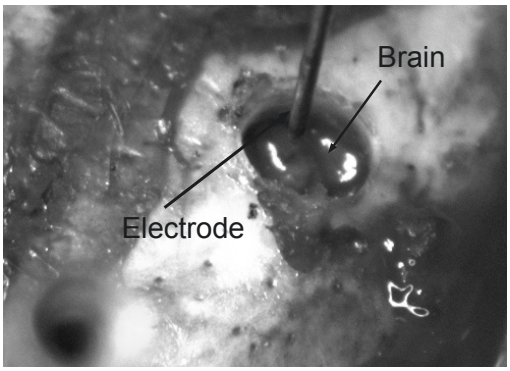

(b) Electrode directly before insertion. The rat skull is opened at the entry position and the brain surface is visible.

Figure 5.10: Stepwise approach of the electrode insertion. (a) Prepositioning of the electrode and (b) final insertion of the electrode.

with the attached probe can be removed from the area of interest to provide sufficient surgical access. Fig. 5.10(a) shows the prepositioning step in the real surgical scenario.

2. Final insertion, which realizes the control of the probe penetrating the brain. After the skull is opened, the probe can be inserted into the brain with a user-defined step size and velocity (see Fig. 5.10(b)).

As joint information from the SASSU can be read out at any time during the implantation, the current probe tip location can be calculated using forward kinematics. Thus, a reliable and precise localization of the measured signal to the intracranial position can be performed during surgery. Fig. 5.11 shows a screenshot of the insertion module. The lower third in Fig. 5.11 constitutes the insertion panel interface featuring functionalities such as prepositioning the tool ([A]) and selecting a desired step size and motion velocity ([C]). The middle part ([B]) shows the desired and current stereotactic coordinates of the probe tip. The graphical display on top shows the current tool position on the coronal drawing taken from the Swanson atlas.

5.1.4 Additional functionalities

Besides the presented functionalities of the stereotactic control framework, additional functionalities to improve the usability are integrated:

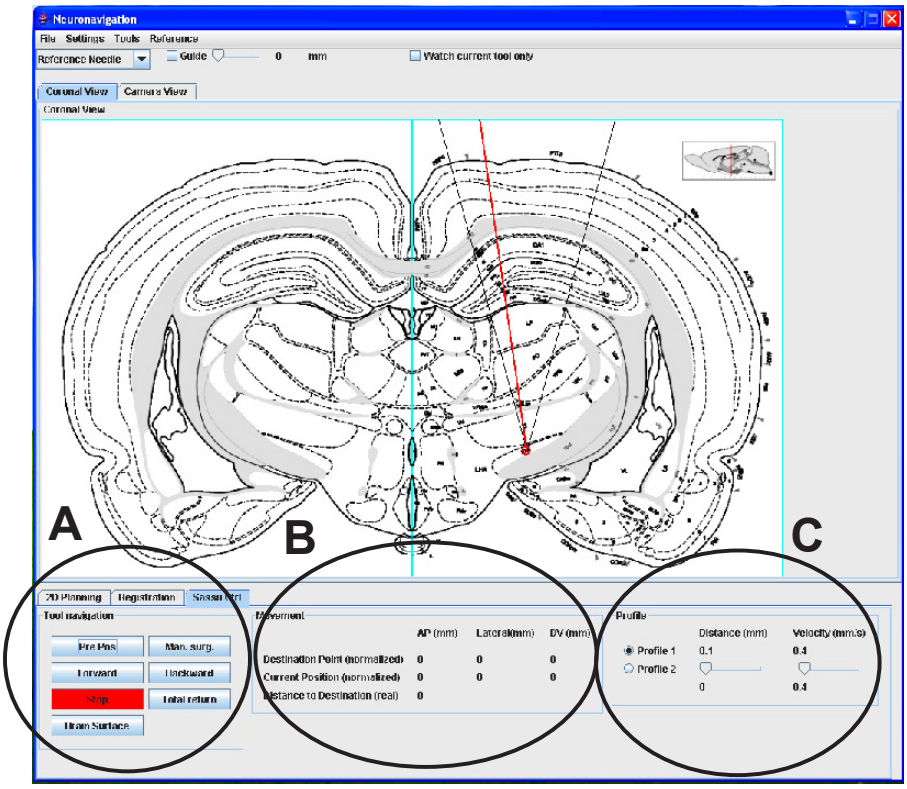

Figure 5.11: Screenshot of the insertion module integrated into the SASSU stereotaxic control software. The module allows to specify the parameters of insertion (step size and velocity) and special movements related to the insertion such as prepositioning and final insertion. Additionally, it provides an interface to turn off the power amplifiers during the insertion. [A] Insertion related movement commands [B] Stereotactic coordinates [C] Movement parameters.

- Save/Load options
  Parameters of any planning and surgical scenario can be saved. This includes planning parameters such as the destination point(s) and the angle(s) of insertion as well as the tool parameters identified by a calibration process. This allows to continue a surgery at any time or to repeat a surgical scenario with a different tool but same target coordinates.

- Unblock functionality
  This functionality allows the surgeon to remove the SASSU and the attached tool from the surgical site to release space for manual surgery such as cutting or drilling. After manual task completion, the SASSU can be returned to a specified position.

5.1.5 Software-based safety features

In addition to the hardware-based safety features, different safety measures have been integrated into the stereotactic control framework:

1. Constraints on motion parameters
   Within the surgical application, the velocity and the accelerations of the respective joints are constrained. Thus, the speed of motion still allows adequate user supervision. In case of an unintended action, motion is executed such that the user is able to stop the movement within a reasonable time.

2. Software-based collision avoidance
   After the registration step, a virtual safety box around the rat skull can be established. For all intended movements, collision of the probe tip with this safety box can be checked.

3. Hardware-based collision avoidance
   As outlined in section 4.1.2, the center-of-arc principle provides an inherent mechanical safety as only axis t_3 (insertion stage) moves the probe into the brain. Other joint movements will not lead to collision of the hardware with the animal.

4. Fast user interaction
   Within the GUI, stop buttons are realized which allow for an immediate interruption of the robots motion by software functionalities.

5. Reduced user interaction
   During the design of the modular software, the options for user interaction have been minimized. If user action is required, the interface is designed such that either no erroneous input is possible (e.g. an input via a slider) or inputs are subject to checks (e.g. input of step sizes).

5.2 OCT-based near field brain exploration

Until now, only the stereotactic control framework integrating the SASSU has been presented. It provides a means of inserting a tool into the small animal brain. To extend the scope of the SASSU-related applications to general brain exploration applications, this section investigates the integration of OCT into the robot-assisted stereotactic setting. In this context, the method of near field navigation is proposed. It refers to the analysis of real-time data measured directly at the probe tip with respect to the true spatial position.

In current (human) stereotactic scenarios, positioning relies on the assumption of accurate registration, rigid probes, no brain compression, and no brain shift [82]. As one or more of these assumptions usually do not hold, stereotactic placement fails the desired target [82]. This triggers the need of online verification methods as presented in section 2.1.2. In reliable DBS probe placement procedures, target verification is done by evaluating microelectrode recordings [40]. If the desired target is not reached, the probe will be repositioned by the surgeon. This approach, the online verification and eventually replacement by the surgeon, can be summarized as (manual) near field navigation.
Introducing robotic assistance opens up the possibility of robot-assisted near field navigation. While this work does not present a complete solution to this idea, it investigates the basic principles. In this connection, two potential near field applications are tested. They comprise (a) robot-assisted electrophysiology and (b) robot-assisted OCT for intracranial imaging. In contrast to the field of electrophysiology, the use of OCT for the purpose of brain research has not been well established. OCT offers multiple advantages in the context of neurosurgery. First, it can be integrated into a minimal-invasive setting. Second, it offers a high resolution, real-time imaging modality which, in addition, is atraumatic in the sense that it does not need to penetrate the area of interest. Therefore, the primary goal of this work is to assess the potential of OCT as a technique for near field navigation in the brain.

5.2.1 Introduction into OCT imaging

This section provides a brief overview of the fundamental concept of OCT imaging which is an important background for the subsequent integration into the context of brain imaging.

Low coherence tomography

Understanding the concept of OCT imaging requires a basic understanding of the principle of low coherence tomography. Detailed introductions of low coherence tomography can be found in numerous textbooks [45], [47], and therefore only fundamental aspects will be summarized. Two effects are crucial for the understanding of low coherence tomography:

1. Interference, which describes the formation of a new light wave pattern resulting from the superposition of two or more light waves.

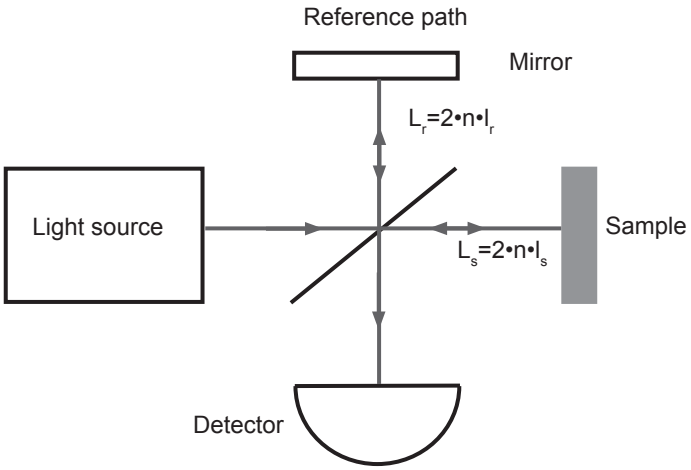

Figure 5.12: Schematics of a simplified Michelson interferometer.

2. Coherence as a property of light waves that measures the ability of light waves to interfere with each other. Two types of coherence can be distinguished: (a) temporal coherence which is the ability of a wave to interfere with a delayed copy of itself and (b) spatial coherence which describes the correlation between signals at different points in space.

The principle of low coherence tomography is to use the interference characteristics of partially coherent light (low temporal coherence but high spatial coherence). The theoretical background can be best illustrated using the example of a simplified Michelson interferometer (see Fig. 5.12): Assuming that the sample is a perfectly reflecting mirror and all polarization effects of light are ignored, the light fields $E_s(t-\frac{L_s}{c})$ and $E_r(t-\frac{L_r}{c})$ represent the beams reflected from the sample and the reference mirror respectively. Here, L_s and L_r are the optical path lengths and c is the speed of light. The resulting intensity at the detector can be written as

$$I_d = \langle [E_s(t)+E_r(t+\tau)][E_s(t)+E_r(t+\tau)]^* \rangle. \tag{5.10}$$

In Eq. 5.10, the angular brackets denote the time average over the integration time at the detector and

$$\tau = \frac{\Delta L}{c} = \frac{L_s - L_r}{c} = \frac{2n(l_s - l_r)}{c} \tag{5.11}$$

is the round-trip-related time delay. The n denotes the refractive index of air and l_r and l_s are the geometric lengths of all arms. Eq. 5.10 can be rewritten as

$$I_d = I_s + I_r + 2\sqrt{I_s I_r}\mathrm{Re}[\frac{\langle E_s(t)+E_r^*(t+\tau)\rangle}{\sqrt{I_s I_r}}]. \tag{5.12}$$

Following some simplifications presented in [124] and [125], Eq. 5.12 can then be expressed as a function of ΔL

$$I_d(\Delta L) = I_s + I_r + 2\sqrt{I_s I_r}|V_{tc}(\Delta L)|\cos(k_0 \Delta L) \tag{5.13}$$

where $V_{tc}(\Delta L)$ is the temporal coherence function, $k_0 = \frac{2\pi}{\lambda_0}$ is the average wave number. In this notation, λ_0 is defined as $\lambda_0 = \frac{c}{f_0}$ with f_0 being the center frequency of the light source. In [125], it is shown that the temporal coherence function is actually the inverse Fourier transform of the power spectral density $S(f)$ of the light source.
The relationship in Eq. 5.13 shows that the measured intensity of two beams is based on the beam intensities I_s and I_r but also dependent on an interference term, which is in turn dependent on the optical path length difference. Eq. 5.13 refers to the so-called time-domain OCT (TD-OCT) which will be explained in the following.

OCT system technology and minimal-invasiveness

Generally, OCT can be considered as being analogous to ultrasound as it measures a back-reflected intensity. It uses, however, infrared light rather than sound. A major difference to ultrasound is that the backreflection intensity is not measured electronically which is due to the high speed of light. Instead, OCT applies the principle of low coherence interferometry (see section 5.2.1). The basic working principle of OCT is best explained by taking the TD-OCT as an example which follows Eq. 5.13 and its derivation. Fig. 5.13(a) shows the fundamental components: light from a broadband light source is evenly splitted by a beam splitter, half of the beam toward the sample and the other half toward the moving mirror. The reflected light from sample and mirror is recombined and directed to the detector. By varying the position of the reference mirror, the path length of the reference arm can be changed. If the light used would be highly coherent (narrow bandwith or single frequency of the light source), interference could be observed for a wide range of path lengths L_r and L_s. In OCT applications, however, it is important to measure absolute distances and dimensions and therefore low coherence length light is used. Low coherence light can be described by the coherence length L_c which is inversely proportional to the bandwidth of the light source [47]. In case of low coherent light, interference is observed only when the path lengths are matched to within the coherence length. Based on this property of low coherent light, the change of the reference mirror position can be used for depth scanning of the sample.
While TD-OCT can be used to illustrate the working principle of OCT, its technique has been mostly displaced by spectral domain methods. One of these methods is Fourier domain OCT (FD-OCT) (see Fig. 5.13(b)). Within this technique, a broadband light source

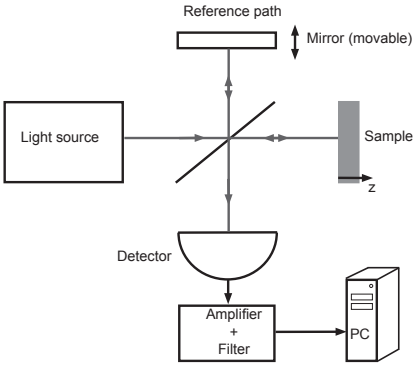

(a) Schematics of time domain OCT (TD-OCT). The mirror in the reference path is movable. Applying the principle of low coherence tomography, this allows depth scanning of the sample.

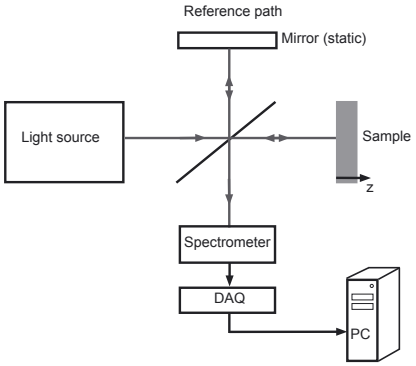

(b) Schematics of fourier domain OCT (FD-OCT). The mirror in the reference path is static. Depth resolution is achieved via a spectrometer applied to the combined signal (reference and sample path).

Figure 5.13: Schematics of time domain and fourier domain OCT.

as in TD-OCT is used but the reference mirror does not move. Instead, the depth information is derived from the spectrum of the returning light. The Fourier transform of the spectrum provides a backreflection profile as a function of depth. Refering to Eq. 5.13, the measured intensity in FD-OCT can be expressed as

$$I_d(k) = I_s + I_r + 2\sqrt{I_s I_r} S(k-k_0)\cos(k\Delta L) \tag{5.14}$$

where ΔL is fixed and the value of k is now investigated.
For both setups, however, the axial resolution is governed by the same principles. As stated previously, the coherence length L_c is governed by the characteristics of the light source. For a source with Gaussian distribution, the axial resolution Δz becomes

$$\Delta z = \frac{2\ln 2}{\pi}\left(\frac{\lambda^2}{\Delta\lambda}\right) \tag{5.15}$$

where $\Delta\lambda$ are the full width at half-maximum (FWHM) of the light source power spectrum and λ is the central wavelength [47]. The transverse resolution of OCT is determined by the focusing properties of the optical beam and can be expressed as

$$\Delta x = \frac{4\lambda}{\pi}\left(\frac{f}{d}\right) \tag{5.16}$$

where d is the spot size on the objective lens and f is its focal length. Note an important advantage of OCT: the axial resolution Δz is decoupled from the transversal resolution

Δx.

Transfering OCT into the field of medical applications, an important property of OCT is that it can be integrated into a minimal-invasive setting. As OCT uses the interference of two light waves in order to provide depth-related intensity information, only the sample path has to be put into close proximity to the target. In the most primitive form this can be realized by a monomode fused silica fibre which directs the light into the target direction. The diameter of such a fibre ranges from 25 μm to 250 μm and thus potentially integrates into a minimal-invasive setting.

Speckle noise and speckle noise reduction

As in any other imaging technique, OCT based images require an adequate processing in order to obtain useful information (e.g. structure boundaries). The major problem for OCT is the occurence of random positive and negative interference maxima also known as speckle noise. This kind of noise reduces the contrast and makes boundaries between highly scattering structures difficult to resolve (see [51] for details). Therefore, speckle removal or feature enhancement is a crucial issue in processing OCT images in order to support the human interpretation or computer-assisted diagnosis. In the case of medical image processing, exemplary applications include the classification of blood vessels or skin layers. Numerous approaches to speckle reduction have been proposed and include spatial averaging [51, 126], frequency compounding [127], polarization averaging [128], and image processing techniques. These image processing techniques originate in the synthetic aperture radar (SAR) community and have also been applied to the field of ultrasonic imaging. To date, commonly applied filters for speckle removal in SAR and ultrasonic images include the Lee [129], the Frost [130] and the Kuan filter [131]. Their disadvantages are the output dependency on the size and the shape of the respective filter kernel and the inability to enhance edges which could destroy important information. These drawbacks have led to the development of edge-sensitive or enhancing filters. Some of these filters are based on the solution of a diffusion equation derived from the heat equation and are also known as partial differential equation (PDE)-based anisotropic filters. This approach was first introduced by Perona and Malik and led to the so-called Perona-Malik filter [132]. Generally, these filters encourage smoothing in homogeneous areas, while prohibiting smoothing in the vicinity of edges [132, 133]. In [134], the PDE-based formulation is extended to a nonlinear complex diffusion process with a complex-valued diffusion coefficient. In recent work on OCT imaging , these two different filtering approaches for OCT images are compared [135].

Other approaches to speckle suppression are based within a framework of multiscale

wavelet analysis. In [136], a pyramid reconstruction scheme is proposed. Coarser scales are combined with a modified interscale in order to preserve edges. In [137], the image is decomposed into two parts and transformed into the wavelet domain. The wavelet coefficients of the respective parts are processed by a thresholding method before the inverse transformation is applied. In most cases, however, the balance between speckle suppression and signal preservation is hard to achieve.

Modeling of OCT intensity and speckle noise

Since being used for imaging purposes in medical applications, analytical models of OCT systems have been developed in order to extract optical properties of tissue. Different approaches have been proposed. The most advanced models incorporate the multiple-scattering contribution to the OCT signal. Two models are used for extraction of tissue parameters: the radiative transport model [138] and the extended Huygens-Fresnel model [139]. Their analytical expression is divided into three terms, one term representing the single-scattering contribution, one term the contribution of multiple-scattering, and the last term denoting the cross relation. See [139] for a detailed explanation. The authors of [140] derive a theoretical model of the OCT signal for layered media which integrates small-angle scattering at low depths as well as light diffusion at large depths. The nonlinear model consists of a set of unknown parameters which are subsequently optimized by a genetic algorithm to fit a measured A-scan profile. Thus, different tissue characteristics can be determined.
In this work, a simplified OCT model based on the single-scattering effect only will be used. Although it does not account for all effects of light propagating through tissue, like multiple scattering, the simplified model allows linear modeling of the OCT intensity signal. Thus, linear filter theory can be applied. In [141], the authors propose a model where the measured intensity is proportional to an exponential decay:

$$I(z) = I_0 exp(-2\mu z), \tag{5.17}$$

where I_0 is the initial intensity and μ denotes the attenuation coefficient, and z the scanning depth. Note that μ comprises the effects of single scattering and absorption. In brain imaging, the results in [142] show that μ differs for various tissue structures (e.g cortex, external capsule) allowing a clear distinction of white and gray matter. This fact motivates the use of the simplified model for OCT analysis despite its theoretical shortcomings.
In addition to modeling the intensity, speckle noise corrupting OCT images can be modeled statistically. It is usually assumed to be a multiplicative random noise. If f denotes

the ideal image and g the speckled image, this assumption can be expressed as

$$g = fu, \tag{5.18}$$

where u is a signal-independent random variable whose probability density function (pdf) depends on the image type [129], [143]. Commonly, the speckle pdf is assumed to follow an exponential distribution described by:

$$p_u(x) = \begin{cases} \lambda \exp(-\lambda x) & \text{if } x \geq 0, \\ 0 & \text{otherwise.} \end{cases} \tag{5.19}$$

In [143], the speckle mean and standard deviation over a homogeneous and featureless area are derived as

$$\bar{g}_{\text{hom}} = \bar{f}\bar{u} \tag{5.20}$$

and

$$\sigma_{g_{\text{hom}}} = \bar{f}\sigma_u. \tag{5.21}$$

This means that the speckle standard deviation is proportional to the mean value of the uncorrupted image in a homogeneous area. The noise level is thus proportional to the local gray level meaning that a bright area will be more corrupted than a low intensity area. This important property of speckle noise complicates the general image processing approaches.
In the following, two contributions to the local intensity at a depth z in an OCT image will be considered

1. Deterministic contribution which evolves from Eq. 5.17 and can be formulated for a certain depth $z + \Delta z$ as

$$I(z+\Delta z) = I_0 exp(-2\mu z) exp(-2\mu \Delta z) = I(z) exp(-2\mu \Delta z). \tag{5.22}$$

2. Statistical noise contribution which, at depth z, will be accounted for according to Eq. 5.20 and Eq. 5.21. This means that noise corruption is proportional to the local gray value $I(z)$ at depth z.

5.2.2 OCT-based identification of brain matter

As outlined at the beginning of this chapter, the primary motivation of integrating OCT into the framework of robot-assisted stereotaxy is to assess its potential as a minimal-invasive technique for brain exploration. In that context, the major question is whether

OCT-based information are usable for the classification of morphological characteristics in the brain and which characteristics might be suitable for that application. Although OCT has been widely used to image tissue structures, little work has been done on brain imaging. Recent research results show that OCT is indeed applicable to image brain morphology ex vivo and in vitro [49]. This work, however, addressed the identification of residual tumour in the resection cavity during tumour surgery. While this is an interesting application, the use of OCT in the context of navigation is motivated by another physical property of OCT. As outlined in the introduction (section 5.2.1), OCT imaging is based on the backreflected intensities. Backreflected intensities, in turn, relate to the scattering properties of the investigated sample. Structures which feature strong backscattering properties will appear bright while structures with low backscattering properties appear gray or dark. This holds especially for white matter in brain tissue. In the context of brain imaging, OCT-based identification of white matter has been shown for rat brains in vitro [28], [142]. The authors analyzed the light intensity and attenuation coefficient of the backscattered signal. Their results showed that these measures differ for various tissue structures (e.g cortex, external capsule) allowing a distinction of white and gray matter. In [50], the authors used a catheter-based OCT probe to examine the possibility of optical guidance in placing a deep brain stimulation electrode. OCT images were acquired by advancing the probe on characteristic tracks in human brains in vitro. Their results show that myelinated fibres are strong backscatterers of light and that penetration of light is shallow.

These findings cleary support the previously proposed idea of OCT being a potential candidate for near field navigation. Results of the above mentioned research activities, however, were obtained manually and no work towards computer-assisted processing of OCT data has been done. This raises the question whether an adequate analysis of OCT data can be used for navigation purposes. This comprises the idea of robot-assisted OCT where the probe is advanced by a precise robotic system. Analysis of the OCT signal could then be done with regard to positioning information.

The major focus of this work is therefore to automatically process OCT data with regard to certain optical tissue characteristics. The first step consists of the discrimination of white and gray brain matter. A potential application is to use OCT in the context of probe insertion in deep brain surgery where OCT analysis integrated into small instruments such as endoscopes could provide a technique for path validation in order to compensate for inaccuracies in e.g. DBS electrode placements. The use of OCT as an intracranial imaging modality which directly provides visual information from the tip of an instrument can be extended to the general neuronavigation setting. OCT information could be used

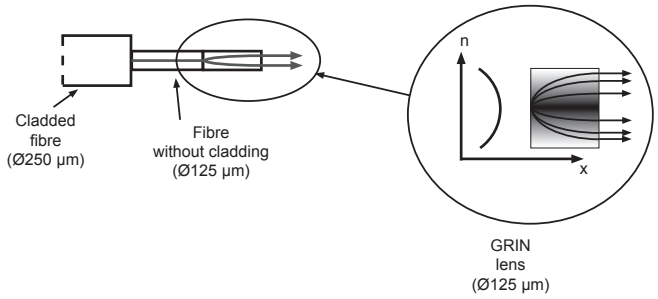

Figure 5.14: Design of the GRIN lens attached to the fibre end. The characteristic optical behaviour of the GRIN lens is shown on the right hand side with n being the refractive index.

to validate the position by e.g. registering OCT information to preooperatively acquired data or detect landmarks such as vessels or white matter tracts. Another useful application comprises the field of optical tumour biopsies.
In the following, the capability of OCT for intracranial imaging is analyzed for the exemplary application of white and gray matter discrimination.

5.2.3 Single fibre imaging

Using OCT as a near field brain exploration modality or for probe guidance requires the OCT probe inserted into the brain to be as small as possible. This eventually leads to single fibre imaging. For OCT, the smallest possible solution to image structures is to use a single fibre guiding the light to the target. Although this fulfills the requirements of MIS, it leads to one-dimensional OCT imaging which is referred to as A-scan imaging. In the first part of the OCT-based brain imaging, the focus is therefore shifted to the analysis of OCT A-scans to discriminate tissue structures in the brain.

Single fibre imaging system

OCT imaging using only a single fibre is performed with a fibre featuring so-called singlemode characteristics. These fibres are designed for a characteristic wavelength and consist of 3 components: (a) fibre core (b) cladding (c) coating. In our system setup, a SM800 fibre (Fibercore Ltd., Southhampton, UK) is used which features a fibre core diameter of 5.6 μm, an outer fibre diameter (core+cladding) of 125 μm and a coating of 125 μm. In this setup, the light is transmitted by the fibre core and the cladding. Theoretically, such a singlemode fibre could be used for OCT imaging. In that case, however, the system is

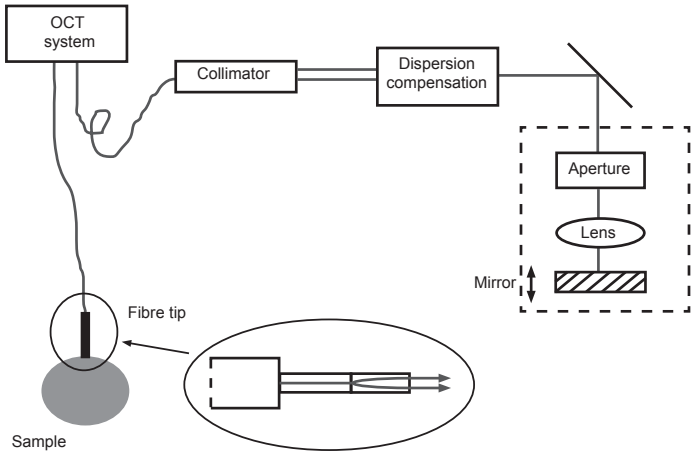

Figure 5.15: System setup and components for single fibre imaging. Shown are the OCT system, the reference path, the sample path, and a close up of the single fibre tip layout.

very sensitive to dirt at the probe tip which easily covers the light emitting spot of the fibre core. Inserting the fibre into a bloody environment such as brain tissue might therefore easily lead to useless signals. In order to obtain robust OCT signals within tissue, a special design of the OCT single fibre probe needs to be found.
Its most important requirements are:

1. minimal-invasiveness,
2. sufficient stiffness to penetrate brain tissue,
3. robustness to fouling.

To meet the above mentioned requirements, the following probe design is proposed: To increase the light emitting part of the singlemode fibre core, a gradient-index (GRIN) lens is attached to the fibre end. The GRIN lens features a parabolic variation of the refractive index n with the radial distance. This property can be used to shape the focus of light entering the lens. In the case of single fibre OCT imaging, the GRIN lens is used to broaden the light emitting part. Fig. 5.14 shows the design of the fibre tip and the characteristics of the GRIN lens regarding the light path. The fibre and the OCT system have been designed by the Medizinische Laserzentrum Luebeck GmbH (Luebeck, Germany). The probe with the GRIN lens design is then integrated into an OCT imaging setup shown in Fig. 5.15. Herein, a FD-OCT system is used and the probe is part of the sample path. The reference path contains a manually adjustable mirror to adjust the

reference position of the OCT signal. The proposed system setup can now be used to obtain robust A-scans in a minimal-invasive and robust setting.

A-scan based white matter detection

Imaging tissue with the single fibre system described in the previous section provides the user with an OCT A-scan signal. An OCT A-scan is a one-dimensional intensity profile over the depth of the scanned sample. In order to extract information from this intensity profile (e.g. structure location), adequate A-scan processing methods have to be developed. The following method relies on the simplified model of OCT intensity stated in Eq. 5.17 and the statistical nature of speckle noise. In a first step, the A-scan course is linearized by applying the natural logarithm operator to Eq. 5.17:

$$\ln(I(z)) = \ln(I_o) - 2\mu z = I'_o + mz. \tag{5.23}$$

In the computational scenario, the intensity course is discretized. If q_z denotes the depth-related pixel, Eq. 5.23 can be transformed to

$$I(q_z + 1) = I(q_z) + m' \tag{5.24}$$

where m' denotes the pixel-related slope resulting from an attenuation coefficient μ. A good indication of white matter areas in A-scans is based on the high optical contrast of a white matter structure which manifests itself as a sudden increase (spike) in the intensity (see Fig. 5.16(b)). The detection of the spike location can therefore be used as an indicator for white matter areas. Calculating the first derivative of the A-scan intensity course and simple thresholding provides the location of potential white matter regions. A spike at q_{z_1} is detected if

$$\frac{\mathrm{d}\, I(q_z)}{\mathrm{d}\, \mathrm{q_z}}|_{q_z=q_{z_1}} > \sigma_1. \tag{5.25}$$

The corresponding threshold σ_1 is based on gray values per pixel difference. Analyzing the first derivative of the intensity according to Eq. 5.25 provides a set of white matter induced peak candidates. The signal, however, is corrupted by speckle noise severely distorting the signal quality. Similar to changes caused by white matter, speckle noise introduces a spiking characteristic to the intensity signal. This complicates the white matter detection in OCT A-scans and a robust classification of white matter has to be designed. To differentiate white matter peaks from speckle noise induced peaks, two cases can be analyzed. Assume a homogeneous area with the gray value intensity f. Speckle noise introduces spikes in two ways:

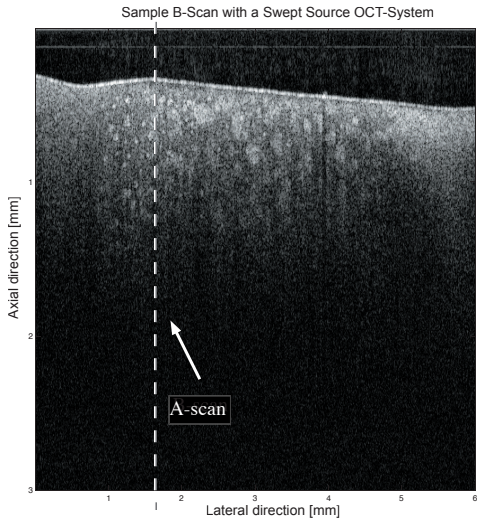

(a) OCT B-scan of a coronal section of the rat brain. The figure shows white fibres embedded into gray brain matter.

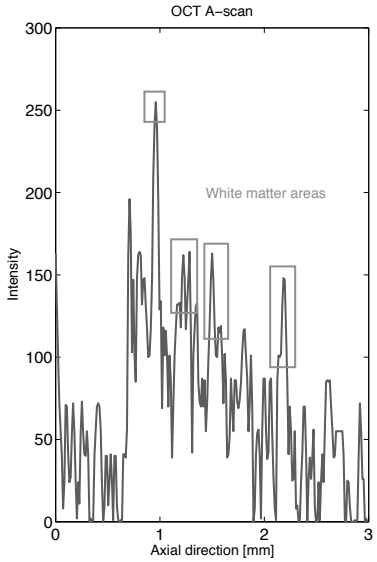

(b) OCT A-scan corresponding to one column of the B-scan in Fig. 5.16(a) with intensity peaks induced by white fibre areas marked by boxes.

Figure 5.16: White matter structures in OCT data. (a) White matter in OCT B-scan (b) White matter in OCT A-scan.

1. First, speckle-related spikes result in an intensity increase. Referring to Eq. 5.18, this corresponds to the case where $u > 1$.
2. Second, speckle results into a sudden decrease of intensity ($u << 1$) which is then followed by a sudden increase to the level of the original intensity f which would subsequently be detected as a peak candidate.

The set of white matter induced peak candidates is therefore refined by analyzing two criteria:

1. Assume an intensity spike because of $u > 1$ at the location q_{z_1} is introduced by speckle noise. Since speckle noise features random characteristics, the intensity at pixels following the spike most propably drop again. White matter areas, however, will show a slow increase with a characteristic slope (see Eq. 5.24). Therefore, white matter can be classified if the ratio

$$\frac{I(q_{z_1}+k)}{I(q_{z_1}+k-1)} > \sigma_2 \text{ for } k = [1 \ldots l_T]. \tag{5.26}$$

Here, σ_2 denotes a slope-related threshold and l_T the length of the white matter tail.

2. For speckle-related spikes according to the second scenario $u << 1$, an additional measure is introduced. It relates the intensity at the detected spike location $I(q_{z_1})$ to the mean of intensities previous to the spike location. A white matter-related spike is detected if
$$\frac{I(q_{z_1})}{(\sum_{k=1}^{N} I(q_{z_1}-k))/N} > \sigma_3. \tag{5.27}$$
Here, N denotes the number of pixel locations previous to the spike which will be taken into account.

White matter detection is now done by analyzing the A-scan and its derivate. A set of peak candidates is found according to the criterion given in Eq. 5.25. Subsequently, criteria in Eq. 5.26 and Eq. 5.27 are used to find the set of true white matter induced peaks. Fig. 5.17 shows results for the exemplary A-scan indicated in Fig. 5.16(b). Performance of the proposed seed detection scheme is strongly dependent on the threshold parameters σ_1, σ_2, and σ_3. Heuristics for the choice of the thresholds and the overall performance evaluation is based on an extensive analysis of simulated A-scans (see section 6.3.1).

5.3 OCT image processing

In a broader context of brain imaging and brain exploration, additional applications for OCT exist which are not restricted to A-scan analysis only. An exemplary application is the integration of OCT into a robot-assisted microscope. Such a system is able to provide the surgeon with information at microscale level intraoperatively which may be used for e.g. identification of residual tumour [144]. An illustrative system setup is shown in Fig. 5.18. In the course of research related to this work, a method for the segmentation of white matter in OCT B-scan images is developed which can be used for automated processing of OCT B-scan images. Based on an physical model of OCT, it applies to the segmentation of other structures in OCT images such as blood vessels. Second, the latter part of this section, presents a novel speckle filtering approach for OCT images. The designed filter enhances the postprocessing of OCT images (e.g. edge detection and segmentation) and is therefore useful in the context of medical imaging.

5.3.1 Segmentation of OCT images

In a very general context, segmentation presents an important method to extract information in medical imaging, e.g. for the quantification of tissue volumes, diagnosis, and

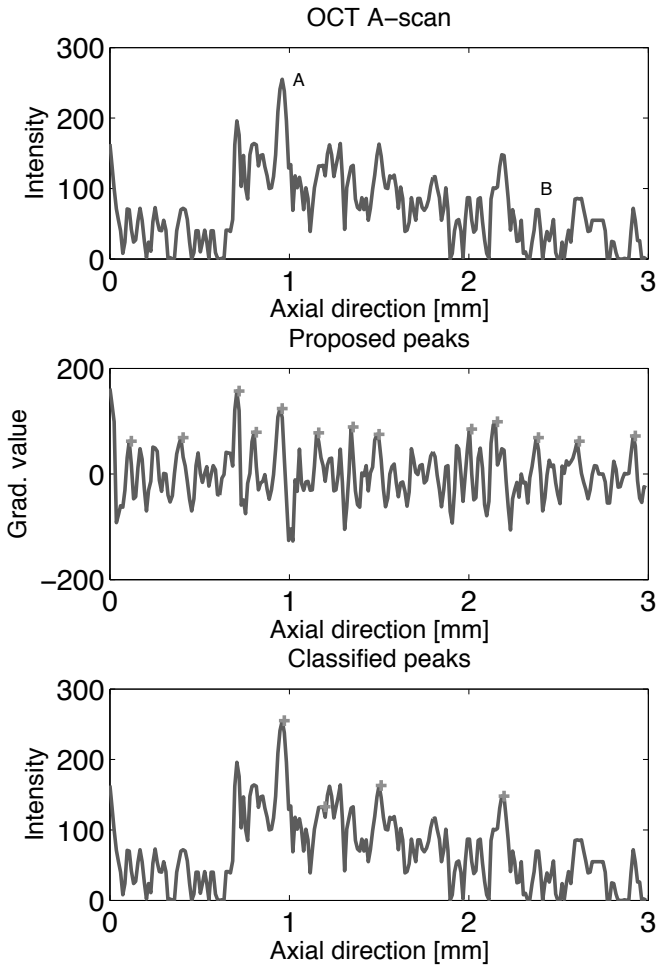

Figure 5.17: White matter detection using A-scans. [top] Original A-scan [middle] First derivative of the A-scan and proposed peaks indicated by gray crosses [bottom] Original A-scan with classified white matter peaks indicated by gray crosses.

localization of pathologies. Approaches to image segmentation is therefore an ongoing issue in medical image processing research. Numerous approaches regarding medical image segmentation have evolved in the past and are summarized in [145]. A common approach to segmentation is the region growing approach. Herein, the goal is to use image characteristics to map individual pixels in an input image to sets of pixels called regions, usually with common properties. Commonly, region growing methods start at the location of a seed and growing is governed by a homogeneity criterion. These criteria can be based on the intensity information and/or edges in the image [146]. General drawbacks of region growing are: its user dependency by manual seed placement, sensitivity to changes

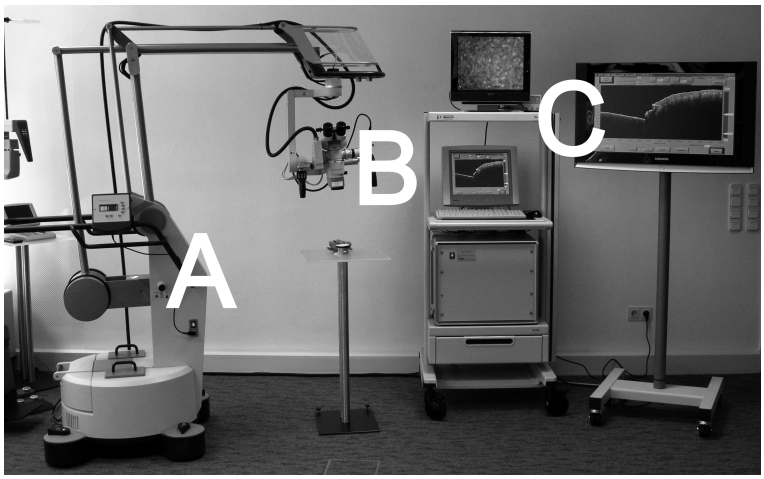

Figure 5.18: Robotized operating microscope with integrated OCT. [A] Operating microscope [B] Objective with OCT modality [C] Visualization unit.

in the seed's location, leakage, and the difference in the nature of the data to be analyzed. Segmentation of OCT images has not been investigated extensively. To our knowledge, only the authors of [147] propose an automated segmentation approach for the identification of retinal layers. Their approach is based on edge-sensitive nonlinear diffusion filtering and a subsequent boundary detection and does not feature general characteristics. The segmentation of OCT images generally faces two major problems. First, the intensity course in OCT images results from absorption and scattering of light in tissue. Thus, intensity of a homogeneous area decreases with increasing imaging depth deterministically. This complicates common segmentation approaches which are usually based on the assumption that intensity variations of homogeneous regions are only due to noise and not inherent to the imaging modality. The second problem is that OCT images are subject to speckle noise which decreases the image quality and complicates the image analysis.
The latter problem has been targeted by the development of many image processing methods for enhancement by the means of speckle noise reduction which have been described in section 5.2.1. In [147], the authors apply edge-sensitive diffusion filtering before the segmentation. As edge-sensitive filters are designed to enhance homogeneous regions, a diffusion filtered image is eventually better suited for a region growing process. Despite this advantage, filtering alters the image in a way that important information may not enter the segmentation step. On the other hand, if segmentation is performed on unfiltered data, common homogeneity criteria tend to fail because of speckle noise corruption.

5.3.2 Automated segmentation of tissue structures in OCT data

Two approaches to automated seeded region growing for the segmentation of OCT images will be presented. Automation of the region growing concerns two issues: the seed finding and the subsequent region growing process. In the first part, a model-based seed detection algorithm which analyzes the intensity profile of an A-scan is applied. Thus, the user-dependency is reduced significantly compared to a manual seed selection. In both approaches, the seed detection is followed by a region growing algorithm. The first approach applies an adaptive neighborhood homogeneity criterion on unfiltered OCT images while the other is based on edge-sensitive filtered images. The ultimate goal of both algorithms is to automatically locate specific structures in OCT images in order to facilitate the usage in diagnosis and/or extraction of morphological information. The approach is illustrated for the detection and identification of white matter fibres, a valuable application for neurosurgical navigation. The application and corresponding results are additionally presented for the segmentation of low and highly scattering structures in multiple OCT images indicating the generality of the proposed approach.
Both segmentation approaches consist of two steps. The first step, which is common to both algorithms, performs an automated, model-based seed detection. This step forms the basis for the automatic characteristic of the approach. Changes of tissue characteristics are detected by analyzing the OCT A-scan intensity courses which are taken from the B-scans (e.g. columns of a B-scan image). The detected seeds are used for a region growing method forming the second step. Two approaches for the region growing featuring different growing criteria are introduced:

1. an adaptive neighborhood region growing approach (ARG),
2. and a filtered image region growing approach based on an edge-sensitive filtered version of the original OCT image (FRG).

While the first approach derives the homogeneity criterion based on an adaptive neighborhood filtering approach and an OCT intensity model, the latter uses statistical measures of the intensity values for the growing process on an edge-sensitve diffusion filtered image. Figs. 5.19(a) and 5.19(b) show flowcharts for both approaches.

Automated Seed Detection

A basic requirement for region growing methods is the specification of seeds, which serve as a starting point for an iterative growing process. A fundamental adept of the proposed

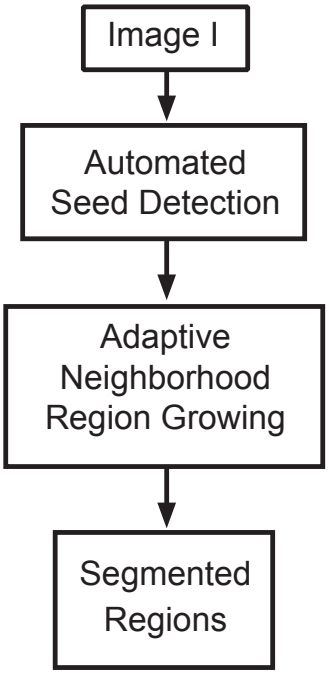

(a) Steps of the adaptive region growing approach (ARG).

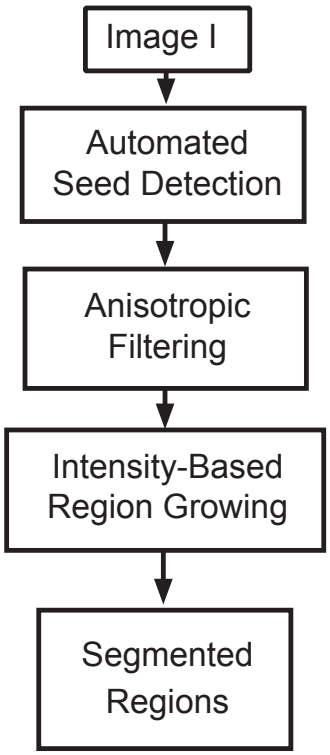

(b) Steps of the region growing on filtered image (FRG).

Figure 5.19: Flowcharts of the proposed region growing approaches.

method is the automated acquisition of the seeds, derived from an A-scan analysis as presented in section 5.2.3. As a matter of fact, the framework of A-scan-based white matter detection can easily be extended to the task of seed detection and already provides an automated seed detection for white matter segmentation.

As the current subject is segmentation of structures in B-scans, the seed detection is extended by an additional robustness measure: After having identified seed candidates in the OCT A-scan, a row consistency check is introduced. The location of detected seeds is compared to the location of detected seeds in the neighboring A-scans. Therefore, an 5×5 pixel window with its center being the current seed is analyzed. If this window contains more than 4 additional seeds, the current seed is approved.

The proposed seed detection algorithm is now summarized in the following definition:

Definition 1 *Let g denote an image. Then*

$$S = seedDetection(g, \sigma_1, \sigma_2, \sigma_3) \tag{5.28}$$

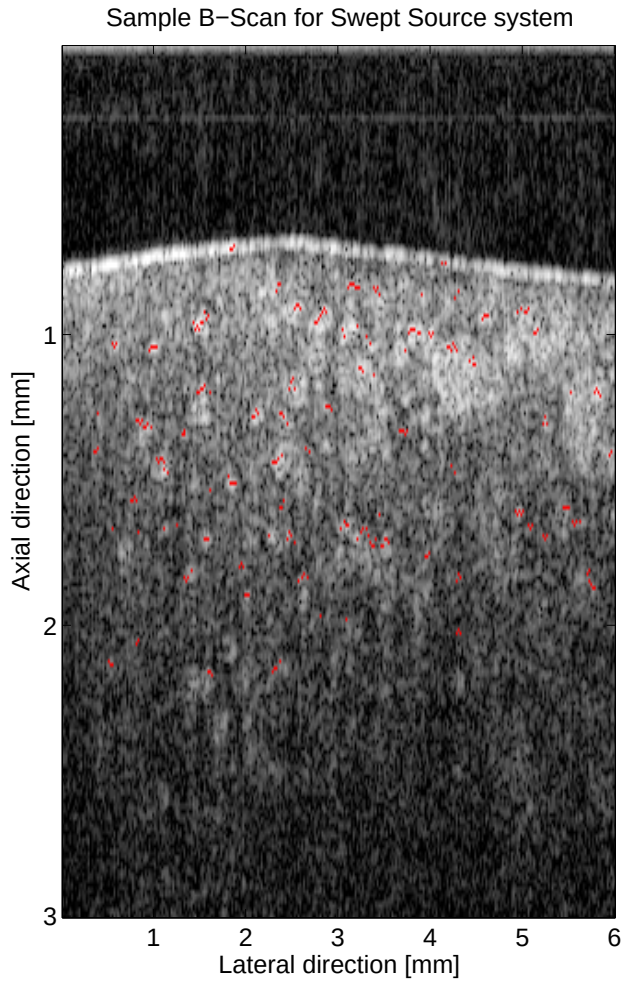

Figure 5.20: White matter detection in an exemplary OCT B-scan: Seeds are indicated by red dots.

is defined as the set of seed pixels provided by the A-scan intensity course-based white matter detection.

Fig. 5.20 shows exemplary seeds detected in an OCT B-scan.

Adaptive neighborhood region growing (ARG)

Common region growing approaches tend to fail in OCT images because of the exponential decay according to Eq. 5.17 and the speckle noise corruption. This is because the OCT signal properties and the dependency of the noise on the local intensity is not reflected by the homogeneity criteria used in common methods. Resulting from research

in the image filtering community, adaptive filters have been developed which estimate the speckle standard deviation σ_u based on the local mean [143]. The approach has proven to be well suited for filtering of SAR images. For OCT images, however, this approach is not optimal as the intensity level additionally follows a deterministic behavior as shown in Eq. 5.17. To perform region growing based on adaptive neighborhood filtering, the approach will be extended by incorporating the OCT intensity model into the homogeneity criterion. This is based on the following ideas:

- The homogeneity or growing criterion for OCT images will be affected by two parts: a deterministic part incorporating the modeled behavior as in Eq. 5.17 and a stochastic part based on the local average and standard deviation.
- The speckle noise standard deviation $\sigma_{g_{\text{hom}}}$ is not known a priori and will be estimated within a local neighborhood according to Eq. 5.21 (as proposed in [143]).

In the following, an adaptive homogeneity criterion, which is based on the evaluation of local statistics and the deterministic model in Eq. 5.17, will be developed. To introduce the approach, the following definitions are made:

Definition 2 *Let s denote a pixel of a speckle noise corrupted image g. Then $\Gamma_n(s)$ denotes the $n \times n$ neighborhood of s and $\Gamma_{n,y}(s)$ denotes the $n \times 1$ row-wise neighborhood (neighboring pixels in the same row).*

Definition 3 *Let s denote a pixel of a speckle noise corrupted image g and $g(s)$ the gray value at pixel s. Let $q \in \Gamma_n(s)$. Then the confidence interval $[T_1, T_2]$ at q is given by*

$$\begin{aligned} T_1(q) &= g_{\text{med}}(q) - c_1 \frac{\sigma_u}{\bar{u}} g_{\text{med}}(q), \\ T_2(q) &= g_{\text{med}}(q) + c_2 \frac{\sigma_u}{\bar{u}} g_{\text{med}}(q). \end{aligned} \tag{5.29}$$

where c_1 and c_2 are confidence interval shift parameters and

$$g_{\text{med}}(q) = \begin{cases} median(\Gamma_{n,y}(s)) exp(-2\mu\Delta z) & \text{if } q_z > s_z, \\ median(\Gamma_{n,y}(s)) & \text{if } q_z = s_z, \\ median(\Gamma_{n,y}(s)) exp(2\mu\Delta z) & \text{if } q_z < s_z \end{cases} \tag{5.30}$$

where s_z and q_z denote the z-coordinate of the pixel which corresponds to the imaging depth and Δz their depth difference. The adaptive region growing homogeneity criterion is then defined as:

$$homARG(q,s) = \begin{cases} \text{true} & \text{if } g(q) \in [T_1, T_2] \\ \text{false} & \text{otherwise.} \end{cases} \tag{5.31}$$

Based on above mentioned observations and definitions, the following steps are taken for the ARG:

1. Obtain an initial seed set S by performing the seed detection.
2. Estimate the local average $\bar{g}_{\text{hom}}$ as the row-wise median $\Gamma_{n,y}(s)$ within the row of the seed pixel s.
3. For every pixel q in a 3×3 neighborhood of a seed pixel s, calculate the confidence interval according to Eq. 5.29 and evaluate the membership to the region according to Eq. 5.31.
4. If membership is given, meaning the homogeneity criterion is fulfilled, include the neighbor pixel q into the seed set S and the set of detected white matter R.
5. Stop the region growing if the seed set S is empty.

The approach is summarized as pseudocode in section 9.1 as algorithm 9.3. The main advantages of the approach are the adaptivity of the homogeneity criterion, the integration of the deterministic intensity decay, and the integration of speckle noise corruption into the homogeneity criterion. Thus, the region growing is able to work on an unfiltered OCT image.

Filtered image region growing (FRG)

As stated in section 5.2.1, numerous noise removal techniques have been developed for the reduction of speckle noise corruption. Filters which do not support edge preservation are generally not suitable for region growing approaches. Edge-sensitive or enhancing filters, however, try to smooth homogeneous regions and prohibit smoothing at edges, thus being good candidate filters for subsequent region growing approaches. Review of recent OCT-related literature [135] shows that the Perona-Malik and the complex diffusion filter are suitable approaches for OCT image filtering. For the rest of this work, the following definitions will be used:

Definition 4 *Let g denote a gray-valued image. Then*

$$\hat{g} = pmFilter(g, N, K) \tag{5.32}$$

is defined as the edge-sensitive filtered version of g according to [132].

In this formulation, N denotes the number of iterations and K denotes the edge threshold parameter. In [134], the concept is extended to a complex diffusion process.

Definition 5 *Let g denote a gray-valued image. Then*

$$\hat{g} = cdFilter(g, N, K) \tag{5.33}$$

is defined as the complex diffusion filtered version of g according to [134].

Filtering according to both approaches incoporates the following features:

1. Region smoothing and
2. edge enhancing.

Region growing for the filtered version of the image follows the same guidelines as the ARG approach except that the homogeneity criterion is chosen differently. This is due to the fact that the intensity distribution in the image is altered and the effect of speckle noise is reduced through the filtering process. In fact, the criterion can now be selected as a simple, intensity-based criterion employing the median operator.

Definition 6 *Let s and denote a pixel of a speckle noise corrupted image g and $\hat{g}$ the filtered version. Let $\hat{g}(s)$ denote the gray value at pixel s. Let $q \in \Gamma_n(s)$. Then the confidence interval $[T_1, T_2]$ at q is given by:*

$$\begin{aligned} T_1(q) &= c_1 \cdot median(\hat{\Gamma}_n(s)), \\ T_2(q) &= c_2 \cdot median(\hat{\Gamma}_n(s)) \end{aligned} \tag{5.34}$$

where c_1 and c_2 are confidence interval shift parameters. The filtered region growing homogeneity criterion is then defined as:

$$homFRG(q,s) = \begin{cases} \text{true} & \text{if } \hat{g}(q) \in [T_1, T_2] \\ \text{false} & \text{otherwise.} \end{cases} \tag{5.35}$$

Algorithm 9.4 in section 9.1 summarizes the approach for the case of Perona-Malik filtering.

5.3.3 Anisotropic Propagation-Separation approach for speckle noise reduction in OCT images

The final part of the OCT image processing section introduces a novel filtering approach to OCT images. Intended to reduce the degrading effect of speckle noise and improve the image quality for postprocessing, it can be classified as an anisotropic filter. It is based on

the propagation-separation (PSEP) method incorporating the concept of steerable filters (see e.g. [148], [149]). These features enable the filter to enhance intraregion smoothing while suppressing interregion smoothing. Following a short introduction into the PSEP method, the theoretical background of the novel approach will be outlined.

Propagation-Separation Method (PSEP)

This section provides a short introduction into the PSEP method. Notation is chosen similar to [150]: Assume X_i to be a vector of explanatory variables belonging to a finite dimensional Euclidean space which corresponds to the image coordinates. Let Y_i belong to a one-dimensional space presenting e.g. the gray value. It is supposed that each Y_i is conditionally distributed on $X_i = x$ with a density $p(\bullet, \theta(x))$ which is parametrized by the function $\theta(x)$. This means that the distribution of Y_i is given by a finite dimensional parameter $\theta = \theta(X_i)$ which depends on X_i.

The goal of the PSEP process is to estimate the function $\theta(X_i)$ in an iterative way. If a global parametric structure is assumed, the parameter θ would not depend on the location x. In this case, the parameter θ can be estimated by a maximum likelihood estimation

$$\hat{\theta} = \text{arginf}_{\theta \in \Theta} \sum_{i=1}^{n} -\log\, p(Y_i, \theta) \tag{5.36}$$

where Θ denotes the set of all θ and $p(Y, \theta)$ denotes the density of the distribution of Y_i. As the global parametric assumption is too restrictive in most applications, a nonparametric approach based on localization is introduced. This means that a parametric assumption is only valid in a local vicinity of the point x. In order to estimate a local model $\theta(x)$, a weight-based maximum likelihood estimate is used which is given by

$$\hat{\theta}(x) = \text{arginf}_{\theta \in \Theta} \sum_{i=1}^{N} w_i(x) \log p(Y, \theta). \tag{5.37}$$

In [151], the authors show that $\hat{\theta}$ corresponds to

$$\hat{\theta} = (\sum_i w_i Y_i) / \sum_i w_i \tag{5.38}$$

for different models of the density function $p(y, \theta)$. The weights w_i in Eq. 5.38 of the local model $\hat{\theta}$ are determined iteratively: For every design point X_i (e.g. pixel), a local model is considered with $W_i = W(X_i) = \{w_{i1}, \ldots, w_{in}\}$ where n denotes the number of samples. The weights w_{ij} are determined by two kernels

$$w_{ij}^{(k)} = K_{\text{loc}}(l_{ij}^{(k)}) K_{\text{st}}(s_{ij}^{(k)}) \tag{5.39}$$

where K_{loc} is a localization kernel, K_{st} is a statistical kernel and k the iteration step. The localization kernel is a function supported on $[-1 \dots 1]$ and l_{ij} is defined as

$$l_{ij}^{(k)} = |X_i - X_j|/h^{(k)} \tag{5.40}$$

where h is the bandwidth (e.g. circle radius in 2D) of the local model. This essentially means that the contribution of the explanatory variables outside a circle with the radius h vanish. The statistical kernel weights the statistical difference of the explanatory variables X_i and X_j by evaluating the Kullback-Leibler distance $\mathcal{K}$ of two probability measures. Therefore, $s_{ij}^{(k)}$ is defined as

$$s_{ij}^{(k)} = (N_i^{(k-1)} \mathcal{K}(\hat{\theta}_i^{(k-1)}, \hat{\theta}_j^{(k-1)}))/\lambda \tag{5.41}$$

where λ denotes a scale parameter and $N_i^{(k)} = \sum_j w_{ij}^{(k)}$.

The algorithm consists of 3 steps:

1. Adaption
   In the first step, the weights are determined by

   $$w_{ij}^{(0)} = K_{\text{loc}}(l_{ij}^{(0)}) \tag{5.42}$$

   where h^0 is the initial bandwidth. From the second step on, the weights are calculated by Eq. 5.39.

2. Local estimation
   The estimate $\hat{\theta}^{(k)}$ is given by

   $$\hat{\theta}^{(k)} = (S_i^{(k)})/(N_i^{(k)}) = (\sum_j w_{ij}^{(k)} Y_i)/\sum_j w_{ij}^{(k)}. \tag{5.43}$$

3. Adaptive control
   In [150], the authors introduce an additional memory kernel to control the quality of estimation

   $$\eta_i = K_{\text{m}}((\sum_j K_{\text{loc}}(l_{ij}^{(k)}) \mathcal{K}(\hat{\theta}_i^{(k)}, \hat{\theta}_i^{(k-1)}))/\tau) \tag{5.44}$$

   where τ is another scale parameter. The adaptively controlled estimate is now calculated as

   $$\hat{\theta}^{(k)} = \eta_i \hat{\theta}^{(k)} + (1 - \eta_i)\hat{\theta}^{(k-1)}. \tag{5.45}$$

After each step, the bandwidth is increased by $h^{(k)} = c_h h^{(k-1)}$ until the maximal bandwidth is reached. The stopping criterion can be chosen as a fixed number of iterations and/or the value of η being smaller than a user-defined threshold. In [150], the kernel functions are chosen as $K_{\text{loc}} = K_{\text{m}} = (1-x^2)_+$ and $K_{\text{st}} = \exp^{-x}$. Furthermore, the scale parameters λ and τ should be chosen as the smallest value satisfying the propagation condition, a value of $\tau = \infty$ would turn off the adaptive control. The update parameter c_h of the bandwidth is proposed to take the form $c_h = 1.25^{1/d}$. Details of the parameter choice are provided in [150].

Steerable filters

The concept of steerable filters is presented in [148]. In general, steerable filters allow the user to rotate a specific filter in a desired direction. In [148], the authors give an example for a steerable gradient filter which yields the first directional derivative. This example will be used in order to illustrate the concept of steerable filters. A standard circular symmetric Gaussian function is given by

$$G(x,y) = \exp^{-(x^2+y^2)}. \tag{5.46}$$

A partial derivative with respect to a certain angle ϕ can be formulated as a linear combination of the first partial derivatives with respect to x ($G_1^{0^\circ}$) and y ($G_1^{90^\circ}$):

$$G_1^{\phi} = \cos\phi G_1^{0^\circ} + \sin\phi G_1^{90^\circ}. \tag{5.47}$$

$G_1^{0^\circ}$ and $G_1^{90^\circ}$ are called basis filters. In image processing, the processed image is a result of a convolution of the original image I with the respective filter G

$$R = G * I. \tag{5.48}$$

As convolution is a linear operation, the filtered image of a steerable filter is given by

$$R_1^{\phi} = \cos\phi R_1^{0^\circ} + \sin\phi R_1^{90^\circ}. \tag{5.49}$$

In [148], [152] and [153] different efficient design schemes for steerable filters are proposed.

Anisotropic Propagation-Separation filtering (APSEP)

Local regression in the PSEP is done by evaluating the distance kernel K_{loc} and the statistical difference kernel K_{st} at each input X_i with respect to all other inputs $X_{j=1\ldots n}$.

As the bandwidth increases equally in all directions with each step of the iteration, an isotropic behavior is achieved. The idea of anisotropic propagation-separation filtering is to use information of the local anisotropy in the local modeling process. Incorporation of anisotropic information can be done by using the concept of steerable filters leading to a novel anisotropic filtering approach. Based on the output of oriented gradient filters a novel kernel is integrated into the PSEP formulation. This information of anisotropy of an image region consequently leads to improved noise reduction while preserving important features like edges. As in [132], gradient information is used in order to estimate the degree of anisotropy at a certain location. Local anisotropy is then used to introduce a novel, additional kernel K_{dir} which establishes the dependency of weights on local gradient information. The weights of the regression are now given by

$$w_{ij}^{(k)} = K_{\text{loc}}(l_{ij}^{(k)})K_{\text{st}}(s_{ij}^{(k)})K_{\text{dir}}(\Phi_{ij}^{(k)}) \tag{5.50}$$

where

$$\Phi_{ij}^{(k)} = (R_1^{\phi_{ij}} - \nabla_{min}^{(k)})/(\nabla_{max}^{(k)} - \nabla_{min}^{(k)}) - \kappa \tag{5.51}$$

and $R_1^{\phi_{ij}}$ is the directional gradient calculated at X_i. The kernel function K_{dir} is defined as

$$K_{\text{dir}}(\Phi_{ij}^{(k)}) = \arctan(\Phi_{ij}^{(k)})/\pi + 0.5 \tag{5.52}$$

which is supported on the interval of $]-1,1[$. In Eq. 5.51, ∇_{min} denotes the minimal gradient and ∇_{max} the maximal gradient in the image. This serves as a normalization of the respective gradient. ϕ_{ij} denotes the angle between the vertical axis of the image and a line connecting X_i and X_j. The parameter κ is a threshold parameter which can be considered as a threshold for the influence of X_j on the weights of the regression model. The kernel is shown for different values of κ in Fig. 5.21. The directional derivative kernel reduces the contribution of observed values at locations X_j if X_j is located in a direction with a large gradient. For small gradients, the determination of the weights follows Eq. 5.39 of the original PSEP. The incorporation of the directional gradient kernel can be considered as an adaption of the bandwidth h by reducing the contribution to the local model in directions of large gradients. This establishes a directional bandwidth h. Consequently, the directional kernel prohibits interregional smoothing.
In the following, the steps of the novel algorithm will be described:

1. Initialization
   Before starting the algorithm, the steering angle range should be defined. Usually, all angles from $\phi \in [0^\circ \dots 360^\circ[$ should be evaluated.

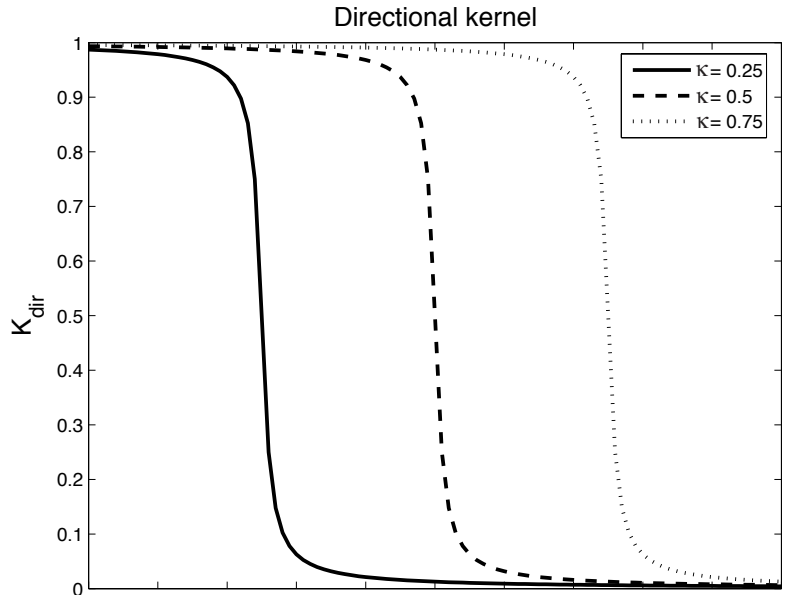

Figure 5.21: Directional kernel value for different gradients κ.

2. Gradient calculation
   Determine the minimal and maximal gradients $\nabla^{(k)}_{min,max}$ in the current image $I^{(k)}$. The steerable filter used to determine the directional gradient is given by

$$G_1^{0^\circ} = \exp^{-(x^2+y^2)/(2\sigma^2)}/(\sigma\sqrt{2\pi}). \tag{5.53}$$

   This is a Gaussian low-pass filter with a standard deviation of σ which will reduce the noise influence on the gradient determination. The standard deviation of the steerable filters should be chosen with respect to the analyzed image. Small standard deviation ensure the locality of the gradient but will not reduce the noise in the same way as higher standard deviations. If the image contains small structures, the standard deviation should be kept small as well.

3. Estimation
   In the third step, the new estimate $\hat{\theta}^{(k+1)}$ of the image is calculated. The weights for every pixel at the location Y_u for the determination of the intensity of the pixel at the location Y_i are caculated by Eq. 5.50. To calculate K_{dir}, the direction of the gradient is determined as the angle between the vertical axis of the image and a line connecting Y_u and Y_i. With $\nabla_{min,max}$ determined by step 2, the value of the directional kernel can be calculated. Usually, this procedure would require to evaluate the directional gradient twice (in step 2 and step 3). To increase the speed of the

algorithm, the directional gradient can be interpolated from the set of directional derivatives obtained by step 2. The update $\hat{\theta}^{(k+1)}$ is calculated by equation

$$\hat{\theta}^{(k)} = \sum_i w_i \hat{\theta}^{(k-1)} / \sum_i w_i. \tag{5.54}$$

Note that the update is based on the previous iteration result and not on the original image as in Eq. 5.43.

4. Updating h and σ
   The bandwidth h is updated with

$$h^{(k+1)} = c_h h^{(k)} = 1.25^{1/d} h^{(k)} \tag{5.55}$$

   If the stopping criterion is not met, the algorithm continues with step 2.

5. Stopping criterion
   The algorithm should stop after a predefined number of iterations or if η_i becomes smaller than a user-selected threshold. See section 5.3.3 for details.

As proposed in [150], an adapative update of the model can be integrated into the estimation process. This is done by incorporation Eqs. 5.44 and 5.45 into the iteration process.

6 Experimental application and results[1]

Adapting to the structure of this work, the following chapter presents experimental testing and the corresponding results for the different subareas adressed previously. For the experimental setups, this chapter provides a detailed description of the material and methods used to obtain the corresponding results which is of special importance for the case of animal experiments.
In the first part of the chapter, results concerning the performance of the SASSU are summarized. This includes the results of the mechanical positioning performance analysis of the SASSU in a simulated testbed environment. Second, results of robot-assisted electrophysiology in vivo are provided.
In the second part of this chapter, results for OCT brain imaging are presented. This part covers results on robot-assisted single fibre imaging as well as the results of the proposed OCT image segmentation and filtering methods.

6.1 Kinematic accuracy analysis

As mentioned in section 4.1.3, the kinematic structure of a manipulator affects the positioning accuracy of the respective system. As positioning accuracy is the most important property with regard to the application in stereotactic surgery, the kinematic properties of the system and their effect on the positioning accuracy will be examined in detail.

6.1.1 Kinematic accuracy measure

To analyze the errors resulting from the kinematic design, differential transformation theory using the DH parameters can be applied [156]. The linear differential error in the position and orientation of the end-effector can be expressed as the sum of partial derivatives of the POSE P with respect to the DH parameters:

$$\Delta P = \sum_i \left(\frac{\partial P}{\partial \theta_i}\Delta\theta_i + \frac{\partial P}{\partial a_i}\Delta a_i + \frac{\partial P}{\partial \alpha_i}\Delta\alpha_i + \frac{\partial P}{\partial d_i}\Delta d_i\right). \tag{6.1}$$

[1] Parts of this chapter have been published in [100, 101, 102, 119, 120, 121, 122, 154, 155].

The spatial positioning error corresponds to the last column (position vector) in ΔP. Eq. 6.1 shows that variations in all DH parameters contribute to the spatial positioning error. In this work, however, the kinematic accuracy is calculated by assuming that variations only exist for the joint variables [109]. This is due to the fact that for an assembled manipulator, the joints ideally present the only dynamic components and all other kinematic parameters can be considered static. Note that in a real system, structural and joint flexibilities are present but these effects are beyond the scope of this analysis.
The performance measure, which is chosen for accuracy analysis, is based on the Jacobian of the respective kinematic structure. The POSE of the end-effector can be expressed as

$$P = f(L, \Theta) \tag{6.2}$$

where L denotes the set of structural parameters (a_i, α, and d_i) and Θ denotes the joint parameters. If the desired spatial position and orientation is given by P_d and the real position and orientation by P_r, the position and orientation error can be written as

$$\Delta P = P_d - P_r = f(L, \Theta) - f(L + \Delta L, \Theta + \Delta\Theta). \tag{6.3}$$

As the structural errors are not considered in this work ($\Delta L = 0$), ΔP can be approximated with the help of the Jacobian. The Jacobian usually defines the relationship between joint velocity and end-effector velocity. For small pertubations in the joint angles, the displacement of the end-effector can be approximated by

$$P(\Theta + \Delta\Theta) \approx P(\Theta) + \frac{\partial P(\Theta)}{\partial \Theta}\Delta\Theta \tag{6.4}$$

which yields

$$P(\Delta\Theta) = \frac{\partial P(\Theta)}{\partial \Theta}\Delta\Theta = J\Delta\Theta. \tag{6.5}$$

For the case of the stereotactic surgery, the translational error is of major interest. It is evaluated by

$$\Delta p = \sqrt{p_x(\Delta\Theta)^2 + p_y(\Delta\Theta)^2 + p_z(,\Delta\Theta)^2} \tag{6.6}$$

where $p_x(\Delta\Theta)$ is the x-entry of the fourth column of $P(\Delta\Theta)$. In order to compare the repeatability of the SASSU structure to another stereotactic system, the DH parameters of the SASI (see Fig. 2.7) are derived and listed in Table 6.1. As stated in section 4.1.3, the major difference between both kinematic structures is that the SASI kinematics can be described by a *RRTTT* chain which is different to the *TTRRT* chain of the SASSU.

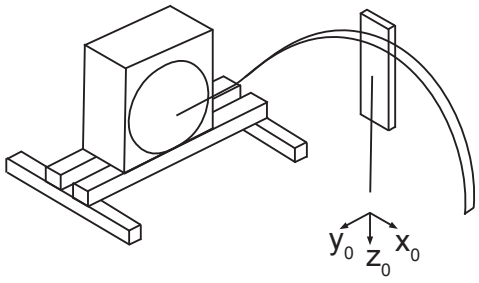

Figure 6.1: Schematic drawing of the SASSU and its base coordinate system for kinematic accuracy analysis.

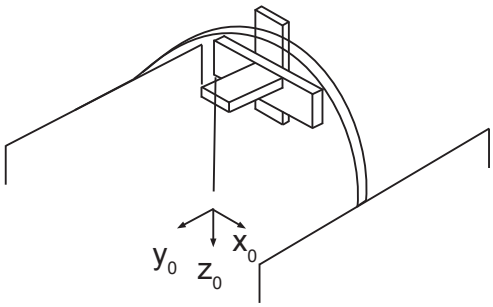

Figure 6.2: Schematic drawing of the SASI and its base coordinate system for kinematic accuracy analysis.

Table 6.1: DH parameters for the SASI manipulator according to the conventions in [1]. a_i and d_i denote translational distances (along the x_i and z_i axes) to the following coordinate frame, α_i and θ_i denote angles of rotation around the x_i and z_i axes.

	a_i	d_i	α_i	θ_i
0	0	0	$-\frac{\pi}{2}$	$-\frac{\pi}{2}$
1	0	0	$-\frac{\pi}{2}$	$q_1+\frac{\pi}{2}$
2	0	0	$\frac{-\pi}{2}$	q_2
3	0	t_1+o_x	$\frac{\pi}{2}$	0
4	0	t_2+o_y	$\frac{\pi}{2}$	$\frac{\pi}{2}$
5	0	z_3+o_z	0	0

6.1.2 Simulation environment

Evaluating the joint variations induced inaccuracies of both, the SASSU and the SASI manipulator, is done using the forward and inverse kinematic equations to determine the translational error Δp if errors in the rotary joints occur. To evaluate the performance of both manipulators in a realistic way, this analysis takes the workspace requirements into account. Table 6.2 shows the dimension of the workspace in terms of the joint ranges for both manipulator configurations. The workspace is given with respect to the base coordinate system of the manipulators which is chosen to be the isocenter of both rotary joints with the orientation given in Figs. 6.1 and 6.2. Considering stereotactic surgery on rats, the desired workspace is given by $x_0 = [-10 \dots 10]$ mm, $y_0 = [-10 \dots 10]$ mm, and $z_0 = [-5 \dots 10]$ mm. The workspace volume is now discretized into steps of 1 mm in x_0-,

Table 6.2: Workspace requirements for the SASSU and the SASI system in terms of joint values.

SASSU		SASI	
Joint	Range	Joint	Range
t_1	$[-15\text{ mm}\dots 15\text{ mm}]$	q_1	$[-15^\circ\dots 15^\circ]$
t_2	$[-15\text{ mm}\dots 15\text{ mm}]$	q_2	$[-15^\circ\dots 15^\circ]$
q_1	$[-15^\circ\dots 15^\circ]$	t_1	$[-15\text{ mm}\dots 15\text{ mm}]$
q_2	$[-15^\circ\dots 15^\circ]$	t_2	$[-15\text{ mm}\dots 15\text{ mm}]$
t_3	$[-15\text{ mm}\dots 15\text{ mm}]$	t_3	$[-15\text{ mm}\dots 15\text{ mm}]$

y_0- and z_0-direction providing a set of points $\mathbb{P}$. Orientations of the tool are given by a set of ring angles α_{x_0} and arc angles α_{y_0}: $\alpha_{x_0} = [-15^\circ\dots 15^\circ]$ and $\alpha_{y_0} = [-15^\circ\dots 15^\circ]$. These will be referred to as set of orientations $\mathbb{O}$. The tool length (e.g. o_{z2}) is set to -30 mm which means that it is located above the isocenter. For every point $p \in \mathbb{P}$ of the workspace, inverse calculation for all orientations $o \in \mathbb{O}$ is performed yielding the corresponding joint variables Θ_c. The translational error is subsequently determined by evaluating the position entry of $P(\Delta\Theta_c)$ as

$$P(\Delta\Theta_c) = J_c \Delta\Theta_c \tag{6.7}$$

where J_c is the Jacobian evaluated at Θ_c. In order to analyze the respective contribution of an error in one rotary joint q_i, the corresponding entry in $\Delta\Theta_c$ is set to $\Delta q_i = 0.1^\circ$ while all other joint values are set to zero. For all points $p \in \mathbb{P}$, the maximal, the minimal and the mean over all orientations $o \in \mathbb{O}$ are evaluated. This leads to a set of errors $\mathbb{E}_{max}$, $\mathbb{E}_{min}$, and $\mathbb{E}_{mean}$ over $\mathbb{P}$.

6.1.3 Results

Table 6.3 shows the maximal, the minimal, and the mean translational error of the respective error sets for different depths z if joint q_1 is subject to an error $\Delta q_1 = 0.1^\circ$. Accordingly, Table 6.4 shows the translational error for joint variations in joint q_2. Fig. 6.3(a) shows the maximal translational error of the SASSU system in a x_0y_0-plane at a constant depth $z_0 = 5$ if all orientations $o \in \mathbb{O}$ are analyzed and the joint value of q_1 is subject to inaccuracies ($\Delta q_1 = 0.1^\circ$). Fig. 6.3(b) shows the corresponding error for the SASI system and Fig. 6.3(c) the difference at the depth $z_0 = 5$.

After having examined the errors induced by the rotary joints, the error induced by deviations of the translational joints can be analyzed. Looking at Eq. 6.6 it can be seen that

Table 6.3: Mean, max., and min. translational positioning error of the SASSU and the SASI resulting from a joint deviation $\Delta q_1 = 0.1°$. Results are obtained if a point at depth z is targeted with a set of orientations $\mathbb{O}$. Smaller positioning errors are printed bold.

Depth	Error	SASSU	SASI
$z = -5$	mean($\mathbb{E}_{mean}$)	**0.5077**	0.6169
	max($\mathbb{E}_{max}$)	**0.5189**	0.7810
	min($\mathbb{E}_{min}$)	0.5004	**0.5000**
$z = 0$	mean($\mathbb{E}_{mean}$)	**0.0000**	0.3231
	max($\mathbb{E}_{max}$)	**0.0000**	0.6000
	min($\mathbb{E}_{min}$)	**0.0000**	**0.0000**
$z = 5$	mean($\mathbb{E}_{mean}$)	**0.5077**	0.6169
	max($\mathbb{E}_{max}$)	**0.5189**	0.7810
	min($\mathbb{E}_{min}$)	0.5004	**0.5000**
$z = 10$	mean($\mathbb{E}_{mean}$)	**1.0154**	1.0662
	max($\mathbb{E}_{max}$)	**1.0378**	1.1662
	min($\mathbb{E}_{min}$)	1.0007	**1.000**

the spatial error magnitude for translational joint deviations is always quantitatively equal to the joint deviation. Both manipulators therefore show the same error magnitude if the translational joints are due to joint deviations.

6.2 Mechanical positioning performance analysis

Examining the positioning performance of the SASSU concentrates on its application to small animal surgery. The following analysis of the SASSU is split into two parts. In the first part, the positioning accuracy in an artificial testbed environment is analyzed. The second part evaluates the performance of the SASSU in animal surgery with a special focus on robot-assisted electrophysiology. In this context, different aspects are highlighted: the general integration into the surgical workflow, its suitability to perform electrophysiology, and the results of the latter. For this purpose, a short introduction into the field of electrophysiological signal processing is given with a special focus on methods used within the evaluation of the robot-assisted recordings.

Table 6.4: Mean, max., and min. translational positioning error of the SASSU and the SASI resulting from a joint deviation $\Delta q_2 = 0.1°$. Results are obtained if a point at depth z is targeted with a set of orientations $\mathbb{O}$. Smaller positioning errors are printed bold.

Depth	Error	SASSU	SASI
$z = -5$	mean($\mathbb{E}_{mean}$)	**0.5151**	0.6117
	max($\mathbb{E}_{max}$)	**0.5359**	0.8789
	min($\mathbb{E}_{min}$)	0.5007	**0.3214**
$z = 0$	mean($\mathbb{E}_{mean}$)	**0.0000**	0.3339
	max($\mathbb{E}_{max}$)	**0.0000**	0.6211
	min($\mathbb{E}_{min}$)	**0.0000**	**0.0000**
$z = 5$	mean($\mathbb{E}_{mean}$)	**0.5151**	0.6117
	max($\mathbb{E}_{max}$)	**0.5359**	0.8789
	min($\mathbb{E}_{min}$)	0.5007	**0.3214**
$z = 10$	mean($\mathbb{E}_{mean}$)	**1.0302**	1.0523
	max($\mathbb{E}_{max}$)	**1.0718**	1.2741
	min($\mathbb{E}_{min}$)	1.0015	**0.8032**

6.2.1 Mechanical accuracy analysis

As the objective of the SASSU system is the precise placement of probes within a small animal brain, positioning accuracy is crucial. To determine the performance of the system with regard to positioning accuracy, two scenarios are analyzed:

1. Repeatability which is defined as the ability of the system to return to the same point in space and
2. mechanical positioning accuracy which is defined as the ability of the system to target one point in space with different orientations of the probe.

Spatial positioning of the probe is measured based on stereoscopic imaging. The testbed setup is chosen as follows: a platinum-iridium microelectrode (PTM23B10, World Precision Instruments, Sarasota, USA) with a tip diameter of approximately 2 μm simulates the probe. Before analysis, the SASSU is calibrated as described in section 4.3. Video monitoring for calibration and accuracy measurements is provided by two cameras (TheImagingSource, Charlotte, NC, USA) featuring two magnifying lenses (Edmund Optics, Karlsruhe, Germany). To provide spatial distances between the reference point and

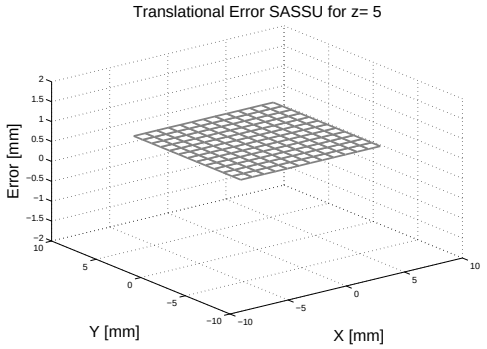

(a) Maximal translational error of the SASSU for the x_0y_0-plane at constant depth $z_0 = 5$ for a joint value error $\Delta q_1 = 0.1°$.

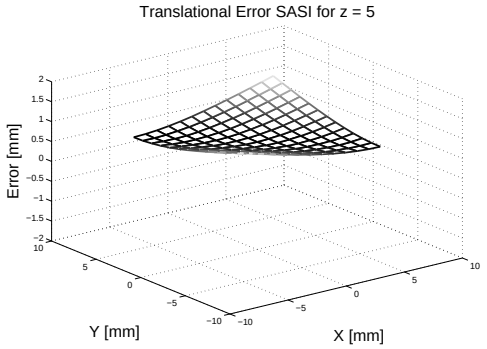

(b) Maximal translational error of the SASI for the x_0y_0-plane at constant depth $z_0 = 5$ for a joint value error $\Delta q_1 = 0.1°$.

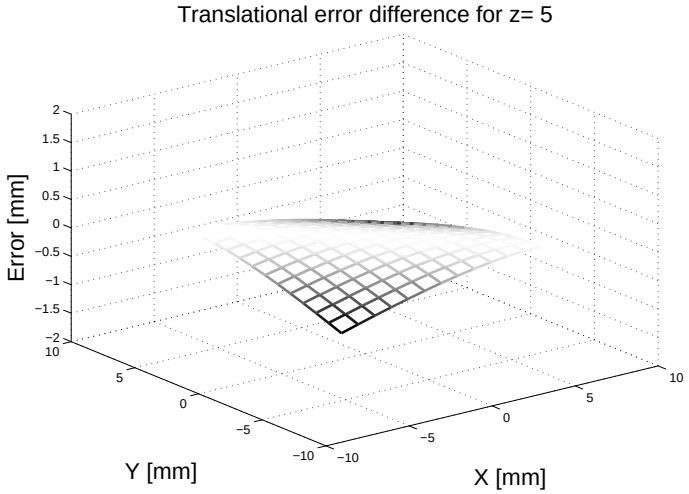

(c) Comparison of translational errors of the SASSU and SASI for the x_0y_0-plane at constant depth $z_0 = 5$ for a joint value error $\Delta q_1 = 0.1°$.

Figure 6.3: Translational error and error differences of the SASSU and SASI for positioning errors in the rotary joints.

the probe tip, cameras are calibrated according to well established stereoscopic camera calibration methods [157]. Distances are now evaluated based on the two dimensional pixel information of both cameras. The following steps are conducted for accuracy measurements.

1. The probe tip is placed at a desired initial position with $q_1 = q_2 = 0°$.
2. A desired target POSE is specified.
3. The corresponding joint values are calculated by the inverse kinematics and joints are actuated accordingly.

Table 6.5: Results of the repeatability testings with the SASSU. Listed are the averaged results over 30 runs for repeated positioning at one point in space.

α_{x_0}	α_{y_0}	Mean displacement	Standard deviation	Max. displacement	Min. displacement
$-10°$	$-10°$	6.8 μm	1.6 μm	9.2 μm	3.6 μm
$-5°$	$-5°$	10.7 μm	3.5 μm	14.8 μm	0.7 μm
$0°$	$0°$	9.6 μm	6.5 μm	21.3 μm	4 μm
$5°$	$5°$	6.9 μm	4.0 μm	18.1 μm	1.3 μm
$10°$	$10°$	8.9 μm	2.2 μm	12.2 μm	3.7 μm

4. Based on the stereoscopic images, the tool tip is automatically identified and the spatial distance to the initial point is evaluated.

To automatically identify the position of the tool tip in the camera images, the needle boundaries are segmented by an edge detection method. Additionally, the centerline of the tool is estimated via a principal component analysis (see section 4.3.2). The tip position is then identified as the intersection of the needle shape and the estimated centerline of the needle. To improve robustness of the edge detection, a white background is introduced and contrast and brightness properties of the camera images are adjusted. Fig. 6.4 shows an exemplary camera image used in the accuracy analysis.

Repeatability measurements

To analyze the repeatability, the probe is placed at five different target positions with different orientations repeatedly (30 times). The orientation of the probe is expressed in terms of the ring angle (α_{x_0}) and the arc angle (α_{y_0}). Results are summarized in Table 6.5. The maximum deviation within the repeatability experiment is lower than 22 μm, the mean deviation is lower than 11 μm.

Mechanical accuracy

For the accuracy measurements, a different scenario is chosen. In a first step, multiple target positions are defined with respect to the initial position. Coordinate details for all tested scenarios are given in Table 6.6. Second, each of the points is targeted with multiple orientations of the probe. Orientation of the target POSE are varied by a ring angle range of $\alpha_{x_0} = [-10° \dots 10°]$ and an arc angle range of $\alpha_{y_0} = [-10° \dots 10°]$ (stepsize of $1°$). The following positions with respect to the initial point have been evaluated. Results of the accuracy measurements are summarized in the Table 6.7. Table 6.8 shows the percentage of the total spatial positioning error which is smaller than 50 μm and 75 μm respectively.

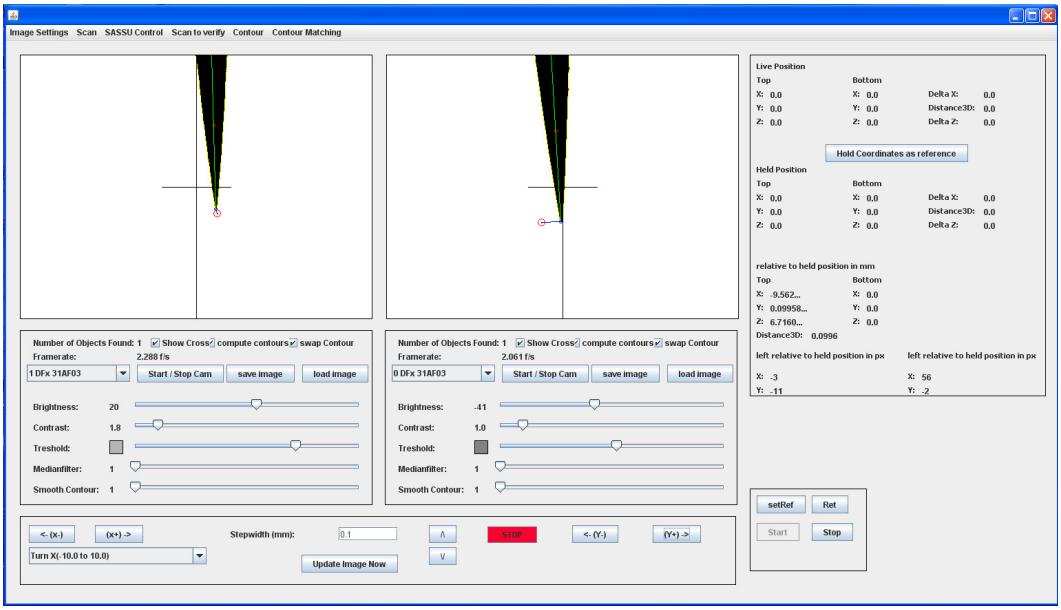

Figure 6.4: Screenshot of the stereoscopic camera images of a microelectrode used for the calibration and the mechanical accuracy analysis. The red dot indicates a virtual reference point, the blue line is the spatial distance of the detected probe tip to the reference point. The lower part of the GUI provides camera parameters adjustments and SASSU control options. The right side provides information on the spatial distance of probe tip and reference point.

In Fig. 6.5, the spatial error in all directions of scenario 3 with respect to all rotary joint values is displayed. Fig. 6.6 provides the corresponding error histogram. The average spatial positioning error within the defined angle range is 32 μm for a scanning range of $\alpha_{x_0} = [-10° \ldots 10°]$ and $\alpha_{y_0} = [-10° \ldots 10°]$.

6.2.2 Electrophysiological recordings

As one of the major goals of this work includes high precise electrophysiology in the rat brain, this part focuses on the performance of the SASSU in animal experiments where microelectrode recordings are obtained in vivo. Results reflect an evaluation of the operational usability of the SASSU. Special emphasis is put on the effect of SASSU induced electrical noise which potentially deteriorates the recording quality. Additionally, this part provides results indicating future applications of the SASSU in robot-assisted electrophysiology. Especially, the mapping of characteristic electrical activity to an intracranial position is investigated.

Table 6.6: Details on the mechanical accuracy measurement scenarios.

Scenario	Offset of the respective target point from the initial position of the probe		
	x-offset [mm]	y-offset [mm]	z-offset [mm]
1	0	0	0
2	0	0	3
3	0	0	5
4	0	0	8
5	0	0	10
6	0	0	-3
7	0	0	-5
8	0	0	-8
9	0	0	-10
10	3	-3	-3
11	-3	-3	-3
12	3	3	-3
13	-3	3	-3
14	3	-3	3
15	-3	-3	3
16	3	3	3
17	-3	3	3
18	2	5	8
19	-2	5	8

Animal experiments

To test the stereotactic framework system under real conditions, electrode recordings were performed for four trajectories in the rat brain using the atlas-based approach. Before operation, a concentric bipolar microelectrode (FHC Inc, Bowdoin, ME, USA) was attached to the adapter of the stereotactic assistant system and a calibration run was made. The electrode had a diameter of 250 μm, a pencil point tip configuration, and a length of 30 mm. The electrode was connected with both channels to a recording system (Tucker Davis Technologies, Alachua, USA). Microelectrode recordings were acquired using a 10 kHz low-pass filter and a 800 Hz high-pass filter as neural spiking activity is typically within the bandwidth of 1 kHz to 5 kHz. The sampling rate was 24 kHz. An approval for all experimental procedures was obtained from the Danish Committee for the Ethical Use of Animals in Research. Experiments were conducted at the Center for Sensory-Motor Interactions at the Department of Health Technology and Science (Aalborg, Denmark). Each rat was anaesthezised using a Ketamin (100mg/kg)-Xylazin (5mg/kg)-Acepromazin (2.5mg/kg) cocktail. Subsequently, it was fixed into the stereotactic frame (see Fig. 6.7(a) and Fig. 6.7(c)). The rat scalp was opened and the Bregma and Lambda points were identified. Registration was performed under visual observation using an operating microscope (Model P-Berg, Nikon Inc., Tokyo, Japan). The target point and the insertion path were specified as in Table 6.9. After the prepositioning of the probe, the entry area

Table 6.7: Results of the mechanical accuracy analysis at different positions with respect to the initial position. Listed are the mean, the max., and the min. error in all spatial directions and the resulting total displacement error.

Scenario	x-displacment [μm]			y-displacment [μm]			z-displacment [μm]			Total displacment [μm]		
	Mean	Max.	Min.	Mean	Max.	Min.	Mean	Max.	Min.	Mean	Max.	Min.
1	26	63	0	7	34	0	2	49	0	37	73	8
2	16	49	9	15	70	0	1	54	0	35	88	11
3	14	45	0	10	53	0	1	26	0	25	54	3
4	32	67	0	1	50	0	7	38	0	40	77	4
5	17	55	0	2	48	0	7	50	0	31	68	8
6	17	42	0	4	46	0	2	40	0	29	56	5
7	17	53	0	15	90	0	10	54	0	38	103	7
8	11	49	0	10	34	0	3	47	0	29	55	8
9	4	39	0	15	53	0	1	53	0	28	58	2
10	12	44	0	7	75	0	1	43	0	28	84	9
11	4	32	0	5	48	0	8	41	0	25	53	4
12	3	37	0	4	51	0	16	45	0	28	62	4
13	2	38	0	22	59	0	18	48	0	35	69	12
14	9	35	0	1	90	0	3	59	0	25	107	4
15	27	55	0	13	76	0	6	43	0	40	89	9
16	23	60	1	8	52	0	13	43	0	35	80	11
17	8	35	0	12	91	0	6	62	0	31	110	4
18	1	47	0	27	79	1	14	59	0	40	92	5
19	18	58	0	11	56	0	7	39	0	34	74	5
Total	11	47	0	4	61	1	5	47	0	32	76	6.5

was marked. The probe was then removed from the surgical area and the skull of the rat was opened by manual drilling. The dura was removed. In a first movement sequence, the SASSU prepositioned the microelectrode outside the rat brain. In the second step, the microelectrode was advanced into the brain with a speed of 0.1 mm/s and different step sizes. During the microelectrode recordings, all other electronic equipments such as room light, power supply of the heating pad, and power electronics of the SASSU were turned off.

In the course of operation, however, the following effect was detected: the brain surface coordinates according to the Swanson-based planning did not correspond to the real surgical scenario where the brain surface was located approximately 100 μm beneath the skull surface (see discussion in section 7.1.4). Therefore, the position of the probe tip was measured as distance to the brain surface and then related to the Swanson atlas information.

Table 6.8: Percentage of total spatial errors smaller than 0.05 and 0.075 mm for all measurement scenarios listed in Table 6.6.

Scenario	1	2	3	4	5	6	7	8	9	10
Error $<$ 0.05 mm [%]	95	89	99	75	90	99	89	97	95	93
Error $<$ 0.075 mm [%]	99	95	100	99	100	100	95	100	100	99
Scenario	11	12	13	14	15	16	17	18	19	
Error $<$ 0.05 mm [%]	99	96	85	97	77	89	90	81	87	
Error $<$ 0.075 mm [%]	100	100	100	98	91	99	97	92	100	

Data analysis

Analysis of electrode recordings can be subdivided into two major classes: (a) spike-related analysis and (b) wave-related analysis. Most of the means of neural analysis are developed for the (statistical) characterization of single and multiple cell activity. In most cases, the analysis is performed on spike trains, which directly refers to spike-related analysis. These trains are considered as a time series of all-or-none events (see e.g. [158]). Obtaining the spike train from a single neuron in the recorded electrophysiological signals generally requires two steps: (a) spike detection and (b) spike sorting. A summary of the respective methods is given in [43] and [159]. Following these steps, different measures to describe the single neuron activity have been developed. Mostly, analysis is based on the assumption that the voltage record is the realization of a stochastic 'point process'. The measures now try to determine the process-related characteristics. The most common characterization determines the average fire rate of a single neuron. Other measures are based on the analysis of the interspike intervals and comprise e.g. the interspike interval histogram or the coefficient of variation [160]. A third approach to characterize single neuron activity uses burst characteristics where bursts are considered a sequence of 'few' action potentials separated by short interspike intervals. Among these measures are the burst index, burst frequency, pause ratio and pause index [161], [162]. All of these measures, however, require the preliminary steps of spike detection and spike sorting. The major disadvantage of spike-related analysis is that the accuracy of spike sorting and detection critically affects the subsequent analysis. Literature review shows that these steps are user-dependent and no Gold standard methods have been established [41].
In contrast to spike-related analysis, the wavetrain-related analysis applies statistical measures directly to the recorded voltage signal. Thus, the user-dependent steps of spike detection and spike sorting are omitted and user-dependency of the analysis is eliminated. The major shortcoming of analyzing the wavetrain directly is that no single cell discrimination can be done. Wavetrain analysis, in contrast, characterizes the behavior of neural

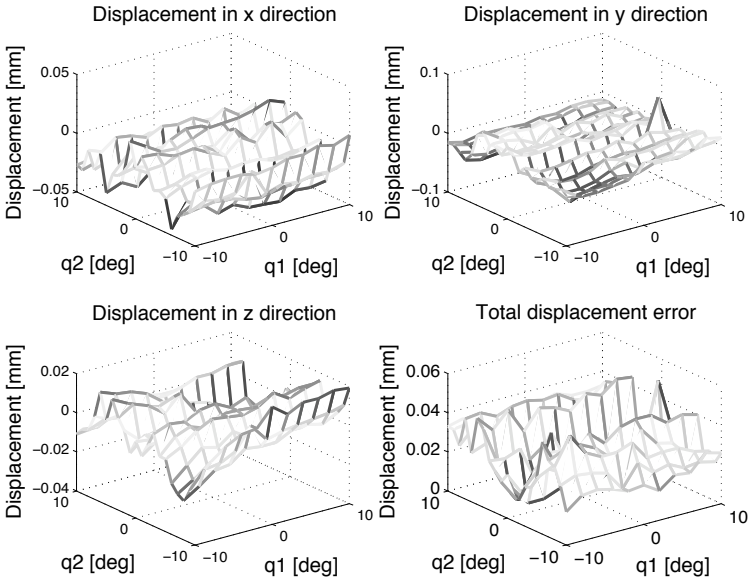

Figure 6.5: Spatial error of the mechanical accuracy analysis scenario 3. The image shows the spatial error for all rotary joint values in all spatial directions. Additionally, the total displacement error is provided.

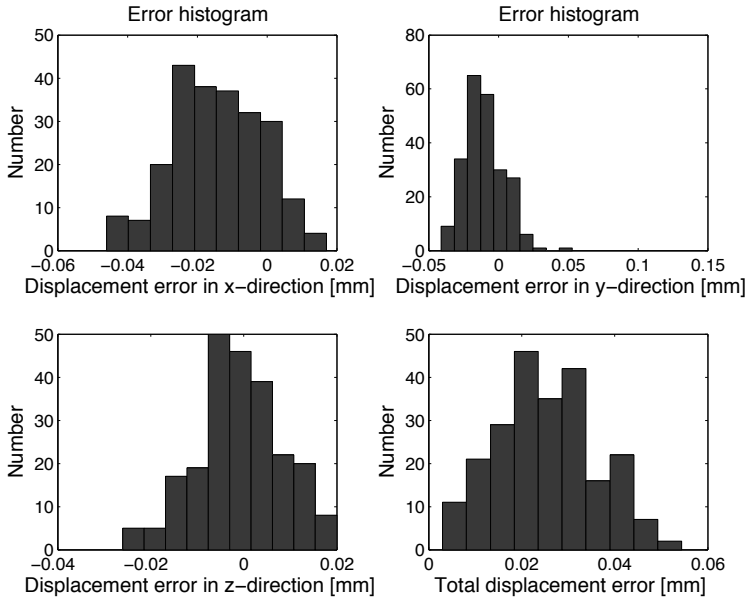

Figure 6.6: Error histogram for the mechanical accuracy analysis scenario 3. Displayed are the histograms of displacments in all spatial directions and the histogram of the total displacement.

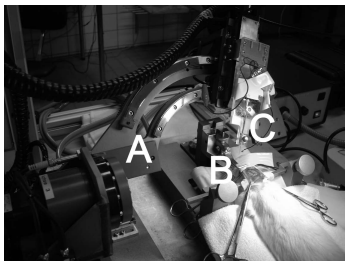

(a) Anaesthesized animal fixed into the stereotactic frame under the SASSU system. (A) SASSU (B) Animal fixed into stereotactic frame (C) Microelectrode.

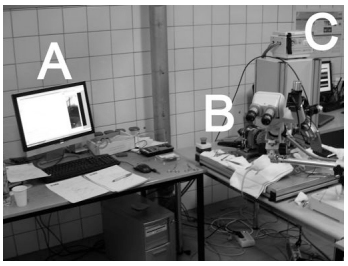

(b) Recording scenario. (A) Planning and Control (B) SASSU with animal (C) Signal Recording Unit.

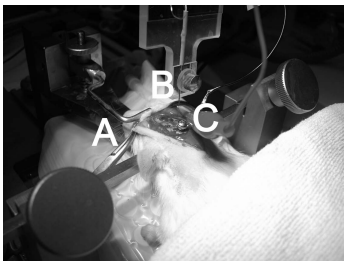

(c) Recording details. (A) Stereotactic fixation (B) Microelectrode (C) Grounding.

Figure 6.7: In vivo microelectrode recordings from the rat brain: surgical and recording scenario.

population in the environment of the probe tip. For the purpose of mapping functional areas or near field navigation, these populations characteristics might be sufficient. In [40] and [44], the authors show the feasibility of mapping a microelectrode trajectory to the STN in terms of different wavetrain-related measures. These measures are determined for a limited recording sequence at different depths and comprise the signals' energy, the power spectral density, the marginal probability density function, and the autocorrelation function.

As for the spike-related analysis, the recorded waveforms are considered to be realizations of a stochastic signal and therefore, statistical measures for characterization can be applied. In [163], additional scalar measures are introduced and their applicability for mapping the STN in electrode recordings along the trajectory to the STN is shown. Following these results, the following measures for robot-assisted brain mapping are proposed:

- Median (med)
  The median is defined as the value of the probability distribution where at most half of the distribution have values less than the median and at most half have values greater than the median.

- Root Mean Square (RMS) value
  The RMS of a signal $x(n)$ is defined as

$$RMS = \sqrt{(\frac{1}{K}\sum_{n=0}^{N} x(n)^2)} \tag{6.8}$$

where n denotes a discrete time step.

- Entropy (ENT)
  The entropy of a stochastic signal is defined by

$$H = -\sum_{j=1}^{m} h_j log(h_j) \tag{6.9}$$

  where $h_j = a_{x_j}/N$ is the relative frequency of an event a_{x_j} with $\sum_{j=0}^{N-1} a_{x_j} = N$. In this work, the measured voltage amplitudes were binned into $N = 100$ categories.

- Power spectral density (PSD)
  The PSD $S_{xx}(\omega)$ expresses the frequency content of a stochastic process. It is usually defined as the discrete fourier transform of the autocorrelation sequence

$$S_{xx}(\omega) = \sum_{m=-\infty}^{\infty} \phi_{xx}(m) exp(-j\omega m\Delta t). \tag{6.10}$$

  As computation of the PSD according to Eq. 6.10 requires an infinite set of autocorrelation coefficients and practically only N signal samples exist, estimators for the PSD have been developed. Among these estimators is the periodogram, which estimates the PSD by using a rectangular window (see [164] for details). Improvement of the PSD estimation have led to the Welch periodogram. This estimator uses triangular windows with a 50% overlap and is used here. The PSD itself is a function of the frequency ω and not a scalar value. In the style of [165], a scalar value P_{2500} will be introduced which adds the values of the PSD within an interval of 800 Hz[2] to 2500 Hz, thus providing a scalar value.

Position resolved microelectrode recordings

Spatial details of the trajectories for microelectrode recordings are summarized in Table 6.9. Note that the trajectories `Th3` and `Th2` are obtained in the same animal but on the laterally mirrored trajectory. The chosen reference position was not the scull surface as mentioned in the Swanson atlas but rather the surface of the brain itself, as the brain surface was located approximately 100 μm beneath the computed position in a likely result of brain shift. Using the brain surface as positional reference is a widely used practice in rat experiments. Contact of the electrode with the brain surface was clearly detected via the audio output of the signal amplifier and may also be done automatically by analyzing

[2]Lower bound of the low-pass filter used in the animal experiments.

Table 6.9: Trajectory specifications for electrophysiological recordings by electrode insertion into the rat brain in vivo.

Name	Animal	Animal weight	AP position (mm)	Lateral position (mm)	Coronal approach angle (deg)
Th3	1	280g	3.96	-2.97	0
Th2	1	280g	3.96	2.97	0
Th1	2	380g	-3.96	2.97	0
We2	3	290g	-3.96	2.97	0

the characteristic change in signal amplitude. Different step sizes between 0.2 mm and 0.4 mm were chosen. Shortly after electrode movement stopped, recording was started. After approximately 10 seconds, the power supply of the SASSU was switched off and, additionally, unplugged. This was done in order to analyze the effects of the motor power supply on the electrode recordings, which will be discussed later in this work. Recordings were then continued for another 120 seconds. Fig. 6.8 shows the results of trajectory Th3 plotted on an anatomic coronal atlas slice taken from the Swanson atlas. Dark dots indicate the positions of recording. On the right hand side, a 5 second interval of selected recordings after the power supply was switched off is shown. Although much more data will have to be gathered in order to form a full electrophysiological rat brain atlas, it is clear that a number of different firing patterns can be seen as the probe is inserted deeper into the brain, allowing for automatic analysis and discrimination of the respective brain region. For each of the wavetrains recorded at the respective depths, statistical analysis measures were computed as discussed in section 6.2.2. Fig. 6.9 shows the three probe trajectories Th3, Th2 (one animal), and We2 (different animal) for each statistical measure. In addition, anatomical structures identified from the respective coronal slice in the Swanson atlas are denoted by an abbreviation (for details see [94]). In order to quantitatively analyze the similarity between the depth-resolved measures for all trajectories, the mutual correlation coefficients were calculated. Table 6.10 shows these coefficients.

Evaluating the statistical measures allows to characterize a spatial position in the brain with multiple features. For the current work, this would result in a four dimensional characterization of a intracranial position. An exemplary visualization of such an multi-dimensional representation is proposed in Fig. 6.10 where the respective statistical measures are represented by size and color-encoded circles.

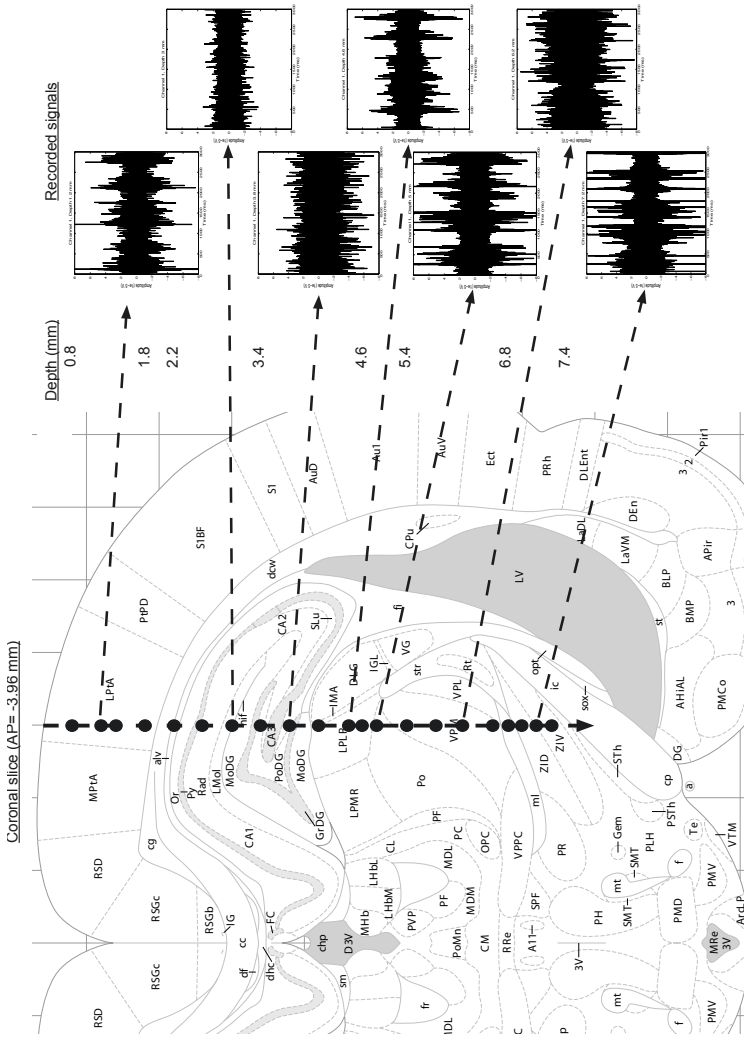

Figure 6.8: Depth-resolved microelectrode recordings. On the left side, the trajectory of the electrode through a coronal section of the rat brain is shown. Recording points are indicated as black dots. The right side shows a 3 second interval of the respective microelectrode recordings, as could be done for an electrophysiological rodent brain atlas.

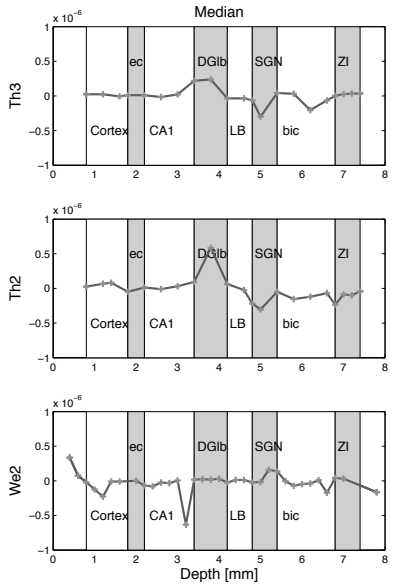

(a) Depth-resolved median for different trajectories. (top) trajectory `Th3` (middle) trajectory `Th2` (bottom) trajectory `We2`.

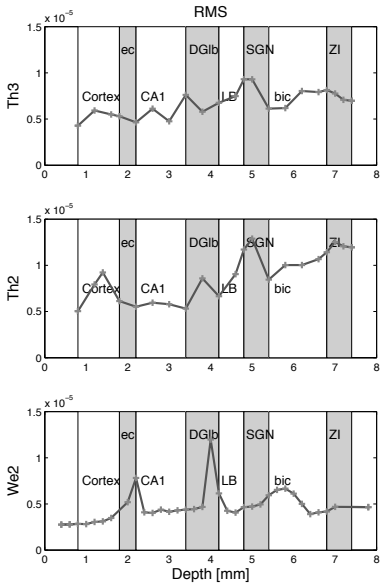

(b) Depth-resolved RMS for different trajectories. (top) trajectory `Th3` (middle) trajectory `Th2` (bottom) trajectory `We2`.

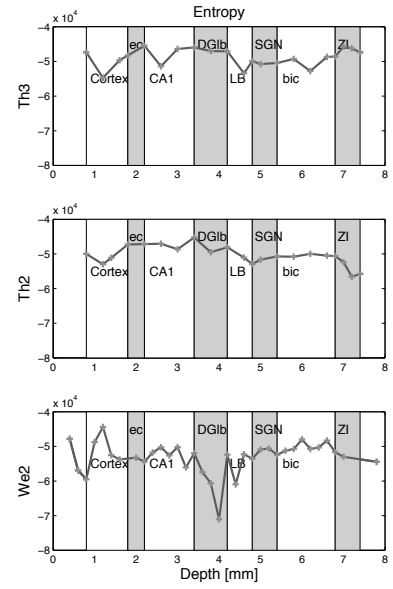

(c) Depth-resolved entropy for different trajectories. (top) trajectory `Th3` (middle) trajectory `Th2` (bottom) trajectory `We2`.

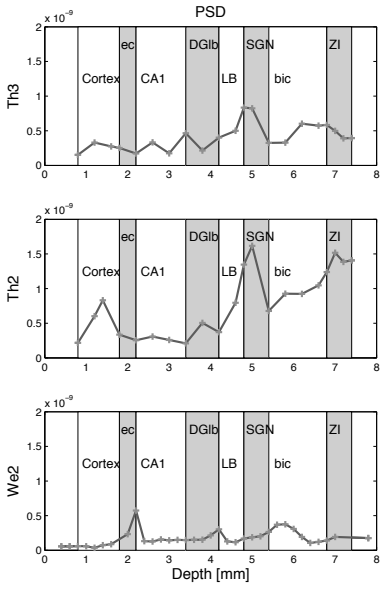

(d) Depth-resolved PSD for different trajectories: (top) trajectory `Th3` (middle) trajectory `Th2` (bottom) trajectory `We2`.

Figure 6.9: Statistical measures for electrode recordings along different trajectories in the rat brain. Abbreviations denote different structures and are taken from a the respective coronal slice of the Swanson atlas.

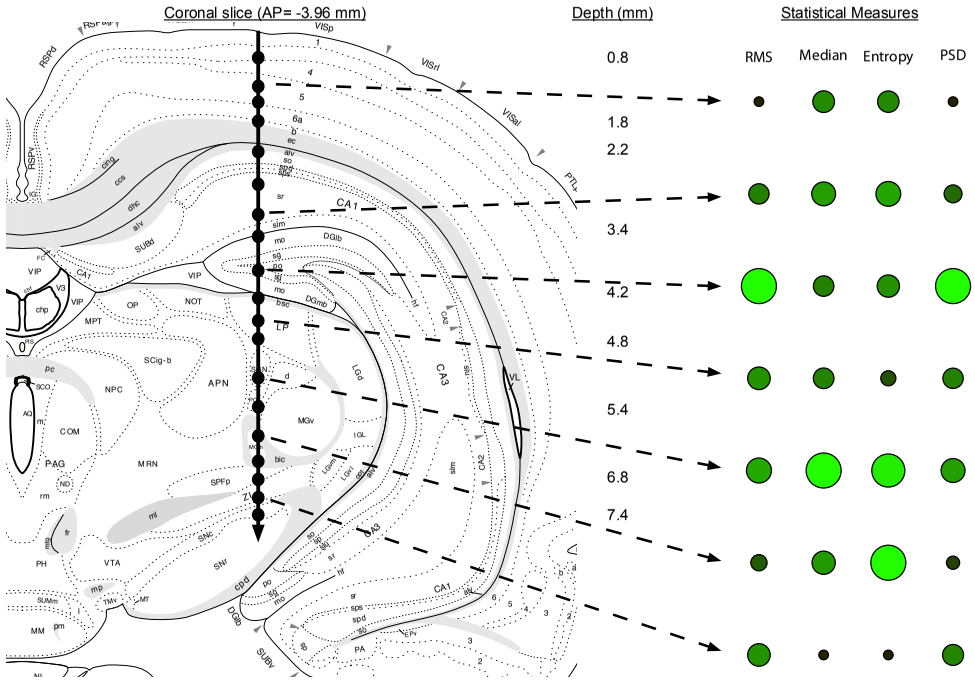

Figure 6.10: Alternative visualization of depth-resolved microelectrode recordings. On the left side, the trajectory of the electrode through a coronal section of the rat brain is shown. Recording points are indicated as black dots. The right side shows four statistical measures which are encoded by size and color. High numerical values are represented by a larger circle and in light green while low numerical values are represented by smaller circles and darker green.

Table 6.10: Correlation coefficients for the median, the RMS, the entropy, and the power spectral density of neural activity recorded along three independent trajectories in the rat brain.

	Channel 1															
	Median				RMS				ENT				PSD			
	We2	Th1	Th2	Th3	We2	Th1	Th2	Th3	We2	Th1	Th2	Th3	We2	Th1	Th2	Th3
We2	1.000	-0.034	-0.636	-0.381	1.000	0.731	0.658	0.769	1.000	-0.002	0.688	0.371	1.000	0.342	0.467	0.514
Th1	-0.034	1.000	0.309	0.145	0.731	1.000	0.651	0.847	-0.002	1.000	-0.482	-0.461	0.342	1.000	0.711	0.825
Th2	-0.636	0.309	1.000	0.740	0.658	0.651	1.000	0.837	0.688	-0.482	1.000	0.632	0.467	0.711	1.000	0.885
Th3	-0.381	0.145	0.740	1.000	0.769	0.847	0.837	1.000	0.371	-0.461	0.632	1.000	0.514	0.825	0.885	1.000

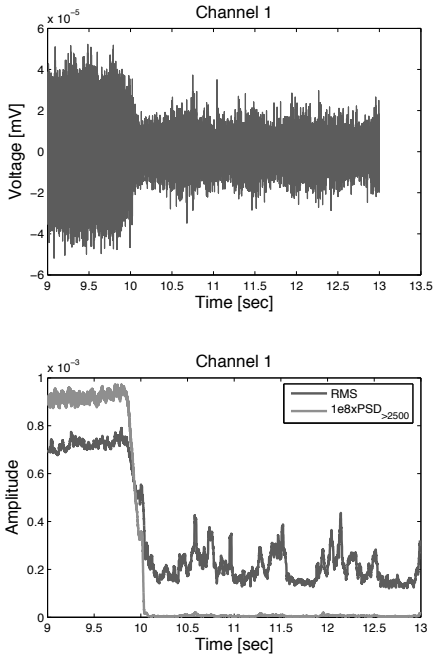

Figure 6.11: Recorded voltage train during the power supply switch off. (top) Voltage train (bottom) Running RMS and PSD values.

Effect of actuators on microelectrode recordings

To analyze the effect of the actuators (e.g. the electrical noise) on the microelectrode recordings, recordings were made during the turning off procedure. Exemplary results are shown in Fig. 6.11. The moment of switch off is clearly identifiable. To show the ability of automated detection of the switch off state for later data analysis, two measures are calculated within a running window of 500 data points: (a) the RMS value and (b) the $PSD_{>2500}$, which sums the contribution of all frequencies over 2500 Hz in the windowed signal. The measures show that a significant drop in the RMS and $PSD_{>2500}$ indicate the power switch off. These results lead to the conclusion that the power supply of the stepper motors has to be switched off during the recordings. Otherwise, strongly corrupting background noise is introduced.

6.3 OCT-based brain exploration

The second part of the results chapter addresses the evaluation of the OCT-based brain imaging. It includes a description of the methods used for the single fibre imaging as

well as the corresponding results. Furthermore, this section comprises results for the proposed OCT image processing methods introduced in section 5.3. First, the results of the automated segmentation of structures in OCT B-scan images are provided and second, results for the anisotropic propagation-separation are summarized.

6.3.1 OCT-based identification of white matter

Simulated OCT signals

Performance evaluation of white matter identification and the following segmentation approaches is achieved through the simulation of white matter fibres in artificial A- and B-Scans. Hereby, an artificial B-scan is composed of a fixed number of artificial A-scans, which are generated according to the intensity model shown in Eq. 5.17. Two tissue structures, namely white and gray brain matter, are incorporated by using different attenuation coefficients μ_{WM} and μ_{GM}, respectively. Generally, the basic decay with increasing depth is assumed to be governed by gray matter attenuation. At random depth locations, white matter areas are introduced by two means:

1. Intensity increase and
2. change of the attenuation coefficient $\mu_{\mathrm{GM}} \rightarrow \mu_{\mathrm{WM}}$.

The intensity increase at a white matter location is given by the peak contrast ratio (PCR), which is defined as:

Definition 7 *Let g denote a gray-valued image. Let $p_{q_{z-1}}$ and p_{q_z} denote neighboring pixels in one column and let $p_{q_{z-1}}$ be an element of a gray matter area and p_{q_z} be an element of white matter area. Then,*

$$PCR = \frac{g(p_{q_z})}{g(p_{q_{z-1}})} \tag{6.11}$$

is defined as the peak contrast ratio (PCR) of white and gray matter areas.

The size of the white matter region can also be chosen randomly. After generating the ideal intensity course, signals were contaminated with artificial multiplicative noise under the model of

$$g = fu,$$

where $u(n)$ is a stationary noise process which has mean 1 and variance σ_u^2. This follows common speckle modeling as presented in section 5.2.1.

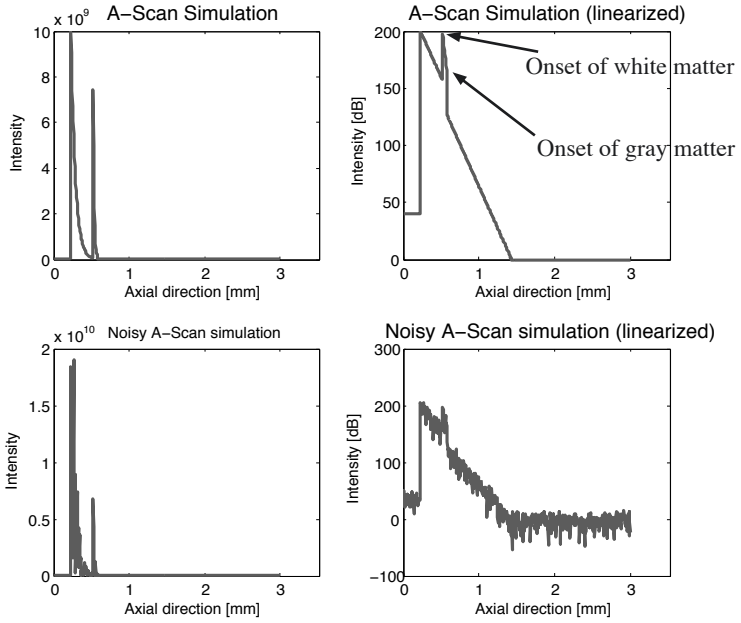

Figure 6.12: Simulated OCT A-scan with one embedded white matter area: [upper left] Uncorrupted A-scan data [upper right] Linearized uncorrupted A-scan data with arrows showing the embedded white matter region [lower left] Corrupted A-scan data [lower right] Linearized corrupted A-scan data.

Fig. 6.12 visualizes the concept. To simulate an OCT B-scan, multiple A-scans were combined. For simulating white fibre identification, a fixed number of white matter fibres was added to each image. Size and location of the fibres were randomly chosen. This way, the simulation reproduced an approximate behavior of the presence of white matter fibres in brain tissue. In Fig. 6.13(b), the artificial B-Scan and the embedded fibres are shown.

White matter detection results

The white matter detection algorithm presented in section 5.2.3 was evaluated in order to find the optimal set of parameters σ_1, σ_2, and σ_3 for different PCR of structures in the image. Therefore, artificial B-scans as described in section 6.3.1 were created and white matter detection performance was evaluated for different parameters σ_1, σ_2, and σ_3. Performance evaluation is based on two measures:

1. Percentage of detected white matter structures which is given by the sensitivity of the seed detection process. It indicates how many structures (not pixels) are identified by at least one seed and will therefore enter the region growing process.

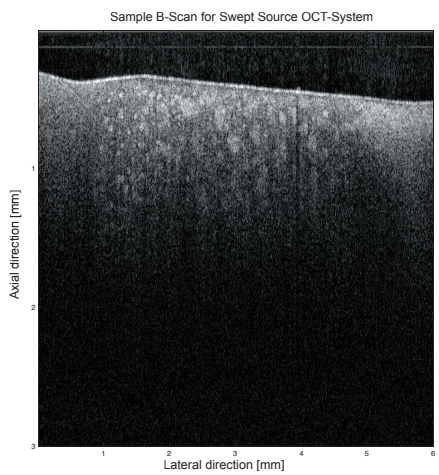

(a) OCT B-scan of a coronal section of the rat brain. The figure shows white fibres embedded into gray brain matter.

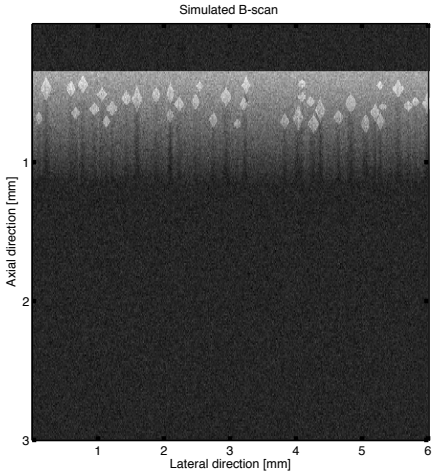

(b) Simulated OCT B-scan of a coronal section of the rat brain. The figure shows simulated white fibres embedded into gray brain matter.

Figure 6.13: Simulation of OCT B-scan images of a coronal section of the rat brain with embedded white fibres.

2. Number of false positive detected white matter pixels which is given by the percentage of false positive seeds against the total number of detected seeds.

Evaluation of the parameters was performed on the averaged results of $n = 100$ artificial B-scans each consisting of $400\times$ 512 pixels. Results are presented in terms of a modified receiver operating curve (ROC curve) [166]. The modified ROC curve plots the percentage of detected white matter structures (equivalent to the sensitivity) against the false positive rate of the white matter detection. Fig. 6.14 shows the ROC curves for different PCR and parameter settings σ_1, σ_2, and σ_3. The following effects of the parameter choice on the seed detection performance can be deduced:

1. Looking e.g. at the second column of Fig. 6.14 shows that for a constant PCR (e.g. PCR = 25), the choice of $\sigma_2 = 1.25$ outperforms other parameter settings in terms of the false positive and the percentage of detected structures.

2. The results of row 3 of Fig. 6.14 indicate that a choice of $\sigma_1 = 40$ (Fig. 6.14(i)) yields the best results. This parameter choice is supported for other PCR scenarios as well (see Fig. 6.14(g) and Fig. 6.14(h)).

3. The choice of σ_3 can be seen as a trade-off between the percentage of detected structure and the false-positive rate. A choice of $\sigma_3 = 0.5$ yields a better sensitivity

for white matter structure detection but a higher false-positive rate. The higher σ_3, the lower the sensitivity and the false positive detected white matter pixels. This leads to a choice of $\sigma_3 = [0.5 \ldots 0.7]$.

Based on the findings, the following parameters are chosen to obtain numerical results of the white matter detection: σ_1 is chosen to be $\sigma_1 = 40$. The parameters σ_2 and σ_3 are set to $\sigma_2 = 1.25$ and $\sigma_3 = 0.5$. Table 6.11 provides the numerical results of the white matter detection performance.

Table 6.11: Averaged white matter detection performance for varying PCR for n=100 evaluations of simulated B-scans. The parameters were chosen as $\sigma_1 = 40$, $\sigma_2 = 1.25$, and $\sigma_3 = 0.5$.

PCR	% of detected white matter structures	% of false positive detected white matter pixels
20	0.91	0.07
25	0.95	0.04
30	0.98	0.02
40	0.98	0.007
50	0.98	0.001

6.3.2 Single fibre imaging

In order to test OCT as a potential method for imaging brain tissue in a minimal-invasive setting, single fibre imaging was conducted using the GRIN lens probe design described in section 5.2.3. The system was tested in vitro on a rat brain. Results are investigated with regard to the identification of optical characteristics of brain tissue.

Material and methods

The brain of a freshly decapitated rat was removed from the skull and put in a petri dish filled with ice-cold Krebs-bicarbonate buffer. The brain was mechanically fixed by injection canulas and subsequently placed within the workspace of the SASSU (see Fig. 6.15(a)). The custom-made single fibre optical probe described in section 5.2.3 was mechanically attached to the SASSU adapter. Fig. 6.15(b) shows a magnified image of the fibre above the rat brain.

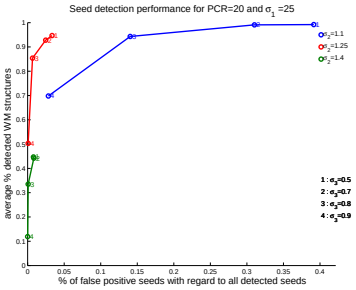

(a) Modified ROC analysis of averaged white matter detection performance for a PCR of 20 and $\sigma_1 = 25$ over $n = 100$ simulated B-scans.

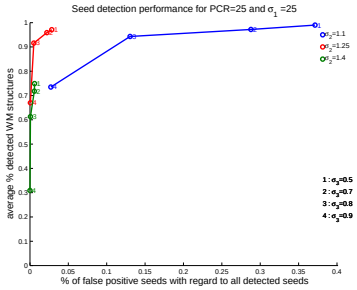

(b) Modified ROC analysis of averaged white matter detection performance for a PCR of 25 and $\sigma_1 = 25$ over $n = 100$ simulated B-scans.

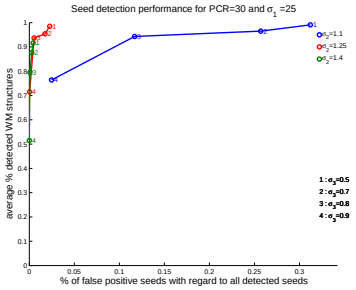

(c) Modified ROC analysis of averaged white matter detection performance for a PCR of 30 and $\sigma_1 = 25$ over $n = 100$ simulated B-scans.

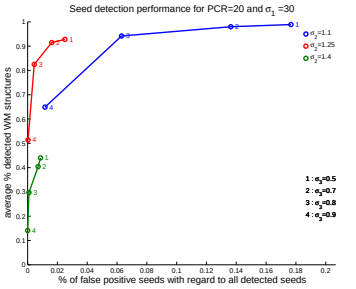

(d) Modified ROC analysis of averaged white matter detection performance for a PCR of 20 and $\sigma_1 = 30$ over $n = 100$ simulated B-scans.

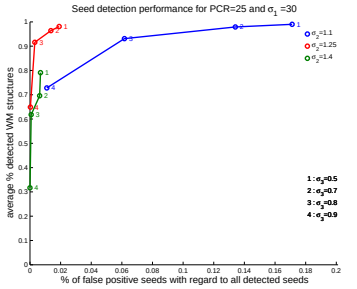

(e) Modified ROC analysis of averaged white matter detection performance for a PCR of 25 and $\sigma_1 = 30$ over $n = 100$ simulated B-scans.

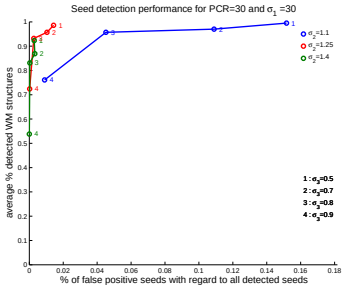

(f) Modified ROC analysis of averaged white matter detection performance for a PCR of 30 and $\sigma_1 = 30$ over $n = 100$ simulated B-scans.

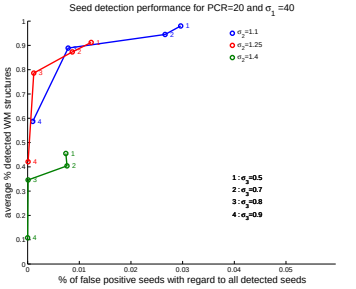

(g) Modified ROC analysis of averaged white matter detection performance for a PCR of 20 and $\sigma_1 = 40$ over $n = 100$ simulated B-scans.

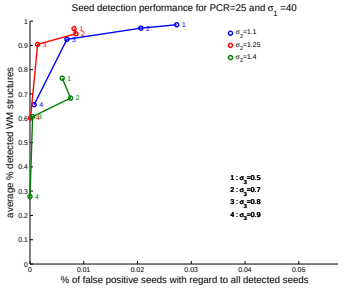

(h) Modified ROC analysis of averaged white matter detection performance for a PCR of 25 and $\sigma_1 = 40$ over $n = 100$ simulated B-scans.

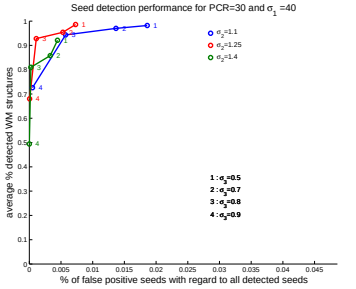

(i) Modified ROC analysis of averaged white matter detection performance for a PCR of 30 and $\sigma_1 = 40$ over $n = 100$ simulated B-scans.

Figure 6.14: Modified ROC analysis for parameters of white matter detection. In each scenario white matter detection parameter σ_2 and σ_3 are indicated.

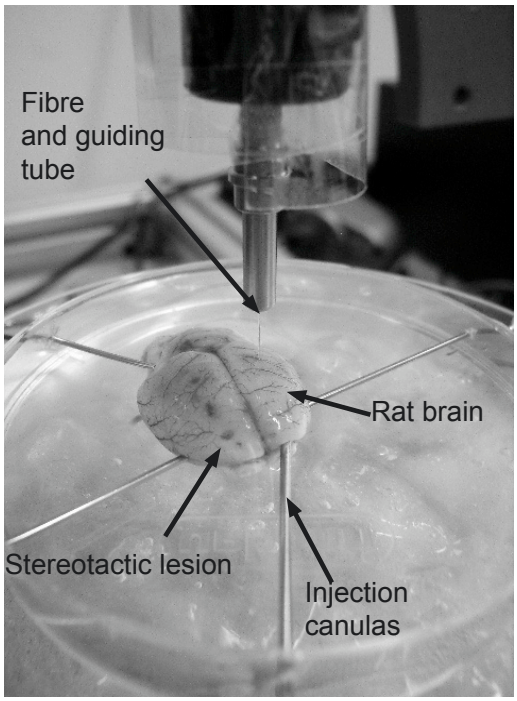

(a) Testbed setup for OCT single fibre imaging: A fresh rat brain mechanically fixed by injection canulas is placed in the workspace of the SASSU which carries the fibre.

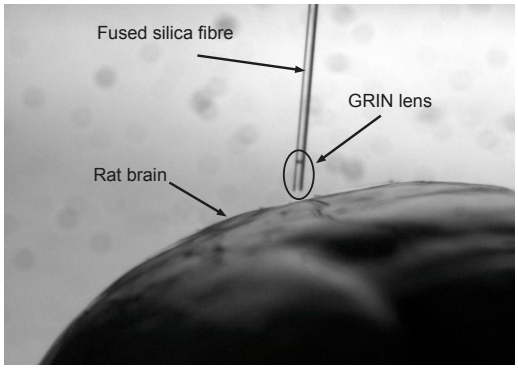

(b) Detailed image of the single fibre used for in vitro brain imaging. The image shows the brain surface, the fibre, and the custom-made GRIN lens.

Figure 6.15: Testbed setup for OCT single fibre imaging of a rat brain in vitro.

The fibre end was connected to a Callisto OCT system (Thorlabs HL GmbH, Luebeck, Germany) with a central wavelength of 840 nm and a bandwidth of 50 nm. The measuring rate of this system is 1400 A-scans per second, the scanning depth amounts to 3.4 mm and the axial resolution is 13.6 μm. Visualization of the OCT intensity signals was done using a common PC. The total testbed setup is shown in Fig. 6.16. As the brain featured a stereotactic lesion resulting from previously placed measurement probes, the skull landmark Bregma could be referenced in terms of SASSU coordinates. Using the stereotactic control software described in chapter 5, the optical probe was guided with predefined step size and velocity along three trajectories. Additionally, the probe's axial depth movement was modulated by a fast period ramp function to reduce the effect of speckle noise.

OCT A-scan analysis

To present the results of OCT-based neuroimaging, the following processing steps have been applied to the recorded OCT data. The current operating software of the OCT visualization automatically applies the logarithmic operator to the intensity signal and converts

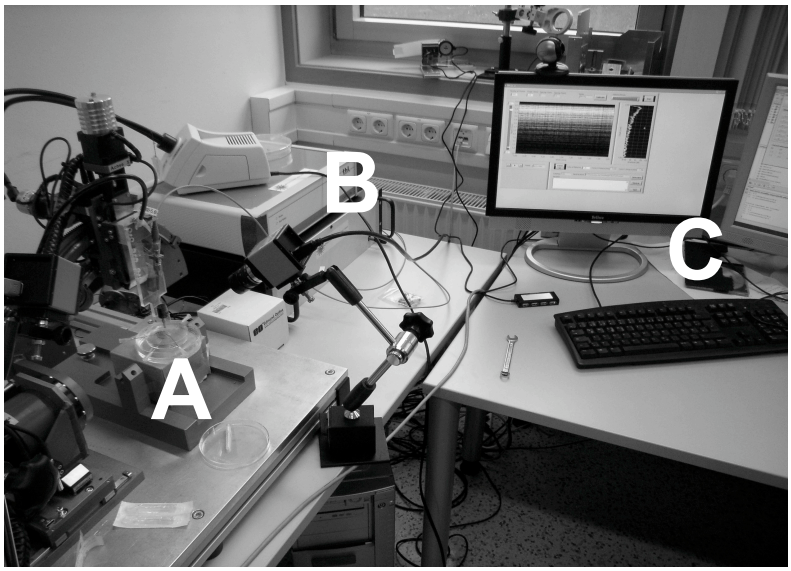

Figure 6.16: Components for single fibre imaging of brain tissue: [A] Mechanically fixed rat brain located in the workspace of the SASSU [B] OCT system [C] Visualization unit.

the resulting signal into gray values. Therefore, the current OCT acquisition system provides a linearized OCT signal as presented in section 5.2.3 is obtained. Fig. 6.17(a) shows an exemplary A-scan recorded at the depth $z = 2.8$ mm below the brain surface. It can be observed that the obtained A-scan does not show pure linear behavior which is due to multiple scattering effects at larger depths. For an axial scanning range of 1.5 mm, however, the assumption of a linear decay holds. Based on that assumption, the attenuation coefficient of all A-scans recorded at discrete depths is obtained by linear fitting on the first part of the signal. An exemplary fitting is shown in Fig. 6.17(b).

Results

Determination of the characteristic attenuation coefficient is performed for multiple measurements along 3 trajectories. Details on the trajectory location are provided in Table 6.12. Again, the depth was measured with regard to the brain surface which was clearly detected in the OCT signal. Different step sizes between 0.1 mm and 0.25 mm were chosen. After completion of the step, OCT A-scans were acquired for approximately 4 seconds. During this interval, the probe's axial depth movement was modulated by a fast period ramp function to reduce the effect of speckle noise. From the set of measured A-scans, 1400 A-scans were averaged to yield the final averaged A-scan. In the same context as presented for the electrophysiological recordings, Fig. 6.18 presents the tra-

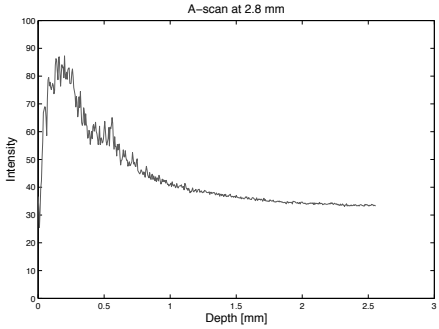

(a) OCT A-scan acquired at depth $z = 2.8$ mm from the brain surface.

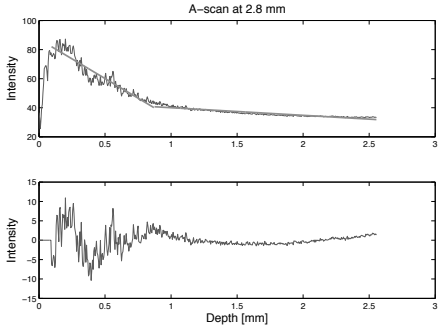

(b) Determination of the characteristic attenuation coefficient by linear fitting of the A-scan at depth $z = 2.8$ mm.

Figure 6.17: OCT A-scan signal obtained in brain tissue at depth z=2.8 mm and determination of the attenuation coefficient via linear fitting.

Table 6.12: Trajectory specifications for the OCT single fibre insertion into the rat brain.

Name	AP position (mm)	Lateral position (mm)
`traj1`	-3.84	3
`traj2`	-3.84	3.2
`traj3`	-3.84	-1

jectory plotted on an anatomical coronal slice taken from the Swanson atlas. Dark dots indicate the positions of recording. On the right hand side, the depth-resolved averaged OCT A-scan profiles are shown for one of the listed trajectories. Looking at the intensity courses, one can detect different intensity spikes modulated on the decay. Considering the intensity spikes as structure-based spikes, this would allow to locate structures in front of the fibre tip. Compared with position information of the robot, this allows deep brain structure identification and subsequent navigation. For each of the OCT signal recorded at the respective depths, the characteristic attenuation coefficient was determined by linear fitting as shown in Fig. 6.17(a). Results for the 3 trajectories listed in Table 6.12 are shown in Fig. 6.19.

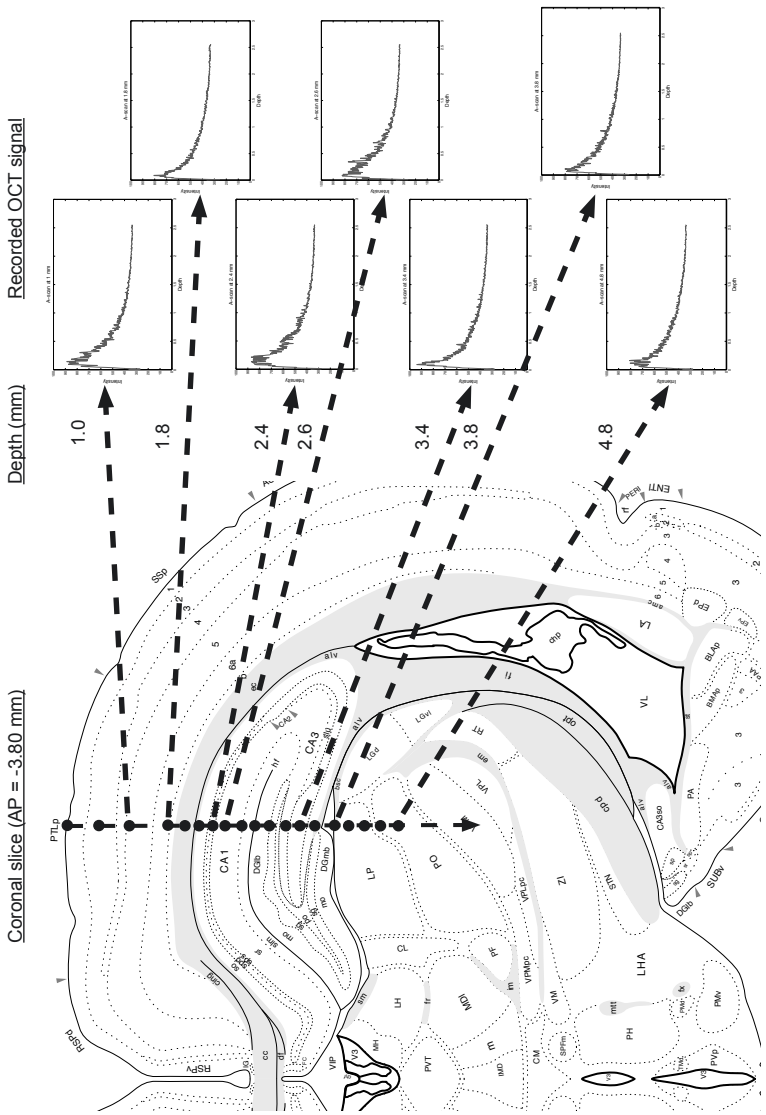

Figure 6.18: Depth-resolved OCT A-scan signals in the rat brain. On the left side, the trajectory of the fibre through a coronal section of the rat brain is shown. Recordings points are indicated as black dots. The left side shows the corresponding A-scan intensity course at the respective depth.

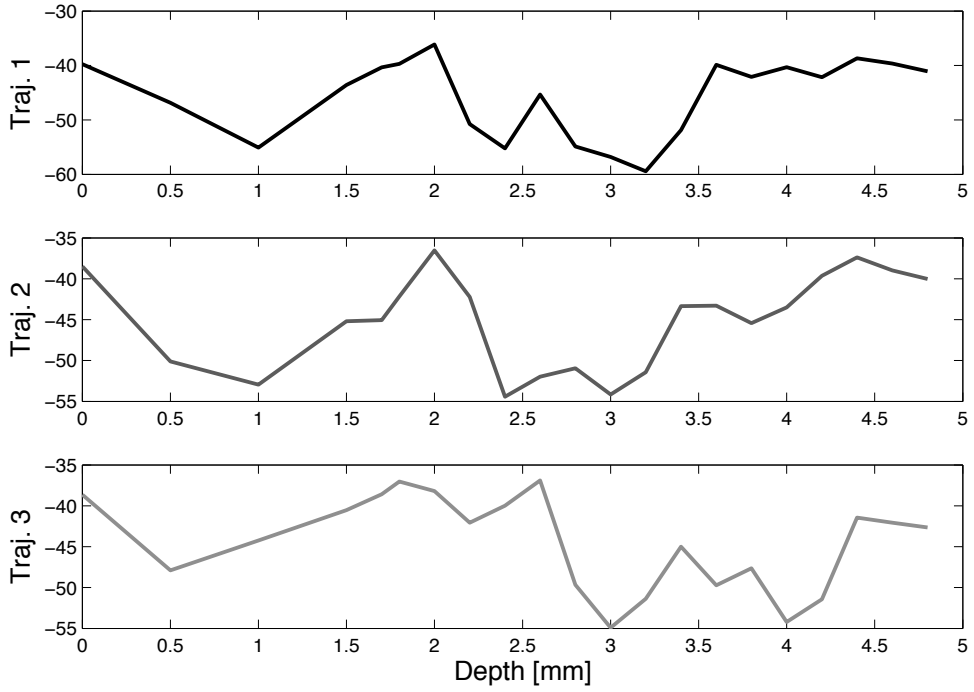

Figure 6.19: Depth-resolved determination of the attenuation coefficient by linear fitting into the OCT A-scan signals. Results are shown for the 3 trajectories provided in Table 6.12.

6.4 OCT image processing

The second part of the result chapter is dedicated to the results of the image processing methods developed in the context of OCT brain imaging. The first part of this chapter adresses the model-based region growing process proposed in section 5.3.2. The second part of this chapter presents the results obtained for the anisotropic propagation-separation approach presented in section 5.3.3.

6.4.1 Model-based region growing

Seed detection

A fundamental part of the model-based region growing approach is the automated location of seeds for the subsequent region growing. As stated in section 5.3.2, seed detection for white matter segmentation is based on the white matter identification process described in

Table 6.13: Overview of segmentation approaches used to obtain results.

Name	Description
ARG	Adaptive Region Growing
PM-FRG	Filtered Region Growing with Perona-Malik filter [132]
CD-FRG	Filtered Region Growing with complex diffusion filter [134]

section 5.2.3. Hence, the results presented in section 6.3.1 analogously reflect the quality of seed detection.

Segmentation performance measures

The performance measures for both region growing approaches (ARG, FRG) were chosen as:

1. The Jaccard (JC) index [167] which is given as

$$JC := \frac{|X \cap Y|}{|X \cup Y|} \tag{6.12}$$

   where X is the set of pixels segmented as class c in one image, Y is the set pixels of the same class in the other (reference) image, and $|\ldots|$ stands for the number of elements. This similarity measure is equal to 1 if X and Y are the same region and zero if they are disjoint regions.

2. The Hausdorff distance (HD) [168] which defines the largest difference between two contours and is a well accepted measure for leakage.

3. Time with all results being obtained on a PC with 2.4 GHz processing unit and 2 GB of RAM.

Simulation results

Automated white matter detection was evaluated on $n = 100$ test images with 400×512 pixels. Twenty white matter regions with random location and random size were simulated in the test images. The images were subsequently corrupted by speckle noise following an exponential PDF as shown in Eq. 5.20. The standard deviation of the noise was chosen to be $\sigma_u = 1$. Different PCRs were analyzed. The filtering approaches listed in Table 6.13 were compared. Segmentation results of both, ARG and FRG approaches

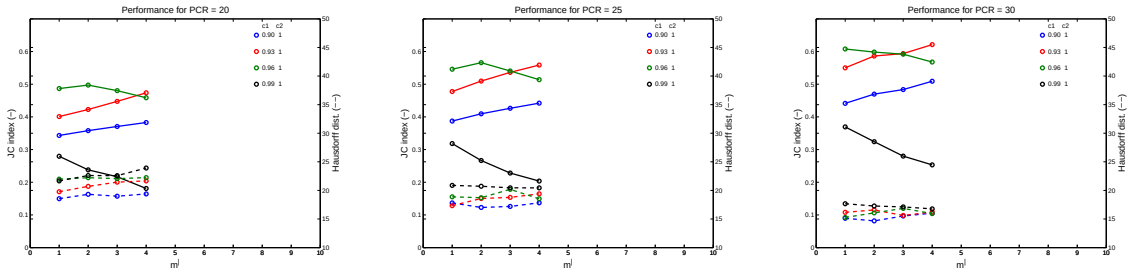

(a) ARG JC index and HD for different filter parameters m' and c_1 and PCR=20.

(b) ARG JC index and HD for different filter parameters m' and c_1 and PCR=25.

(c) ARG JC index and HD for different filter parameters m' and c_1 and PCR=30.

Figure 6.20: ARG JC index and HD for different filter parameters m' and c_1 and different PCR.

with edge-sensitive filtering, are dependent on certain parameters. To derive an adequate choice of parameters, different parameter settings were analyzed with respect to the Jaccard index and the Hausdorff distance.

1. ARG parameters

   In the ARG scenario, the parameters to be varied are the attenuation coefficient m' and the confidence interval shift parameters c_1 and c_2. In Fig. 6.20, the JC index and HD is shown for different PCRs and parameter sets. The following observations can be made: generally, the higher the JC index, the higher the HD which requires the user to find a trade-off between segmentation quality and leakage. For all PCR scenarios, the following effect of the confidence shift parameter can be observed: a low shift parameter (e.g. $c_1 = 0.90$) leads to a small JC index and a low HD. A high shift parameter (e.g. $c_1 = 0.99$) also leads to a small JC index but a higher HD. The optimum value of the shift parameter is therefore in the range $c_1 = 0.93 \ldots 0.97$. Evaluating two other measures namely (a) the ratio of correctly identified white matter pixels over the number of existing white matter pixels r_1 and (b) the ratio of falsely identified white matter pixels over the number of existing white matter pixels r_2 give a possible explanation. These measures show that an increasing parameter c_1 leads to decreasing ratios r_1 and r_2. This indicates that a lower interval shift parameter imposes less constraints on the growing process and therefore identifies more structures of interest but results into a higher false positive rate. For a high interval shift parameter $c_1 = 0.99$, the ARG identifies only a small subpart of the white matter structures which leads to the low JC index. Interestingly, the HD is still high. This is due to the fact that the largest difference between the two

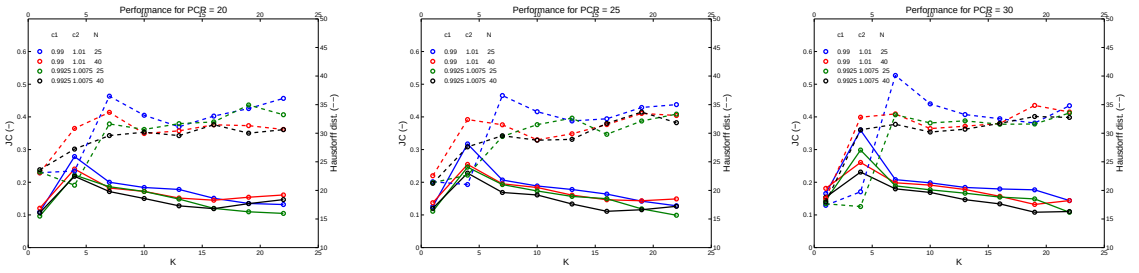

(a) PM-FRG JC index and HD for different filter parameters N, K and c_1 and PCR=20.

(b) PM-FRG JC index and HD for different filter parameters N, K and c_1 and PCR=25.

(c) PM-FRG JC index and HD for different filter parameters N, K and c_1 and PCR=30.

Figure 6.21: PM-FRG JC index and HD for different filter parameters N, K and c_1 and different PCR.

contours is not due to leakage but due to the difference of the true contour to the much stricter edges of the segmented version. Extensive simulations have shown that the parameter c_2 does not influence the results in the white matter detection scenario significantly. This is due to the fact that seeds are already located in high intensity areas. Leakage mostly occurs if the lower bound of the confidence interval is chosen too low which leads ot the integration of neighboring gray matter.
The attenuation coefficient m' is actually a characteristic property of distinct tissue structures. The exact numerical value, however, is not necessarily known before the segmentation. Therefore, the choice of different m' has been examined. According to Fig. 6.20, an increasing attenuation coefficient m', which influences the growing process (see Eq. 5.29), leads to an increase of the JC index and the HD. A good trade-off between JC index and HD is therefore achieved if $c_1 = 0.93$, $c_2 = 1$, and $m' = 4$.

2. FRG
   For the FRG parameters, the two scenarios PM-FRG and CD-FRG have been evaluated. In both cases, the following parameters can be varied: the edge threshold parameter K, the number of iterations N, and, as for the ARG case, the choice of confidence interval shift parameters c_1 and c_2 (see Eq. 5.34). The results for the PM-FRG scenario are shown in Fig. 6.21 for different PCRs. The following observations can be made: with increasing number of iterations, the JC index increases and the HD decreases. For decreasing values of the confidence interval shift parameter c_1, the same observation holds. With increasing edge threshold parameter K,

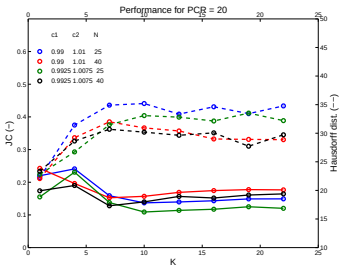

(a) CD-FRG JC index and HD for different filter parameters N, K and c_1 and PCR=20.

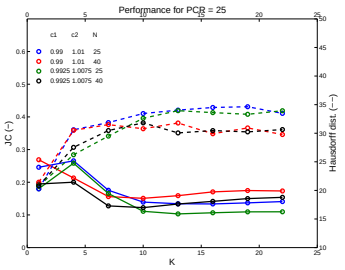

(b) CD-FRG JC index and HD for different filter parameters N, K and c_1 and PCR=25.

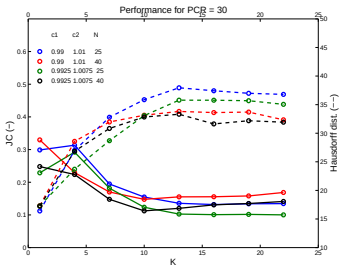

(c) CD-FRG JC index and HD for different filter parameters N, K and c_1 and PCR=30.

Figure 6.22: CD-FRG JC index and HD for different filter parameters N, K, c_1 and different PCR.

the HD increases almost linearily while the JC index features a local optimum at threshold parameters $K = 4 \ldots 10$. For $K = 11 \ldots 20$, the JC index decreases. The performance of the CD-FRG (see Fig. 6.22) almost features the same characteristics although at PCR=20, the local optimum of the JC index is not distinct. A good trade-off between JC index and HD is therefore achieved for low values of K e.g. $K = 3 \ldots 5$. The number of iterations and the confidence interval parameter c_1 should be chosen according the desired leakage performance.

The major difference between the ARG and the FRG approaches can already be observed. For all parameter settings, the FRG approaches perform worse in term of the JC index and the HD distance. For an equal HD performance, the JC index of the FRG approaches is much lower than for the ARG approach and there is no parameter choice for the FRG approaches which would provide the same performance. For the following comparison of both, ARG and FRG, the parameters N, K, and c_1 were chosen as $N = 40$, $K = 4$, and $c_1 = 0.99$ and $c_2 = 1.01$.

In order to further elaborate the different characteristics of ARG and FRG approaches, Table 6.14 shows averaged quantitative results for $n = 100$ simulated B-scans at a PCR of 20. Fig. 6.23 visualizes the performance for different contrast ratios based on an evaluation of $n = 100$ simulated B-scans. Fig. 6.24 shows an exemplary segmentation result for a PCR of 20. In all cases, the parameters were chosen as dicussed above.

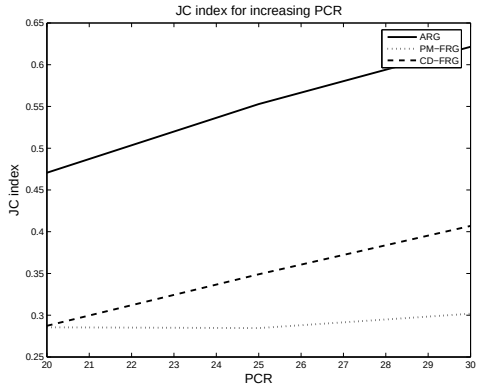

(a) JC index of white matter detection in simulated B-scans for different speckle noise levels for Adaptive Neighborhood Region Growing and Filtered Image Region Growing for different PCR.

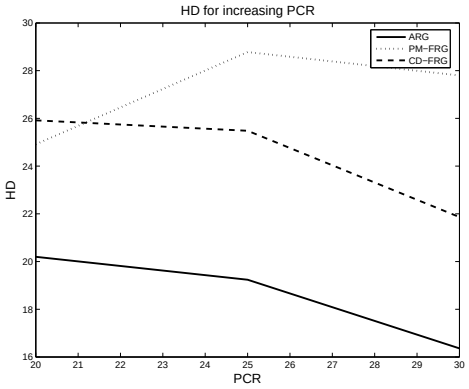

(b) HD of white matter detection in simulated B-scans for different speckle noise levels for Adaptive Neighborhood Region Growing and Filtered Image Region Growing for different PCR.

Figure 6.23: Averaged JC index and averaged HD of white matter segmentation for different PCR in simulated OCT B-scans.

Table 6.14: Averaged results for region growing approaches for $n = 100$ simulated B-scans. Shown are the mean, maximal and minimal JC index, HD and time consumption for a contrast ratio of PCR= 20 of the simulated B-scans. Parameters of the respective filters were chosen as given in the text.

	JC index			HD			Time (sec)		
	Mean	Maximum	Minimum	Mean	Maximum	Minimum	Mean	Maximum	Minimum
ARG	0.4887	0.5442	0.4168	19.05	31.95	13.60	1.57	2.15	0.93
PM-FRG	0.2869	0.3486	0.2273	22.30	36.72	12.73	0.53	0.75	0.41
CD-FRG	0.3025	0.4549	0.1925	25.91	47.38	13.60	0.89	1.15	0.75

Real results

To show the performance of the 3 approaches listed in Table 6.13 for the segmentation of real OCT images of biological tissue, two image types with different segmentation criteria were tested:

1. Segmentation of highly scattering structures such as white matter
   Possible applications of white matter segmentation include the integration of OCT into neurosurgical settings, e.g. into an operating microscope. This would provide the surgeon with detailed tissue information during the operation which would benefit especially within delicate surgeries. Two test images were acquired from the

brain of a freshly decapitated rat. The brain was dissected and scanned along a coronal section crossing the cortex, the external capsule and the striatum.

2. Segmentation of low scattering structures such as blood vessels
   Here, the seed detection and the region growing is performed on the inverted gray-scale image. Thus, dark areas of low scattering structures (e.g. vessel) are assigned a high intensity while areas of high scattering (e.g. tissue) are featuring low intensities. Thus, the seed detection and the region growing algorithms can be applied as described.

Table 6.17 gives the details of all tested segmentation scenarios. For the evaluation of the segmentation performance for real images, a manual segmentation was performed by an OCT expert with 10 years of experience in OCT imaging. Visual results are presented in Figs. 6.25, 6.26, 6.27, 6.28, 6.29, and 6.30. Numerical results provide sensitivity and FPR with regard to the manual segmentation results and are listed in Tables 6.15 and 6.16.

Table 6.15: Results of ARG, PM-FRG, and CD-FRG for segmentation of highly scattering tissue with regard to expert manual segmentation.

Scenario	JC index			HD			Time (sec)		
	ARG	PM-FRG	CD-FRG	ARG	PM-FRG	CD-FRG	ARG	PM-FRG	CD-FRG
wm1	0.3347	0.3232	0.3316	44.55	63.28	44.55	1.7	0.9	2.8
wm2	0.2371	0.077	0.1446	61.07	59.21	63.02	2.2	1.6	3.3
onion	0.3013	0.2564	0.2687	129.71	139.17	112.29	2.4	1.4	2.8

Table 6.16: Results of ARG, PM-FRG, and CD-FRG for segmentation of low scattering tissue with regard to expert manual segmentation.

Scenario	JC index			HD			Time (sec)		
	ARG	PM-FRG	CD-FRG	ARG	PM-FRG	CD-FRG	ARG	PM-FRG	CD-FRG
urothel	0.2101	0.1352	0.0974	54.64	59.07	59.07	0.3	0.7	0.26
intestine	0.3139	0.3018	0.1250	39.05	37.64	38.47	0.4	1.3	1.0
egg	0.6443	0.4330	0.3610	52.08	56.23	56.24	4.3	2.7	2.3

Table 6.17: Details on the real OCT imaging scenarios.

Scenario	Region of interest	Figure	Imaging system
wm1	white matter fibres in coronal rat brain section	Fig. 6.25	Swept Source Microscope System (Thorlabs, Inc., Newton, USA)
wm2	white matter fibres in coronal rat brain section	Fig. 6.26	Spectral radar OCT imaging system (Thorlabs HL GmbH, Luebeck, Germany), center wavelength of 930 nm
onion	onion cell walls	Fig. 6.27	Spectral radar OCT imaging system (Thorlabs HL GmbH, Luebeck, Germany) center wavelength of 830 nm
urothel	vessels embedded into urothel	Fig. 6.28	Time domain OCT imaging system (4optics Gmbh, Heidelberg, Germany), center wavelength of 1310 nm
intestine	vessels embedded into intestine wall	Fig. 6.29	Spectral radar OCT imaging system (Thorlabs HL GmbH, Luebeck, Germany), center wavelength of 830 nm
egg	vessel embedded inner skin of egg	Fig. 6.30	Spectral radar OCT imaging system (Thorlabs HL GmbH, Luebeck, Germany), center wavelength of 940 nm

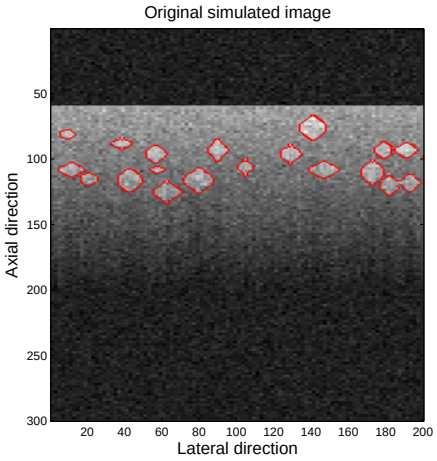

(a) Exemplary simulated OCT B-scan showing white matter structures with ideal segmentation results (PCR=20).

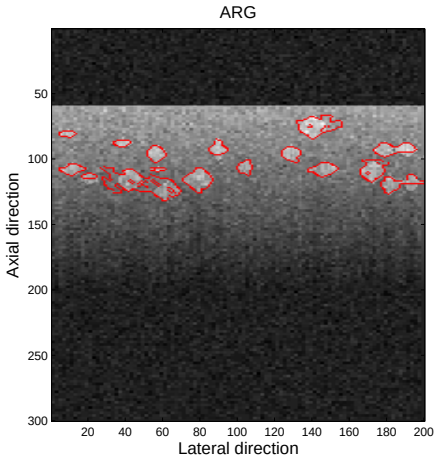

(b) Segmentation of simulated white matter fibres by adaptive neighborhood region growing (PCR=20).

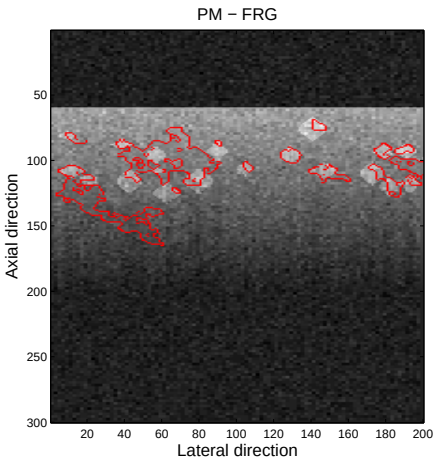

(c) Segmentation of simulated white matter fibres by PM-filtered image region growing (PCR=20).

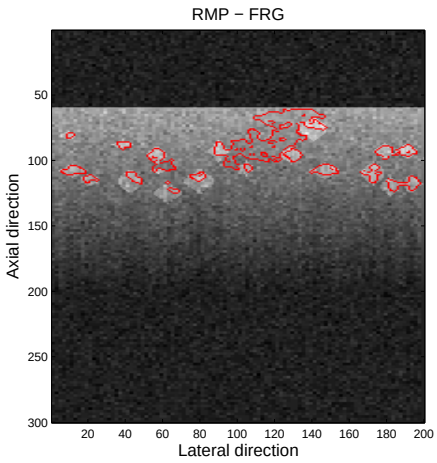

(d) Segmentation of simulated white matter fibres by CD-filtered image region growing (PCR=20).

Figure 6.24: Comparison of 3 region growing approaches for segmentation of a white matter fibres in simulated B-scans of brain matter (PCR=20).

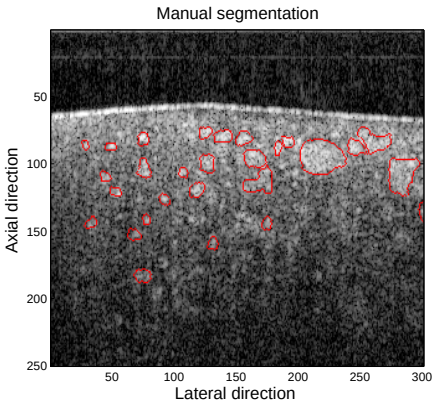

(a) Scenario wm1: OCT B-scan showing brain matter with embedded white matter fibres.

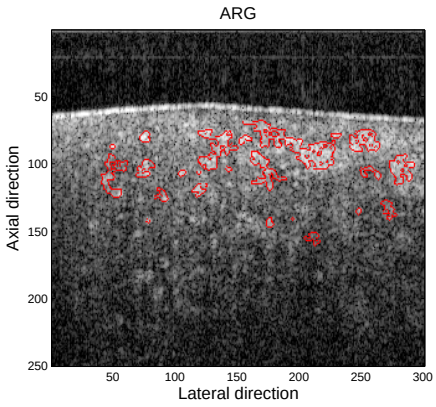

(b) Scenario wm1: Fibre segmentation by adaptive neighborhood region growing.

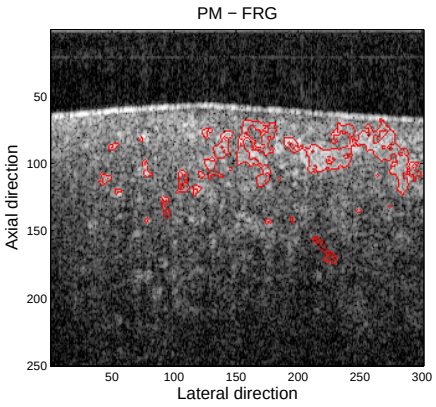

(c) Scenario wm1: Fibre segmentation by PM-filtered image region growing.

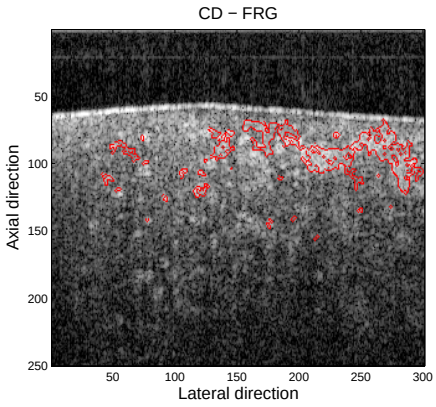

(d) Scenario wm1: Fibre segmentation by CD-filtered image region growing.

Figure 6.25: Scenario wm1: Comparison of 3 region growing approaches for segmentation of a white matter fibres brain tissue.

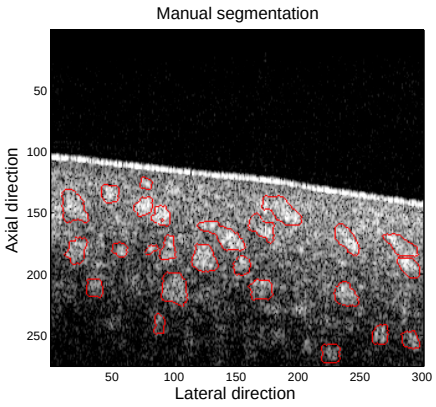

(a) Scenario wm2: OCT B-scan showing brain matter with embedded white matter fibres.

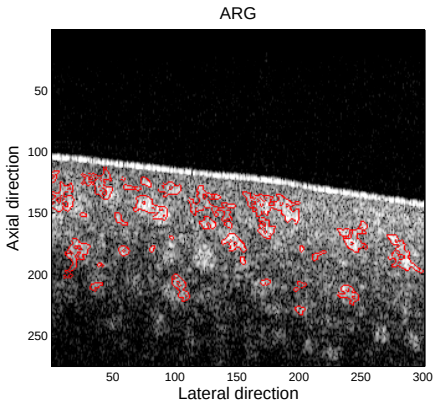

(b) Scenario wm2: Fibre segmentation by adaptive neighborhood region growing.

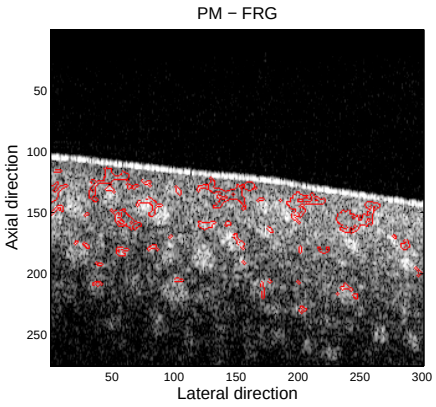

(c) Scenario wm2: Fibre segmentation by PM-filtered image region growing.

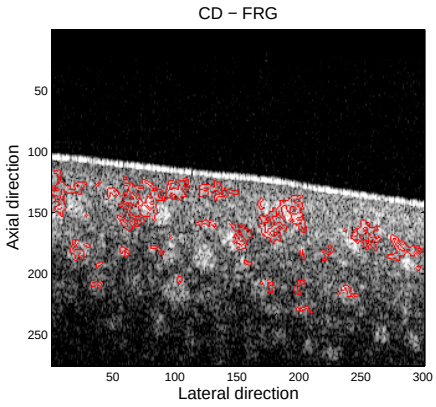

(d) Scenario wm2: Fibre segmentation by CD-filtered image region growing.

Figure 6.26: Scenario wm2: Comparison of 3 region growing approaches for segmentation of a white matter fibres in brain tissue.

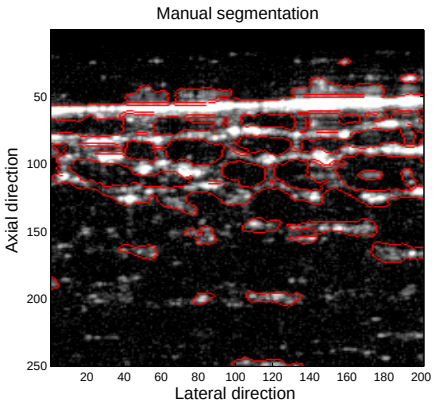

(a) Scenario onion: OCT B-scan showing cell structures of an onion.

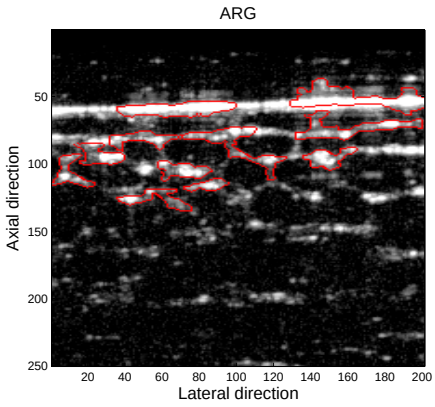

(b) Scenario onion: Fibre segmentation by adaptive neighborhood region growing.

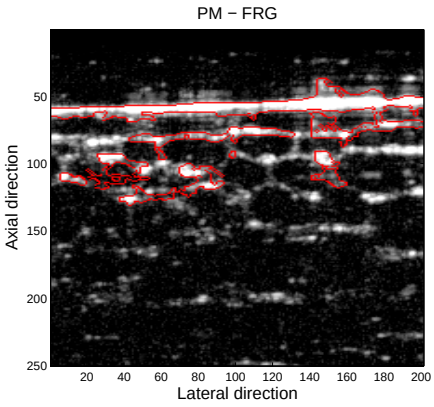

(c) Scenario onion: Fibre segmentation by PM-filtered image region growing.

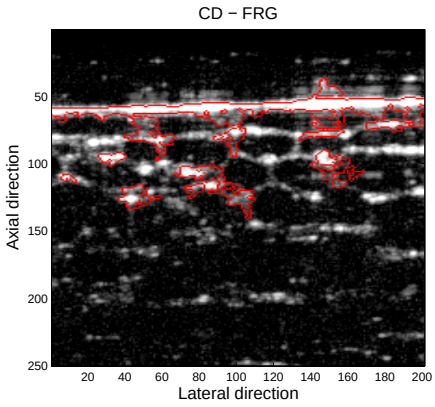

(d) Scenario onion: Fibre segmentation by CD-filtered image region growing.

Figure 6.27: Scenario onion: Comparison of 3 region growing approaches for segmentation of cell walls of onion tissue structure.

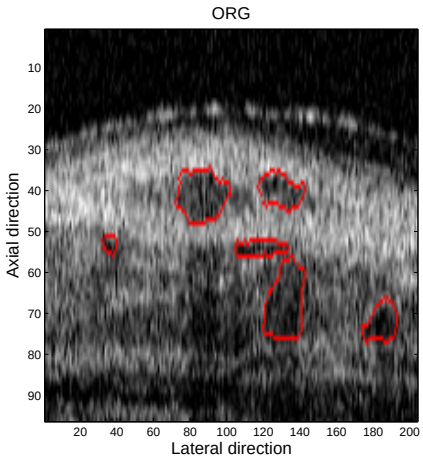

(a) Scenario urothel: OCT B-scan showing the urothel with an embedded vessel and the results of the manual segmentation.

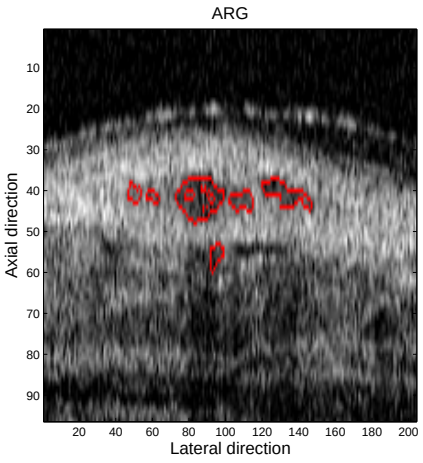

(b) Scenario urothel: Urothel vessel segmentation by adaptive neighborhood region growing.

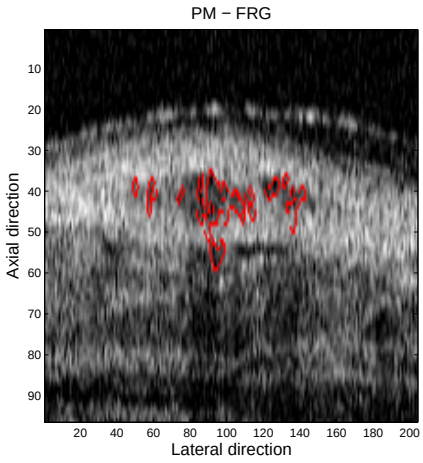

(c) Scenario urothel: Urothel vessel segmentation by PM-filtered image region growing.

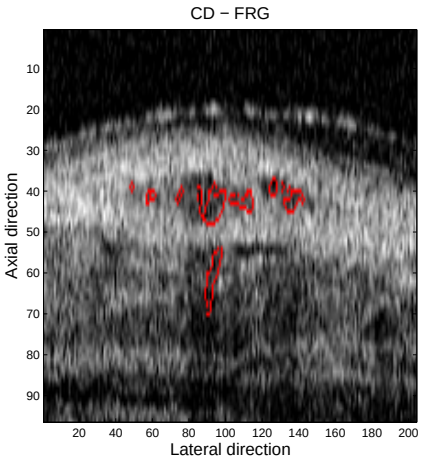

(d) Scenario urothel: Urothel vessel segmentation by CD-filtered image region growing.

Figure 6.28: Scenario urothel: Comparison of 3 region growing approaches for segmentation of vessels embedded into the urothel in an OCT image.

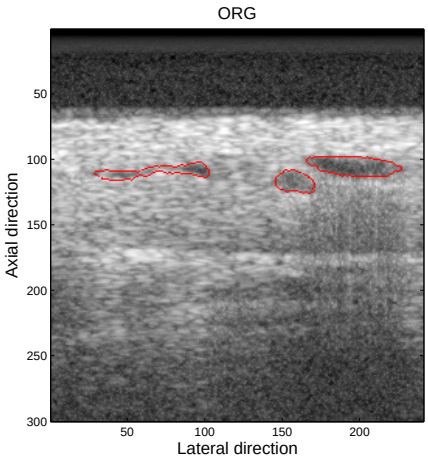

(a) Scenario intestine: OCT B-scan showing vessels embedded into the intestine wall and the results of the manual segmentation.

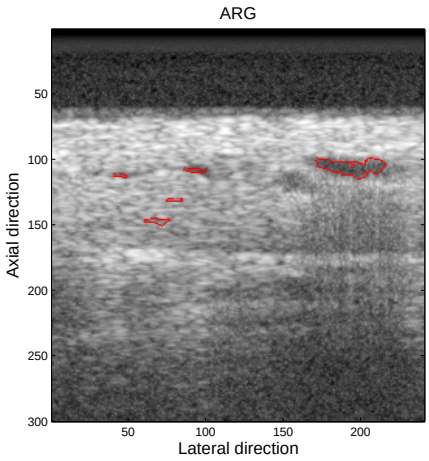

(b) Scenario intestine: Intestine vessel segmentation by adaptive neighborhood region growing.

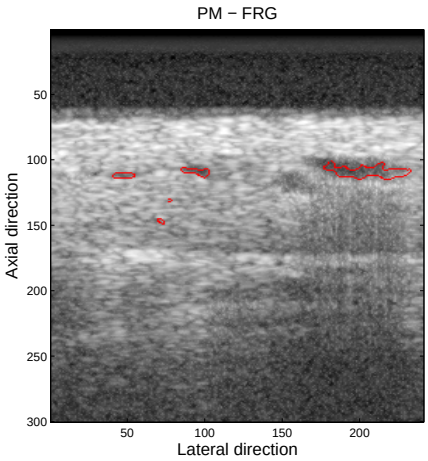

(c) Scenario intestine: Intestine vessel segmentation by PM-filtered image region growing.

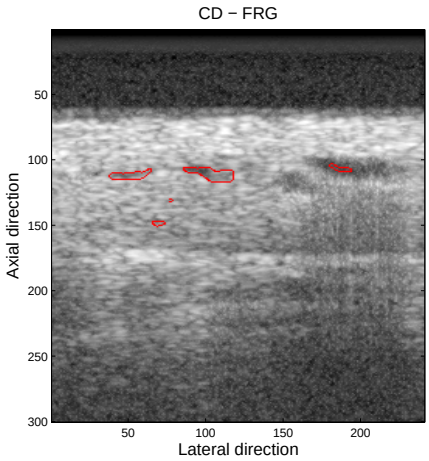

(d) Scenario intestine: Intestine vessel segmentation by CD-filtered image region growing.

Figure 6.29: Scenario intestine: Comparison of 3 region growing approaches for segmentation of vessels embedded into the intestine wall.

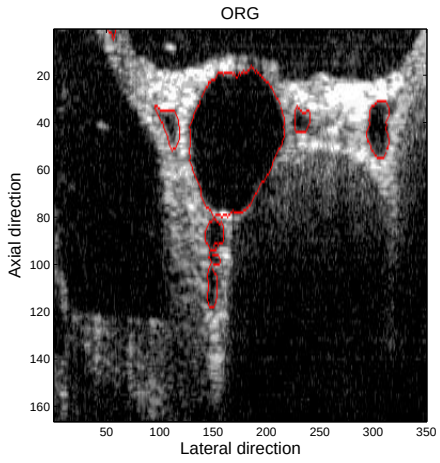

(a) Scenario egg: OCT B-scan showing vessels embedded into the inner skin of an egg and the results of the manual segmentation.

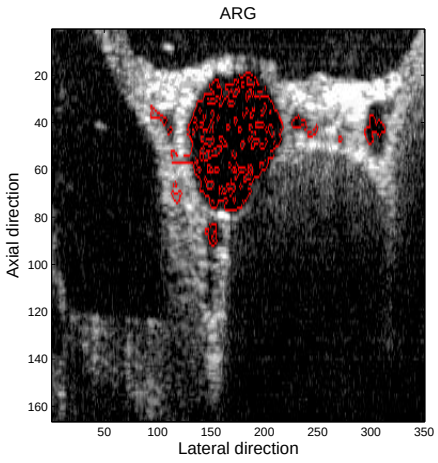

(b) Scenario egg: Egg vessel segmentation by adaptive neighborhood region growing.

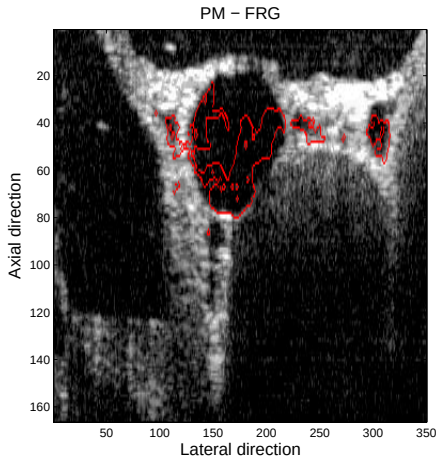

(c) Scenario egg: Sclera vessel segmentation by PM-filtered image region growing.

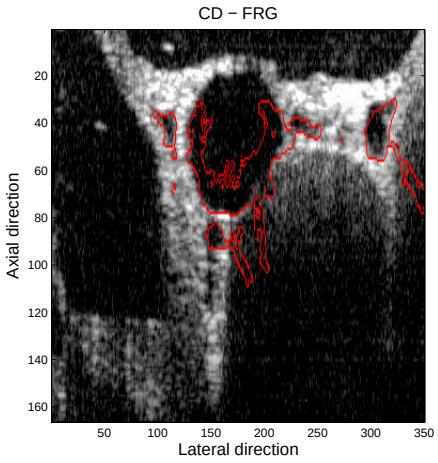

(d) Scenario egg: Egg vessel segmentation by CD-filtered image region growing.

Figure 6.30: Scenario egg: Comparison of 3 region growing approaches for segmentation of vessels embedded into the inner skin of an egg.

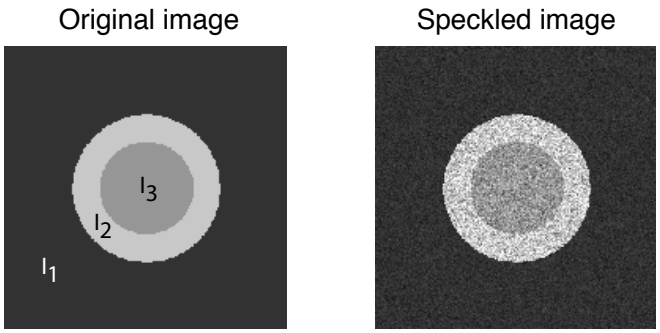

Figure 6.31: Test image simulating a section of a blood vessel: [left] Original image [right] Speckled image. I_1, I_2, and I_3 denote intensity gray-values of the respective region.

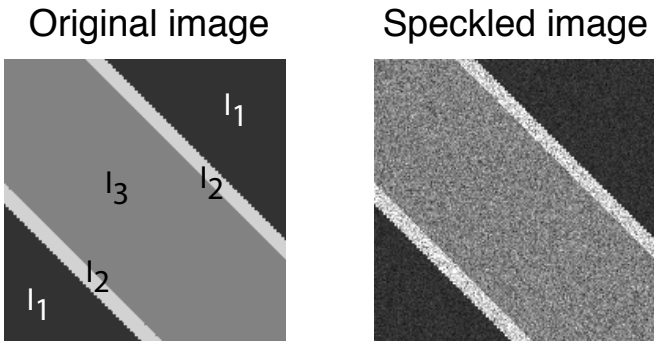

Figure 6.32: Test image simulating different tissue layers: [left] Original image [right] Speckled image. I_1, I_2, and I_3 denote intensity gray-values of the respective region.

6.4.2 Anisotropic propagation-separation filtering

Test scenarios and performances measures

In order to simulate realistic OCT imaging scenarios, two tri-modal test images were created. The first test image simulates a section of a blood vessel. Fig. 6.31 shows the simulated vessel and the speckled image where speckle noise was added following Eq. 5.18 with $\sigma_u^2 = 0.04$. The second test image is chosen such that different layers within a tissue scan are modeled. Fig. 6.32 shows the original image and the speckled image where speckle noise was again added following Eq. 5.18 with $\sigma_u^2 = 0.04$. Intensities I_1, I_2, and I_3 of both test images are given as gray values in the range of $[0...255]$. In all test

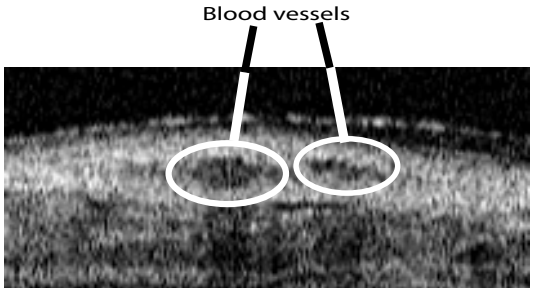

Figure 6.33: OCT image of blood vessels in human urothel acquired by a spectral-domain OCT system with a central wavelength of 830 nm.

runs, only I_2 was varied while $I_1 = 50$ and $I_3 = 150$ for simulated vessel and simulated layer image. This allows a comparison for varying intensity differences.
Results of the proposed method are additionally obtained for real OCT images of human tissue. The image shown in Fig. 6.33 was acquired by a spectral-domain OCT system with a central wavelength of 830 nm. It shows the urothel containing a blood vessels in vivo. The principal goal in analyzing OCT images of the human urothel is to improve diagnostics of urinary bladder tumorigenesis. Diagnosis is based on thickness measurements of the urothel and detection of important structures (e.g. vessels). Fig. 6.33 clearly shows that image quality and feature extraction is negatively affected by speckle noise which complicates subsequent image processing steps such as segmentation or layer thickness measurements. These features, however, are of importance for diagnosis or navigation purposes where image-based information can be used.
In order to compare the results of the novel filter to existing filtering approaches, different performance measurements for the simulated test images and the true OCT image are introduced. For each scenario, the measures evaluate edge preservation and noise suppression of the compared filtering techniques. For the simulated images, edge preservation or edge enhancement is evaluated by Pratt's figure of merit (FOM) [169]. It is given by

$$FOM = 1/(\max \hat{N}, N_{\text{ideal}}) \sum_{i=1}^{\hat{N}} 1/(1 + d_i^2 \lambda) \tag{6.13}$$

where $\hat{N}$ and N_{ideal} are the numbers of detected and ideally detected edge pixels. The constant λ is usually assumed to be $\frac{1}{9}$ and the factor d_i is the Euclidean distance between the i-th detected edge pixel and the nearest ideal edge pixel. The higher the FOM, the better edges between the original and the processed image match. Similarity between ideal and filtered image is measured by the peak signal-to-noise ratio (PSNR)

$$PSNR = 10 \cdot \log_{10}(g_{\max}^2 / MSE) \tag{6.14}$$

where $g_{\max}$ is the upper-bound intensity of the image and MSE is the mean square error of the intensities in original and filtered image:

$$MSE = 1/(M \cdot N) \sum_{i=1}^{N} \sum_{j=1}^{M} (\hat{J}(i,j) - J_{\text{ideal}(i,j)})^2 \tag{6.15}$$

where $M \times N$ denotes the pixel size of the images.

For the true image where no original or clean image is known, the following approach was taken. Structures of interest (e.g. blood vessels) in the real OCT image were segmented by an expert thus providing a ground truth. Then, the original image is filtered and a simple threshold-based segmentation is performed in the region-of-interest which contains the blood vessels. Subsequently, the following performance measures were evaluated:

1. *Sensitivity*= $\frac{\text{TP}}{\text{TP+FN}}$
   The sensitivity is a measure of the method's ability to locate the pixels which truly correspond to the structure of interest. TP denotes the true positives and FN the false negatives.

2. *False Positive Rate*= $\frac{\text{FP}}{\text{TN + FP}}$
   The false positive rate (FPR) expresses the probability that a pixel NOT belonging to the structure of interest is identified as belonging to such a structure. Here, FP denotes the false positives and TN the true negatives.

For all test images, denoising and structure enhancement was performed by the original propagation-separation approach proposed in [150] and the extended anisotropic propagation-approach. In order to compare the performance to existing diffusion filters, two edge enhancing diffusion filters presented in [135] were tested. In total, the following filters were applied:

1. Perona-Malik anisotropic diffusion filtering (PM)([132])
2. ramp preserving filtering (a realization of CD filtering)(RMP) ([134])
3. Isotropic propagation separation (PSEP) ([150])
4. Anisotropic propagation separation (APSEP)

Parameter evaluation

Results of all filtering approaches depend on certain parameters. In order to analyze the sensitivity of the filtering performance based on the parameter settings, an extensive parameter testing has been carried out. Table 6.18 lists the major parameters involved into

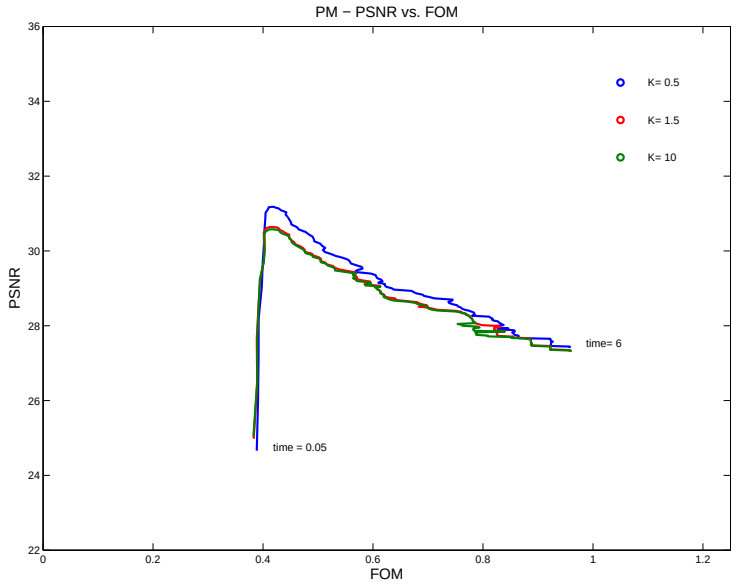

Figure 6.34: PSNR vs. FOM for different parameter settings of the PM filtering. Shown are the results for different edge threshold parameters K and for increasing total evaluation times (N×dt).

the respective filtering processes. The notation of the filter parameters follows the notation

Table 6.18: Description and notation of filter-dependent parameters of the tested filters.

Filter	Parameters			
	K	N	dt	σ
PM	edge threshold parameter	number of iterations	time increment	
RMP	edge threshold parameter	number of iterations	time increment	
PSEP	-	number of steps	-	-
APSEP	gradient threshold parameter	number of steps	-	std of steerable filter

in [132], [134], and [150]. In addition to the parameters listed in Table 6.18, the APSEP and the PSEP approach also feature the following parameters: λ (statistical penalty parameter), d (bandwidth update parameter) , τ (weight penalty parameter). Details of the choice of these parameters is provided in [150]. Within the following testings it has been found that these parameters only have a minor influence on the results. Therefore, the following parameter settings are chosen for all of the following performance evaluation scenarios: $\lambda = 1$, $d = 0.9999$, $\tau = 10^{40}$. The standard deviation of the directional kernel was set to $\sigma = 1$.

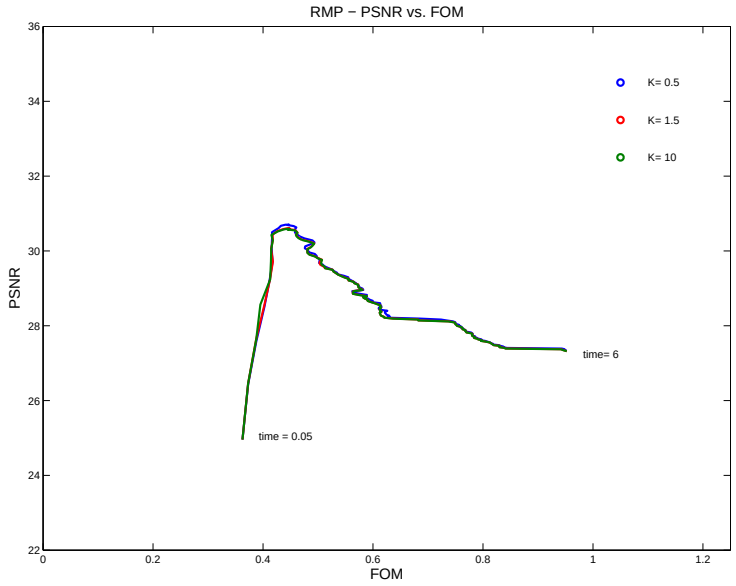

Figure 6.35: PSNR vs. FOM for different parameter settings of the RMP filtering. Shown are the results for different edge threshold parameters K and for increasing total evaluation times (N$\times$dt).

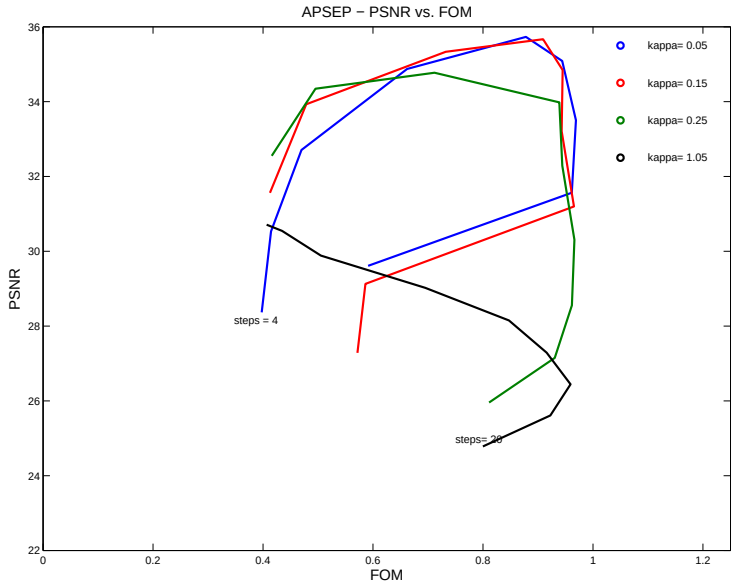

Figure 6.36: PSNR vs. FOM for different parameter settings of the APSEP filtering. Shown are the results for different gradient threshold parameters κ and for increasing number of steps N.

Results for simulated images

Filter performance was tested in terms of the FOM and PSNR. All filters were applied to the same noisy image of the simulated vessel shown in Fig. 6.31 with $I_2 = 175$, $\gamma = 1$

and $\sigma_u^2 = 0.04$. In order to show the improvement of the additional kernel integration, the PSEP is run with the same parameter settings as the APSEP (namely the number of steps) approach in the following. Fig. 6.34 shows the performance of the PM filter and Fig. 6.35 of the RMP filter for varying parameters. Note that for the PM and the RMP approach, the number of iterations N times the time increment dt yields the total evaluation time which is shown in the respective figures. In Fig. 6.36, the performance of the APSEP filtering is visualized. Based on the extensive simulations, parameter settings for filtering the simulated images can be chosen to visualize the results. For the following scenario, parameters were chosen such that all, the PM, the RMP, and the APSEP filter reach the maximal PSNR. The corresponding parameters are summarized in Table 6.19. As before, the additional parameters for the propagation-separation approaches are set to

Table 6.19: Simulated image scenarios: Parameter settings of the four different filters.

Filter	Parameters			
	K	N	dt	
PM	0.5	13	0.05	
RMP	0.5	13	0.05	
APSEP	0.15	10	-	
PSEP	-	10	-	-

$\lambda = 1$, $d = 0.9999$, $\tau = 10^{40}$.

All filters were again applied to the same noisy image of the simulated vessel. Subsequent edge detection for all filtered images was performed with the Canny detector [113] where threshold and standard deviation were constant for all filters and all test runs. The filtered images and subsequent edge detection are shown in Figs. 6.37 and 6.38. Qualitative measures for the filtering process are summarized in Table 6.20 which also provides quantitative results for different values of I_2. Results were also obtained for the simulated

Table 6.20: Results for the simulated vessel scenario with different intensities I_2.

	$I_2 = 225$		$I_2 = 200$		$I_2 = 175$	
Method	FOM	PSNR	FOM	PSNR	FOM	PSNR
PM	0.506	29.45	0.456	30.13	0.421	31.25
RMP	0.489	28.23	0.454	29.31	0.422	30.71
PSEP	0.492	29.76	0.456	30.49	0.421	31.61
APSEP	0.946	32.42	0.939	33.77	0.903	35.71

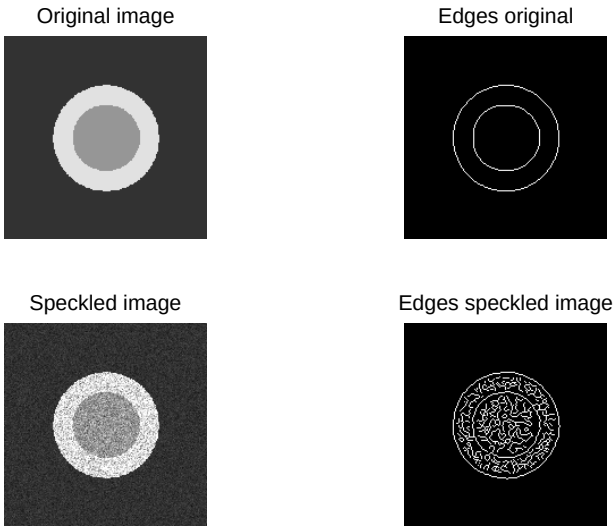

Figure 6.37: Test image of the simulated vessel scenario. [upper left] Original image [upper right] Edge detection on original image [lower left] Speckled image [lower right] Edge detection on speckled image.

layer image in Fig. 6.32 applying the parameter settings listed in Table 6.19. Table 6.21 summarizes the results for the processing of the simulated layer image. The corresponding test scenario is shown in Fig. 6.39. Results for the simulated layer are only shown for the PM and APSEP filtered versions (see Fig. 6.40). As for the simulated vessel image, the Canny edge detector was applied with the same parameter settings for all filters.

Table 6.21: Results for the simulated layer scenario with $I_2 = 175$.

Method	FOM	PSNR
PM	0.153	29.04
RMP	0.153	28.83
PSEP	0.153	28.84
APSEP	0.787	31.95

Results for real images

The performance of the different filters was tested on a real OCT image. Fig. 6.41 shows an OCT-scan of the urothel with embedded blood vessels. The image additionally shows the results of manual blood vessel segmentation done by an OCT expert. As for the simulated images, an extensive parameter testing was performed. After filtering, the subpart of the image containing the vessel structures was segmented using a simple threshold approach. The threshold was set constant for all filtering approaches.
Now, instead of evaluation the FOM and PSNR, the sensitivity and the false-positive rate are calculated with respect to the manual segmentation considered to be the ground truth. Results are shown for PM, RMP, and APSEP in form of a ROC analysis (see Figs. 6.42, 6.43, and 6.44 respectively). To quantify and visualize the results for a single parameter setting scenario, filtering was performed with the parameters providing the highest sensitivity (see Table 6.22). Results of filtering the real OCT image of the urothel are provided

Table 6.22: Filter parameter settings for filtering the OCT image of the urothel.

Filter	Parameters		
	K	N	dt
PM	0.5	12	0.05
RMP	0.5	14	0.05
APSEP	0.35	6	
PSEP	-	6	-

in Table 6.23. True and filtered images are shown in Fig. 6.45.

Table 6.23: Numerical results of filtering and subsequent segmentation of blood vessels in the urothel in terms of sensitivity and FPR.

Method	Sensitivity	FPR
PM	0.7720	0.0042
RMP	0.7675	0.0041
PSEP	0.7878	0.0033
APSEP	0.7607	0.006

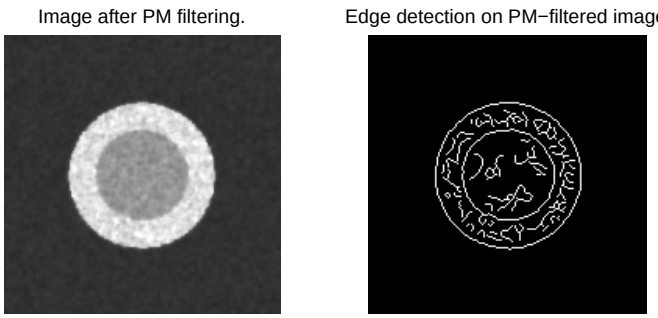

(a) Results for PM filtering and subsequent edge detection of the simulated vessel scenario.

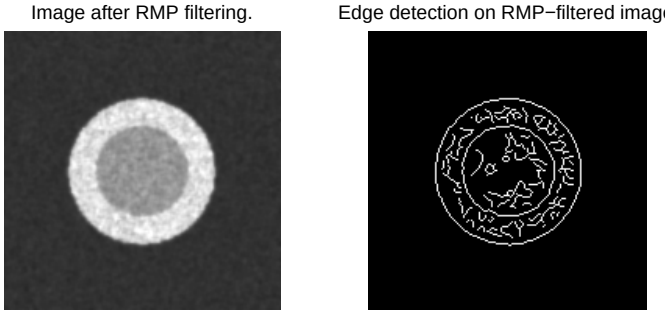

(b) Results for RMP filtering and subsequent edge detection of the simulated vessel scenario.

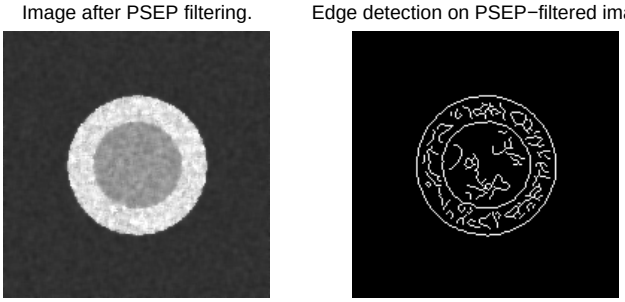

(c) Results for PSEP filtering and subsequent edge detection of the simulated vessel scenario.

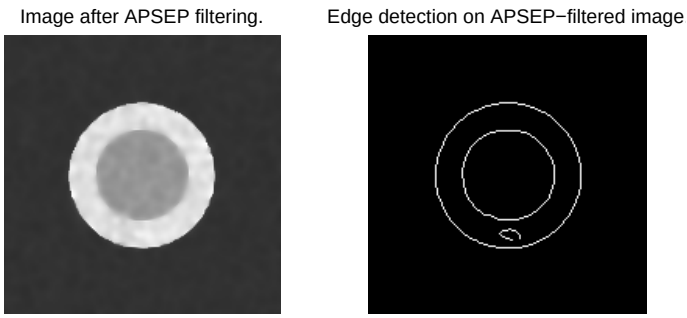

(d) Results for APSEP and subsequent edge detection of the simulated vessel scenario.

Figure 6.38: Results for the different filtering approaches for the simulated vessel scenario. [left] Filtered image [right] Edge detection on filtered image.

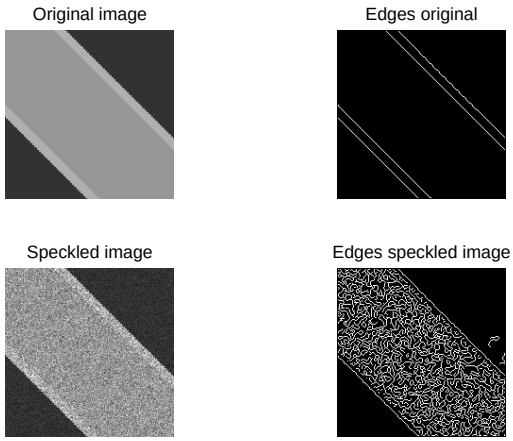

Figure 6.39: Test image of the simulated layer scenario. [upper left] Original image [upper right] Edge detection on original image [lower left] Speckled image [lower right] Edge detection on speckled image.

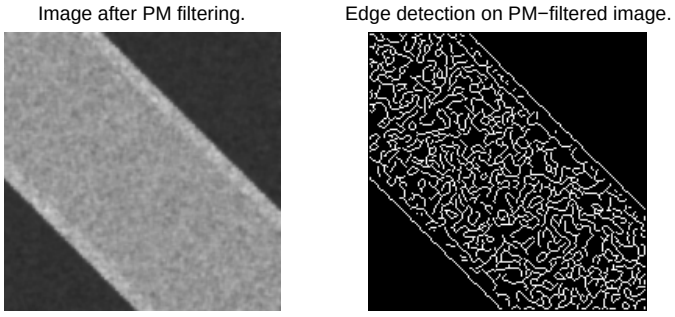

(a) Results for PM filtering and subsequent edge detection of the simulated layer scenario.

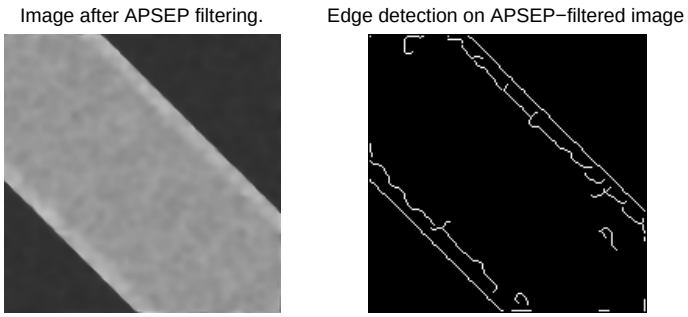

(b) Results for APSEP filtering and subsequent edge detection of the simulated layer scenario.

Figure 6.40: Results for simulated layer filtering of the simulated layer scenario. [left] Filtered image [right] Edge detection on filtered image.

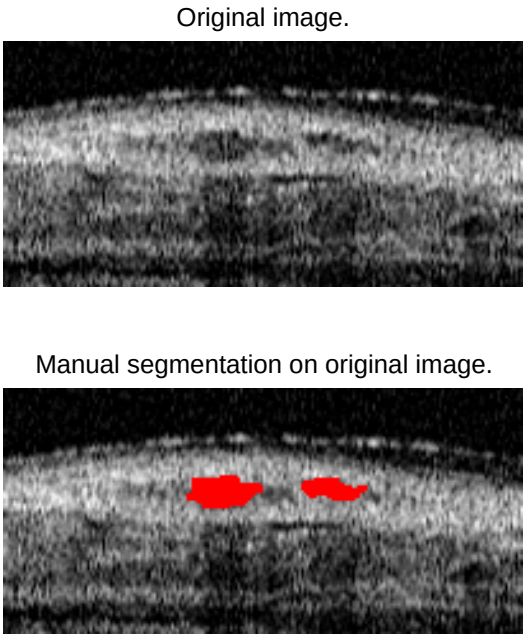

Figure 6.41: True OCT image of urothel with an embedded blood vessel. [top] Original image [bottom] Manual segmentation of the blood vessels.

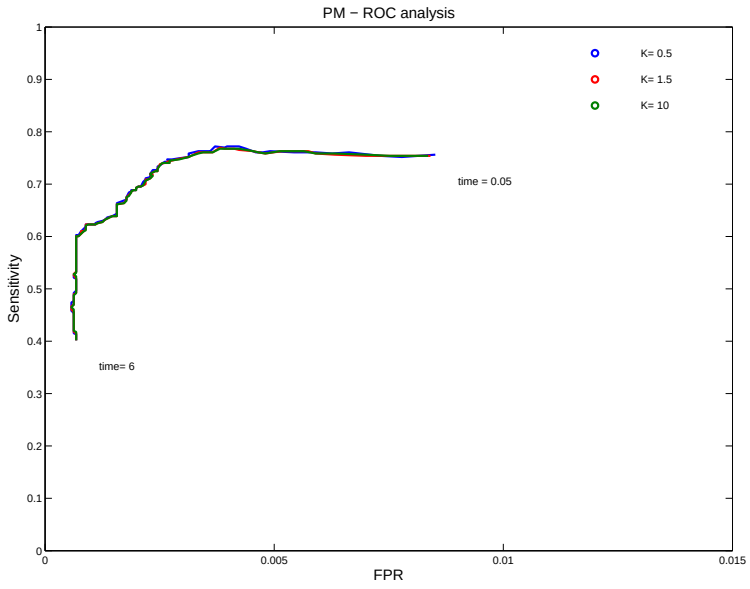

Figure 6.42: ROC analysis for different parameter settings of the PM filtering on the original image. Shown are the results for different edge threshold parameters K and for increasing total evaluation times (N$\times$dt).

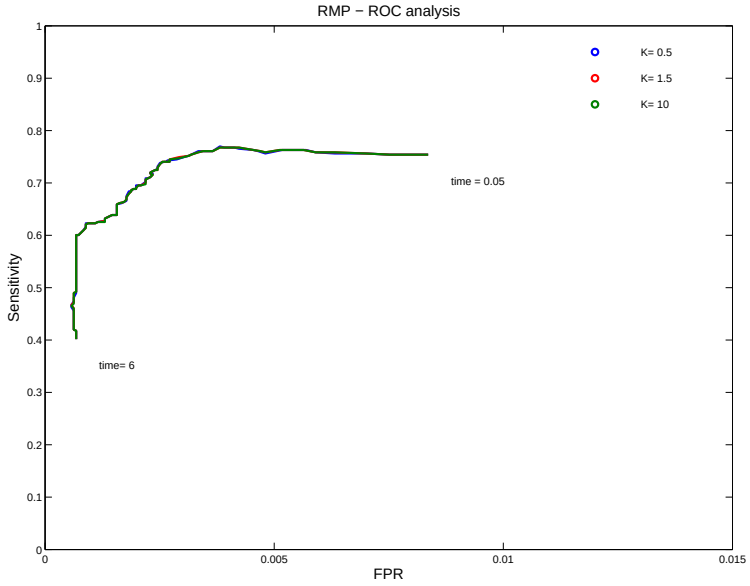

Figure 6.43: ROC analysis for different parameter settings of the RMP filtering on the original image. Shown are the results for different edge threshold parameters K and for increasing total evaluation times (N$\times$dt).

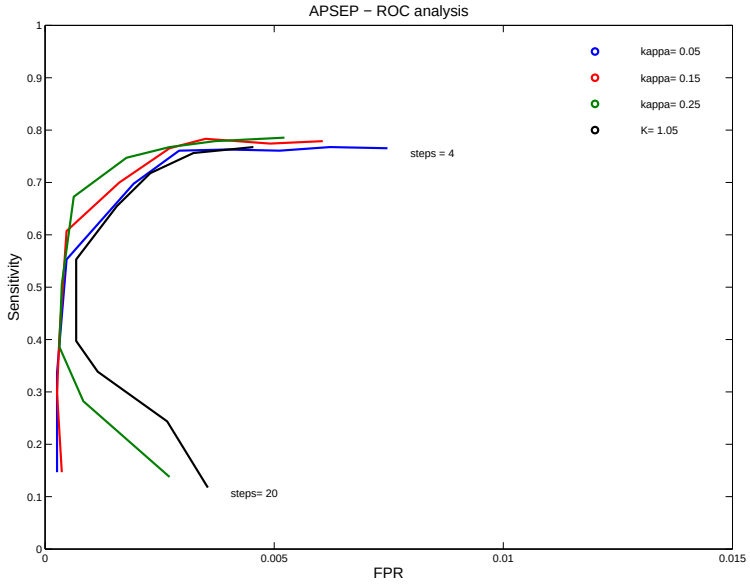

Figure 6.44: ROC analysis for different parameter settings of the APSEP filtering on the original image. Shown are the results for different edge threshold parameters κ and for increasing total evaluation times (N$\times$dt).

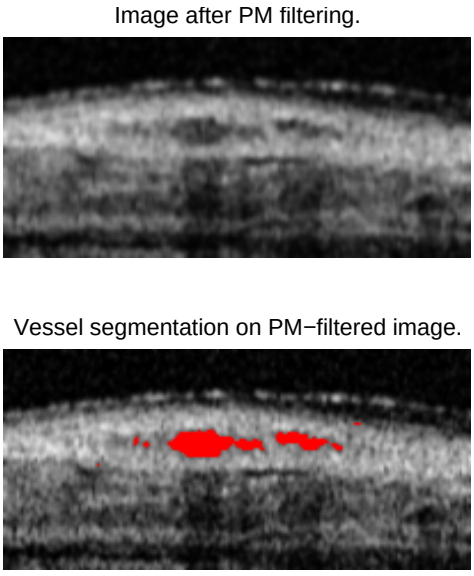

(a) Results for PM filtering and subsequent segmentation of blood vessels in the OCT image of the urothel.

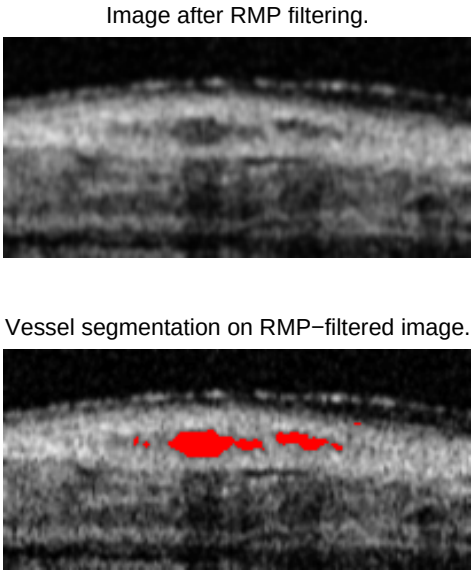

(b) Results for RMP filtering and subsequent segmentation of blood vessels in the OCT image of the urothel.

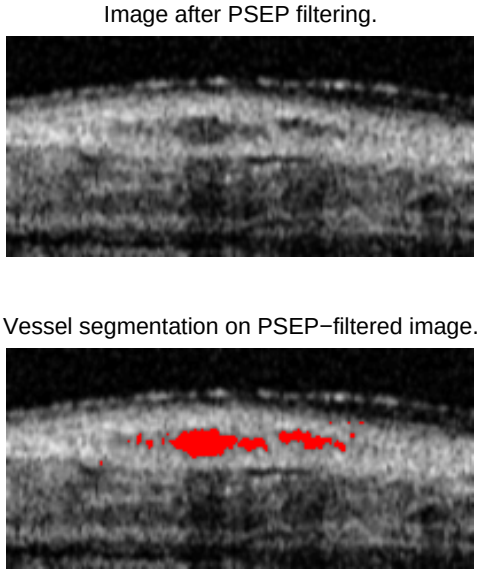

(c) Results for PSEP filtering and subsequent segmentation of blood vessels in the OCT image of the urothel.

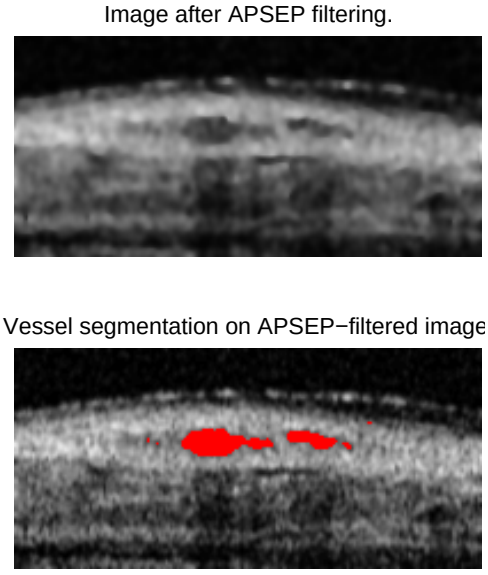

(d) Results for APSEP filtering and subsequent segmentation of blood vessels in the OCT image of the urothel.

Figure 6.45: Results for filtering and subsequent segmentation of blood vessels in the OCT image of the urothel.

7 Discussion

This chapter successively discusses the results presented in chapter 6. The first part focuses on design and performance of the stereotactic manipulator. It concentrates on the design, positioning accuracy performance, results of animal experiments, and the integration of the SASSU into the general setting of small animal neurosurgery. The second part debates the brain exploration part of this work. It comprises a discussion of the single fibre imaging and OCT-based white matter detection as well as the performance of the presented OCT image processing methods.

7.1 Stereotactic manipulator

7.1.1 Kinematic design

Choosing the kinematic design of the robot structure affects performance e.g. in terms of workspace, positioning accuracy, safety, and complexity of operation. Different choices of the kinematic structure would have been suitable to meet the particular requirements listed in chapter 3. Two criteria, however, motivated the choice of a spherical structure featuring a center-of-arc design: the inherent mechanical safety and the potential of future adaption to human applications. This motivation is strongly supported by successfully established stereotactic devices for human surgery, which feature the center-of-arc design. Prominent systems include the Leksell system [55], the Riechert-Mundinger system [57] and the Todd-Wells systems [61].
The finalized kinematic structure meets the requirements of probe positioning during stereotactic procedures on small animals. Five DOF are provided by a $TTRRT$ joint sequence. These allow to place a linear probe at a desired target with a desired orientation. Compared to existing translational kinematic designs in the area of small animal neurosurgery (e.g. the Lab Standard Stereotaxic in Fig. 2.5), the chosen design provides one more (rotary) DOF. Compared to existing center-of-arc systems (e.g. the SASI system in Fig. 2.7), the chosen kinematic sequence is less prone to positioning errors which are induced by joint variations. This is due to the fact that the SASSU allows the isocenter of rotation to be translated by using the first two translational axes t_1 and t_2 (see section 7.1.3). That allows to shift the isocenter of rotation in the xy-plane and thus reduces the arm of lever (e.g. length of probe advancement). A shorter arm of lever, in turn, results in

a smaller positioning error if rotary joint deviations occur.

7.1.2 Mechanical design

The mechanical design of the SASSU can be discussed from different perspectives:

1. The specified dimensions and joint ranges exceed the required workspace coverage for small animal brain surgery. This allows to apply the SASSU to other small animals such as rabbits or canines. As an additional feature, the SASSU can be removed from the operational field which provides the surgeon with sufficient space to perform manual surgical tasks such as drilling or cleaning (see Fig. 7.1).

2. The material of all mechanical parts allows cleaning and sterilization. Guiding rails, however, are lubricated and may therefore not be grogged. As the animal is fixed into the stereotactic frame and usually does not contact any parts of the robot, cleaning and sterilization of robotic parts is not a major issue, also because rules for animal experiments are less strict. For human adaption, the problem of cleaning needs to be solved. A potential solution is the introduction of sterilized surgical drapes.

3. All of the chosen motors and gears exceed the required motion resolution. This, in turn, reduces the effect of the joint error addition which is a characteristic of serial kinematic chains. Step loss of the stepper motors is compensated by the introduction of external encoders which again reduces the possibility of joint errors.
   The stepper motors require power supply to keep their respective position. As experimental conditions possibly require the minimization of all electrical noise, additional brakes are mounted onto the shafts. Brakes are locked if power is switched off and therefore allow to take the stepper motors off the power supply.
   Speed of the motors allows adequately fast movement of the probe. As most of the required motions do not demand for high dynamics, the chosen components fulfill the desired requirements. Tasks such as motion compensation of tracking of pulsation, however, might require a more dynamic setup.

4. Resolution of the optical encoders integrated into each stage exceed the motion resolution of the motion stages. This allows to implement a positioning control scheme where sensors feed back the current position which is subsequently compared to the desired one. Thus, step loss or backlash can be compensated. This is of particular importance for the fourth stage (second rotary joint) where the pinion features an extreme backlash if the direction of motion is reversed.

An important attribute of the mechanical assembly is the inherent safety of operation. It is provided by the means of inherent collision avoidance through the center-of-arc design of the manipulator and the integration of mechanical end stops on each axis. Additional safety measures are implemented by the software controlled adjustement of motion parameters.
Despite the advantages of the assembly, some shortcomings are to be mentioned. Different effects related to the construction of the system lead to a decreased positioning performance. The most prominent one is the free end of the arc. This allows levitation of the arc, which, in turn, results in a decreased positioning performance. Compensation of these inaccuracies requires additional efforts which are adressed in section 7.1.4.

7.1.3 Kinematic accuracy

The simulation results in section 6.1.2 show that the translational error based on the kinematic structure of the SASSU manipulator is less sensitive to joint variations in the rotary joints. For different depths z and different joint variations Δq_1 and Δq_2, the SASSU system shows a smaller mean error and a smaller maximal error over the total workspace. If all points and orientations within the workspace are equally important, the SASSU system therefore excels the SASI structure in terms of kinematic structure-based accuracy. For all z, the SASI system provides a smaller minimum error. At a certain POSE within workspace, the translational error induced by joint variations is therefore smaller for the SASI structure.
The essential advantage of the SASSU system can be derived looking at Fig. 6.3(a). The maximal error over all orientations $o \in \mathbb{O}$ is constant. This is due to the fact that the isocenter of rotation can be translated by the first two translational axes t_1 and t_2. Thus, the translational error induced by joint variations depends on the length of the last translational axis and can therefore be interpreted as a cantilever induced error. The adjustable isocenter causes the length of the cantilever to be constant for a constant depth z resulting in a translational error of equal magnitude for all points $p \in \mathbb{P}$. Due to the kinematic structure, the isocenter of rotation of the SASI is constant and cannot be translated. To reach a point p in the workspace, the axes t_1, t_2, and t_3 have to be adjusted. Referring to the cantilever approach, a constant isocenter requires larger adjustments of the translational axes resulting in an increased length of the cantilever. This explains the increase of the translational error as the point p moves to the edges of the workspace (see Fig. 6.3(b)).

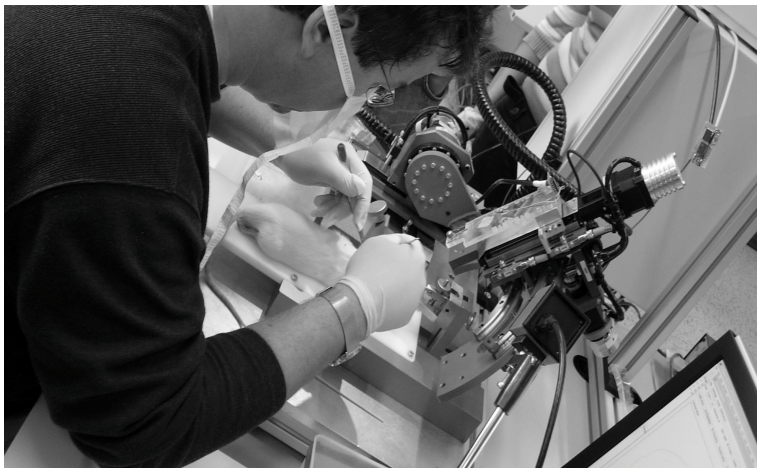

Figure 7.1: SASSU in the surgical position providing sufficient operational space for manual surgery.

7.1.4 Operation

Stereotactic control framework

The implemented stereotactic control software provides a convenient interface for the planning and execution of neurosurgical surgeries on small animals. It supports and integrates the planning for a single and for multiple tools. It disposes the need for tedious calculations of target coordinates and the corresponding coordinates and joint values of the manipulator. It supports and enhances the registration of the robot to the rat coordinate system which is a major deficiency in current stereotactic approaches to small animal brain research. Surgical duration, compared to normal approaches, is not prolonged for single probe implantation and shortened for multiple implantation. Another benefit of the framework is given by the the integrated collision avoidance which, for normal operation, prevents the probe and/or the animal from damage caused by irregular robot motion.

Planning

The atlas-based planning assumes morphological similarity between all animals having the same weight. While the SASSU might still place the probe tip at the desired stereotactic coordinates, neural structures at this coordinates might not correspond to the atlas information. The image-based approach solves this problem by providing individual image data for the respective animal. Ideally, this data consists of both, CT and MRI data which would subsequently be fused for planning and surgical control. If planning is performed in this way, the probe position can directly be related to neural structures without featur-

ing the uncertainties of the atlas-based approach. An important disadvantage, however, is that devices such as (small animal) MRI and CT are not readily available and usage is expensive. Therefore, the atlas-based approach, which is the current state-of-the-art, should still be integrated into the stereotactic control framework.

Registration

As presented in section 5.1.2, registration is performed under visual observation and by moving the tool tip to characteristic landmarks. This approach presents the cheapest and most common approach in small animal stereotaxy. Visual observation, however, introduces accuracy errors. Additionally, fragile probes such as thin microelectrodes might be bent or damaged during the registration procedure. These shortcomings of the registration process will subsequently deteriorate the accuracy of the probe placement. There are different ways to improve the registration process. The first option focuses on avoiding the damage of the probe by using a robust calibrated touch sensor instead of the probe. The sensor indicates the contact with the skull. After having stored the coordinates, the sensor is replaced by the probe used for the surgery. As both, the touch sensor and the measurement probe, are calibrated before registration, only the software-based tool characteristics would have to be changed. This option presents a robust and cheap way to perform registration but does not eliminate the inaccuracies caused by visual observation. To compensate for these inaccuracies, a second scenario is proposed: As for the human application, registration of the skull to the physical workspace can be realized by the incorporation of small animal computed or magnetic resonance tomography data. On the one hand, the respective image data would have to display the rat skull and on the other hand, structures with a known spatial POSE in the physical space of the robot. Then, the position and orientation of the rat skull with regard to these structures can be determined by either manual selection of landmarks in the image data or automated registration procedures to a standardized rat skull (via an ICP algorithm for example). This approach promises more accuracy while significantly increasing the cost and effort of small animal stereotaxy and will be subject of future work.

Mechanical positioning accuracy

The results show that the mean mechanical positioning accuracy of the SASSU is 32 μm and the mean repeatability is about 10 μm. This positioning performance meets the requirements of targeting small structures in the brain. The STN, for example, features a size which is well covered by the positioning performance of the SASSU (see e.g.

[92]). Compared to the existing stereotactic device presented by [97] which features a mechanical positioning accuracy of 500 μm, the SASSU shows a more accurate positioning performance. To our knowledge, no other studies investigate the mechanical positioning accuracy of small animal stereotactic frames. The SASSU outperforms the mechanical accuracy of human stereotactic frames for which the mechanical accuracy has been reported to be in the submillimeter range [74]. Particularly, the maximum positioning error of the SASSU which was found to be 110 μm is significantly smaller than the errors reported in [74]. The mechanical positioning accuracy of the SASSU can also be compared to standard industrial robots. According to its data sheet, the Kuka KR 5 (KUKA Roboter GmbH, Augsburg, Germany) provides a repeatability smaller than 0.2 mm. No details on the absolute positioning accuracy are given. According to [112], the absolute positioning accuracy of standard uncalibrated industrial robots is between 0.1 mm to 1 mm. After special calibration procedures, a repeatability of 0.02 mm and an absolute positioning accuracy of 0.167 mm can be reached (Kuka KR 45). It can thus be stated that the SASSU also outperforms the positioning accuracy of standard industrial robots (serial kinematic chains).

Different issues regarding the positioning performance, however, should be pointed out. The maximum positioning error of 110 μm does not fulfill the requirements of targeting structures such as the STN which eventually leads to missing the desired target (e.g. the STN). Looking at the results of the positioning trials, the maximal positioning errors mostly occur at an angle of $q_2 = 6^\circ - 8^\circ$. This allows to relate the positioning error to a fabricational error: The guiding rail which leads the slide along the rim of the arc cannot be manufactured in one piece. At the transition of the first guiding rail to the second, the slide is not kept in the same circular path. The transition itself is approximately located at an angular position of $q_2 = 6^\circ$ and thus induces positioning inaccuracies at this respective angle. Other issues affecting the accuracy are based on deflection of the system due to gravity. This effect will cause deflection of the levitating arc if the last linear stage is moved towards the free end. Other issues affecting the accuracy are based on the effect of the deflection of the system due to gravity. Despite these fabricational issues, 90% of all positioning errors are smaller than 50 μm. Along with the mean positioning accuracy, this indicates a robust positioning performance.

One approach to reduce the effect of hardware-related positioning inaccuracies is the introduction of a software-based inaccuracy compensation. Partial compensation of the resulting positioning inaccuracies can be done by integration of a deflection compensation algorithm into the control software (see section 4.3.3). Quantitative evaluation of the positioning improvement by deflection compensation shows that the mechanical position-

ing accuracy increases by nearly 0.17 mm (maximal positioning error before deflection compensation of 0.2 mm and maximal positioning error after deflection compensation of 0.032 mm). Additionally, it has been found that the deflection compensation algorithm holds for different probe weights smaller than 300 grams. This offers the opportunity to adapt a range of different probes from microelectrodes to mechanical drills.
Although software-based deflection compensation does improve the system performance in terms of accuracy, it does not totally compensate for the positioning error. This is most probably due to the fact that a linear deflection compensation model does not express all effects correctly. Application of nonlinear models, e.g. of quadratic nature or look up tables, have been examined. Although showing minor improvements in comparison to the linear model, parameter identification of nonlinear models requires significantly more effort. As the measured positioning accuracy, which is smaller than 32 μm, meets the previously defined positioning accuracy for small animal stereotaxy, the linear deflection compensation model has been found suitable for the operation of the SASSU.

Surgical positioning accuracy

As outlined in section 2.2.4, the overall positioning accuracy in small animal stereotaxy is affected by multiple factors. The kinematic structure of the SASSU and the results of the mechanical positioning accuracy analysis have shown that the system overcomes the hardware-related inaccuracies. Although the system shows a positioning error performance which meets the requirements of targeting small functional areas in the rat brain, the application accuracy will be affected by the biology-related factors as well.
Although not being investigated in an experimental setting, different strategies of compensation of biology-related effects are proposed. The image-based planning modality does reflect the morphology of the individual animal and thus allows to avoid atlas-based inaccuracies. Image-based registration will also improve the quality of the surgical outcome as it prevents from the best fit approach and the side-effects from visual identification of the respective landmarks. For the brain tissue-related sources of positioning errors, an effective insertion strategy should be used. One approach is to *shake* the probe into the tissue. Herein, the probe is advanced while a high frequent up-down movement is modulated onto the axial penetration. This eventually reduces the effect of brain compression.

Calibration

Results of the mechanical positioning performance analysis reveal that the proposed calibration process does not deteriorate the system performance such that accuracy require-

ments are not met. There are, however, certain aspects to be discussed in this matter: As the calibration process is camera-based, additional equipment needs to be introduced into the system setup. This increases the hardware costs of the total system. Additionally, camera adjustments and image processing require a lot of user interaction thus increasing the time of operation before animal surgery. Although camera-based calibration has been automated by the means of special algorithms and customized image processing, a more convenient approach to calibration is desirable.
One such option is the design of an external calibration module. The calibration module consist of two parts: a probe adapter which is similar to the SASSU probe adapter and a reference tip which is movable in all 3 cartesian directions. In a first step, a calibrated probe is adapted to the calibration module and the reference axis position adjusted until it touches the probe tip. This position of the reference tip will subsequently be the initial position of the calibration module. If another, uncalibrated probe is now attached to the calibration module, the reference tip is again positioned such that its tip touches the probe tip. Now, the parameters of the uncalibrated probe can be calculated by allocating the amount of motion of the reference tip with the known offset parameters of the initial probe. Such a calibration approach promises to be more convenient in terms of time consumption and ease of use.

Robot-assisted electrophysiological brain exploration

Results presented in Fig. 6.9 show that the four chosen measures (a) vary for different depths and (b) correlate between the same tracks in one animal (laterally mirrored) and in different animals. In Table 6.10, the correlation coefficients for the different measures and the different trajectories are shown. These results support the hypothesis of a similar and characteristic neural activity obtained on the same tracks in one animal (laterally mirrored) and in different animals. Not all measures, however, display the similarity in the same quality. For the RMS (0.66-0.85) and the PSD (0.34-0.89), a stronger correlation than for the ENT (0.0-0.68) and the Median (0.03-0.74) value can be observed. The fact that no exact quantitative correspondence is observed is due to different aspects, which could negatively influence the measurements and thus lead to less significant correlation. These effects include the accuracy of the registration process and the shortcomings of planning on the basis of Paxinos atlas information. The results motivate future application of the system in the direction of electrophysiological brain mapping. A premise is the preoperative acquisition of individual small animal MRI- or CT-data. Then, neural activity can directly be related to neural structures identified from the preoperative data. The robot-assisted framework will provide the required spatial positioning accuracy. Such a

mapping would trigger research activities addressing the intelligent characterization and comparison of neural signals. In a large scale, such a mapping could provide a functional atlas. Neurophysiological characteristics, however, are dependent on many factors such as anesthetics, electrodes, recording systems, etc. Establishing such an atlas therefore requires a careful choice of the surgical setting. Once established, such an atlas could establish a novel modality for neuronavigation where the specific signal characteristics could be compared to the multi-dimensional brain map and thus allow determination of the current position of the probe tip in situ. This would augment existing neuronavigation modalities. In this context, however, multiple questions have to be answered: Is there a one-to-one mapping of spatial position to electrophysiological signal characteristics? Which characteristics of the signal should be evaluated for reliable spatial mapping? How do signal characteristics change from region to region (steady or unsteady)?
Moreover, this work motivates the idea of establishing a multi-dimensional brain atlas as proposed in Fig. 6.10. In this context, also other modalities then electrophysiological recordings could be integrated into the characterization of certain intracranial areas. One possible application is the use of OCT which is discussed later in this chapter.

Shortcomings of the atlas-based approach

Atlas-based surgery features a significant disadvantage. The planning and insertion is always based on a standardized scenario (e.g. the normalized atlas data). Matching the normalized data with the surgical truth can therefore be of good or bad, which subsequently affects the positioning of the probe at the desired target area. Another disadvantage was revealed during experimental testings. During all surgeries performed with the robot-assisted system, the following observation was made: After craniotomy, the position of the brain surface did not correspond to the position calculated according the Swanson information, although coordinates were scaled according to the Lambda-Bregma distance. The actual brain surface was, in all cases, located deeper than calculated by the planning software. This observation leads to the following conclusions: morphological information such as the information from the Swanson atlas may not conform exactly with the real operational scenario. Especially the effect of brain shift after craniotomy and different skull morphology will falsify the planning procedure itself. Moreover, it is questionable if the skull size scales linearily with the Lambda-Bregma distance as assumed by most researchers.
Both shortcomings can be compensated by providing an individual planning for each animal. This could be done by integrating CT or MRI data as outlined in section 7.1.4 or, later, on a complete functional atlas.

Electromagnetic compatibility

A well known problem in electrophysiology, particulary in the field of microelectrode recordings, is the electric noise, which is introduced by electrical systems close to the recording site (e.g. light sources). As the stereotactic system features five stepper motors and the corresponding power electronics, noise introduced by these components might corrupt the measurements. Results, however, have shown that turning off the power supply of the SASSU allows qualitatively good microelectrode recordings. No effect of the power electronics in the turned-off state could be monitored. Furthermore, the powering off procedure creates a distinguishable waveform in the recording data. Thus, potential noise contribution by the stereotactic system can be discriminated in the data analysis. In conclusion, the stereotactic assistant provides a good electromagnetic compatibility and allows applications in the field of microelectrode recordings.

7.2 OCT-based brain exploration

The integration of OCT into the brain exploration framework is done with regard to two fields of work: (a) the methodology of white matter detection in OCT A-scans and (b) the single fibre imaging of rat brain structures in vitro. Both will be discussed separately.

White matter detection

Numerical results shown in Table 6.11 indicate that the method described in section 5.3.2 provides a robust way to locate white matter areas. Performance of the white matter detection, however, is naturally dependent on the PCR. The higher the difference of the scattering properties of different structures, the easier these structures can be discriminated. That is due to the step-wise approach of white matter detection: the determination of the white matter candidates is based on an analysis of the first derivative of the intensity course. A low PCR will not lead to a significant change in the intensity. Thus, such structures cannot be differentiated leading to a small set of candidates.
The numerical evaluation of extensive tests led to robust heuristics for the choice of the threshold paramaters depending on the PCR (see Fig. 6.14). Results show that for different PCR, the optimal parameters σ_1, σ_2, and σ_3 of the white matter detection do not change. Thus, a constant set of parameters can be used for detection without previous determination of the PCR. This property enables the automatic nature of the white matter detection.

For the real OCT images, the presented results indicate an adequate performance of the white matter detection. This especially applies to the task of detecting structures in low scattering structures such as blood vessels as the PCR of these structures in the inverted gray-scale images is relatively high. For the white matter identification in real OCT images, the PCR is found to be PCR$\approx 20 \ldots 25$. Transfering the results shown in Table 6.11 to real images, the detection algorithm provides identification of over 90 percent of the structures in the real images.

7.2.1 Single fibre-based imaging

In existing work on single fibre OCT brain imaging [28] and [50], OCT signals have only been evaluated with regard to intensity decay over a region of interest. Herein, the attenuation coefficient has been determined by least-square fitting of the initial slope of the OCT intensity decay. The data showed that different brain tissue features different characteristic attenuation coefficients. In [28], OCT scanning was performed perpendicular to a coronal slice of the brain which is not suitable for in vivo use. Single fibre imaging in DV direction was investigated by [50]. They used a rotary OCT probe which did not investigate tissue in front of the probe tip but provides a L-mode projection of a layer perpendicular to the fibre. A major shortcoming of this setup is that the fibre tip needs to penetrate the region of interest in order to provide an OCT signal. Thus, the atraumatic nature of OCT is lost. Evaluation of the measured OCT signals along a trajectory targeting the human STN, however, show that different anatomic structures show characteristic intensities.

Our system setup presented in 5.2.3 combines two advantages: (a) it is single fibre based and (b) able to investigate tissue ahead of the probe tip. Evaluating the OCT A-scan signals as in [28] along a trajectory in DV direction indicate that the optical properties of brain tissue lead to a characteristic attenuation coefficient at different depths. The attenuation of the intensity with increasing depth, however, does not only depend on the scattering properties of the tissue. It is also based on properties of the light detector in the scanning setup, focal properties of the sample path, and absorption characteristics of the sample tissue. While the first two factors are system-dependent, the latter is sample-dependent. Therefore, comparing results of the same system gives a good indication whether OCT is usable for determination of tissue characteristics. Fig. 6.19 shows that the attenuation coefficient course of trajectory 1 correlates well in depth with the attenuation coefficient course of trajectory 2 which is located in close proximity (0.2 mm lateral). Correlation with the trajectory 3 (4.0 mm lateral to trajectory 1) does not show the same

correlation performance. Interestingly, the course of trajectory 3 seems to be shifted to deeper depth. This can be explained by looking at the atlas data provided in Fig. 6.18. Both, trajectory 1 and 2 were obtained close to the displayed trajectory. Trajectory 3, however, is located closer to the midline. For that trajectory, the external capsule (ec) is located deeper which potentially causes the shift of the intensity course. This indicates that the attenuation coefficient can be used to identify the probe tip position which, in turn, points towards OCT-based navigation.
Until now, only the evaluation of the averaged intensity has been used with regard to brain tissue identification. The relevance of spikes in the OCT A-scan signal has not been focused on although it potentially contains valuable information. Looking at the results provided in Fig. 6.18, the intensity courses shown on the right hand side indicate that brain tissue characteristics lead to different spiking characteristics of the respective OCT signal. This can be especially seen at low imaging depths of 0 mm to 0.5 mm. Here, different spike characteristics can be observed at different depths (see e.g. the signals at $z = 2.4$ mm and $z = 2.6$ mm).
Summarizing these observations, the results strongly support the idea of OCT A-scan brain imaging and near field navigation. Results, however, were obtained only in vitro. Although brain tissue was relative close to the in vivo status, effects like blood flow of neural activity might affect the OCT signal. Another issue to be discussed is the effect of fouling. Although a GRIN lens is attached to the probe tip in order to broaden the light emitting and collecting part of the fibre, fouling can always degenerate the signal quality and may thus falsify the information deduced from the intensity signal. Thus, a more robust design would still be of advantage.

7.3 OCT image processing

This section provides the discussion of the results obtained for the proposed automated region-growing approach for segmentation of white matter structures in OCT images. Furthermore, in the second part, the performance of the anisotropic propagation-separation approach will be analyzed.

7.3.1 Model-based region growing

Comparing the ARG and the FRG approach, it can be stated that both are dependent on certain parameters which have already been discussed in section 6.4.1. Parameters for the simulation scenarios were chosen as specified in section 6.4.1. In all test scenarios, the

ARG and both of the FRG have been applied with equal settings of the seed detection. Observing the simulation results in Table 6.14 and in Fig. 6.23, the following statements can be made: for all PCRs, the ARG approach provides a higher JC index while featuring a lower HD. This indicates less leakage though a better similarity between segmented and original regions is provided. This especially holds at a PCR of 20 which approximately corresponds to the contrast ratio in real OCT images of brain matter.
It can be seen that for increasing PCR, the increase of the JC index of the RMP-FRG is more substantial: The RMP-FRG JC index increases by 46% for PCR increase from 20 to 30 while the ARG JC index increases only by 31% (see Fig. 6.23(a)). This indicates that the higher the PCR, the better the edge sensitive filtering applies to the OCT images. Results of the ARG approach in Fig. 6.24(b) show that the adaptive homogeinity criterion applies well to the problem as the white matter structures are well segmented and only minor leakage can be observed. The results of the PM-FRG in Fig. 6.24, however, show that some leakage occurs. This is indicates the major shortcoming of the FRG approaches in comparison to the ARG approach: the edge-sensitive filtering does alter the image. If the edge threshold parameter K is chosen too high, the edges will be blurred and the region growing will lead to leakage. This especially holds for the deeper edges of the white matter structures as these feature a less distinct intensity difference to the neighboring regions than the higher edges. If the parameter K, however, is chosen too small, speckle noise corruption will not be compensated and the subsequent region growing will lead to a lower JC index as no homogeneous regions are provided after filtering.
Segmentation results performed on real images show the capability of the algorithm for real OCT images. Segmentation of different tissue types is demonstrated as two types of structures, one being bright, one being dark regions have been examined. Visual inspection indicates that both algorithms are good candidates for automated segmentation of desired structures. Results show that (a) white matter from real OCT B-scans of brain matter and (b) cell walls of an onion sample are reliably identified (see Table 6.15 and Figs. 6.25, 6.26, 6.27). The numerical comparison to the manual segmentation of an OCT expert in Table 6.15 shows two tendencies: (1) for a comparable JC index (e.g. wm1), the HD of the ARG approach is smaller than for the results of the FRG approaches and (2) if a comparable HD is achieved (e.g. wm2), the JC index of the ARG is higher than for the results of the FRG approaches. For the identification of low scattering structures, this tendency also holds (see Table 6.16). Visual inspection of the results supports the conclusion that incorporation of OCT modeling into the segmentation approach provides a better structure identification. Interestingly, the time consumption characteristics differ for both scenarios. While for identification of high scattering structures, the PM-FRG

approach outperforms the ARG, the opposite behaviour can be observed for the identification of low scattering structures. In general, one would expect the FRG approach to be computationally more expensive than the ARG approach as an additional filtering step is required. Note, however, that time consumption incorporates the process of region growing. A higher JC index at a comparable HD means that the region growing process took longer as more structures of interest were segmented. Thus, time consumption does not directly allow a qualitative comparison of the approaches.
Considering the parameter sensitivity for both region growing approaches, heuristics can be drawn from extensive simulations (see section 6.4.1). As stated in section 6.4.1, results from simulated images indicate a preferable choice of parameters. For the ARG approach, this leads to a choice of $c_1 = 0.93 \ldots 0.97$, $c_2 = 1$, and $m' = 4$. For the FRG approaches, a well performing set of parameters N, K, and c_1 are given by $N = 40$, $K = 4$, and $c_1 = 0.99$ and $c_2 = 1.01$.
Both, seed detection and ARG, are inherently dependent on the speckle size. While for the illustrated theoretical approach, the speckle size is assumed to equal one pixel in the image, this does not necessarily correspond to a real measurement scenario. There, the speckle size is related to the point-spread function of the measurement system. Therefore, speckle size might include more than one pixel. In that case, the outlined approach would have to be adapted, namely by the extension of the pixel-related criteria based on an estimation of speckle size. For the seed detection for instance, the ratio in Eq. 5.26 would compare the intensity at $I(q_{z_1} + k)$ with the intensity $I(q_{z_1} + k - s_z)$, where s_z would be the axial number of pixels occupied by a speckle. Equally important, the $n \times n$ neighborhood would have to be adapted to the speckle size (the larger the speckle size, the larger n).
The proposed region growing approach is presented for the identification of two distinct tissue structures. If tissue structures with more homogeneities are subject to segmentation (e.g. the retinal structure which is a layered composite), the approach would have to be adapted. In this case, adaption would mostly affect the seed detection intelligence which would have to robustely identify at least one seed in each layer. As the growing criterion relies on a general OCT model, it should apply in its present form. Parameters, however, may have to be adapted to the respective task.

7.3.2 Anisotropic propagation-separation filtering

Summarizing the results of filter performance testing on simulated and real OCT images, it can be stated that the APSEP approach cleary features anisotropic behaviour. The filtered images indicate that the incorporation of the additional directional kernel

leads to an improved edge preservation and significantly decreased blurring and over-smoothing. Evaluation of the APSEP performance in comparsion to existing edge enhancing anisotropic filters show that the proposed method achieves a comparable edge enhancement or edge preservation while providing a higher peak signal-to-noise ratio. Performance of all filters, however, is dependent on the choice of filtering parameters. In the following, the effect of the parameter choice will be discussed.

Parameter variation for simulated images

The Figs. 6.34, 6.35, and 6.36 show the effect of different parameter choices on the filter performance. For the PM and the RMP filter, the following statements can be made: the larger the total evolution time of the respective filters, the higher the achieved FOM. The PSNR, however, increases for little evolution time and falls off for higher evolution times showing a clear maximum. This indicates that higher evolution times enhance edges while the similarity between filtered and original image is decreased. Interestingly, different values of the edge threshold parameter K do not have a significant impact on the filter performance. Both, the PM and the RMP filter show almost equal performance in terms of PSNR and FOM.
The APSEP approach generally shows the same characteristics. For increasing number of steps N, the PSNR shows a distinct maximum. In contrast to the PM and RMP approach, the FOM for the APSEP does not increase constantly with the number of steps but decreases at $N > 15$. This indicates that with increasing number of steps, blurring of edges occurs which is a difference to the PM and the RMP approach. As a result, the parameter settings for the APSEP feature a distinct optimum whereas for the PM and RMP a trade-off between FOM and PSNR has to be found. Unlike the edge threshold parameter K for the PM and the RMP scenario, the gradient threshold parameter κ does have a significant effect on the performance of the APSEP. For the simulated vessel image, the value of κ showed a clear optimum at $\kappa = 0.15$.
Comparing the filtering performance of all filters, an important observation can be made. For a comparable FOM value in the range from 0.4 to 1, the PSNR of the APSEP filter always outperforms the PSNR provided by the PSEP, the PM, and the RMP filter. This is shown in Figs. 6.34 to 6.36 and also indicated by the numerical results for different test scenarios provided in Table 6.20 and 6.21. Looking at the visual results provided in Figs. 6.38 and 6.40, it can be stated that under the condition of constant edge detection parameters for all filters, the PM, RMP, and PSEP filter show irregular edges after filtering.
To summarize, the APSEP achieves a better performance in terms of edge detection and/or preservation and noise suppression if compared to other edge-enhancing diffusion ap-

proaches such as the PM and the RMP filter. It does, however, require the correct choice of parameters which will be discussed in the following:

- Parameter κ
  κ is the gradient threshold value and has to be chosen depending on the image. If the image features important structures who induce only small gradients, κ should be small. This will, however, increase the influence of image noise on the anisotropic directional kernel. Tests for multiple images show that κ is preferably to be chosen in an interval $[0.1 \ldots 0.4]$.

- Parameter N
  The number of steps controls the level of smoothing. If chosen to high, blurring and/or over-smooting will occur. Results of the simulated and the real image indicate that a choice of $N = [10 \ldots 15]$ provides good qualitative results.

The proposed APSEP is an iterative method. With increasing bandwidth h, computational costs increase as an increasing number of points has to be evaluated for the local modeling. This limits the real-time capability of the APSEP.

Parameter variation for real image

The results of parameter analysis on the real OCT image of the urothel support the statements made before. The results of the threshold-based segmentation after filtering indicate that the APSEP provides a higher sensitivity while simultaneously providing a lower FPR. Looking at the ROC analysis in Figs. 6.42 to 6.44, it can be seen that the APSEP approach provides results closer to the upper left corner which is considered the optimal result. This leads to the conclusion that while identifying structures of interest with a higher quality, less blurring and/or smoothing occurs in case of the APSEP filtering.

8 Conclusion and Outlook

8.1 Summary

This work introduces the concept of robot-assisted stereotaxy on small animals. Two major elements have been elaborated on: the design of the robotized, stereotactic assistant SASSU and its integration into a brain exploration framework. The system performance has been tested in both, a testbed environment and in surgical application. Using the SASSU as a tool for precise probe insertion, the idea of OCT-based and electrophysiological near field navigation has been pursued. Results have been obtained for in vivo microelectrode recordings and in vitro single fibre imaging of brain matter as well as for OCT image segmentation and processing methods.

Regarding the SASSU, details on the hardware design have been presented. Starting from an extensive analysis of existing systems, surgical conditions, and future applications, design criteria for robot-assisted small animal stereotaxy have been deduced. Based on these findings, the kinematic design process of the assistant has been outlined. Details on the mechanical construction and the components have been provided. Additionally, analytical expressions for the forward and inverse kinematics of the system have been derived. Having presented the hardware design and the kinematic analysis, details on the system operation have been adressed. A special focus has been put on the calibration problem. Furthermore, the software-based motion control of the SASSU has been introduced. Besides basic functionalities for system operation, it realizes compensation of hardware-induced positioning inaccuracies. Results analyzing the performance of the system show that the system features a mechanical positioning accuracy of 32 μm which meets the requirements of targeting small functional areas in the animal brain.

In the second part of this work, the SASSU system has been integrated into the surgical scenario of small animal stereotaxy. A software-based stereotactic control framework has been presented which provides modules for surgical planning, registration, and probe insertion control. Two options for planning and registration are outlined: an atlas-based approach which presumes a normalized morphological structure of all animals and an image-based approach which incorporates the individual anatomy. The integration of the SASSU system into the surgical workflow of neurosurgical operations on rats has been depicted. Performance of the total framework has been analyzed in terms of mechanical positioning analysis. The total framework allows to compensate for hardware-related in-

accuracies of current stereotactic approaches. The integration of image-based planning is a promising candidate to reduce also the effects of biology-related inaccuracies such as non-standard brain morphology.
After having developed fundamental elements, the framework is used to pursue the idea of OCT-based and electrophysiological near field navigation. For that purpose, the framework has been tested in the context of robot-assisted microelectrode recordings. Results of data acquisition and analysis support the hypothesis that robot-assisted stereotaxy allows precise investigation of functional areas in the brain of small animals. For OCT-based near field navigation, the SASSU has been applied in a single fibre imaging setup which is characterized by its minimal-invasiveness. Results showing different characteristic attenuation coefficients for different scanning depths in the brain have been obtained. In this context, an approach to A-scan-based white matter identification has been proposed which can be seen as an exemplary approach to brain tissue identification in single fibre signals. Extending the work on OCT imaging, image processing methods for OCT B-scans have been developed. This comprises a methodology for segmentation of white matter areas in OCT images of brain tissue as well as an approach to anisotropic filtering via propagation-separation.

8.2 Robot-assisted small animal stereotaxy

The SASSU system and the stereotactic control environment present a computer- and robot-assisted stereotactic framework for precise neurosurgery on small animals. The SASSU features 5 DOF for placement of one or multiple probes with a desired orientation at a desired target. Its kinematic design follows the center-of-arc approach which provides a higher inherent mechanical safety than other kinematic structures. As this design approach is well known from non-robotized human stereotaxy, the design process provides valuable experiences for the adaption to the human application. The choice and combination of components provides adequate means for the required positioning precision. The basic operational functionalities such as calibration and motion control allow a precise control of the system. Moreover, mechanically induced positioning inaccuracies can be partially compensated for.
The stereotactic control software design comprises functionality for the integration of the robotic assistant into the surgical scenario. It allows the user to perform planning on (a) morphological atlas data and (b) individual image data such as preoperatively acquired CT/MRI data. Additionally, it provides a control interface for the SASSU during the registration and/or probe insertion process. Furthermore, it integrates additional function-

alities such as safety checks which provide a convenient user interface.
Combination of design, components, mechanical construction and control software result into multiple benefits: First, the framework allows to reduce the hardware-based inaccuracies presented in section 2.2.4. Although not being extensively tested, the integration of image-based planning and new modalities of near field navigation present promising means to compensate for the biology-related inaccuracies. Furthermore, it provides an easy-to-use and convenient tool for small animal stereotaxy as it disposes the need of tedious manual calculation as in existing manual frames. Third, the user is able to reliably correlate the probe tip position to preoperatively existing data in an automated fashion. Fourth, multiple probes can easily be placed at the same target. And fifth, the combination conveniently allows to repeat a surgical scenario using another animal. To conclude, the proposed framework allows standardized and improved brain research on the small animal model.

8.3 OCT-based brain exploration

8.3.1 Single fibre imaging

OCT-based imaging via a single fibre presents a promising modality for high-resolution, real-time intracranial imaging. The integration into a minimal-invasive setup and the high resolution offer unique characteristics with comparison to other intraoperative imaging modalities such as ultrasound or MRI. The results of this work indicate that the determination of tissue-related optical characteristics from OCT signals provides a methodology to optically label brain areas. In a further step, this idea can be extended to navigate the probe based on the OCT information. A major concern in this context, however, is the presence of speckle noise which needs to be dealt with.

8.3.2 Structure segmentation in OCT images

Both of the presented approaches to structure segmentation in OCT images are able to identify specified regions of interest reliably. Generally, the ARG approach provides a better segmentation for all contrast ratios of different tissue structures. This indicates that the ARG approach is more suitable for segmentation of structures in OCT images. Thus, it can be concluded that incorporation of an OCT model (deterministic intensity decay and speckle noise) better serves the structure identification than an additional image filtering step which alters image information.

As OCT has not yet been widely applied to neurosurgery, automated image processing opens the door to novel applications in the field of optical diagnostics and navigation. Segmentation of vessel structures, which was shown to be possible, could be used in many other medical applications. As the proposed algorithm is based on a general formulation of the OCT intensity model, it may be adapted for other segmentation tasks as well.

8.3.3 Anisotropic propagation-separation

The anisotropic propagation-separation filter presents a new filtering method in the context of anisotropic filtering. It combines the advantages of the isotropic approach with information on local anisotropy provided by oriented gradient filters. This is done by introducing an additional gradient-based kernel which provides improved locality information compared to the convential statistical difference measure of the propagation separation. The APSEP offers a user-adjustable trade-off between edge preservation and noise suppression. Results for different test images show that the novel filter robustely outperforms common anisotropic filters in terms of noise suppression and edge preservation. This enhances feature extraction based on the filtered images and therefore offers a new filtering approach in medical image processing, especially for the analysis of speckled image data like optical coherence tomography images.

8.4 Outlook

Future work can be categorized in different fields of work. Considering the hardware setup of the stereotactic assistant, solving the constructional issues which induce the positioning inaccuracies (e.g. having one semi-circular guiding rail) could improve the system performance. Performing robot-assisted stereotactic procedure on other animals such as monkeys eventually requires to adapt the scale and the range of motion of the translational stages and the stereotactic frame.

Considering operational issues, manifold tasks to improve usability and performance could be pursued. A major improvement of the stereotatic framework consists of an improved integration of CT or MRI data of the individual animal into the planning process. Such an integration would improve the registration process and additionally eliminate the inaccuracies related to the standardized atlas planning. Another usability improvement would be the creation of an external calibration module which would eliminate the need of the time-consuming camera-based approach. For such a module, however, correctness of calibration needs to be carefully verified.

Besides improvements of the existing system, a very promising field of future work is the application of the robot-assisted framework for precise brain research. In a first step, future work should examine the real application accuracy of the system. This includes the scenarios where the probe passes through different media such as brain or fluids. After having done so, the system can be applied to detailed research on the rodent model. In the context of movement disorders, an exemplary field of research is to investigate circuit models of neural activity in healthy and diseased animals in order to improve current forms of treatment and/or diagnosis. Another visionary idea is to establish a multi-dimensional atlas of e.g. the rat brain which integrates different kinds of intracranially measured signals (e.g. electrophysiological and optical properties). Such an atlas could, in a further step, be used for near field navigation of the probe tip as current signal characteristics could be compared to standard characteristics provided by the atlas. This would augment existing neuronavigation modalities and provide improved positioning accuracy. This idea feeds the motivation to continue OCT-based imaging of brain tissue. Single fibre imaging is a promising methodology for probe guidance or optical investigation of brain structures. In this context, robust methods of OCT intensity signal processing need to be developed. These comprise e.g. algorithms to determine different types of tissue from the optical signal. In a further step, these algorithms could be used for tissue identification (e.g. optical biopsies) and finally be integrated into the robot-assisted neuronavigation framework. A special regard, however, has to be paid to the effects of speckle noise which present a major challenge to signal processing. In the context of OCT image processing, the field of intelligent, OCT-adapted processing methods still lies idle. This comprises the design of novel filtering processes and, in a subsequent step, the further post-processing. If OCT is to be integrated into a neuronavigation setup, methods for registering OCT-based image data to other image data such as atlas information or CT/MRI data is of great interest.

Acknowledgements

This work was partially funded by the program Forschungsschwerpunkt Biomedizintechnik at the University of Luebeck, Germany, and the BMBF project BiCIRTS 13N9190. The authors wish to acknowledge the support of the Department of Neurology (Prof. Dr. med. A. Moser) for his encouragement. Additionally, the authors thanks Prof. Winnie Jensen and the staff at the Biomedicinsk Laboratorium, Aalborg Hospital, Denmark for assistance during the animal experiments.

9 Appendix

9.1 Algorithms

Algorithm 9.1 Calibration procedure.

procedure CALIBRATION

$Q \leftarrow \begin{bmatrix} q_{1,1} & q_{2,1} \\ q_{1,2} & q_{2,2} \\ \vdots & \\ q_{1,n} & q_{2,n} \end{bmatrix}$.

$\Delta T \leftarrow \emptyset$

$A \leftarrow \emptyset$

Initialize: $q_1 = q_2 = t_1 = t_2 = t_3 \leftarrow 0$.

while $|Q| \neq \emptyset$ **do**

$q_1 \leftarrow Q_{1,1}$, $q_2 \leftarrow Q_{1,2}$, perform rotational movement

$\Delta\tilde{t}_1 \leftarrow$ returnAxis(1)

$\Delta\tilde{t}_2 \leftarrow$ returnAxis(2)

$\Delta\tilde{t}_3 \leftarrow$ returnAxis(3)

$\Delta T \leftarrow \Delta T \cup \begin{bmatrix} \Delta\tilde{t}_1 \\ \Delta\tilde{t}_2 \\ \Delta\tilde{t}_3 \end{bmatrix}$

$A \leftarrow A \cup \begin{bmatrix} \cos q_2 - 1 & 0 & -\sin q_1 & 0 \\ -\sin q_1 \sin q_2 & -\sin q_1 & -\sin q_1 \cos q_2 & 1 - \cos q_1 \\ \cos q_1 \sin q_2 & \cos q_1 - 1 & \cos q_1 \cos q_2 - 1 & -\sin q_1 \end{bmatrix}$

$Q \leftarrow Q \setminus [Q_{1,1},\ Q_{1,2}]$

end while

$[o_x,\ o_{z1},\ o_{z2},\ o_y] \leftarrow \left(A^\top \cdot A\right)^{-1} \cdot A^\top \cdot \Delta T$

end procedure

procedure RETURNAXIS(i) ▷ return probe tip to initial position in axis i

return Δt_i

end procedure

Algorithm 9.2 Automated axis return

procedure RETURNAXISAUTO(i, thr) ▷ Adjust axis i based on a pixel threshold thr
  $\Delta\tilde{t}_i \leftarrow 0$
  $stepsize \leftarrow 0.1$
  while getPixelDifference(i, p_c^{c1}, p_c^{c2}) $<$ thr **do**
    $direction \leftarrow sign$(getPixelDifference($i$, p_c^{c1}, p_c^{c2}))
    $t_i \leftarrow direction \cdot stepsize$, perform translational movement
    $\Delta\tilde{t}_i \leftarrow \Delta\tilde{t}_i + direction \cdot stepsize$
    p_c^{c1},p_c^{c2} ←tipDetection(I^{c1},I^{c2})
    if $sign$(getPixelDifference(i, p_c^{c1}, p_c^{c2})) $\neq direction$ **then**
      $direction \leftarrow sign$(getPixelDifference($i$, p_c^{c1}, p_c^{c2}))
      $stepsize \leftarrow stepsize/2$
    end if
  end while
  return $\Delta\tilde{t}_i$
end procedure
procedure GETPIXELDIFFERENCE(i, p_c^{c1}, p_c^{c2}) ▷ evaluates pixel difference
  if i = 1 **then return** $x_c^{c1} - x_r^{c1}$
  end if
  if i = 2 **then return** $y_c^{c2} - y_r^{c2}$
  end if
  if i = 3 **then return** $z_c^{c1} - z_r^{c1}$
  end if
end procedure

Algorithm 9.3 Adaptive neighborhood region growing

```
1:  procedure ARG(g)
2:      S ← seedDetection(g)
3:      R ← S
4:      while |S| ≠ ∅ do
5:          s ← S_1
6:          N ← Γ_n(s)
7:          while |N| ≠ ∅ do
8:              q ← N_1
9:              if homARG(s,q) then
10:                 R ← R ∪ q
11:                 S ← S ∪ q
12:             end if
13:             N ← N \ q
14:         end while
15:     end while
16:     return R
17: end procedure
```

Algorithm 9.4 Filtered image-based region growing.

procedure FRG(g)
    $S \leftarrow seedDetection(g)$
    $\hat{g} \leftarrow pmFilter(g, K, N)$
    $R \leftarrow S$
    while $|S| \neq \emptyset$ **do**
        $s \leftarrow S_1$
        $N \leftarrow \Gamma_n(s)$
        while $|N| \neq \emptyset$ **do**
            $\hat{q} \leftarrow N_1$
            if homFRG($s, \hat{q}$) **then**
                $R \leftarrow R \cup \hat{q}$
                $S \leftarrow S \cup \hat{q}$
            end if
            $N \leftarrow N \setminus \hat{q}$
        end while
    end while
    return R
end procedure

9.2 Denavit-Hartenberg conventions

Table 9.1: Definition of the DH parameters according to [1].

Parameter	Definition
d_i	the distance from the axis x_{i-1} to x_i measured along z_i
θ_i	the angle from x_{i-1} to x_i measured about z_i
a_i	the distance from z_i to z_{i+1} measured along x_i
α_i	the angle from z_i to z_{i+1} measured about x_i

9.3 Homogeneous transformations

This section gives a very brief overview on the representation of positions, rotations, and the resulting concept of homogeneous transformations.

9.3.1 Representing positions

According to [104], a position with respect to a cartesian coordinate system which is often the case for robot tasks can be defined as a vector

$$p = \begin{pmatrix} p_x \\ p_y \\ p_z \end{pmatrix}. \tag{9.1}$$

where p_x denotes the x-coordinate with respect to the origin of the cartesian coordinate frame.

9.3.2 Representing orientations

A rotation in 3 dimensions about the x,y, or z-axis can be expressed by 3×3 rotation matrices. Accordingly, a rotation about the z-axis is expressed by matrix multiplication with

$$R_z(\theta) = \begin{pmatrix} \cos\theta & -\sin\theta & 0 \\ \sin\theta & \cos\theta & 0 \\ 0 & 0 & 1 \end{pmatrix}. \tag{9.2}$$

where θ denotes the angle of rotation. Following the same notation, a rotation about the y-axis is expressed as

$$R_y(\theta) = \begin{pmatrix} \cos\theta & 0 & \sin\theta \\ 0 & 1 & 0 \\ -\sin\theta & 0 & \cos\theta \end{pmatrix} \tag{9.3}$$

and a rotation about the x-axis as

$$R_x(\theta) = \begin{pmatrix} 1 & 0 & 0 \\ 0 & \cos\theta & -\sin\theta \\ 0 & \sin\theta & \cos\theta \end{pmatrix}. \tag{9.4}$$

9.3.3 Representing total transformation

Combining both, translation and rotation, results in the so-called homogeneous transformations. A 4×4 homogeneous transformation matrix is composed as

$$H = \begin{pmatrix} R & p \\ 0 & 1 \end{pmatrix} \tag{9.5}$$

where R denotes a 3×3 rotational part and p is the translational vector. Following e.g. the yaw, pitch, roll convention, Eq. 9.5 can be expressed as

$$H = \begin{pmatrix} R_z(\theta_1)R_y(\theta_2)R_x(\theta_3) & p \\ 0 & 1 \end{pmatrix}. \tag{9.6}$$

9.4 Details on fabrication

9.5 Data sheets

The following pages provide data sheets available for specific components of the SASSU.

Table 9.2: Data sheets

Part	Axis	Manufacturer	Part number	Figure	Details
Gear	1	THK	KR	-	http://www.thk.com
	2	THK	KR	-	http://www.thk.com
	3	Harmonic Drive	CPU-17A-100-M		http://www.harmonicdrive.de
	4	Nanotec	GPLL22-25	Fig. 9.1	
	5	THK	KR	-	http://www.thk.com
Stepper motor	1	Nanotec	ST4209M1206 ss	Fig. 9.2	http://de.nanotec.com
	2	Nanotec	ST4209M1206 ss	Fig. 9.2	
	3	Nanotec	ST4209L1206 ds	Fig. 9.4	
	4	Nanotec	ST2818S-1006 ds	Fig. 9.3	
	5	Nanotec	ST4209M1206 ss	Fig. 9.2	
Encoder	1	Numerik Jena	MT-40BP80 / LIK41		http://www.numerikjena.de
	2	Numerik Jena	MT-40BP80 / LIK41		
	3	Nanotec	HEDL5540	Fig. 9.5	
	4	Numerik Jena	MR11-40BP00202-203 / RIA20CPIX		
	5	Numerik Jena	MT-40BP80 / LIK41		
Brake			no brake mounted		
			no brake mounted		
	3	Nanotec	BK-0,4-5,0	Fig. 9.6	
	4	Nanotec	BL-0,24-5,0	Fig. 9.6	
	5	Nanotec	BL-0,24-5,0	Fig. 9.6	

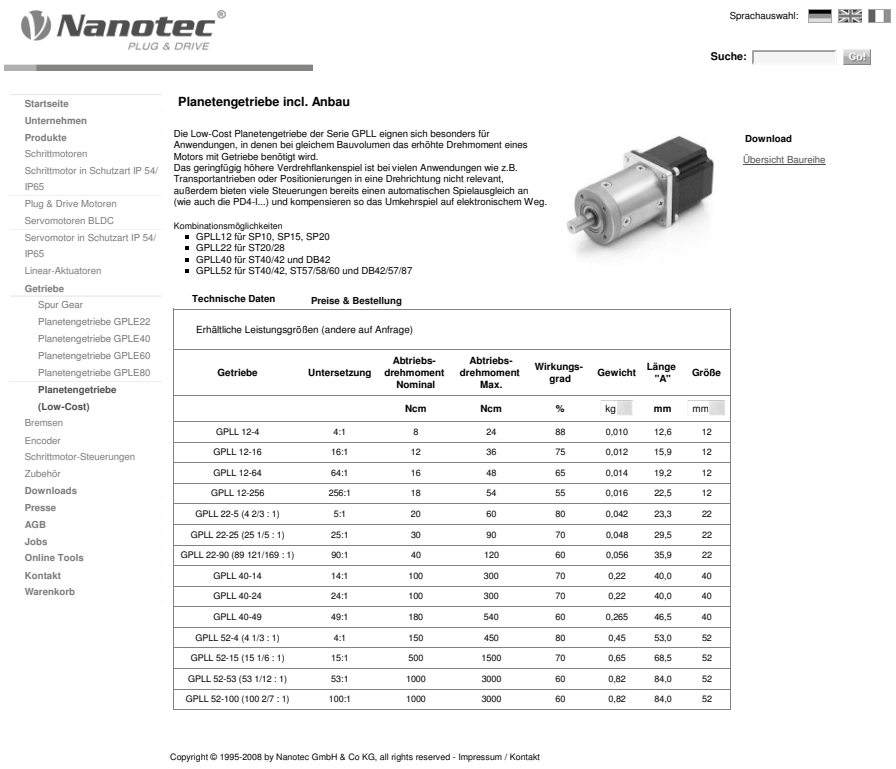

Nanotec PLUG & DRIVE

Sprachauswahl:

Suche: Go!

Startseite
Unternehmen
Produkte
Schrittmotoren
Schrittmotor in Schutzart IP 54/ IP65
Plug & Drive Motoren
Servomotoren BLDC
Servomotor in Schutzart IP 54/ IP65
Linear-Aktuatoren
Getriebe
Spur Gear
Planetengetriebe GPLE22
Planetengetriebe GPLE40
Planetengetriebe GPLE60
Planetengetriebe GPLE80
Planetengetriebe (Low-Cost)
Bremsen
Encoder
Schrittmotor-Steuerungen
Zubehör
Downloads
Presse
AGB
Jobs
Online Tools
Kontakt
Warenkorb

Planetengetriebe incl. Anbau

Die Low-Cost Planetengetriebe der Serie GPLL eignen sich besonders für Anwendungen, in denen bei gleichem Bauvolumen das erhöhte Drehmoment eines Motors mit Getriebe benötigt wird.
Das geringfügig höhere Verdrehflankenspiel ist bei vielen Anwendungen wie z.B. Transportantrieben oder Positionierungen in eine Drehrichtung nicht relevant, außerdem bieten viele Steuerungen bereits einen automatischen Spielausgleich an (wie auch die PD4-I...) und kompensieren so das Umkehrspiel auf elektronischem Weg.

Kombinationsmöglichkeiten
- GPLL12 für SP10, SP15, SP20
- GPLL22 für ST20/28
- GPLL40 für ST40/42 und DB42
- GPLL52 für ST40/42, ST57/58/60 und DB42/57/87

Download
Übersicht Baureihe

Technische Daten **Preise & Bestellung**

Erhältliche Leistungsgrößen (andere auf Anfrage)

Getriebe	Untersetzung	Abtriebs-drehmoment Nominal	Abtriebs-drehmoment Max.	Wirkungs-grad	Gewicht	Länge "A"	Größe
		Ncm	Ncm	%	kg	mm	mm
GPLL 12-4	4:1	8	24	88	0,010	12,6	12
GPLL 12-16	16:1	12	36	75	0,012	15,9	12
GPLL 12-64	64:1	16	48	65	0,014	19,2	12
GPLL 12-256	256:1	18	54	55	0,016	22,5	12
GPLL 22-5 (4 2/3 : 1)	5:1	20	60	80	0,042	23,3	22
GPLL 22-25 (25 1/5 : 1)	25:1	30	90	70	0,048	29,5	22
GPLL 22-90 (89 121/169 : 1)	90:1	40	120	60	0,056	35,9	22
GPLL 40-14	14:1	100	300	70	0,22	40,0	40
GPLL 40-24	24:1	100	300	70	0,22	40,0	40
GPLL 40-49	49:1	180	540	60	0,265	46,5	40
GPLL 52-4 (4 1/3 : 1)	4:1	150	450	80	0,45	53,0	52
GPLL 52-15 (15 1/6 : 1)	15:1	500	1500	70	0,65	68,5	52
GPLL 52-53 (53 1/12 : 1)	53:1	1000	3000	60	0,82	84,0	52
GPLL 52-100 (100 2/7 : 1)	100:1	1000	3000	60	0,82	84,0	52

Figure 9.1: Technical data for the gear of axis 4 with part number GPLL22-25.

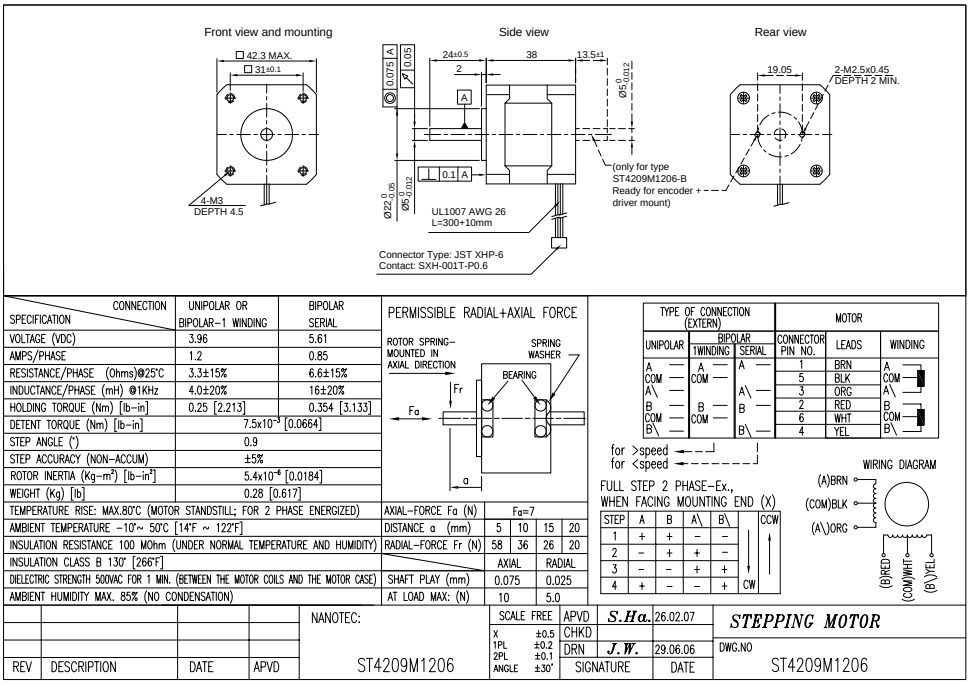

Figure 9.2: Technical data for the motor of axes 1,2,5 with part number ST4209M1206.

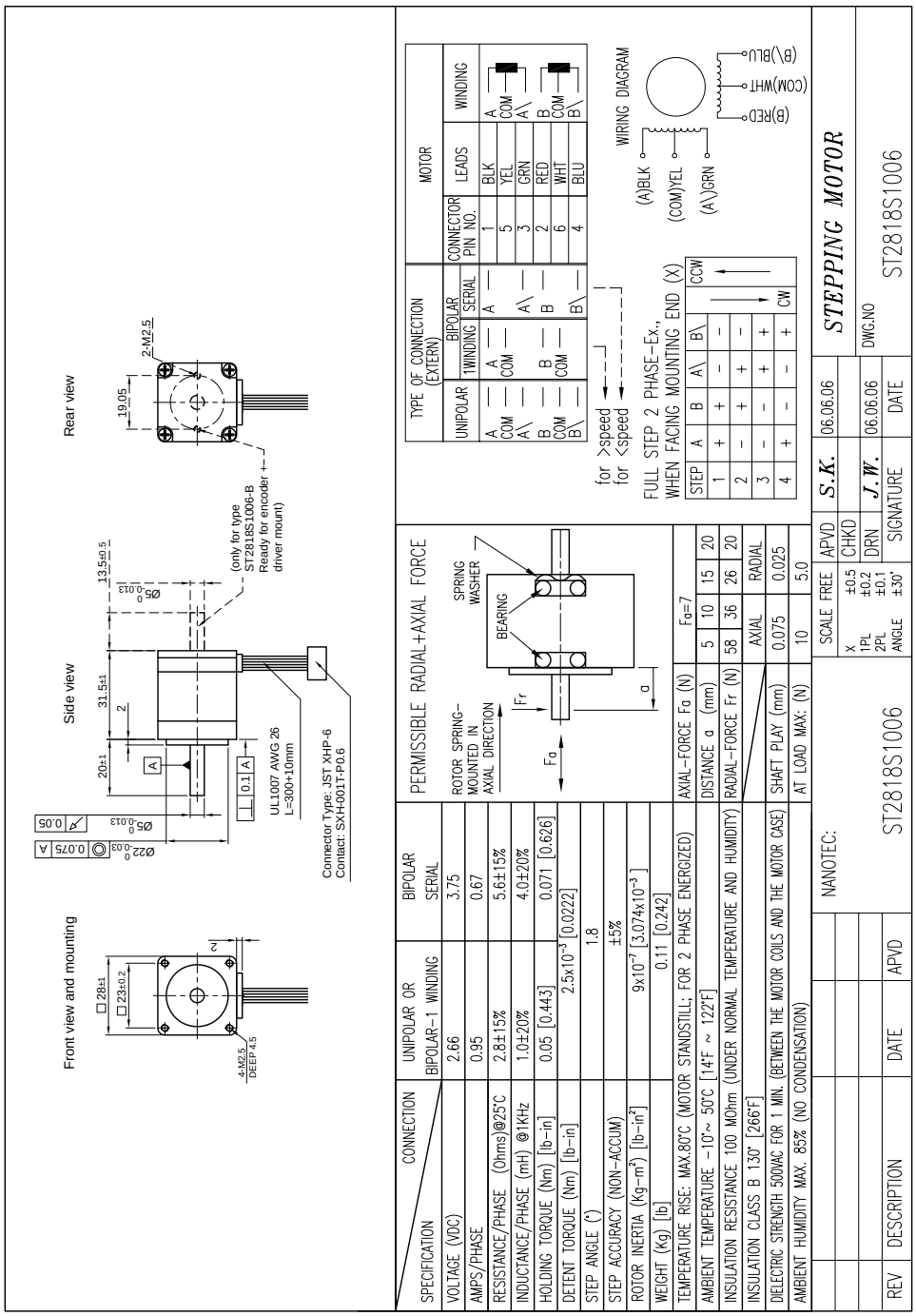

CONNECTION / SPECIFICATION	UNIPOLAR OR BIPOLAR-1 WINDING	BIPOLAR SERIAL
VOLTAGE (VDC)	2.66	3.75
AMPS/PHASE	0.95	0.67
RESISTANCE/PHASE (Ohms)@25°C	2.8±15%	5.6±15%
INDUCTANCE/PHASE (mH) @1KHz	1.0±20%	4.0±20%
HOLDING TORQUE (Nm) [lb-in]	0.05 [0.443]	0.071 [0.626]
DETENT TORQUE (Nm) [lb-in]	$2.5x10^{-3}$ [0.0222]	
STEP ANGLE (°)	1.8	
STEP ACCURACY (NON-ACCUM)	±5%	
ROTOR INERTIA ($Kg-m^2$) [$lb-in^2$]	$9x10^{-7}$ [$3.074x10^{-3}$]	
WEIGHT (Kg) [lb]	0.11 [0.242]	
TEMPERATURE RISE: MAX.80°C (MOTOR STANDSTILL; FOR 2 PHASE ENERGIZED)		
AMBIENT TEMPERATURE -10°~ 50°C [14°F ~ 122°F]		
INSULATION RESISTANCE 100 MOhm (UNDER NORMAL TEMPERATURE AND HUMIDITY)		
INSULATION CLASS B 130° [266°F]		
DIELECTRIC STRENGTH 500VAC FOR 1 MIN. (BETWEEN THE MOTOR COILS AND THE MOTOR CASE)		
AMBIENT HUMIDITY MAX. 85% (NO CONDENSATION)		

AXIAL-FORCE Fa (N)	Fa=7		
DISTANCE a (mm)	5	10	15	20
RADIAL-FORCE Fr (N)	58	36	26	20
	AXIAL		RADIAL	
SHAFT PLAY (mm)	0.075		0.025	
AT LOAD MAX: (N)	10		5.0	

	SCALE FREE	APVD	S.K.	06.06.06
X	±0.5	CHKD		
1PL	±0.2	DRN	J.W.	06.06.06
2PL	±0.1	SIGNATURE		DATE
ANGLE	±30'			

TYPE OF CONNECTION (EXTERN)			MOTOR		
UNIPOLAR	BIPOLAR TWINDING	BIPOLAR SERIAL	CONNECTOR PIN NO.	LEADS	WINDING
A —	A —	A —	1	BLK	A
COM —	COM —		5	YEL	COM
A\ —		A\ —	3	GRN	A\
B —	B —		2	RED	B
COM —	COM —	B —	6	WHT	COM
B\ —		B\ —	4	BLU	B\

STEP	A	B	A\	B\	
1	+	+	–	–	CCW
2	–	+	+	–	
3	–	–	+	+	
4	+	–	–	+	CW

REV	DESCRIPTION	DATE	APVD

DWG.NO ST2818S1006

Figure 9.3: Technical data for the motor of axis 4 with part number ST2818S-1006.

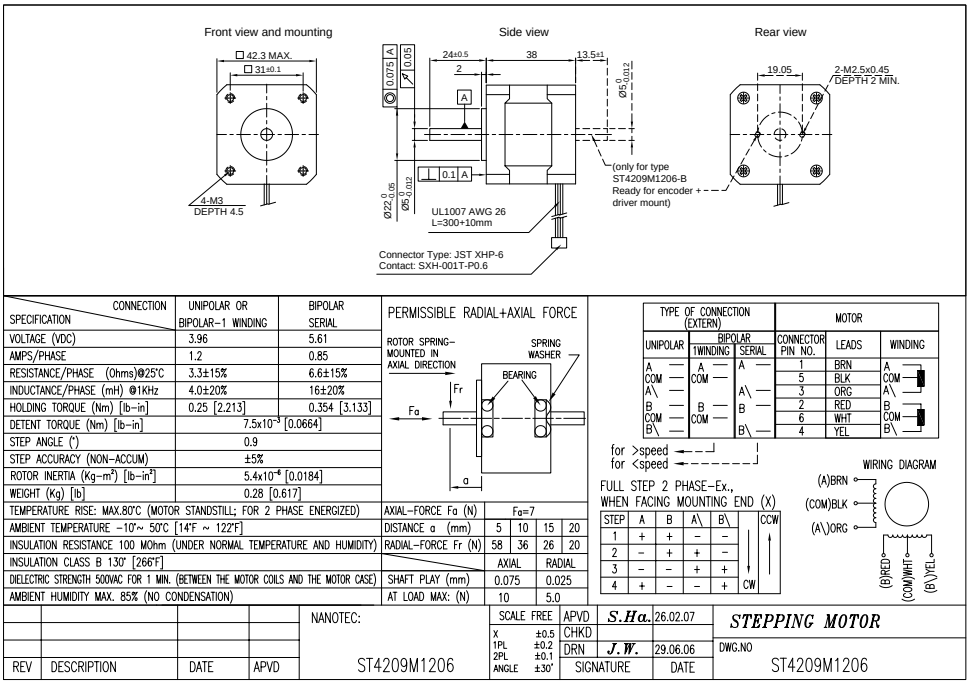

CONNECTION / SPECIFICATION	UNIPOLAR OR BIPOLAR–1 WINDING	BIPOLAR SERIAL
VOLTAGE (VDC)	3.96	5.61
AMPS/PHASE	1.2	0.85
RESISTANCE/PHASE (Ohms)@25°C	3.3±15%	6.6±15%
INDUCTANCE/PHASE (mH) @1KHz	4.0±20%	16±20%
HOLDING TORQUE (Nm) [lb–in]	0.25 [2.213]	0.354 [3.133]
DETENT TORQUE (Nm) [lb–in]	$7.5x10^{-3}$ [0.0664]	
STEP ANGLE (°)	0.9	
STEP ACCURACY (NON–ACCUM)	±5%	
ROTOR INERTIA (Kg–m^2) [lb–in^2]	$5.4x10^{-4}$ [0.0184]	
WEIGHT (Kg) [lb]	0.28 [0.617]	
TEMPERATURE RISE: MAX.80°C (MOTOR STANDSTILL; FOR 2 PHASE ENERGIZED)		
AMBIENT TEMPERATURE –10°~ 50°C [14°F ~ 122°F]		
INSULATION RESISTANCE 100 MOhm (UNDER NORMAL TEMPERATURE AND HUMIDITY)		
INSULATION CLASS B 130° [266°F]		
DIELECTRIC STRENGTH 500VAC FOR 1 MIN. (BETWEEN THE MOTOR COILS AND THE MOTOR CASE)		
AMBIENT HUMIDITY MAX. 85% (NO CONDENSATION)		

AXIAL–FORCE Fa (N)	Fa=7			
DISTANCE a (mm)	5	10	15	20
RADIAL–FORCE Fr (N)	58	36	26	20
	AXIAL		RADIAL	
SHAFT PLAY (mm)	0.075		0.025	
AT LOAD MAX: (N)	10		5.0	

STEP	A	B	A\	B\
1	+	+	–	–
2	–	+	+	–
3	–	–	+	+
4	+	–	–	+

Figure 9.4: Technical data for the motor of axis 3 with part number ST4209L1206.

Nanotec® PLUG & DRIVE

Sprachauswahl:

Suche: Go!

Startseite
Unternehmen
Produkte
Schrittmotoren
Schrittmotor in Schutzart IP 54/ IP65
Plug & Drive Motoren
Servomotoren BLDC
Servomotor in Schutzart IP 54/ IP65
Linear-Aktuatoren
Getriebe
Bremsen
Encoder
HEDS/ HEDL-5540
HEDS-6545
HEDM-1600
NEDS/ NEDL-5540
Schrittmotor-Steuerungen
Zubehör
Downloads
Presse
AGB
Jobs
Online Tools
Kontakt
Warenkorb

3-Kanal Encoder inkl. Anbau

Die Encoder von NANOTEC zeichnen sich neben der kleinen Bauform und der äußerst geringen Eigenmasse vor allem auch durch die schnelle und einfach Monatage aus.

Die Encoder der Baureihe **HEDS** sind 3-Kanal-Encoder mit einem 5V TTL Signal (A und B) und dem Indexsignal I˙ einmal auf 360°

Die **HEDL** Encoder besitzen einen Line-Trieber, der zusätzlich zum Encodersignal noch ein invertiertes Signal zur besseren Störsicherheit ausgibt. Dieser Encoder wird mit einem Flachbandkabel geliefert.

Bei den **HEDM** Encodern handelt es sich um 2-Kanal-Encoder (ohne Indexer), allerdings mit einer sehr hohen Auflösung.

Download
Übersicht Baureihe

Sonstiges
Dimensionen

Technische Daten **Preise & Bestellung**

Erhältliche Leistungsgrößen (andere auf Anfrage)

Typ	Impulse pro Umdrehung	für Wellen-durchmesser	Index	Line-Treiber	Art
		mm			
HEDS-5540 E06	200	6,35	x	-	
HEDS-5540 H14	400	5	x	-	
HEDS-5540 H06	400	6,35	x	-	
HEDS-5540 A02	500	3	x	-	
HEDS-5540 A14	500	5	x	-	
HEDS-5540 A12	500	6,0	x	-	
HEDS-5540 A06	500	6,35	x	-	
HEDS-5540 A13	500	8	x	-	
HEDS-5545-A10	500	10	x	-	Hohlwelle
HEDL-5540 E06	200	6,35	x	x	
HEDL-5540 H14	400	5	x	x	
HEDL-5540 H06	400	6,35	x	x	
HEDL-5540 A02	500	3	x	x	
HEDL-5540 A14	500	5	x	x	
HEDL-5540 A12	500	6,0	x	x	
HEDL-5540 A06	500	6,35	x	x	
HEDL-5540 A13	500	8,0	x	x	
HEDL-5545-A10	500	10	x	x	Hohlwelle
HEDS-6440-B06	1000	6,35	x	-	
HEDM-5500 B14	1000	5	-	-	
HEDM-5500 B06	1000	6,35	-	-	

Dimensionen

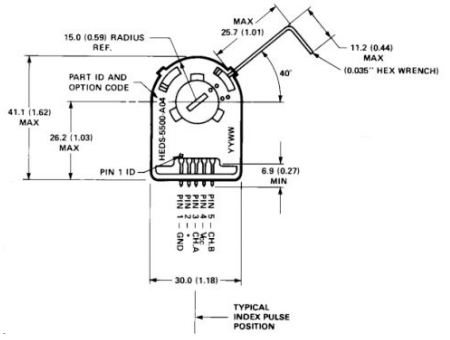

Figure 9.5: Technical data for the encoder of axis 4 with part number HEDL5540.

Nanotec®
PLUG & DRIVE

Sprachauswahl:

Suche: Go!

Startseite
Unternehmen
Produkte
Schrittmotoren
Schrittmotor in Schutzart IP 54/ IP65
Plug & Drive Motoren
Servomotoren BLDC
Servomotor in Schutzart IP 54/ IP65
Linear-Aktuatoren
Getriebe
Bremsen
Bremse BKE
Bremse BW
Archiv
Encoder
Schrittmotor-Steuerungen
Zubehör
Downloads
Presse
AGB
Jobs
Online Tools
Kontakt
Warenkorb

Bremse für Schrittmotoren und Servomotoren

Die Sicherheitsbremsen von Nanotec haben eine kompakte Flansch-Bauweise, sind verschleißarm und mit asbestfreien Reibbelägen ausgestattet und bieten eine einfache und schnelle Montage durch den fest eingestellten Luftspalt. Die Bremsen werden elektromagnetisch gelüftet und kommen überall dort zum Einsatz, wo bewegte Massen in kürzester Zeit zu verzögern sind, bzw. definiert gehalten werden müssen und das erzeugte Bremsmoment - auch bei Netzausfall - zur Verfügung steht.

Die Bremskraft wird mit Hilfe einer Druckfeder (Brake-BW), bzw. eines Permanentmagneten (Brake-BKE) aufgebracht. Bei allen Bremsen muß zum Lüften eine Spannung DC24V angelegt werden.

Das Nano-Brake-Modul (PWM-Regler) reduziert die Leistungs- und Wärmeverluste um 35%, ermöglicht eine höhere Stand- und Einschaltzeit der Motoren und eliminiert die externe Löschdiode.

Die Preise sind incl. Anbau. Sie können die Bremsen nicht selbst an einen Schrittmotor anbauen. Freianbau = Selbstmontage an andere Teile/ Achsen.

Technische Daten **Preise & Bestellung**

Erhältliche Leistungsgrößen (andere auf Anfrage)

Typ	Halte moment	für Wellen-durchmesser	Größe	Gewicht
	Ncm	mm	mm	kg
BRAKE-BKE-0,4-5,0	40	5	32	0,08
BRAKE-BKE-1,0-6,35	100	6,35	34	0,11
BRAKE-BKE-2,0-6,35	200	6,35	42	0,18

Figure 9.6: Technical data for the motor of axis 5 with part number BK-0,4-5,0.

Table 9.3: Setting of digital inputs within the MCFG software interface.

Description	Axis				
	1	2	3	4	5
LSR SMD	I1	I3	I17	I19	I5
LSL SMD	I2	I4	I18	I20	I6

9.6 Software structure

In order to present the software structure of the SASSU, a class diagram is provided in Fig. 9.7. It shows the different classes and their mutual dependencies.

9.7 Parameter settings of the MCU-3000 interface

As described in section 4.1.5, the motion of all axes is controlled by a motion control unit MCU-3000 PCI-card interface (Roesch und Walter, Schwanau, Germany). Along with the MCU-3000 comes the software interface MCFG which allows to specify motion and axes parameters. The settings made for the described SASSU system are listed in the following.

Axis parameters are shown in Fig. 9.8. Note that only one exemplary translational axis setting scenario is displayed. The other translational axes (namely 2 and 5) feature the same parameter settings.

Motion parameters are provided in Fig. 9.9. Note that all translational axes and all rotary axes feature the same motion parameter settings.

Another important setting of within the MCFG is the specification of the digital input bits. These input bits are set if the end stop functionality (positioning sensor and screw) is enabled. If set, the motion is stopped with the deceleration defined by the stop deceleration shown in Fig. 9.10.

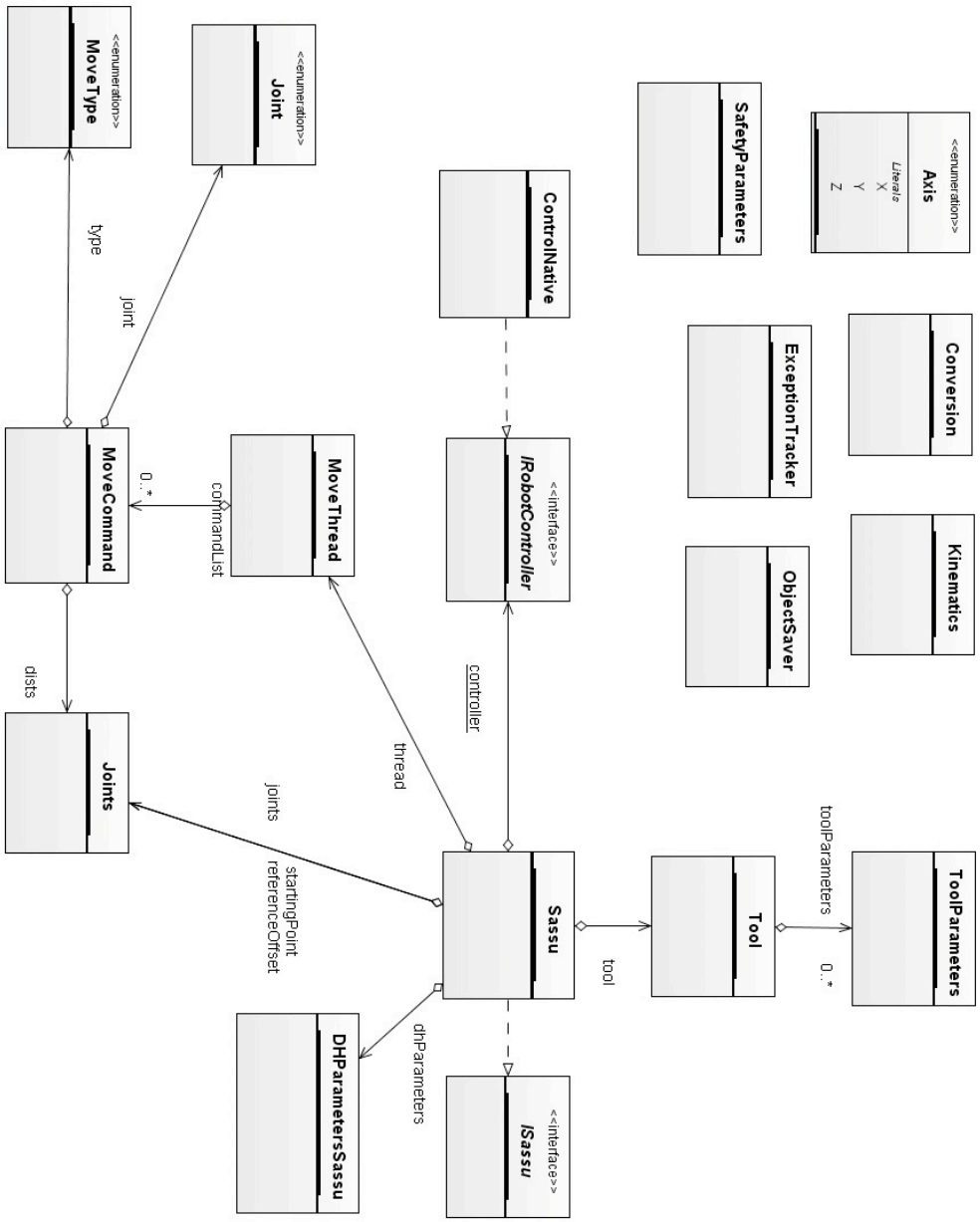

Figure 9.7: Class diagram of the motion control software showing the different classes and their mutual dependencies.

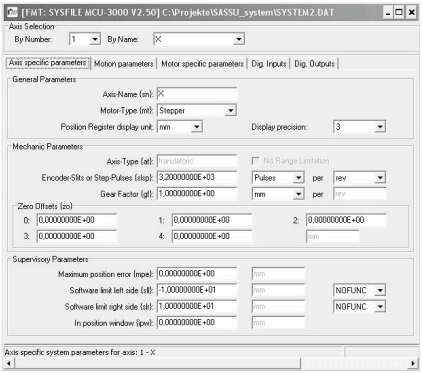

Axis parameters of axis 1

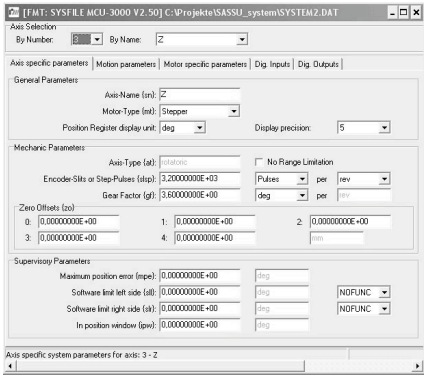

Axis parameters of axis 3

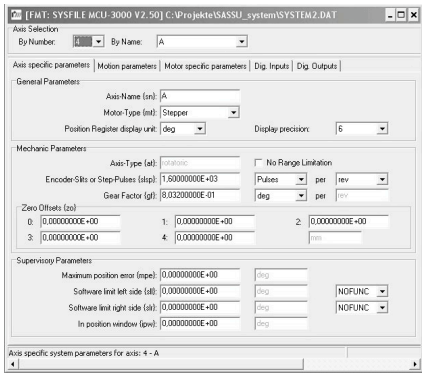

Axis parameters of axis 4

Figure 9.8: Parameter settings within the software interface MCFG of the MCU-3000. [top] Parameter settings of translational axis 1, the other two translational axes feature the same settings [middle] Parameter settings of rotary axis 3 [bottom] Parameter settings of rotary axis 4.

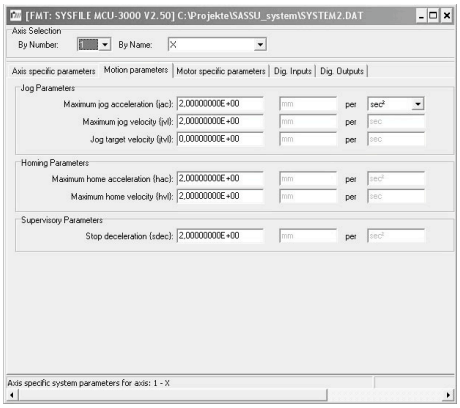

Motion parameters of the translational axes

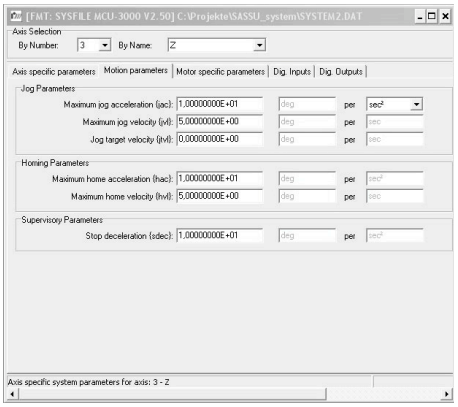

Motion parameters of the rotary axes

Figure 9.9: Motion settings within the software interface MCFG of the MCU-3000. [top] Parameter settings of translational axis 1, the other two translational axes feature the same settings [middle] Parameter settings of rotary axis 3, the other rotary axis features the same settings.

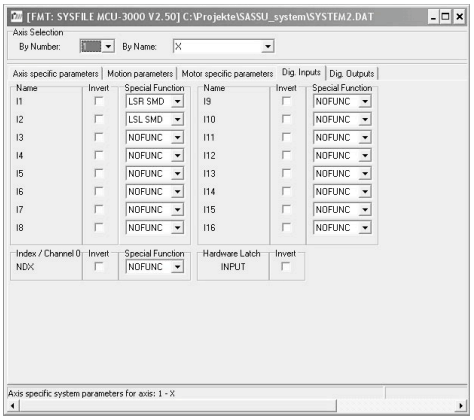

Digital input settings

Figure 9.10: Digital input settings within the software interface MCFG of the MCU-3000 for axis 1.

10 Curriculum vitae

Lukas Ramrath was born in Kronberg/Taunus, Germany, on January 22, 1979. He received his Master degree in mechanical engineering from the State University of New York at Buffalo in 2003 with a thesis on repetitive control for rejection of harmonic disturbances. In 2005, he received the degree Dipl.-Ing. for Control Engineering from Darmstadt University of Technology. From October 2005 to December 2008, he has been a Research Associate at the Institute for Robotics and Cognitive Science at the University of Luebeck, Germany. His research interest were in medical robotics and image processing for medical navigation.

Bibliography

[1] H.-J. Siegert and S. Bocionek. *Robotik: Programmierung intelligenter Roboter*. Springer, 1996.

[2] P.D. LeRoux, H. Das, S. Esquenzani, and P.J. Kelly. Robot-assisted microsurgery: A feasbility study in the rat. *Neurosurgery*, 48(3):584–589, 2001.

[3] URL `http://www.neurostar.de`.

[4] S.G. Waxman. *Clinical Neuroanatomy*. McGraw-Hill, 2002.

[5] D. Purves, G.J. Augustine, D. Fitzpatrick, W.C. Hall, A. LaMantia, J.O. McNamara, and S.M. Williams, editors. *Neuroscience*. Sinauer Associates, 2001.

[6] J. Jankovic and E. Tolosa, editors. *Parkinson's Disease and Movement Disorders*. Urban & Schwarzenberg, 1988.

[7] A.B. Young and J.B. Penney. Biochemical and functional organization of the basal ganglia. In *Parkinson's Disease and Movement Disorders*. Urban & Schwarzenberg, 1988.

[8] R.L. Albin, A.B. Young, and J.B. Penney. The functional anatomy of basal ganglia disorders. *Trends Neurosci*, 12:366–375, 1989.

[9] A.P. Georgopoulos M.R. DeLong, G.E. Alexander, M.D. Crutcher, S.J. Mitchell, and R.T. Richardson. Role of basal ganglia in limb movements. *Hum Neurobiol*, 2:235–244, 1984.

[10] G. C. Cotzias. L-dopa for parkinsonism. *N Engl J Med*, 278(14):630, 1968.

[11] A. Kumar, Z. Huang, and R. Fuente-Fernandez. Mechanisms of motor complications in treatment of parkinson's disease. *Adv. Neurol*, 91:193–199, 2003.

[12] B.L. Walter and J.L. Vitek. Surgical treatment for parkinson's disease. *Lancet Neurol*, 3(12):719–728, 2004.

[13] T.J. Putnam and E. Herz. Results of spinal pyramidotomy in the treatment of the parkinsonian syndrome. *Arch Neurol Psychiat Chicago*, 63:357–366, 1950.

[14] R. Meyers. Surgical experiments in the therapy of certain extrapyramidal diseases: A current evaluation. *Acta Neurol Scand Suppl*, 67:1–42, 1951.

[15] R.G. Grossmann. Surgery for movement disorders. In *Parkinson's Disease and Movement Disorders*. Urban & Schwarzenberg, 1988.

[16] L.V. Laitinen. Brain targets in surgery for parkinson's disease. Results of a survey of neurosurgeons. *J Neurosurgq*, 62:349–351, 1985.

[17] P.L. Gildenberg. Evolution of basal ganglia surgery for movement disorders. *Stereotactic and Functional Neurosurgery*, 84(4):131–135, 2006.

[18] A.L. Benabid, A. Benazzouz, and P. Pollak. Mechanisms of deep brain stimulation. *Movement Disorders*, 17:73–74, 2002.

[19] A.L. Benabid, P. Cinquin, S. Lavalle, J.F. Le Bas, J. Demongeot, and J. de Rougemont. Computer-driven robot for stereotactic surgery connected to CT scan and magnetic resonance imaging. *Appl Neurophysiol*, 50:153–154, 1987.

[20] A.L. Benabid, P. Pollak, C. Gerason, D. Hoffmann, D.M. Gao, M. Hommel, J.E. Perret, and J. de Rougemont. Long-term suppression of tremor by chronic stimulation of the ventral intermediate thalamic nucleus. *Lancet*, 337:403–406, 1991.

[21] F.J.G. Vingerhoets, J.G. Villemure, P. Temperli, C. Pollp, E. Pralong, and J. Ghika. Subthalamic DBS replaces levodopa in parkinsons disease: two-year follow up. *Neurology*, 58:396–401, 2002.

[22] R.E. Gross and A.M. Lozano. Advances in neurostimulation for movement disorders. *Neurological Research*, 22:247–258, 2000.

[23] V.M. Tronnier, W. Fogel, M. Krause, M. Bonsanto, J. Tronnier, A. Heck, K. Munkel, and S. Kunze. High frequency stimulation of the basal ganglia for the treatment of movement disorders: current status and clinical results. *Minimally Invasive Neurosurgery*, 45:91–96, 2002.

[24] P. Krack, A. Benazzouz, P. Pollak, P. Limousin, B. Piallat, D. Hoffmann, J. Xie, and A.L. Benabid. Treatment of tremor in parkinson's disease by subthalamic nucleus stimulation. *Movement Disorders*, 13:907–914, 1998.

[25] A. Benazzouz and M. Hallet. Mechanisms of deep brain stimulation. *Neurology*, 55:13–16, 2000.

[26] P.F. D'Haese, E. Cetinkaya, P.E. Konrad, C. Kao, and B.M. Dawant. Computer-aided placement of deep brain stimulators: From planning to intraoperative guidance. *IEEE Trans Med Imaging*, 24(11):1469–1478, 2005.

[27] M.L. Kringelbach, N. Jenkinson, S.L. Owen, and T.Z. Aziz. Translational principles of deep brain stimulation. *Nature Reviews Neuroscience*, 8:623–635, 2007.

[28] S.W. Jeon, M.A. Shure, K.B. Baker, D. Huang, A.M. Rollins, A. Chahlavi, and A.R. Rezai. A feasibility study of optical coherence tomography for guiding deep brain probes. *Journal of Neuroscience Methods*, 154:96–101, 2006.

[29] I. Hyde. A microelectrode and unicellular stimulation of single cells. *Biol Bull*, 40:130–133, 1921.

[30] F. Ervin and V. Mark. Stereotaxic thalatomy in the human: II. physiologic observations on the human thalamus. *Arch Neurol (Chic)*, 3:368–380, 1960.

[31] D. Albe-Fessard, G. Arfel, G. Guiot, and et al. Derviation d'activités spontanées et evoquées dans des structures cérébrales perfondes de l'homme. *Rev Neurol (Paris)*, 106:89–105, 1962.

[32] R. Hassler, F. Mundinger, and T. Riechert. Pathophysiology of tremor at rest derived from the correlation of anatomical and clinical data. *Confin Neurol*, 32:79–87, 1970.

[33] H. Bergman, T. Wichmann, and M.R. DeLong. Reversal of experimental parkinsonism by lesions of the subthalamic nucleus. *Science*, 249:494–506, 1990.

[34] T. Wichmann, H. Bergman, and M.R. DeLong. The primate subthalamic nucleus: I. functional properties in intact animals. *J Neurophysiol*, 72:494–506, 1994.

[35] T. Wichmann, H. Bergman, and M.R. DeLong. The primate subthalamic nucleus: II. neuronal activity in the mptp model of parkinsonism. *J Neurophysiol*, 72:507–520, 1994.

[36] T. Wichmann, H. Bergman, and M.R. DeLong. The primate subthalamic nucleus: III. changes in motor behavior and neuronal activity in the internal pallidum induced by subthalamic inactivation in the mptp model of parkinsonism. *J Neurophysiol*, 72:521–530, 1994.

[37] A.M. Lozano, W.D. Hutchinson, R.R. Tasker, A.E. Lang, F. Junn, and J.O. Dostrovsky. Microelectrode recordings define the ventral posteromedial pallidotomy target. *Stereotact Funct Neurosurg*, 71:153–163, 1998.

[38] M. Dogali, A. Beric, D. Sterio, D. Eidelberg, E. Fazzini, S. Takikawa, D.R. Samelson, O. Devinsky, and E.H. Kolodny. Anatomic and physiological considerations in pallidotomy for parkinson's disease. *Stereotact Funct Neurosurg*, 62:53–60, 1994.

[39] M.C. Rodriguez-Oroz, M. Rodriguez, J. Guridi, K. Mewes, V. Chockkman, J. Vitek, M.R. DeLong, and J.A. Obeso. The subthalamic nucleus in parkinson's disease: Somatotopic organization and physiological characteristics. *Brain*, 124: 1777–1790, 2001.

[40] C. Moll, A. Struppler, and A. Engel. Intraoperative Mikroelektrodenableitungen in den Basalganglien des Menschen. *Neuroforum*, 1:11–20, 2005.

[41] E.N. Brown, R.E. Kass, and P.P. Mitra. Multiple neural spike train data analysis: State-of-the-art and future challenges. *Nature Neuroscience*, 7(7):456–461, 2004.

[42] Y. Gao, I. Kontoyiannis, and E. Bienenstock. From the entropy to the statistical structure of spike trains. In *2006 IEEE International Symposium on Information Theory*, Seattle, WA, USA, July 2006.

[43] M.S. Lewicki. A review of methods for spike sorting: The detection and classification of neural action potentials. *Network: Comput. Neural Syst.*, 9:53–78, 1998.

[44] K. Menne and U.G. Hofmann. Automatic neurophysiological identification of the human subthalamic nucleus for the implantation of deep brain stimulation electrodes based on statistical signal processing methods and unsupervised classification. In *EMBEC 2005 - 3rd European Medical & Biological Engineering Conference*, 2005.

[45] M.E. Brezinski. *Optical Coherence Tomography - Principles and Application*. Academic Press, 2006.

[46] J.G. Fujimoto. Biomedical imaging using optical coherence tomography. In *Quantum Electronics Conference, IQEC. Technical Digest*, 1998.

[47] B.E. Bouma and G.J. Tearney. *Handbook of Optical Coherence Tomography*. Marcel Dekker, Inc., 2002.

[48] K. Bizheva, A. Unterhuber, B. Hermann, B. Povazay, H. Sattmann, W. Drexler, A. Stingl, T. Le, M. Mei, and R. Holzwarth. Imaging ex vivo and in vitro brain morphology in animal models with ultrahigh resolution optical coherence tomography. *J. Biomedical Optics*, 9:719–724, 2004.

[49] H.J. Boehringer, J. Leppert, E. Lankenau, G. Huettmann, and A. Giese. Non-invasive intraoperative optical coherence tomography of the resection cavity during surgery of intrinsic brain tumours. In *57. Jahrestagung der Deutschen Gesellschaft für Neurochirurgie*, May 2006.

[50] M.S. Jafri, S. Farhang, R.S. Tang, N. Desai, P.S. Fishman, R.G. Rohwer, C. Tang, and J.M. Schmitt. Optical coherence tomography in the diagnosis and treatment of neurological disorders. *Journal of Biomedical Optics*, 10(5):1–11, 2005.

[51] J.M. Schmitt, S.H. Xiang, and K.M. Yung. Speckle in optical coherence tomography. *Journal of Biomedical Optics*, 4:95–105, 1999.

[52] R.R. Tasker. *Stereotactic and Functional Neurosurgery*. McGraw-Hill, 1998.

[53] V. Horsley and R.H. Clarke. The structure and functions of the cerebellum examined by a new method. *Brain*, 31:45–124, 1908.

[54] E.A. Spiegel, H.T. Wycis, and M. Marks. Stereotaxic apparatus for operations on the human brain. *Science*, 106:349–350, 1947.

[55] L. Leksell. A stereotaxic apparatus for intracerebral surgery. *Acta Chir Scand*, 99: 229–233, 1949.

[56] J. Tailarach, M. David, P. Tournoux, H. Corredor, and T. Kvasina. *Atlas d'Anatomie Stéréotaxique*. Masson et Cie, 1957.

[57] T. Riechert and M. Wolff. New aiming apparatus for intracranial electric derivation and exclusion. *Arch Psychiatry*, 186:225–230, 1951.

[58] G.N. Hounsfield, J. Ambrose, B.J. Perry, and C. Bridges. Computerized transverse axial scanning (tomography). *British Journal of Radiology*, 46:1016–1051, 1973.

[59] N. Tamaki and K. Ehara, editors. *Computer-Assisted Neurosurgery*. Springer, 1997.

[60] R. A. Hayne and R. Meyers. An improved model of a human stereotaxic instrument. *J. Neurosurg.*, 7:463–466, 1950.

[61] E.M. Todd. *Todd-Wells Manual Stereotaxic Procedures*. Codman & Shurtleff, 1967.

[62] R.A. Brown. A computerized tomography-computer graphics approach to stereotaxic localization. *J Neurosurg*, 50:715–720, 1979.

[63] P.J. Kelly. *Tumor Stereotaxis*. W.B. Saunders Company, 1991.

[64] E. Watanabe, T. Watanabe, S. Manaka Y. Myanagi, and K. Takakura. Three-dimensional digitizer (neuronavigator): New equipment for computer tomography-guided stereotaxic surgery. *Surg Neurol*, 27:543–547, 1987.

[65] Y. Kosugi, E. Wantanabe, J. Goto, T. Watanabe, S. Yoshimoto, K. Takakura, and J. Ikebe. An articulated neurosurgical navigation system using MRI and CT images. *IEEE Trans Biomed Eng*, 35:147–1562, 1988.

[66] D.W. Roberts, J.W. Strohbehn, J.F. Hatch, W. Murry, and H. Kettenberger. A frameless stereotaxic integration of computerized tomographic imaging and the operating microscope. *J Neurosurg*, 65:545–549, 1986.

[67] R. L. Galloway. *Frameless Stereotactic Systems*, chapter 21, pages 1–77182. McGraw-Hill, 1998.

[68] E. Watanabe, Y. Mayanagi, Y. Kosugi, S. Manaka, and K. Takakura. Open surgery assisted by the neuronavigator, a stereotactic articulated, sensitive arm. *Neurosurgery*, 28:792–800, 1991.

[69] E.M. Friets, W. Strohbehn, J.F. Hatch, and D.W. Roberts. A frameless stereotactic operating microscope for neurosurgery. *IEEE Trans Biomed Eng*, 36:608–617, 1989.

[70] R.L. Galloway, R.J. Maciunas, W.A. Bass, and D. Crouch. An optical device for interactive image-guided neurosurgery. In *Proc Annual Conf IEEE EMBS*, volume 15, pages 954–955, 1993.

[71] B.L. Guthrie, R. Kaplan, and P.J. Kelly. Neurosurgical stereotactic operating arm. *Stereotactic Funct Neurosurg*, 54:497–505, 1990.

[72] S.J. Zinreich, S.A. Tebo, D.M. Long, H. Brem, D.E. Mattox, M. E. Loury, C. A. Vander Kolk, W.M. Koch, W.W. Kennedy, and R.N. Bryan. Frameless stereotaxic integration of CT imaging data: Accuracy and initial applications. *Radiology*, 188:735–742, 1993.

[73] A. Schweikard, M. Bodduluri, and J.R. Adler. Planning for camera-guided radiosurgery. *IEEE Trans Robotics and Automation*, 14(6):951–962, 1998.

[74] American Society for Testing and Materials Committee F-4.05. Standard performance specification for cerebral stereotactic instruments. Technical report, American Society for Testing and Materials, 1990.

[75] R.J. Maciunas, R.L. Galloway, and J.W. Latimer. The application accuracy of stereotactic frames. *Neurosurgery*, 35:682–695, 1994.

[76] R.L. Galloway, R.J. Maciunas, and J.W. Latimer. The accuracies of four stereotactic frame systems: An independent assessment. *Biomed Instrum Technol*, 25: 457–460, 1991.

[77] R.J. Maciunas, R.L. Galloway, J.W. Latimer, C. Cobb, E. Zaccharias, A. Moore, and V.R. Mandava. An independent application accuracy evaluation of stereotactic frame systems. *Stereotact Func Neurosurg*, 58:103–107, 1992.

[78] R.L. Galloway and R.J. Maciunas. Stereotactic neurosurgery. *Crit Rev Biomed Eng*, 18:181–205, 1990.

[79] P. Grunert, J. Maeurer, and W. Mueller-Forell. Accuracy of stereotactic coordinate transformation using a localisation frame and computed tomographic imaging-part I. influence of the mathematical and physical properties of CT on the image of rods of the localisation frame and the determination of their centres. *Neurosurg Rev*, 22: 173–187, 1999.

[80] P. Grunert. Accuracy of stereotactic coordinate transformation using a localisation frame and computed tomographic imaging-part II. analysis of matrix-based coordinate transformation. *Neurosurg Rev*, 22:188–203, 1999.

[81] R.L. Galloway, R.J. Maciunas, and C.A. Edwards. Interactive image-guided neurosurgery. *IEEE Trans Biomed Eng*, 39:1226–1231, 1992.

[82] N.D. Kitchen, L. Lemieux, and D.G.T. Thomas. Accuracy in frame-based and frameless stereotaxy. *Stereotact Func Neurosurg*, 61:195–206, 1993.

[83] Y.S. Kwoh, J. Hou, E.A. Jonckheere, and S. Hayati. A robot with improved absolute positioning accuracy for CT guided stereotactic brain surgery. *IEEE Trans Biomed Eng*, 35:153–160, 1988.

[84] C.W. Burckhart, P. Flury, and D. Glauser. Stereotactic brain surgery. *IEEE Engineering in Medicine and Biology*, 14:314–317, 1995.

[85] M. Zimmermann, R. Krishnan, A. Raabe, and V. Seifert. Robot-assisted navigated neuroendoscopy. *Neurosurgery*, 51:1446–1451, 2002.

[86] K. Masamune, E. Kobayashi, Y. Masutani, M. Suzuki, T. Dohi, H. Iseki, and K. Takakura. Development of an MRI-compatible needle insertion manipulator for stereotactic neurosurgery. *Journal of Image Guided Surgery*, 1:242–248, 1995.

[87] S. Lavallee, J. Troccaz, L. Gaborit, P. Cinquin, A.L. Benabid, and D. Hoffmann. Image-guided operating robot: A clinical application in stereotactic neurosurgery. In R.H. Taylor, S. Lavallee, G.C. Burdea, and R. Mosges, editors, *Computer-Integrated Surgery*. MIT Press, 1995.

[88] M. Shoham, H. Liebermann, E.C. Benzel, D. Togawa, E. Zehavi, B. Zilberstein, M. Roffman, A. Bruskin, A. Fridlander, L. Joskowicz, S. Brink-Danan, and N. Knollier. Robotic assisted spinal surgery - from concept to clinical practice. *Computer Aided Surgery*, 12:105–115, 2007.

[89] M.F. Lythgoe, N.R. Sibson, and N.G. Harris. Neuroimaging of animal models of brain disease. *British Medical Bulletin*, 65:235–257, 2003.

[90] M. LeDoux, editor. *Animal Models of Movement Disorders*. Elsevier, 2005.

[91] A. Cenci, I.Q. Whishaw, and T. Schallert. Animal models of neurological deficits: How relevant is the rat? *Nature Reviews Neuroscience*, 3:574–579, 2002.

[92] G. Paxinos and C. Watson. *The Rat Brain in stereotaxic coordinates*. Elsevier Inc., 2007.

[93] R.K.W. Schwarting and J.P Huston. The unilateral 6-hydroxydopamine lesion model in behavioural brain research. Analysis of functional deficits, recovery and treatments. *Prog. Neurobiol*, 50:275–331, 1996.

[94] L.W. Swanson. *Brain Maps: Structure of the Rat Brain*. Elsevier Science Pub Co, 1st edition, 1993.

[95] J.G. Bjaalie. Localization in the brain: New solutions emerging. *Nature Reviews Neuroscience*, 3:322–325, 2002.

[96] M. Litza, A. Hiller, A. Moser, and U.G. Hofmann. Deep brain stimulation and simultaneous neurotransmitter detection. In *Biomedizinische Technik*, volume 50 (Supp 1), pages 1487–1488. Congress of the German Society for Biomedical Engineering, 2005.

[97] H.T. Chung, Y.S. Chung, D.G. Kim, S.H. Paek, and K.-T. Cho. Development of a stereotactic device for gamma knife irradiation of small animals. *J. Korean Neurosurg Soc*, 43:26–30, 2008.

[98] U. Knopp, W. Jensen, D.T. Kewley, J.M. Bower, K. Yoshida, and U.G. Hofmann. Compression of the cerebral cortex during corticotomy: A study of dimpling in rats. In *55. Ann' Jahrestagung der Deutschen Gesellschaft für Neurochirurgie, German Medical Sciences.*, 2004.

[99] URL `http://www.thomasrecording.de`.

[100] L. Ramrath, U.G. Hofmann, and A. Schweikard. Spherical assistant for stereotactic surgery. In *Proc. 2007 IEEE International Conference on Intelligent Robots and Systems*, San Diego, CA, USA, 2007.

[101] L. Ramrath, U.G. Hofmann, and A. Schweikard. A robotic assistant for stereotactic neurosurgery on small animals. *Int. J. on Medical Robotics and Computer Assisted Surgery*, 2008.

[102] L. Ramrath, S. Vogt, W. Jensen, U.G. Hofmann, and A. Schweikard. Computer- and robot-assisted stereotaxy for high-precision small animal brain exploration. *Biomedizinische Technik*, accepted for publication, 2008.

[103] J.J. Craig. *Introduction to Robotics*. Pearson Prentice Hall, Zug, Switzerland, 2005.

[104] M.W. Spong, S. Hutchinson, and M. Vidyasagar. *Robot Modeling and Control*. John Wiley & Sons, Inc., 2006.

[105] T. Arai, K. Cleary, T. Nakamura, H. Adachi, and K. Homma. Design, analysis and construction of a prototype parallel link manipulator. *IEEE International Workshop on Intelligent Robotics*, 1990.

[106] J.-P. Merlet. *Parallel Robots*. Kluwer Academic Publishers, 2000.

[107] M.J.H. Lum, J. Rosen, M.N. Sinanan, and B. Hannaford. Kinematic optimization of a spherical mechanism for a minimally invasive surgical robot. In *IEEE International Conference on Robotics and Automation*, pages 829–834, New Orleans, USA, April 2004.

[108] J. Rosen, M. Lum, D. Trimble, B. Hannaford, and M. Sinanan. Spherical mechanism analysis of a surgical robot for minimally invasive surgery - analytical and experimental approaches. In *Studies in Health Technology and Informatics*, pages 442–448, Long Beach, CA, 2005. Medicine Meets Virtual Reality.

[109] P. Shiakolas, K. Conrad, and T. Yih. On the accuracy, repeatability, and degree of influence of kinematics parameters for industrial robots. *The International Journal of Modeling and Simulation*, 22(3):1–10, 2002.

[110] A. Albu-Schaeffer and G. Hirzinger. Parameter identification and passivity based joint control for a 7DOF torque controlled light weight robot. In *Proc. 2001 IEEE Int. Conf. on Robotics and Automation*, pages 2852–2858, 2001.

[111] O. Khatib, J.J. Craig, and T. Lozanzo-Perez, editors. *The Robotics Review*, chapter A Survey of Kinematic Calibration, pages 207–242. MIT Press, Cambridge, MA, 1989.

[112] L. Beyer. *Genauigkeitssteigerung von Industrierobotern*. PhD thesis, Helmut-Schmidt-Universitaet, Hamburg, 2004.

[113] J. Canny. A computational approach to edge detection. *IEEE Trans on Pattern Analysis and Machine Intelligence*, 8(6):679–698, 1986.

[114] K. Kozlowski. *Modelling and Identification in Robotics*. Springer, London, 1998.

[115] C.H. An, C.G. Atkeson, and J.M. Hollerbach. *Model-Based Control of a Robot Manipulator*. MIT Press, 1988.

[116] M.W. Spong. Modeling and control of elastic joint robots. *Journal of Dynamic Systems, Measurement, and Control*, 109(4):310–319, 1987.

[117] L.K. Huat, editor. *Industrial Robotics, Programming, Simulation, and Application*. Pro Literatur Verlag, Germany, 2006.

[118] G. N. Vanderplaats. *Numerical Optimization Techniques for Engineering Design*. Vanderplaats Research & Development, Inc., 2001.

[119] F. Gasca and L.Ramrath. Model-based detection of white matter in optical coherence tomography data. In *Intl. Conference IEEE EMBS*, Lyon, France, August 2007.

[120] L. Ramrath, U.G. Hofmann, G. Huettmann, A. Moser, and A. Schweikard. Towards automated OCT-based identification of white brain matter. In *Bildverarbeitung für die Medizin*, Munich, Germany, March 2007.

[121] L. Ramrath, H. Fuellgraf, C. Winter, U. Hofmann, G. Huettmann, A. Moser, and A. Schweikard. 3D visualization and identification of rat brain structures using optical coherence tomography. In *5. Jahrestagung der Dt. Gesellschaft fuer Computer- und Roboterassistierte Chirurgie*, Hannover, Germany, 2006.

[122] L. Ramrath, B.M. Pohl, S. Loeffler, K. Mankodiya, Y. Xie, U.G. Hofmann, and A. Schweikard. Single fibre optical coherence tomography for brain imaging - a preliminary in vitro study. In *7. Jahrestagung der Dt. Gesellschaft fuer Computer- und Roboterassistierte Chirurgie*, Leipzig, Germany, 2008.

[123] Y. Chen and G. Medioni. Object modeling by registration of multiple range images. In *Proc. IEEE Conf. on Robotics and Automation*, 1991.

[124] Y. Pan, J. Rosperich, R. Birngruber, and R. Engelhardt. Low-coherence optical-tomography in turbid-tissue: Theoretical analysis. *Applied Optics*, 34(28):6564–6574, 1995.

[125] J. Schmitt. Optical coherence tomography: A review. *IEEE J. Sel. Top. Quant. Electron.*, 5:1205–1215, 1999.

[126] A.E. Desjardins, B.J. Vakoc, G.J. Tearney, and B.E. Bouma. Speckle reduction in OCT using massively-parallel detection and frequency-domain ranging. *Optics Express*, 14:4736–4745, 2006.

[127] M. Pircher, E. Gotzinger, R. Leitgeb, A.F. Fercher, and C.K. Hitzenberger. Speckle reduction in optical coherence tomography by frequency compounding. *J. Biomed. Optics*, 8:565–569, 2003.

[128] J.F. deBoer, S.M. Drinivas, B.H. Park, T.H. Pham, Z.P. Chen, T.E. Milner, and J.S. Nelson. Polarization effects in optical coherence tomography of various biological tissues. *IEEE J. Selections Top. Quantum Electron.*, 5:1200–1204, 1999.

[129] J.S. Lee. Digital image enhancement and noise filtering by use of local statistics. *IEEE Trans. Pattern Anal. Mach. Intell.*, PAMI-2:165–168, 1980.

[130] V.S. Frost, J.A. Stiles, K.S. Shanmugan, and J.C. Holtzmann. A model for radar images and its application to adaptive filtering of multiplicative noise. *IEEE Trans. Pattern Anal. Mach. Intell.*, 4:157–165, 1982.

[131] D.T. Kuan, A.A. Sawchuk, T.C. Strand, and P. Chavel. Adaptive restoration of images with speckle. *IEEE Trans. Acoustics, Speech, and Signal Processing*, 35: 373–383, 1987.

[132] P. Perona and J. Malik. Scale-space and edge detection using anisotropic diffusion. *IEEE Trans. Pattern Anal. Mach. Intell.*, 12(7):629–639, 1990.

[133] J. Weickert. Coherence-enhancing diffusion filtering. *Int. J. of Computer Vision*, 31(2/3):111–127, 1999.

[134] G. Gilboa, N. Sochen, and Y.Y. Zeevi. Image enhancement and denoising by complex diffusion processes. *IEEE Trans. Pattern Anal. Mach. Intell.*, 25(8):1020–1036, 2004.

[135] H.M. Salinas and D.C. Fernandez. Comparison of PDE-based nonlinear diffusion approaches for image enhancement and denoising in optical coherence tomography. *IEEE Trans Med Imag*, 26(6):761–771, 2007.

[136] F. Sattar, L. Floreby, G. Salomonsson, and B. Loevstroem. Image enhancement based on a nonlinear multiscale method. *IEEE J. Image Processing*, 6(6):888–895, 1995.

[137] X. Hao, S. Gao, and X. Gao. A novel multiscale nonlinear thresholding method for ultrasonic speckle suppression. *IEEE J. Medical Image Processing*, 18(9):787–794, 1999.

[138] L.S. Dolin. A theory of optical coherence tomography. *Radiophys. Quantum Electronics*, 41(10):850–873, 1998.

[139] P.E. Andersen, L. Thrane, H.T. Yura, A. Tycho, T.M. Jorgensen, and M.H. Frosz. Advanced modelling of optical coherence tomography systems. *Phys. Med. Biol.*, 49:1307–1327, 2004.

[140] I. Turchin, E. Sergeeva, L. Dolin, V. Kamensky, and N. Shakhova. Novel algorithm of processing optical coherence tomography images for differentiation of biological tissue pathologies. *Journal of Biomedical Optics*, 10(6):1–11, 2005.

[141] J.M. Schmitt, A. Knuttel, M. Yadlowsky, and M.A. Eckhaus. Optical-coherence tomography of a dense tissue: Statistics of attenuation and backscattering. *Phys. Med. Biol.*, 39:1705.1720, 1994.

[142] S.W. Jeon, M.A. Shure, K.B. Baker, and et.al. Optical coherence tomography and optical coherence domain reflectometry for deep brain stimulation probe guidance. In K.E. Bartels, editor, *Photonic Therapeutics and Diagnostics. Proceedings of the SPIE*, volume 5686, pages 487–494, 2005.

[143] M. Ciuc, P. Bolon, E. Trouve, V. Buzuloui, and J.-P. Rudant. Adaptive-neighborhood speckle removal in multitemporal synthetic aperture radar images. *Applied Optics*, 40(32):5954–5966, 2001.

[144] E. Lankenau, D. Klinger, C. Winter, A. Malik, H. Mueller, S. Oelckers, H.-P. Pau, T. Just, and G. Huettmann. *Combining Optical Coherence Tomography (OCT) with an Operating Microscope*. Springer, 2007.

[145] D.L. Pham, C. Xu, and J.L. Prince. Current methods in medical imaging. *Annu. Rev. Biomed. Eng.*, 2:315–337, 2000.

[146] R.M. Haralick. Image segmentation techniques. *Comput. Vision Graph. Image Proc.*, 29:100–132, 1985.

[147] D.C. Fernandez, H.M. Salinas, and C.A. Puliafito. Automated detection of retinal layer structures on optical coherence tomography images. *Optics Express*, 13(25): 10200–10216, 2005.

[148] W.T. Freeman and E.H. Adelson. The design and use of steerable filters. 13(9): 891–906, 1991.

[149] S. Roth and M.J. Black. Steerable random fields. In *Int. Conf. on Computer Vision, ICCV*, 2007.

[150] J. Polzehl and V. Spokoiny. Spatially adaptive regression approach: Propagation-separation method. Preprint, Weierstrass-Institut, Berlin, 2004.

[151] J. Polzehl and V. Spokoiny. Local likelihood modeling by adaptive weights smoothing. Technical report, Weierstrass-Institut für Angewandte Analysis und Stochastik, 2002.

[152] M. Jacob and M. Unser. Design of steerable filters for feature detection using canny-like criteria. *IEEE Trans on Pattern Analysis and Machine Intelligence*, 26 (8):1007–1019, 2004.

[153] J.-M. Geusebroek, A.W.M. Smeulders, and J. van de Weijer. Fast anisotropic Gauss filtering. *IEEE Journal of Image Processing*, 12(8):938–943, 2003.

[154] B.M. Pohl, L. Ramrath, and U.G. Hofmann. A force controlled micro-drill for roboterized small animal stereotaxy. In *MBEC 2004 - 4th European Medical & Biological Engineering Conference*, Amsterdam, Netherlands, 2008.

[155] S. Loeffler, L. Ramrath, U.G. Hofmann, A. Schweikard, and A. Moser. Robot assisted stereotaxic targeting for STN-DBS in the rat brain. In *Klin. Neurophysiol. (1), 52. Jahrestagung der DGKN*, Magdeburg, 2008.

[156] R. Paul. *Robot Manipulators - Mathematics, Programming, and Control*. MIT Press, 7th edition, 1986.

[157] G. Xu and Z. Zhang. *Epipolar Geometry in Stereo Motion and Object Recognition*. Springer, 1996.

[158] J.D. Victor. Spike train metrics. *Current Opinion in Neurobiology*, 15:585–592, 2006.

[159] B.C. Wheeler and W.J. Heetderks. A comparison of techniques for classification of multiple neural signals. *IEEE J Biomed Eng*, 29:752–759, 1982.

[160] C. Koch and I. Segev, editors. *Methods in Neural Modeling - From Ions to Networks*. MIT Press, 2 edition, 1998.

[161] W.D. Hutchinson, R.J. Allan, H. Opitz, R. Levy, J.O. Dostrovsky, A.E. Lang, and A.M. Lozano. Neurophysiological identification of the subthalamic nucleus in surgery for parkinson's disease. *Ann Neurol*, 44(4):622–628, 1998.

[162] J. Favre, J.M. Taha, T. Baumann, and K.J. Burchiel. Computer analysis of the tonic, phasic, and kinesthetic activity of pallidal discharges in parkinson patients. *Surg Neurol*, 51:665–673, 1999.

[163] K. Menne. *Computerassistenz zur Implantation von Tiefenhirnstimulatoren - Von der Merkmalsbestimmung fuer Gehirnsignale zur Datenbank für Elektrophysiologie*. PhD thesis, University of Luebeck, 2005.

[164] B. Mulgrew, P. Grant, and J. Thompson. *Digital Signal Processing*. Palgrave MacMillan, 2003.

[165] A. Pesenti, M. Rohr, M. Egidi, P. Rampini, F. Tamma, M. Locatelli, E. Caputo, V. Chiesa, A. Bianchi, S. Barbieri, G. Baselli, and A. Priori. The subthalamic nucleus in parkinson's disease: Power spectral density analysis of neural intraoperative signals. *Neurol Sci*, 24:367–374, 2003.

[166] T.A. Lasko, J.G. Bhagwat, K.H. Zhou, and L. Ohno.Machado. The use of receiver operating characteristic curves in biomedical informatics. *J. of Biomedical Informatics*, 38(5):404–415, 2005.

[167] W.P. Jones and G.W. Furnas. Pictures of relevance: a geometric analysis of similarity measure. *Journal American Society for Information Science*, 38:420–422, 1987.

[168] V. Chalana and Y. Kim. A methodology for evaluation of boundary detection algorithms on medical images. *IEEE Trans. on Med. Imaging*, 16:642–652, 1997.

[169] W.K. Pratt. *Digital Image Processing*. Wiley, New York, NY, USA, 1978.